THE FIRST *FERMI*-LAT GAMMA-RAY BURST CATALOG

M. Ackermann[1], M. Ajello[2], K. Asano[3], M. Axelsson[4,5,6], L. Baldini[7], J. Ballet[8], G. Barbiellini[9,10], D. Bastieri[11,12], K. Bechtol[13], R. Bellazzini[14], P. N. Bhat[15], E. Bissaldi[16], E. D. Bloom[13], E. Bonamente[17,18], J. Bonnell[19,20], A. Bouvier[21], T. J. Brandt[19], J. Bregeon[14], M. Brigida[22,23], P. Bruel[24], R. Buehler[13], J. Michael Burgess[15], S. Buson[11,12], D. Byrne[25], G. A. Caliandro[26], R. A. Cameron[13], P. A. Caraveo[27], C. Cecchi[17,18], E. Charles[13], R. C. G. Chaves[8], A. Chekhtman[28,69], J. Chiang[13], G. Chiaro[12], S. Ciprini[29,30], R. Claus[13], J. Cohen-Tanugi[31], V. Connaughton[15], J. Conrad[5,32,33,70], S. Cutini[29,30], F. D'Ammando[34], A. de Angelis[35], F. de Palma[22,23], C. D. Dermer[36], R. Desiante[9], S. W. Digel[13], B. L. Dingus[37], L. Di Venere[13], P. S. Drell[13], A. Drlica-Wagner[13], R. Dubois[13], C. Favuzzi[22,23], E. C. Ferrara[19], G. Fitzpatrick[25], S. Foley[25,38], A. Franckowiak[13], Y. Fukazawa[39], P. Fusco[22,23], F. Gargano[23], D. Gasparrini[29,30], N. Gehrels[19], S. Germani[17,18], N. Giglietto[22,23], P. Giommi[29], F. Giordano[22,23], M. Giroletti[34], T. Glanzman[13], G. Godfrey[13], A. Goldstein[15], J. Granot[40], I. A. Grenier[8], J. E. Grove[36], D. Gruber[38], S. Guiriec[19], D. Hadasch[26], Y. Hanabata[39], M. Hayashida[13,41], D. Horan[24], X. Hou[42], R. E. Hughes[43], Y. Inoue[13], M. S. Jackson[5,6], T. Jogler[13], G. Jóhannesson[44], A. S. Johnson[13], W. N. Johnson[36], T. Kamae[13], J. Kataoka[45], T. Kawano[39], R. M. Kippen[37], J. Knödlseder[46,47], D. Kocevski[13], C. Kouveliotou[48], M. Kuss[14], J. Lande[13], S. Larsson[4,5,32], L. Latronico[49], S.-H. Lee[50], F. Longo[9,10], F. Loparco[22,23], M. N. Lovellette[36], P. Lubrano[17,18], F. Massaro[13], M. Mayer[1], M. N. Mazziotta[23], S. McBreen[25,38], J. E. McEnery[19,20], S. McGlynn[51], P. F. Michelson[13], T. Mizuno[52], A. A. Moiseev[20,53], C. Monte[22,23], M. E. Monzani[13], E. Moretti[5,6], A. Morselli[54], S. Murgia[13], R. Nemmen[19], E. Nuss[31], T. Nymark[5,6], M. Ohno[55], T. Ohsugi[52], N. Omodei[13], M. Orienti[34], E. Orlando[13], W. S. Paciesas[56], D. Paneque[13,57], J. H. Panetta[13], V. Pelassa[15], J. S. Perkins[19,53,58,59], M. Pesce-Rollins[14], F. Piron[31], G. Pivato[12], T. A. Porter[13], R. Preece[15], J. L. Racusin[19], S. Rainò[22,23], R. Rando[11,12], A. Rau[38], M. Razzano[14,21], S. Razzaque[60], A. Reimer[13,16], O. Reimer[13,16], T. Reposeur[42], S. Ritz[21], C. Romoli[12], M. Roth[61], F. Ryde[5,6], P. M. Saz Parkinson[21], T. L. Schalk[21], C. Sgrò[14], E. J. Siskind[62], E. Sonbas[19,56,63], G. Spandre[14], P. Spinelli[22,23], D. J. Suson[64], H. Tajima[13,65], H. Takahashi[39], Y. Takeuchi[45], Y. Tanaka[55], J. G. Thayer[13], J. B. Thayer[13], D. J. Thompson[19], L. Tibaldo[13], D. Tierney[25], M. Tinivella[14], D. F. Torres[26,66], G. Tosti[17,18], E. Troja[19,71], V. Tronconi[12], T. L. Usher[13], J. Vandenbroucke[13], A. J. van der Horst[48,71], V. Vasileiou[31], G. Vianello[13,67], V. Vitale[54,68], A. von Kienlin[38], B. L. Winer[43], K. S. Wood[36], M. Wood[13], S. Xiong[15], and Z. Yang[5,32]

[1] Deutsches Elektronen Synchrotron DESY, D-15738 Zeuthen, Germany
[2] Space Sciences Laboratory, 7 Gauss Way, University of California, Berkeley, CA 94720-7450, USA
[3] Interactive Research Center of Science, Tokyo Institute of Technology, Meguro City, Tokyo 152-8551, Japan
[4] Department of Astronomy, Stockholm University, SE-106 91 Stockholm, Sweden
[5] The Oskar Klein Centre for Cosmoparticle Physics, AlbaNova, SE-106 91 Stockholm, Sweden
[6] Department of Physics, Royal Institute of Technology (KTH), AlbaNova, SE-106 91 Stockholm, Sweden
[7] Università di Pisa and Istituto Nazionale di Fisica Nucleare, Sezione di Pisa I-56127 Pisa, Italy
[8] Laboratoire AIM, CEA-IRFU/CNRS/Université Paris Diderot, Service d'Astrophysique, CEA Saclay, 91191 Gif sur Yvette, France
[9] Istituto Nazionale di Fisica Nucleare, Sezione di Trieste, I-34127 Trieste, Italy
[10] Dipartimento di Fisica, Università di Trieste, I-34127 Trieste, Italy
[11] Istituto Nazionale di Fisica Nucleare, Sezione di Padova, I-35131 Padova, Italy
[12] Dipartimento di Fisica e Astronomia "G. Galilei," Università di Padova, I-35131 Padova, Italy
[13] W. W. Hansen Experimental Physics Laboratory, Kavli Institute for Particle Astrophysics and Cosmology, Department of Physics and SLAC National Accelerator Laboratory, Stanford University, Stanford, CA 94305, USA; nicola.omodei@stanford.edu, giacomov@slac.stanford.edu
[14] Istituto Nazionale di Fisica Nucleare, Sezione di Pisa, I-56127 Pisa, Italy
[15] Center for Space Plasma and Aeronomic Research (CSPAR), University of Alabama in Huntsville, Huntsville, AL 35899, USA
[16] Institut für Astro- und Teilchenphysik and Institut für Theoretische Physik, Leopold-Franzens-Universität Innsbruck, A-6020 Innsbruck, Austria
[17] Istituto Nazionale di Fisica Nucleare, Sezione di Perugia, I-06123 Perugia, Italy
[18] Dipartimento di Fisica, Università degli Studi di Perugia, I-06123 Perugia, Italy
[19] NASA Goddard Space Flight Center, Greenbelt, MD 20771, USA
[20] Department of Physics and Department of Astronomy, University of Maryland, College Park, MD 20742, USA
[21] Santa Cruz Institute for Particle Physics, Department of Physics and Department of Astronomy and Astrophysics, University of California at Santa Cruz, Santa Cruz, CA 95064, USA
[22] Dipartimento di Fisica "M. Merlin" dell'Università e del Politecnico di Bari, I-70126 Bari, Italy
[23] Istituto Nazionale di Fisica Nucleare, Sezione di Bari, 70126 Bari, Italy
[24] Laboratoire Leprince-Ringuet, École Polytechnique, CNRS/IN2P3, Palaiseau, France
[25] University College Dublin, Belfield, Dublin 4, Ireland
[26] Institut de Ciències de l'Espai (IEEE-CSIC), Campus UAB, 08193 Barcelona, Spain
[27] INAF-Istituto di Astrofisica Spaziale e Fisica Cosmica, I-20133 Milano, Italy
[28] Center for Earth Observing and Space Research, College of Science, George Mason University, Fairfax, VA 22030, USA
[29] Agenzia Spaziale Italiana (ASI) Science Data Center, I-00044 Frascati (Roma), Italy
[30] Istituto Nazionale di Astrofisica - Osservatorio Astronomico di Roma, I-00040 Monte Porzio Catone (Roma), Italy
[31] Laboratoire Univers et Particules de Montpellier, Université Montpellier 2, CNRS/IN2P3, Montpellier, France; piron@in2p3.fr, vlasios.vasileiou@lupm.in2p3.fr
[32] Department of Physics, Stockholm University, AlbaNova, SE-106 91 Stockholm, Sweden
[33] The Royal Swedish Academy of Sciences, Box 50005, SE-104 05 Stockholm, Sweden
[34] INAF Istituto di Radioastronomia, 40129 Bologna, Italy
[35] Dipartimento di Fisica, Università di Udine and Istituto Nazionale di Fisica Nucleare, Sezione di Trieste, Gruppo Collegato di Udine, I-33100 Udine, Italy
[36] Space Science Division, Naval Research Laboratory, Washington, DC 20375-5352, USA
[37] Los Alamos National Laboratory, Los Alamos, NM 87545, USA
[38] Max-Planck Institut für extraterrestrische Physik, 85748 Garching, Germany

[39] Department of Physical Sciences, Hiroshima University, Higashi-Hiroshima, Hiroshima 739-8526, Japan
[40] Department of Natural Sciences, The Open University of Israel, 1 University Road, POB 808, Ra'anana 43537, Israel
[41] Department of Astronomy, Graduate School of Science, Kyoto University, Sakyo-ku, Kyoto 606-8502, Japan
[42] Université Bordeaux 1, CNRS/IN2p3, Centre d'Études Nucléaires de Bordeaux Gradignan, 33175 Gradignan, France
[43] Department of Physics, Center for Cosmology and Astro-Particle Physics, The Ohio State University, Columbus, OH 43210, USA
[44] Science Institute, University of Iceland, IS-107 Reykjavik, Iceland
[45] Research Institute for Science and Engineering, Waseda University, 3-4-1, Okubo, Shinjuku, Tokyo 169-8555, Japan
[46] CNRS, IRAP, F-31028 Toulouse cedex 4, France
[47] GAHEC, Université de Toulouse, UPS-OMP, IRAP, Toulouse, France
[48] NASA Marshall Space Flight Center, Huntsville, AL 35812, USA
[49] Istituto Nazionale di Fisica Nucleare, Sezione di Torino, I-10125 Torino, Italy
[50] Yukawa Institute for Theoretical Physics, Kyoto University, Kitashirakawa Oiwake-cho, Sakyo-ku, Kyoto 606-8502, Japan
[51] Exzellenzcluster Universe, Technische Universität München, D-85748 Garching, Germany
[52] Hiroshima Astrophysical Science Center, Hiroshima University, Higashi-Hiroshima, Hiroshima 739-8526, Japan
[53] Center for Research and Exploration in Space Science and Technology (CRESST) and NASA Goddard Space Flight Center, Greenbelt, MD 20771, USA
[54] Istituto Nazionale di Fisica Nucleare, Sezione di Roma "Tor Vergata," I-00133 Roma, Italy
[55] Institute of Space and Astronautical Science, JAXA, 3-1-1 Yoshinodai, Chuo-ku, Sagamihara, Kanagawa 252-5210, Japan
[56] Universities Space Research Association (USRA), Columbia, MD 21044, USA
[57] Max-Planck-Institut für Physik, D-80805 München, Germany
[58] Department of Physics and Center for Space Sciences and Technology, University of Maryland Baltimore County, Baltimore, MD 21250, USA
[59] Harvard-Smithsonian Center for Astrophysics, Cambridge, MA 02138, USA
[60] University of Johannesburg, Department of Physics, University of Johannesburg, Auckland Park 2006, South Africa; soebur.razzaque@gmail.com
[61] Department of Physics, University of Washington, Seattle, WA 98195-1560, USA
[62] NYCB Real-Time Computing Inc., Lattingtown, NY 11560-1025, USA
[63] Adıyaman University, 02040 Adıyaman, Turkey
[64] Department of Chemistry and Physics, Purdue University Calumet, Hammond, IN 46323-2094, USA
[65] Solar-Terrestrial Environment Laboratory, Nagoya University, Nagoya 464-8601, Japan
[66] Institució Catalana de Recerca i Estudis Avançats (ICREA), Barcelona, Spain
[67] Consorzio Interuniversitario per la Fisica Spaziale (CIFS), I-10133 Torino, Italy
[68] Dipartimento di Fisica, Università di Roma "Tor Vergata," I-00133 Roma, Italy

ABSTRACT

In three years of observations since the beginning of nominal science operations in 2008 August, the Large Area Telescope (LAT) on board the *Fermi Gamma-Ray Space Telescope* has observed high-energy ($\gtrsim$20 MeV) γ-ray emission from 35 gamma-ray bursts (GRBs). Among these, 28 GRBs have been detected above 100 MeV and 7 GRBs above ~20 MeV. The first *Fermi*-LAT catalog of GRBs is a compilation of these detections and provides a systematic study of high-energy emission from GRBs for the first time. To generate the catalog, we examined 733 GRBs detected by the Gamma-Ray Burst Monitor (GBM) on *Fermi* and processed each of them using the same analysis sequence. Details of the methodology followed by the LAT collaboration for the GRB analysis are provided. We summarize the temporal and spectral properties of the LAT-detected GRBs. We also discuss characteristics of LAT-detected emission such as its delayed onset and longer duration compared with emission detected by the GBM, its power-law temporal decay at late times, and the fact that it is dominated by a power-law spectral component that appears in addition to the usual Band model.

Key words: catalogs – gamma-ray burst: general – methods: data analysis

Online-only material: color figures

1. INTRODUCTION

Prior to the *Fermi Gamma-Ray Space Telescope* mission, high-energy emission from gamma-ray bursts (GRBs) was observed with the Energetic Gamma-Ray Experiment Telescope (EGRET) covering the energy range from 30 MeV to 30 GeV (Hughes et al. 1980; Kanbach et al. 1988; Thompson et al. 1993; Esposito et al. 1999) on board the *Compton Gamma-Ray Observatory* (*CGRO*; 1991–2000) and, more recently, by the Gamma-Ray Imaging Detector (GRID) on board the *Astro-rivelatore Gamma a Immagini LEggero* spacecraft (*AGILE*; Giuliani et al. 2008; Tavani et al. 2008, 2009). Despite the effective area and dead-time limitations of EGRET, substantial emission above 100 MeV was detected for a few

GRBs (Sommer et al. 1994; Hurley et al. 1994; González et al. 2003), suggesting a diversity of temporal and spectral properties at high energies. Of particular interest was GRB 940217, for which delayed high-energy emission was detected by EGRET up to ~90 minutes after the trigger provided by *CGRO*'s Burst And Transient Source Experiment (BATSE).

The *Fermi* observatory was placed into orbit on 2008 June 11. It provides unprecedented breadth of energy coverage and sensitivity for advancing the knowledge of GRB properties at high energies. It has two instruments: the Gamma-Ray Burst Monitor (GBM; Meegan et al. 2009) and the Large Area Telescope (LAT; Atwood et al. 2009), which together cover more than 7 decades in energy. The GBM comprises twelve sodium iodide (NaI) and two bismuth germanate (BGO) detectors sensitive in the 8 keV–1 MeV and 150 keV–40 MeV energy ranges, respectively. The NaI detectors are arranged in groups of three at each of the four edges of the spacecraft and the two BGO detectors are placed symmetrically on opposite

sides of the spacecraft, resulting in a field of view (FoV) of $\sim$9.5 sr. Triggering and localization are determined from the NaI detectors, while spectroscopy is performed using both the NaI and BGO detectors. Localization is performed using the relative event rates of detectors with different orientations with respect to the source and is typically accurate to a few degrees. The GBM covers roughly four decades in energy and provides a bridge from the low energies (below $\sim$1 MeV), where most of the GRB emission takes place, to the less explored energy range that is accessible to the LAT.

The LAT is a pair-production telescope sensitive to γ-rays in the energy range from $\sim$20 MeV to more than 300 GeV. The instrument and its on-orbit calibrations are described in detail in Atwood et al. (2009) and Abdo et al. (2009c). The telescope consists of a 4×4 array of identical towers, each including a tracker of silicon strip planes with foils of tungsten converter interleaved, followed by a cesium iodide calorimeter with a hodoscopic layout. This array is covered by a segmented anti-coincidence detector of plastic scintillators that is designed to efficiently identify and reject charged particle background events. The wide FoV ($\sim$2.4 sr at 1 GeV) of the LAT, its high observing efficiency (obtained by keeping the FoV on the sky with scanning observations), its broad energy range, its large effective area ($>$1 GeV is $\sim$6500 cm^2 on-axis), its low dead time per event ($\sim$27 μs), its efficient background rejection, and its good angular resolution ($\sim$0°.8 at 1 GeV) are vastly improved in comparison with those of EGRET. As a result, the LAT provides more GRB detections, higher statistics per detection, and more accurate localizations ($\lesssim$1°).

Fermi has been routinely monitoring the γ-ray sky since 2008 August. From this time until 2011 August, when a new event analysis ("Pass 7"; Ackermann et al. 2012a) was introduced, the GBM detected about 730 GRBs, approximately half of which occurred inside the LAT FoV. In ground processing, we search for LAT counterparts to known GRBs, following each trigger provided by the GBM and other instruments. In addition, we also undertake blind searches for bursts not detected by other instruments in the entire sample of LAT data, with however no independent (i.e., not detected by other instruments) detections so far.

Owing to the detection of temporally extended emission by EGRET from GRB 940217 and the interest in studying GRB afterglow emission at high energies, *Fermi* was designed with the additional capability to repoint in the direction of a bright GRB and keep its position near the center of the FoV of the LAT (where the effective area to γ-rays is maximal) for several hours (5 hr initially; 2.5 hr since 2010 November 23), subject to Earth-limb constraints. This repointing occurs autonomously in response to requests to the *Fermi* spacecraft from either the GBM or the LAT (Autonomous Repoint Request, or ARR hereafter), with adjustable brightness thresholds and has resulted in more than 60 extended GRB observations between 2008 October 8, when the capability was enabled, and 2011 August 1.

This article presents the first catalog of LAT-detected GRBs. It covers a three-year period starting at the beginning of routine science operations in 2008 August. In Section 2, we describe the data used in this study and the list of GRB triggers that we searched for LAT detections. In Section 3, we give a detailed description of the analysis methods that we applied to detect and localize GRBs with the LAT, as well as the methodology that we followed to characterize their temporal and spectral properties. In Sections 4 and 5, we present and discuss our results, with a special emphasis both on the most interesting bursts and

on the common properties revealed by the LAT. The physical implications of our observations are addressed in Section 6, where we also discuss several open questions and topics of interest for future analysis. In Appendix A, we investigate the possible sources of systematic uncertainties via testing different instrument response functions (IRFs) and configurations for the analysis. Finally, in Appendix B, we discuss each individual GRB in the catalog, reporting the details of its observation and considering it in the context of multiwavelength observations.

2. DATA PREPARATION

In this section, we describe the data analyzed in this study and the list of GRB triggers that we searched for LAT detections.

The results of this paper were produced using two sets of LAT events corresponding to different quality levels and corresponding IRFs in the event reconstruction: the Transient event class (Atwood et al. 2009), which requires the presence of a signal in both the tracker and the calorimeter of the LAT, and the "LAT Low Energy" (LLE) event class (Pelassa et al. 2010), which requires a signal in only the tracker and essentially consists of all the events that pass the on board γ filter having a reconstructed direction (Ackermann et al. 2012a).

The LAT event classes underwent many stages of refinement and were released as different versions (or "passes") of the data. This catalog uses the entire "Pass 6" event dataset, in particular, the Pass 6 version 3 Transient event class ("P6_V3_TRANSIENT"). The LAT team has switched from using "Pass 6," which had been used since the beginning of science operations, to "Pass 7" data on the 1st of August 2011, the end of the time period covered by this catalog.

As cross checks, we repeated some of the Transient-class analyses using instead the "P6_V3_DIFFUSE" event class to search for possible systematics that might arise from the choice of event selection. Both the Transient and Diffuse classes offer good energy and angular resolutions, along with large effective areas above 100 MeV and reasonable residual background rates.[72] The Diffuse class uses a very selective set of cuts to keep the highest quality γ-ray candidates. As a result, it has a relatively narrow point-spread function (PSF; 68% containment radius of several degrees at 100 MeV and $\sim$0°.25 at 10 GeV) and a smaller background contamination with respect to the Transient class. On the other hand, the Transient class, which is defined with a less selective set of cuts, offers a significantly larger effective area, especially below 1 GeV. The LLE class corresponds to looser selection criteria, compared with the other two classes, and is designed to provide a far larger effective area at lower energies (especially below 100 MeV) and at larger off-axis angles (especially above $\sim$60°). The LLE PSF is wide (with a 68% containment radius of $\sim$20°, $\sim$13°, and $\sim$7° at 20 MeV, 50 MeV, and 100 MeV, respectively) and has a much higher background contamination ($\sim$300 Hz over the entire FoV) than the other two event classes. Since the flux of a GRB is typically a decreasing function of energy, the LLE class provides very good statistics, which are useful for detailed studies of the temporal structure of GRB emission. It also allows us to examine GRBs with soft spectra or those that occur at a high off-axis angle, which are not detectable by the other two event classes.

Our baseline LAT-only analysis (namely, localization, detection, spectral fitting, and duration estimation) uses the

---

[72] For more information on these event classes, see http://www.slac.stanford.edu/exp/glast/groups/canda/archive/pass6v3/lat_Performance.htm.

Transient-class data. We use the LLE data only for source detection and duration measurement. As discussed above, the LAT Diffuse data are used only as a cross-check of some of the analysis results for the Transient class.

We perform joint GBM-LAT spectral fitting using the LAT Transient-class data, the GBM Time-Tagged Event (TTE) data and the GBM RSP/RSP2 response files.[73] We also use GBM CSPEC data to produce our background model (see Section 3.1.2).

All of our analyses also use the LAT FT2 data, which contain information on the pointing history and the location of the *Fermi* spacecraft around the Earth. We use FT2 files with 1 s binning.

2.1. Data Cuts

2.1.1. LAT Data

We select Transient class data with reconstructed energies in the 100 MeV–100 GeV range. The lower limit is chosen to reject events with poorly reconstructed directions and energies. Moreover, for Pass 6, the LAT response is not adequately verified at $E < 100$ MeV energies and the contamination from cosmic rays misclassified as gamma-rays is also significantly increased. The upper limit (UL) was chosen at 100 GeV since we do not expect to detect GRB photons at such high energies due to the opacity of the universe and the limited effective area of the LAT. We select events in a circular region of interest (ROI) that is centered on the best available GRB localization. The LAT PSF depends on the event energy and off-axis angle and has been studied using Monte Carlo simulations. We use the resulting description of the PSF to increase the sensitivity of our analyses. For the event-counting and joint spectral-fitting analyses, we select a variable ROI radius that depends on the event energy and the off-axis angle of the GRB in such a way as to select almost all the events consistent with the position of the GRB given our PSF while rejecting much of the residual cosmic-ray background, increasing the signal-to-noise ratio of the selected data. To accomplish this, we split the events in logarithmically spaced bins in energy and for each bin we select only the events contained in an ROI around the source having a radius corresponding to the 95% containment radius of the PSF evaluated at an energy equal to the geometric mean of the bin's energy range. For the duration estimation using Transient data, we deal with longer time periods, thus we dynamically adjust the radii of the energy-dependent ROIs to follow the variation of the off-axis angle with time. On the other hand, for the LLE duration estimations and the joint GBM-LAT spectral analyses, we use a single set of radii calculated using the PSF corresponding to the GRB off-axis angle at trigger time. The exact dependence of the LLE PSF on the off-axis angle is not available yet. Instead, only two possible LLE PSFs are available for setting the ROI radii: one for observations with off-axis angles greater than 40° and the other for observations closer to the center of the FoV. Finally, for cases for which the GRB localization error is non-negligible (i.e., for GBM or LAT localizations), we increase the radius of each ROI by setting it equal to the sum in quadrature of the localization error and the 95% containment radius of the PSF. For GRBs localized by the *Fermi* GBM, we also added in quadrature a 3° systematic error. The maximum-likelihood analysis utilizes the PSF information internally while calculating the probability of each event being associated with the GRB, thus no optimization of the ROI radius,

as above, is necessary. For the maximum-likelihood analyses, we use a fixed-radius ROI set at 12°, a value larger than the 99% containment radius of the Transient LAT PSF evaluated for a 100 MeV event on axis.

We apply a cut to limit the contamination from γ-rays produced by interactions of cosmic rays with the Earth's upper atmosphere. For our maximum-likelihood analysis, we use the *Fermi* Science Tool *gtmktime*[74] to select only the time intervals (the "Good Time Intervals" or GTIs) in which no portion of the ROI is too close to the Earth's limb. Because the Earth's limb lies at a zenith angle of 113° and we wish to take into account the finite angular resolution of the detector, we exclude any events taken when the ROI is closer than 8° to the Earth's limb or equivalently when it intersects the fiducial line at 105° from the local zenith. For special cases, when the position of the GRB is very close to the Earth's limb, we compensate for the loss of exposure due to this cut by reducing the size of the ROI and simultaneously increasing the maximum zenith angle to 110°. This increases the duration of the GTI significantly, allowing deeper exposures for searches of late γ-ray activity. For all the other analyses (namely, event-counting analyses and joint spectral fitting), we do not apply a cut to select GTIs as above, but rather we process the whole observation and instead reject individual events reconstructed farther than 105° from the local zenith.

2.1.2. GBM Data

The response of a GBM detector depends on the continuously varying position of the GRB in its FoV, with its effective area decreasing as the angular distance between the detector boresight and the source (θ_{GBM}) increases. Because of this, when θ_{GBM} is large, any systematic effects due to imperfect modeling of the spacecraft or the individual detectors become relatively important (Goldstein et al. 2012). For this reason, we use the data from the GBM NaI detectors that have angles $\theta_{GBM} < 50°$ at the time of the trigger and the BGO detector facing the GRB at the time of the trigger.

We also exclude any detector occulted by other detectors or the spacecraft during any part of the analyzed time interval, as advised in Goldstein et al. (2012).

Since θ_{GBM} usually changes with time, the GBM Collaboration released RSP2 files that contain several response matrices corresponding to short consecutive time intervals (every 2° of slew of the detector about the source). With a suitable weighting scheme, as described in Section 3.4.1, these files provide an adequate description of the GRB detector responses.

Finally, in some cases, bright GRBs trigger an ARR, causing rapid variations of θ_{GBM} with time for some of the GBM detectors. These variations create further variations in those detector responses and background rates. In fact, due to its orbital and angular dependence, the background of those detectors can be very hard to predict. Also, since the RSP2 files might not be binned finely enough in time to cover these rapid variations, we excluded data from detectors that have such rapid variations.

2.2. Input GRB List

To search for GRBs in the LAT data, we use as input a list comprising 733 bursts that triggered the GBM from 2008 August 4 to 2011 August 1 (GBM triggers bn080804456 to bn110731465). We use the localizations provided by the GBM,

---

[73] All available from the *Fermi* Science Support Center (FSSC): http://fermi.gsfc.nasa.gov/ssc/data/access/gbm/.

[74] http://www.slac.stanford.edu/exp/glast/wb/prod/pages/sciTools_gtmktime/gtmktime.htm

unless a localization from the *Swift* observatory (Gehrels et al. 2004), obtained either from the Burst Alert Telescope (*Swift*-BAT; Barthelmy et al. 2005), the X-Ray Telescope (*Swift*-XRT; Burrows et al. 2005), or the UV-Optical Telescope (*Swift*-UVOT; Gehrels et al. 2004), is available via the Gamma-Ray Burst Coordinates Network (GCN).[75]

We analyzed all GRBs in the input list whether or not they occurred in the LAT FoV at the time of the trigger, since a GRB that is initially outside the LAT FoV can be observable at later times due to an ARR or simply due to the standard scanning mode. As a reference, 368 GBM bursts were in the LAT FoV at the time of the GBM trigger, with the FoV considered to have a $70°$ angular radius. In 64 of these cases, an ARR was performed. It should be noted that the sensitivity of the LLE event class extends to larger off-axis angles $\theta \approx 90°$.

In order to characterize our detection algorithm, we also created a list of "fake" GBM triggers by considering trigger times earlier than the true GBM trigger time by 11466 s (approximately two orbits). Since the most common observing mode for the *Fermi* spacecraft is to rock between the northern and southern orbital hemispheres on alternate orbits, with the exception of ARRs, the burst triggers of the "fake" sample have the desirable property of having very similar background conditions as those of the true sample.

3. ANALYSIS METHODS AND PROCEDURE

We implemented a standard sequence of analysis steps for uniformity. The sequence consists of event-counting analyses performed on the Transient-class and LLE data for source detection and duration estimation (Section 3.3), unbinned maximum likelihood analysis performed on the Transient-class data for source detection, spectral fitting, localization (Section 3.2), and a spectral fitting analysis performed jointly on the LAT Transient-class and the GBM data (Section 3.4). Details of the implementation of the analysis sequence are given in Section 3.5. Estimation of the backgrounds is a central part of all the analyses and is described below.

3.1. Background Estimation

3.1.1. LAT

The background in the LAT data is composed of charged cosmic rays (CRs) misclassified as γ-rays, astrophysical γ-rays coming from Galactic and extragalactic diffuse and point sources, and γ-rays from the Earth's limb produced by interactions of CRs in the upper atmosphere. The backgrounds for the Transient-class and LLE data are dominated by the CR component, while for the cleaner Diffuse class the backgrounds are dominated by astrophysical γ-rays. The CR component of the background depends primarily on the geomagnetic coordinates of the spacecraft and on the direction of the GRB in instrument coordinates (since the LAT's effective area varies strongly with inclination angle). The component from the Earth's atmosphere depends on the angle between the GRB and the limb (i.e., on the zenith angle of the GRB) and is strongest toward the limb. Finally, the astrophysical background γ-ray component depends on the GRB direction and is typically stronger at low Galactic latitudes.

For the Transient event class analyses, we use the Background Estimation tool (Vasileiou 2013; "BKGE," hereafter), which

was developed by the LAT collaboration and takes into account all of these dependencies. It can estimate the total expected backgrounds for any given ROI and period of time with an accuracy of $\sim$10–15% (Abdo et al. 2009e). It also provides separate estimates for the Galactic diffuse emission and for everything else, namely the sum of CRs and extragalactic diffuse emission (the "isotropic component"). Note that the BKGE cannot estimate the backgrounds from the Earth's limb. However, the zenith angle cut described in Section 2 is very effective at reducing this component to negligible levels, thus this limitation does not generally constitute an obstacle.

Our maximum likelihood analysis of Transient-class data uses a background model calculated by a combination of the isotropic component provided by the BKGE tool and the Galactic diffuse emission template provided by the LAT Collaboration.[76]

The maximum likelihood analysis using the cleaner Diffuse class data, which was performed for validation studies (see Appendix A), uses the Galactic diffuse emission template plus the public template describing the "isotropic background" (extragalactic diffuse emission and CR background) as a single spectrum of the intensity averaged over the whole sky. The BKGE does not produce estimates for Diffuse-class events. For the time scales analyzed in this study, the contribution from point sources is typically negligible, so we do not take them into account in the background models.

For the joint GBM-LAT spectral analysis, we used the estimates provided by BKGE of the total background in the energy-dependent ROI for the background for the LAT. For technical reasons related to the broad PSF of the LLE class, we cannot use the BKGE to estimate the LLE background. Instead, we evaluate it directly from the LLE data associated with each individual observation. First, in order to ensure enough events in every time bin, we bin the LLE data in time with a coarse binning of 5 s, from well before the trigger time to well after the end of the burst, as measured by the GBM. We then fit the background rate as a function of time $b(t)$ by taking into account the variation of the exposure due to the changing orientation of the LAT. Phenomenologically, we adopt the function $b(t) = p_0 + p_1 C(t) + p_2 C(t)^2$, where $C(t) = \cos[\theta(t)]$ and θ is the off-axis angle. The parameters p_0, p_1, and p_2 are obtained by fitting the "pre-burst" and "post-burst" time windows simultaneously. We use a conservative definition of these time windows based on the burst duration as measured by the GBM. In particular, the "post-burst" data start well after the end of the low-energy emission as seen by the GBM. Finally, the fit parameters allow us to compute the background rate at any time during the burst and we use the covariance matrix from the fit to evaluate the uncertainty of this prediction. We compared this simple model with an alternative prescription $b(t) = \mathrm{pol}(t) * C(t)$, where the degree of the polynomial function $\mathrm{pol}(t)$ is increased until a good fit to the data is obtained. Typically, a polynomial of degree 1 or 2 was sufficient, although in a few cases a higher degree (3 or 4) was necessary. The expression above is motivated by the fact that, as a first approximation, the effective area of the LAT to CRs scales as $\cos(\theta)$ and that we can model the CR contribution on-axis ($\theta = 0$) with a polynomial. The two prescriptions gave very similar results in all cases. An example of the standard prescription is shown in Figure 1. The excess visible at $\sim$200 s after the trigger time T_0 is significantly above the estimation of the background and we claim this is due to
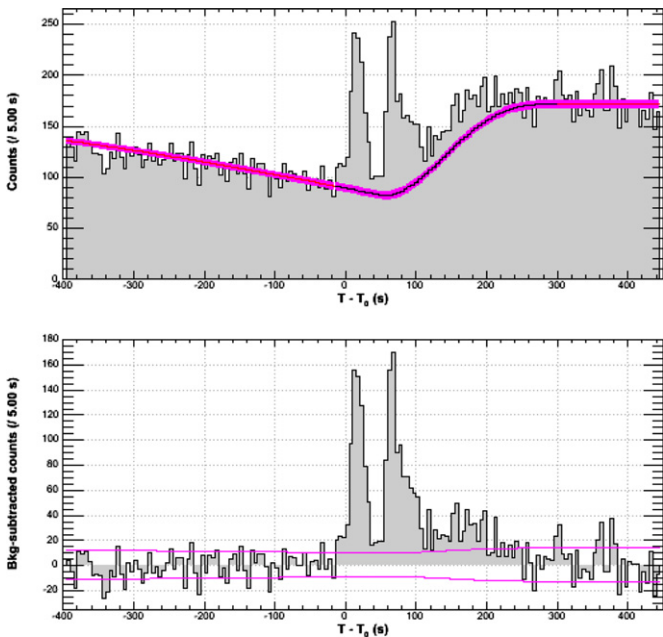

Figure 1. LLE background estimation for GRB 090323. The top panel shows the time history of the LLE count rate (histogram) and the background level estimated from a fit to the two off-pulse regions [−400 s, −15 s] and [300 s, 450 s] (curve). The bottom panel shows the background-subtracted LLE light curve. Magenta curves indicate the statistical error of the fit background (top panel) and the statistical fluctuation of the background-subtracted signal in the null hypothesis (bottom panel).

(A color version of this figure is available in the online journal.)

the GRB emission. Note also that in this case, the background estimation was particularly difficult due to the contamination of the Earth's limb caused by the ARR while in several other cases the background is smoother.

3.1.2. GBM

We use the GBM CSPEC event data from before and after the GRB prompt phase to obtain a model for the background, similar to the procedure followed for the LLE data above. For each selected detector, we integrate the CSPEC spectra over all the energy channels to obtain a light curve and then select two off-pulse time intervals: one before and one after the GRB prompt emission (see the left panel in Figure 2). We fit polynomial functions $f(t)$ of increasing degree D to the data from these two time intervals, minimizing the χ^2 statistic, until we reach a good fit (i.e., with a reduced $\chi^2 \simeq 1$). Then, we consider the light curves corresponding to each of the 128 channels separately, again with data from the off-pulse intervals, and we fit them with a polynomial of degree D by minimizing the Poisson log-likelihood function.[77] After each fit, we check by eye that the residuals are consistent with the statistical fluctuations. If this is not the case, we repeat the procedure from the beginning, changing our choice for the off-pulse intervals, until a good fit is achieved. The set of 128 polynomial functions constitutes our *background model* and the predicted number of background events b_i in the ith channel of the background spectrum is the integral of the corresponding polynomial function f_i (describing

the rate) between t_1 and t_2:

$$b_i = \frac{\int_{t_1}^{t_2} f_i(t) dt}{t_2 - t_1}. \qquad (1)$$

The statistical error of the integral is computed using the co-variance matrix from the fit.[78] Since the background for GBM detectors is much less predictable than for LLE data, we determine the off-pulse regions manually. In order to minimize the statistical and systematic errors (and hence ensure a reliable background estimate), the off-pulse time intervals must be close to the GRB's signal, have a long enough duration, and also possibly have a smooth part of the light curve without bumps or other structures. Moreover, the number of counts in each channel is much smaller than the total number of counts used to determine D. Thus, the larger the value of D, the more f_i can pick up statistical fluctuations in some channels, giving a slightly wrong interpolation for those channels in the pulse region. Thus, we try to find off-pulse intervals well described by low-order polynomials (ideally, $D = 1$). Unfortunately, this is not always possible. For example, for GRBs triggering ARRs, the background can vary quickly in response to the change of pointing, requiring higher order polynomials to describe it. This effect introduces some additional noise in the spectrum, but it is unlikely to introduce any bias in the fit results, given its random nature. Note that it is not possible to fix the shape of the polynomial, since the background shows spectral evolution and thus every channel needs to be considered independently. In some cases, even with high-order polynomials, fitting the model to the background can be difficult and even impossible without being completely arbitrary (see the right panel in Figure 2 for an example). In those cases, we opt for excluding the problematic detector from the analysis. These issues are not solvable at present given our current understanding of the detectors and their backgrounds. More advanced techniques to deal with the backgrounds are currently under investigation by the *Fermi*-GBM Collaboration (Fitzpatrick et al. 2012).

3.2. Maximum Likelihood Analysis

We perform an unbinned maximum likelihood analysis using the tools in the *Fermi* ScienceTools software package, version 09-26-02.[79] An overview of the method and its application for this study is given below. For more information, see Band et al. (2009) and references therein.

The unbinned analysis computes the log-likelihood of the data using the reconstructed direction and energy of each individual γ-ray and the assumed sky model folded through the IRFs of the LAT. The sky model includes the GRB under investigation modeled as a point source, typically with a power-law (PL) spectrum, as well as other components that describe the other sources that are expected to be present in the data. For the short time scales ($\lesssim$10–100 s) considered, these are predominantly diffuse emission from the Galaxy and residual charged particle backgrounds, although in principle a bright, nearby point source, such as Vela, may be included. To estimate the spectral properties of the GRB, the model parameters are varied in order to maximize the log-likelihood given the data. Usually, the GRB coordinates are held fixed, but if a localization

---

[77] Using the `Fit` method implemented in
http://root.cern.ch/root/html/TH1.html.

[78] Using the `IntegralError` method from: http://root.cern.ch/root/html/TF1.html.

[79] The likelihood method is described at: http://fermi.gsfc.nasa.gov/ssc/data/analysis/scitools/ref_likelihood.html.
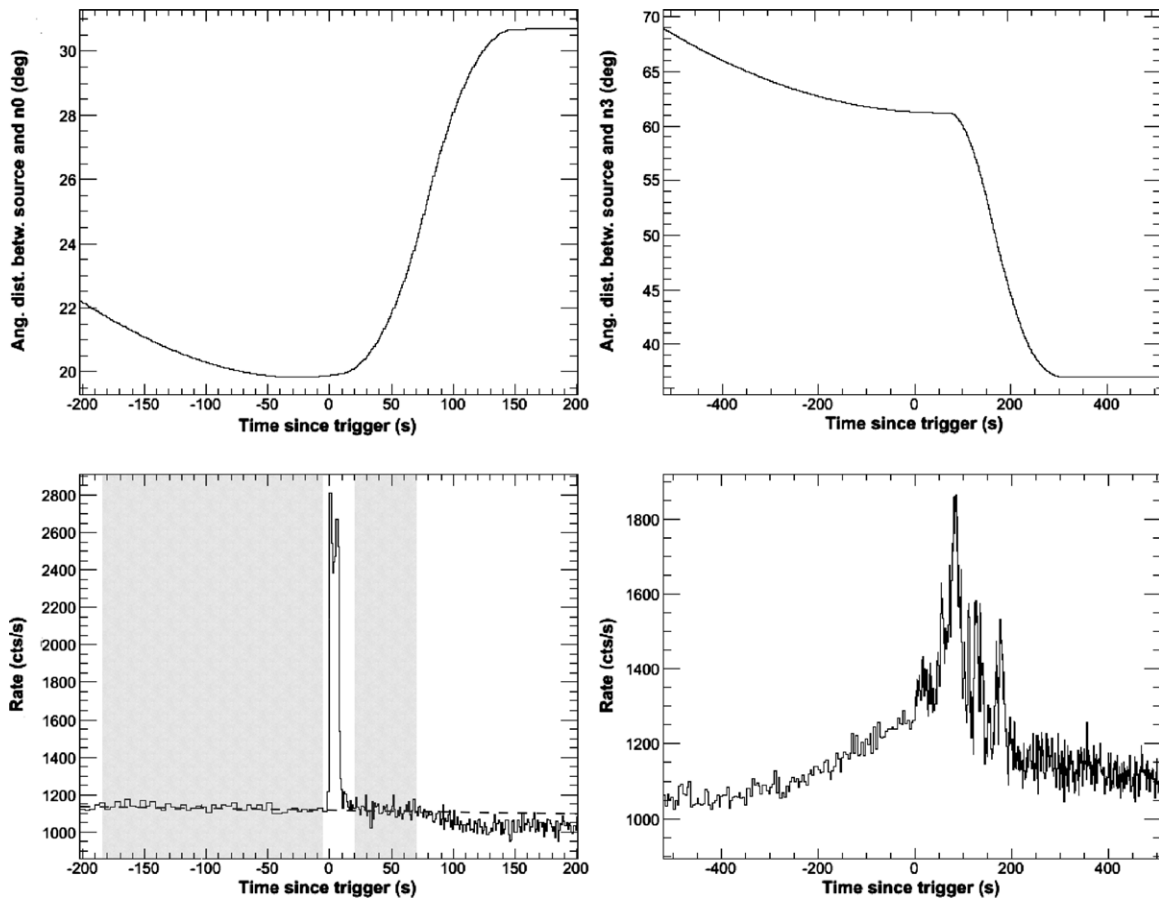
Figure 2. (Left) Example of a selected GBM detector (NaI_0) and its background fit (lower panel) and the angular distance between the axis of the detector and the GRB position (upper panel). The shaded regions mark the selected off-pulse intervals, while the dashed line is the best-fitting polynomial model (see text). (Right) Example of an excluded detector (NaI_3): the change in angular distance between the detector axis and the source is too fast (upper panel), producing a change in the light curve that cannot be modeled satisfactorily with a polynomial model.

using the LAT data is desired, those parameters can also be varied.

The fitting in the *Likelihood* tools is performed using an underlying engine such as MINUIT[80] to perform the maximization. Currently, the unbinned analysis does not take into account energy dispersion. However, given the good energy resolution of the LAT ($\lesssim$15% above 100 MeV), the moderate energy dependence of the LAT effective area at the energies considered, and the simple PL spectral form that we consider, approximating the true energy by the reconstructed one is justified. The uncertainties of the best-fit values of the parameters or any upper/lower limits are estimated from the shape of the log-likelihood surface around the best fit.

We apply the likelihood analysis to Transient-class events and, as a cross check, we also analyze Diffuse class events, with the data cuts described in Section 2. We cannot apply a similar unbinned maximum likelihood analysis to the LLE data, since the PSF, energy dispersion, effective area for the LLE events, and the expected backgrounds are not adequately known and/or verified yet. The analysis of LLE data is similar to that of the GBM data and is described below.

The background model is constructed as described in Section 3.1. The normalization of the "isotropic background" provided by the BKGE, used for the analysis of Transient-class events, is one of the free parameters of the fit and has a Gaussian

prior of mean 1 and a width set to encompass any associated statistical and systematic errors (typically around 15%). The normalization of the "isotropic background" template, used for the analysis of Diffuse class data, is free to vary with no prior and no constraints. To avoid increasing the number of free parameters, we keep the normalization of the template for Galactic diffuse emission fixed to 1 for the analyses based on both event classes.

3.2.1. Source Detection

To determine the significance of the detections of sources using the maximum likelihood analysis, we consider the "Test Statistic" (TS) equal to twice the logarithm of the ratio of the maximum likelihood value produced with a model including the GRB over the maximum likelihood value of the null hypothesis, i.e., a model that does not include the GRB. The probability distribution function (PDF) of the TS under the null hypothesis represents the probability that a measured signal is consistent with the statistical fluctuations. The PDF in such a source-over-background model cannot, in general, be described by the usual asymptotic distributions expected from Wilks' theorem (Wilks 1938; Protassov et al. 2002). However, it has been verified by dedicated Monte Carlo simulations (Mattox et al. 1996) that the cumulative PDF of the TS in the null hypothesis (i.e., the integral of the TS PDF from some TS value to infinity) is approximately equal to a $\chi^2_{n_{\rm dof}}/2$ distribution, where $n_{\rm dof}$ is the number of degrees of freedom (dof) associated with the GRB. The factor

---

of 1/2 in front of the TS PDF formula results from allowing only positive source fluxes.

Since we model the GRB spectrum as a PL with two dof and we fix the localization, the TS distribution should nominally follow $(1/2)\chi_2^2$. This is formally correct if the localization of the GRB is provided by an independent dataset (i.e., from another instrument). However, when the input localization is not sufficiently precise, we optimize it using the same dataset used for detecting the source, thereby introducing two additional free parameters (R.A. and Decl.). In this case, the TS distribution should follow $(1/2)\chi_4^2$. In practice, the steps of detection and localization are iterated many times and a detection step is performed using an ROI centered on the position found by a prior localization step. Therefore, the datasets used in each step are not exactly overlapping. For this reason, we expect some deviation from $(1/2)\chi_4^2$ distribution. For simplicity, we set a unique threshold of $TS_{min} = 20$ for our analysis independent of the origin of the localization. This formally corresponds to two slightly different one-sided Gaussian equivalent thresholds, 4.1σ for χ_2^2 and 3.5σ for χ_4^2. Additionally, we check the calibration of the detection algorithm on a sample of "fake GBM triggers" generated as described in Section 2.2. With the aforementioned value of TS_{min}, we obtain zero false detections on the "fake GBM triggers" sample (see Section 4.1 for more details).

3.2.2. Localization

We compute the localizations with the LAT in two steps. The first step provides a coarse estimation of the GRB position and is performed using the *Fermi* ScienceTool *gtfindsrc*. At this stage, we look for an excess consistent with the LAT PSF and we do not assume a particular background model. Although this method is quick and robust, it assumes that the likelihood function is parabolic and symmetric in azimuth around the found position and so the provided localization error can be slightly underestimated. Therefore, this step is only used to obtain an initial seed for the follow-up analysis.

For a more accurate localization, we use the *Fermi* Science-Tool *gttsmap*, which starts from the best-fit background model obtained by the likelihood fit and builds a map of the TS in a grid around the best available localization of the source. The GRB spectral parameters are fit at each position in the grid, along with all free parameters of the background model. The grid size and spacing are set based on the localization error obtained in the first step. The final LAT localization corresponds to the position of the maximum of the TS map. Its statistical uncertainty is derived by examining the distribution of TS values around it. Following Mattox et al. (1996), we interpret changes in the TS values in terms of a χ^2 distribution with two dof to account for the flux and spectral index of the GRB. Specifically, a confidence-level (CL) uncertainty is given by the TS map contour that corresponds to a decrease from the maximum value by a value equal to the CL quantile of the χ_2^2 distribution. For example, the 90% (68%) CL corresponds to a decrease of the TS from its maximum value by 4.61 (2.32).

3.2.3. Event Probability

We estimate the probability of each γ-ray being associated with the GRB by using the *Fermi* ScienceTool *gtsrcprob*. The probability computation takes into account the spectral, spatial (extent), and temporal (flux) information of all the components in the source model and the response of the LAT (PSF and effective area) to the particular event. The probabilities are assigned via likelihood analysis and are computed starting from

the best-fit model. In particular, the probability that a photon is produced by a component i is proportional to M_i, given by

$$M_i(\epsilon', p', t) = \int d\epsilon\, dp\, S_i(\epsilon, p, t)\, R(\epsilon, p; \epsilon', p', t), \quad (2)$$

where $S_i(\epsilon, p, t)$ is the predicted counts density from the component at energy ϵ, position p, and (observed) time t, and the integral is the convolution over the instrument response $R(\epsilon, p; \epsilon', p', t)$. In general, the predicted count density is the sum of the different contributions $S_i(\epsilon, p, t)$, including the extended backgrounds (such as the isotropic component and the Galactic diffuse emission), background point sources (nearby bright sources), and the GRB under study. Each contribution is described by a model, the parameters of which are optimized during the maximum likelihood fit. We simplify the calculation by not including nearby bright sources since, in these short time scales, they do not contribute significantly to the total number of counts. Once we compute the maximum likelihood model for the observed number of counts, we assign to each event the probability of it being associated with a particular component i.

Because the flux varies with time, we perform the calculation in several time bins so that the flux is never averaged over long time intervals. We tested schemes for defining the time intervals including linear, logarithmic, and Bayesian-blocks (Scargle et al. 2013) binnings and the results were stable among the different choices. For consistency with the other parts of the analysis, we chose the same logarithmically spaced time bins used in the time-resolved spectral analysis described in Section 3.5 below.

3.3. Event Counting Analyses

As discussed in the previous section, the effective area of the Transient class decreases strongly for off-axis angles greater than $\sim70°$ or for energies less than ~100 MeV. For this reason, in addition to the maximum likelihood analysis applied to Transient-class data described above, we search for sources using the LLE class. This class provides a significantly larger effective area below 100 MeV and a wider acceptance, although with a higher background level. We use it to obtain another duration measurement as well, which is dominated by events below 100 MeV and is thus complementary to the duration measurement obtained with Transient-class data.

3.3.1. Source Detection Using LLE Data

Consider a GRB as an impulse $f(t)$ superimposed on a background signal $b(t)$. Depending on the unknown shape of $f(t)$, there will be a particular time scale δt and a particular start time t_0 maximizing the quantity

$$S = \frac{\int_{t_0}^{t_0+\delta t} f(t) dt}{\sqrt{\int_{t_0}^{t_0+\delta t} b(t) dt}}, \quad (3)$$

which is the significance of the signal in the Gaussian regime. The pair $\delta t, t_0$ corresponds to the highest sensitivity to the signal of this particular GRB. Our source-detection method searches for the closest pair to $\delta t, t_0$ by resizing and shifting the time bins and selecting the light curve that contains the single bin with the highest significance. Since the typical event rate inside the LLE ROI is not particularly large (~10–20 Hz for the background), the Gaussian approximation implicit in

Equation (3) is not always justified. The significance S in each bin is thus derived from the Poisson probability of obtaining the observed number of counts given the expectation from the background, by converting this probability to an equivalent sigma level for a one-sided standard normal distribution. Our algorithm starts by defining a conservative window around the trigger time, with a total duration depending on the GBM burst duration T_{90}. Then, a set of 10 bin sizes δt is defined depending on T_{90}. For each of these bin sizes, the algorithm computes 11 light curves with shifted bins, i.e., with bins centered on $t_0 + (i/20)\ \delta t$ ($i = 0...10$). For each of these 10×11 light curves, the background function $b(t)$ is fit to the data outside the GRB window (as described in Section 3.1) and the algorithm seeks the bin with the largest significance S inside the GRB window. This value is then corrected for the number of trials, i.e., by the number of bins N in the current light curve. If p is the probability corresponding to S, then the corrected-for-trials probability is $p' = 1 - (1 - p)^N$. This new probability is converted to a Gaussian-equivalent significance S' and the pre-trials significance for the detection of the GRB is defined as $S_{\mathrm{pre}} = \max(S')$, where the maximum is computed over the 110 light curves. Since the data have been rebinned multiple times, a post-trial probability is finally computed to account for these dependent trials. For this purpose, we performed 3×10^6 Monte Carlo simulations of the background, running our algorithm and recording S_{pre} for each realization. The resulting distribution of S_{pre} is well described by a Lorentzian function $1 + [(x - x_0)/r_c]^2]^{-\beta}$, with $x_0 = 1.36$, $r_c = 7.38$, and $\beta = 41.8$ ($\chi^2 = 43.2$ with 38 dof). We use this function to convert the pre-trials significance S_{pre} into a post-trials significance S_{post}.

We consider as LLE-detected the GRBs that have post-trial significances $S_{\mathrm{post}} > 4\sigma$, which correspond to chance probabilities $P < 3 \times 10^{-5}$. We ran our algorithm on the 733 GRBs of the GBM sample (see Section 2.2) and so we expect no false-positive detections using this arbitrary threshold.

3.3.2. Duration Measurement

We describe the duration of a GRB detected by the LAT using the parameter T_{90} (Kouveliotou et al. 1993). A simple measurement of T_{90} starts with the construction of the integral distribution of the number of background-subtracted events accumulated since the trigger time. As the GRB becomes progressively fainter, the distribution flattens and eventually reaches a plateau.

The calculation of the duration of the emission consists of finding the times where the integral distribution reaches the 5% and 95% levels of its total height (called T_{05} and T_{95}, respectively), and calculating their difference $T_{90} \equiv T_{95} - T_{05}$. Our duration estimation method is based on the above simple prescription, but is also extended to estimate the statistical uncertainty of the results and accounts for the effects of effective area variations over time (for its application to the Transient-class events).

Because of the unavoidable statistical fluctuations involved in the process of detecting incoming GRB flux, a GRB observed under identical conditions by a number of identical detectors will in general produce different detected light curves and hence different duration estimates. Our method quantifies the uncertainties on the duration estimates associated with these statistical fluctuations. In short, it accomplishes this by treating the detected light curve as the true one (i.e., that of the incoming γ-ray flux), producing a set of simulated light curves by applying Poissonian fluctuations on the detected one, estimating the durations of the simulated light curves, and calculating a single duration estimate and its uncertainty from the distribution of simulated duration estimates.

Our method starts by constructing the integral distribution of the accumulated background-subtracted events curve in small steps in time. For each step, the number of expected background events is estimated and the number of detected events is counted. At the end of each step, an algorithm checks for the presence of a plateau by searching for statistically significant increases in the average value of the points added last to the curve. If a certain number of steps does not increase the integral distribution, a plateau is reached and the construction stops. A set of simulated light curves are then produced by adding Poisson noise to the observed light curve and the corresponding integral distributions are produced. A duration estimation is made for each of the simulated light curves and the results (T_{05}, T_{95}, and T_{90}) are recorded. After the durations of all the simulated light curves have been measured, the median and a (minimum-width) 68% containment interval are calculated for each distribution and used as our measurements and $\pm 1\sigma$ errors. In case the light curve contains multiple peaks separated by quiescent periods, the algorithm, depending on the intensity of each peak and the duration of the intermittent quiescent periods, might set the beginning of the plateau at the end of the last peak or during a quiescent period. In the latter case, some of the late emission might not be fully accounted for by the produced duration. However, the returned statistical errors would be appropriately increased in both cases, indicating the uncertainty of identifying the end of the emission.

Any changes in the off-axis angle of the GRB during an observation will change the effective area of the LAT, affecting the light curve. For example, a GRB observation that involves an ARR will in general start with a moderate to large off-axis angle that will then rapidly decrease and stay small for most of the rest of the observation. Because the effective area of this observation will be small before the ARR starts, the count rate will be artificially decreased and this would cause a bias in the measurement of T_{05} if it were simply based on counts. To account for this effect, we weight the simulated light curves by the inverse of the exposure.

To illustrate this method, we present in Figure 3 the case of GRB 080916C and the duration measurement using the Transient-class data. These curves are used as the basis for the simulations. Figure 4 shows the distribution of T_{05}, T_{95}, and T_{90}, as measured from the simulations. These distributions are used to define the duration and associated error. In this particular case, some excess events were observed at late times (about $\sim$400 s), as can be seen in Figure 3. Consequently, a small fraction of the simulated light curves gave T_{90} and T_{95} values that were very close to $\sim$400 s, which caused a small increase in the duration estimates and the errors for the positive fluctuations.

In some cases, a GRB observation can be interrupted before the GRB emission becomes too weak to be detectable (i.e., before reaching a plateau in the integral distribution).

Such interruptions can happen if the GRB exits the FoV of the LAT, it becomes occulted by the Earth, or the LAT enters the South Atlantic Anomaly (SAA), suspending observations. In these cases, only a lower limit on the duration can be obtained (with no errors), equal to the time interval between T_{05} and the interruption of the observation.

We apply this method to both Transient-class data and LLE data. In the former case, we use the BKGE to estimate the
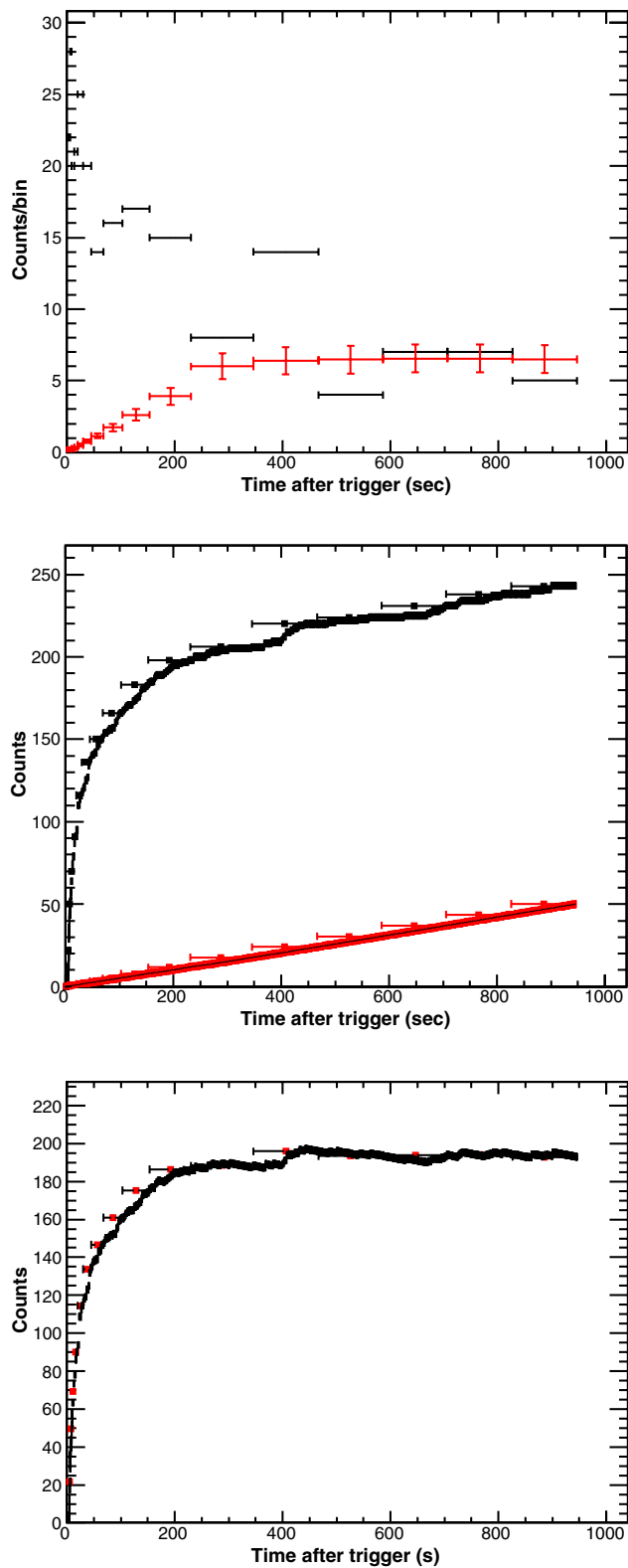
Figure 3. Duration estimation of GRB 080916C using Transient-class data. Top: number of detected counts (black) and estimated background (red) per time interval. Middle: accumulated number of detected counts (black) and expected background (red) since the trigger time. Bottom: accumulated number of background-subtracted events.

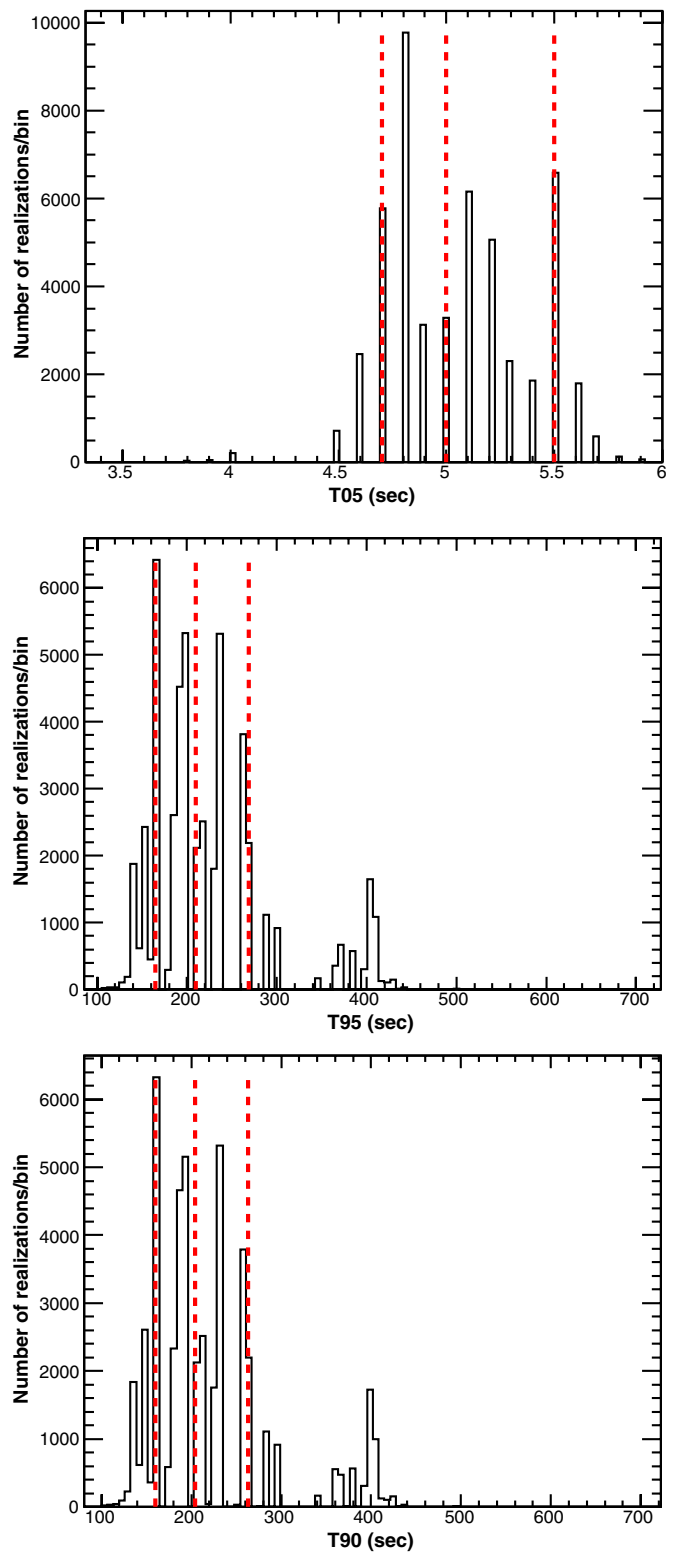(A color version of this figure is available in the online journal.)

Figure 4. Duration estimation of GRB 080916C using Transient-class data. Curves: distributions of T_{05} (top), T_{95} (middle), and T_{90} (bottom) as measured from the simulations. Middle vertical dashed lines: median of the distributions, constituting our best estimate of the duration. Left- and right-hand vertical dashed lines: 68% containment intervals, constituting our estimated error for the duration.

(A color version of this figure is available in the online journal.)

background, while for the latter case we use the polynomial fit, as described in Section 3.1.1. Note however that in the calculation of the duration the exposure weighting is performed only for Transient-class data, since the effective area for the LLE class has not been characterized yet.

As a cross check, we also apply a different algorithm to the LLE data. We consider the light curve with the binning that gives the highest significance, as obtained by the algorithm explained in Section 3.3.1, and we measure T_{05}, T_{95}, and T_{90} on the integral distribution obtained from that light curve. We verified that the numbers obtained with this simple method are always within the errors obtained with the other method. Thus, we will only provide the set of results related to the first algorithm.

3.4. Joint LAT-GBM Spectral Analysis

We performed joint GBM-LAT spectral fits for every GRB detected by the LAT.

3.4.1. Data Preparation

We start by selecting the GBM detectors as described in Section 2 and estimate the expected backgrounds as described in Section 3.1.2. We then use the *Fermi* Science Tool *gtbin* to extract the observed spectrum (source + background) from the GBM TTE data. We obtain the response of a GBM detector in the interval to be analyzed (t_1–t_2) using the RSP2 file for the detector for the time interval. Because the RSP2 file contains several response matrices corresponding to consecutive time intervals that in general are shorter than t_1–t_2, we sum the matrices of all the sub-intervals included in t_1–t_2 using an appropriate weighting scheme. Specifically, if c_i is the counts detected in the sub-interval covered by the ith matrix and $C = \sum_j c_j$ is the number of counts detected between t_1 and t_2, then the weight for the ith response matrix is

$$w_i = \frac{c_i}{\sum_j c_j}. \tag{4}$$

To sum the matrices, we use the tool *addrmf*, part of NASA HEASARC's FTOOLS.[81]

For the analysis of LAT observations of all GRBs detected inside the LAT FoV, we use the Transient-class events as described in Section 2. We bin the LAT data in 10 logarithmically spaced energy bins between 100 MeV and 250 GeV and use an energy-dependent ROI as described in Section 2.1.1. We derive the observed spectrum and the response matrix using the *Fermi* Science Tools *gtbin* and *gtrspgen*. We also use the BKGE to obtain a background spectrum containing the contributions from all the background sources, as described in Section 3.1.1.

Note that for GRBs detected by the LLE photon counting analysis outside the LAT FoV, we used only GBM data for the spectral analysis.

3.4.2. Spectral Fit

We load the spectra and response matrices in XSPEC v.12.7.[82] For GBM data, we exclude from the fit all of the NaI channels between 33 keV and 36 keV (corresponding to the iodine K-edge; see Meegan et al. 2009) and ignore the channels at the extremes of the spectra (channels below 8 keV and channels 127 and 128 for NaI; channels 1, 2, 127, and 128 for BGO). We do not exclude any energy bin in the LAT spectrum, since

we already selected the data before binning them. We jointly fit the GBM and LAT data with several models (described below), minimizing the negative log-likelihood. This likelihood function is derived from a joint probability distribution, obtained by modeling the spectral counts as a Poisson process and the background counts as a Gaussian process. For the latter, the Gaussian standard deviation for the ith channel is given by $\sigma_i = \sqrt{\sigma_{\mathrm{stat},i}^2 + \sigma_{\mathrm{sys},i}^2}$, where $\sigma_{\mathrm{stat},i}^2$ and $\sigma_{\mathrm{sys},i}^2$ are the statistical and the systematic variances, respectively. The maximum likelihood principle assures that the derivatives of the likelihood function with respect to the parameters are null for the best-fitting set of parameters. Exploiting this, one can treat the means of the Gaussian functions describing the background counts as *nuisance* parameters and remove them from the fitting procedure by expressing them as functions of the other parameters. This is a rather standard statistical procedure and leads to the formulation of a so-called *profile* likelihood function. PG-stat is defined as the natural logarithm of this function (see the XSPEC website[83] for more details). The fitting algorithms implemented in XSPEC find local minima for the statistic, but they can fail to converge to the global minimum. This is a known issue with gradient-descent algorithms (Arnaud et al. 2011). To mitigate this problem, we perform multiple fits (from 10 to 40) for each model, each time starting from a different set of values for the parameters, and we keep as the putative best fit the set giving the lowest overall value for the statistic. If the fitting algorithm finds an even better minimum for the statistic while computing error contours for this set of parameters, we adopt that as the new putative best fit and restart the error computation, iterating the procedure until no new minimum is found.

3.4.3. Spectral Models

Traditionally, GRB spectra have been described using the phenomenological "Band function" (Band et al. 1993) or a model consisting of a PL with an exponential cutoff (also called a "Comptonized model"). Another common choice is the smoothly broken power law (SBPL; Ryde 1999). Recently, the logarithmic parabola has been shown to be a good description the spectra of some GRBs, especially in time resolved analyses (Massaro et al. 2010; Massaro & Grindlay 2011). We call these four spectral models *main components*. One of the first results by *Fermi* was the need for multi-component spectral models for some GRBs, showing a high-energy excess over the main component that has been modeled with an additional PL (Ackermann et al. 2010b; Abdo et al. 2009a). In one case, *Fermi* observed a high-energy cutoff that required the addition of an exponential cutoff to the PL component in the spectral model (Ackermann et al. 2011), for a total of three components (Band, power law, and exponential cutoff). In the following, we will call the PL and the exponential cutoff functions *additional components*, to emphasize the fact that we add them to the main components when needed. Some authors have claimed the presence of a thermal component, modeled by a blackbody emission spectrum (see e.g., Guiriec et al. 2011; Zhang et al. 2011, and references therein). However, a careful time-resolved analysis is needed in order to investigate and characterize such a component, which is beyond the scope of the present analysis. Thus, we did not include a blackbody component in our spectral fits. Hereafter, $N(E)$ is the differential photon flux (in units of cm^{-2} s^{-1} keV^{-1}) expected from a model at a given energy E

---

[81] Available at: http://heasarc.nasa.gov/ftools.
[82] http://heasarc.nasa.gov/docs/xanadu/xspec/

[83] http://heasarc.nasa.gov/xanadu/xspec/manual/XSappendixStatistics.html

(in keV) and k is a normalization constant whose units depend on the model. We have four main model components:

1. *Comptonized model* (a PL with an exponential cutoff):

$$N(E) \equiv k E^{-\alpha} e^{-\frac{E}{E_0}}, \qquad (5)$$

where α is the photon index and E_0 is the cutoff energy.

2. *Logarithmic parabola*, defined following Equation (9) in Massaro et al. (2010):

$$N(E) \equiv \frac{S_p}{E^2} 10^{-b \log E/E_p^2}, \qquad (6)$$

where S_p is the height of the spectral energy distribution at the peak frequency, E_p is the peak energy, and b represents the curvature of the spectrum.

3. *Band model* (Band et al. 1993): two PLs joined by an exponential cutoff:

$$B(E) = N(E)$$
$$\equiv k \begin{cases} E^\alpha e^{-E/E_0} & \text{when } E < (\alpha - \beta) E_0 \\ [(\alpha - \beta) E_0]^{\alpha - \beta} & \\ \times E^\beta e^{-(\alpha - \beta)} & \text{when } E > (\alpha - \beta) E_0 \end{cases}.$$
$$(7)$$

Note that this is the representation that uses the e-folding energy E_0 (keV) instead of the peak energy E_p, where $E_p = (2 + \alpha)E_0$. α and β are the (asymptotic) photon index at low energy and the photon index at high energy, respectively.

4. *Smoothly broken power law* (Ryde 1999): two PLs joined by a hyperbolic tangent function with an adjustable transition length:

$$N(E) \equiv k \left(\frac{E}{E_{\text{piv}}} \right)^{\frac{\alpha+\beta}{2}} \left[\frac{\cosh\left(\frac{\log(E/E_0)}{\delta}\right)}{\cosh\left(\frac{\log(E_{\text{piv}}/E_0)}{\delta}\right)} \right]^{\frac{\alpha+\beta}{2}\delta \log_e} (10)$$
$$(8)$$

where E_{piv} is a fixed pivot energy, α and β are, respectively, the photon index of the low-energy and the high-energy PLs, E_0 is the e-folding energy, and δ is the energy range over which the spectrum changes from one PL to the other.

Here are the definitions of our additional model components:

1. *Power law*: $N(E) \equiv k E^{-\alpha}$, where α is the photon index.

2. *Exponential cutoff*: $e^{-\frac{E}{E_0}}$.

Because of the variety of spectral models, we have considered a number of functions composed of one main component and one or more additional components: Band, Band + power law, Band + power law with exponential cutoff ($\equiv B(E) + k E^{-\alpha} e^{-E/E_0}$), Band with exponential cutoff ($\equiv B(E)e^{-E/E_0}$), Comptonized, Comptonized + power law, Comptonized + power law with exponential cutoff, logarithmic parabola, SBPL, and SBPL + power law.

To take into account the relative unknown uncertainties in the inter-calibration between the different detectors, for bright bursts we also apply an effective area correction (Bissaldi et al. 2011): we scale the model under examination by a multiplicative constant, with the constant being fixed to 1 for the LAT (taken as reference detector), but free to assume different values for all the other detectors. For GRBs for which we do not use LAT data, we choose one of the NaI detectors as the reference. While
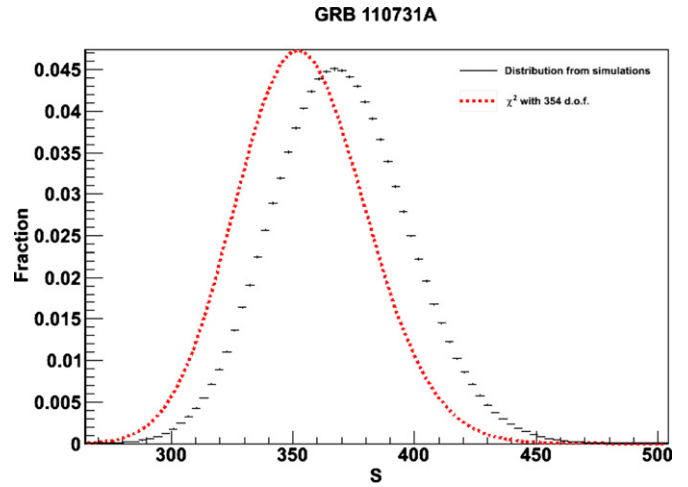

Figure 5. Distribution for the PG-stat as obtained from Monte Carlo simulations for GRB 110731A using the Band model as a null hypothesis (black points). We report the χ^2 distribution for the same number of dof for reference (red dashed line).

(A color version of this figure is available in the online journal.)

for bright bursts adding such a correction changes the best-fit parameters and the value of the statistic, for the other bursts it is essentially inconsequential, since in the latter cases statistical errors dominate over the inter-calibration uncertainties. For such spectra, the multiplicative factors are unconstrained during the fit and therefore we removed them. After the best fit is found, we fix all the factors to their best-fit values and we proceed with the error computation. The correction factors typically have values between 0.95 and 1.05 for the NaI detectors and between 0.75 and 1.25 for the BGO detectors.

3.4.4. Definition of a Good Fit and Model Selection

The main focus of the spectral analysis performed here is to characterize the GRB spectrum, which requires selecting the most appropriate spectral model. We define the best model for a given GRB as the simplest one giving a "good" value for the test statistic (PG-stat, S in the following) and no evident structures in the residuals. Since S is based on a Poisson likelihood, we do not have a simple goodness-of-fit test comparable with the χ^2 test when minimizing the χ^2 statistic. The actual expected value S^* for the statistic S is a function of the number of counts N in the spectrum and the background model and its uncertainties and can be estimated using Monte Carlo simulations. We assume a model $m_0(\boldsymbol{p})$ (for example, the Band model) with the best-fitting set of parameters $\boldsymbol{p}_0$ as the null hypothesis and we generate 1 million realizations of $m_0(\boldsymbol{p}_0)$ and the corresponding background spectrum using the *fakeit* command of XSPEC. Each realization $r_{p_0}^i$ is obtained by adding Poisson noise to the count spectrum obtained by summing the observed background spectra and $m_0(\boldsymbol{p}_0)$. Correspondingly, each realization of the background spectrum is obtained by adding Gaussian noise to the observed background spectrum, using a total variance composed of the statistical and the systematic variance of the observed background. Then, we fit $m_0(\boldsymbol{p})$ to $r_{p_0}^i$ and we record the value for the statistic S_i. In Figure 5, we show an example of a distribution for S obtained using the Band model and a χ^2 distribution for the same number of dof as reference. Note that depending on the case, the two distributions can be very different. We can now use the distribution for S resulting from the simulations to compute the probability of obtaining the observed
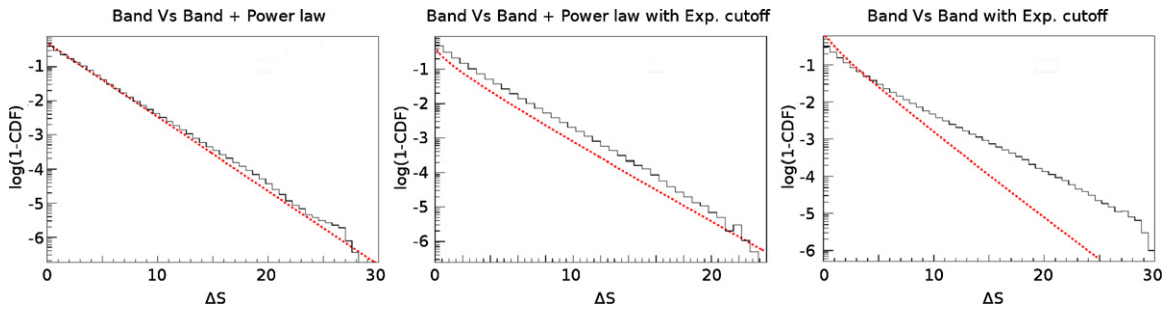
Figure 6. Complementary cumulative distribution function $(1 - \mathrm{CDF})$ for ΔS, for three different pairs of models: Band vs. Band + power law (left panel), Band vs. Band + power law with exponential cutoff (center panel), and Band vs. Band with exponential cutoff (right panel). The dashed line corresponds to the complementary CDF of $\chi_n^2/2$ with $n = n_{0,\mathrm{dof}} - n_{1,\mathrm{dof}}$ (see the text).

(A color version of this figure is available in the online journal.)

value for S under the null hypothesis m_0. This approach requires a large number of simulations, so we applied it just for the subsample of GRBs for which we claim the detection of an extra component (see below and Section 4.4.1).

In order to compare different models, we considered them in pairs. Let us consider the model m_0 with $n_{0,\mathrm{dof}}$ and m_1. If $S_0 < S_1$ and $n_{0,\mathrm{dof}} \leqslant n_{1,\mathrm{dof}}$, then m_0 describes the data better using fewer or the same number of parameters and we consider it a better fit following the definition given at the beginning of this section. If $S_0 \simeq S_1$ and $n_{0,\mathrm{dof}} = n_{1,\mathrm{dof}}$, the two models are equivalent and we should report the results for both models. Anyway, this never happened in our analysis. On the other hand, if $S_0 > S_1$, then m_1 better fits the data and we have to decide if the improvement is significant enough to justify the added complexity. In the literature, there are different ways to quantify this improvement, sometimes incorrectly (see, for example, the discussion in Protassov et al. 2002). One of the standard methods is the likelihood-ratio test, which uses as a test statistic the difference in S (ΔS) between the two models. In the case of nested models m_0 and m_1, Wilks' theorem (Wilks 1938) assures under certain hypotheses that the quantity ΔS asymptotically follows a χ^2 distribution with $n = n_{0,\mathrm{dof}} - n_{1,\mathrm{dof}}$ dof. Unfortunately, in all the cases of interest here, the theorem's hypotheses are not satisfied and the reference distribution for ΔS is not known. In general, one should perform dedicated Monte Carlo simulations to obtain the reference distribution. Performing such simulations for each pair of models is not practical. Thus, we select three cases of interest (i.e., Band versus Band + power law, Band versus Band with exponential cutoff, and Band + power law versus Band + power law with exponential cutoff) and we perform several million simulations to evaluate the reference distributions. We use the same procedure as above, using the simplest model as the null hypothesis, but we fit both m_0 and m_1 to each simulated dataset, recording ΔS. At the end of the simulation, the distribution for ΔS is used to compute the probability P of obtaining a ΔS greater than the observed value, which corresponds to the complement of the cumulative distribution function. In Figure 6, we plot this function for the three cases. We fix an arbitrary threshold at $P_{\mathrm{th}}(> \Delta S) = 1 \times 10^{-5}$, where the statistical error on the simulated distribution, visible toward the tail, is still low. P_{th} corresponds to a significance level of $\sim 4.2\sigma$ and defines a threshold for ΔS above which we claim a significant detection of an extra component. Specifically, P_{th} corresponds to $\Delta S = 25$ for Band versus Band + power law, $\Delta S = 28$ for Band versus Band with exponential cutoff, and $\Delta S = 20$ for Band + power law versus Band + power law with exponential cutoff.
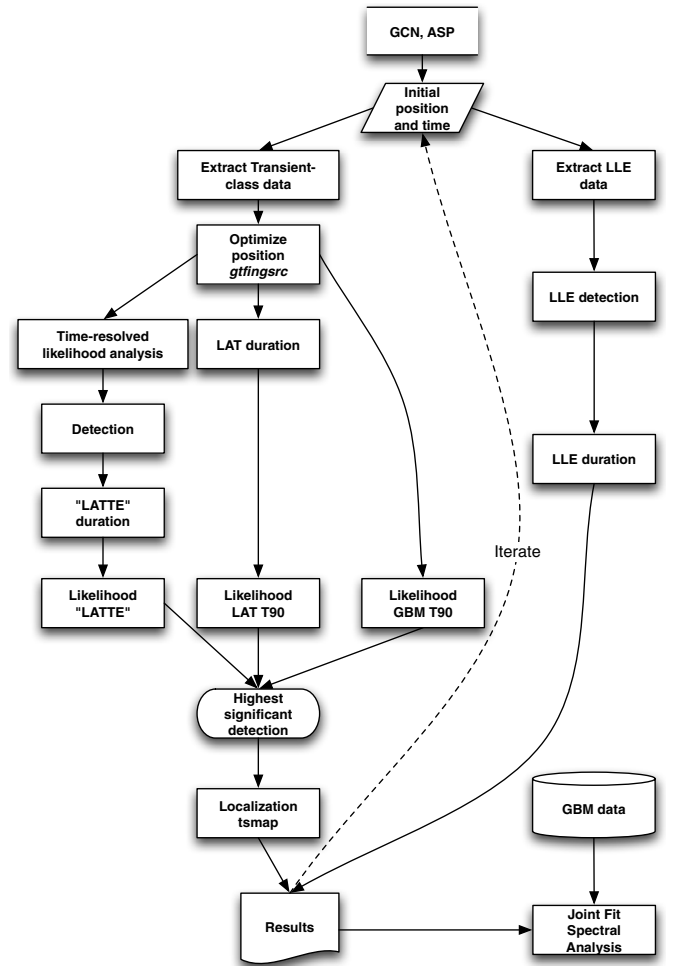

Figure 7. Schematic representation of the analysis sequence adopted in this work.

3.5. Analysis Sequence

The sequence of analyses performed in this work is graphically represented in Figure 7. We start our analysis using the best available localization provided via GCN typically by *Swift* or the GBM and in some cases by other observatories. Detections occurring in Automated Science Processing (ASP) of LAT data (Band et al. 2009) are also used as inputs. We then extract both Transient-class and LLE data. We use the Transient-class data to optimize the location of the GRB. However, if the reported position error is significantly smaller than the angular

resolution of the LAT, there is no room for improvement and we adopt the GCN position. This is the case for localizations provided by *Swift* or by optical observatories. On the other hand, if the reported position has an error larger than the characteristic size of the LAT Transient-class PSF ($\sim$0.5 deg at 1 GeV)—most notably those typically provided by the GBM—we repeat most of the steps in our analysis sequence multiple times, starting each iteration with the best position obtained during the localization step of the previous one, until we cannot improve the localization further. Typically, we repeat the analysis 2–3 times until the localization obtained in the last step is within the error on the localization of the previous iteration. This introduces a small number of trials, which are also strongly correlated since they only involve small changes in the analysis configuration/data. High confidence localization errors (90%–95%) are not affected and we therefore decided to ignore this trial factor. The analysis of Transient-class data consists of the following steps.

1. *Duration Measurement*. We apply the techniques described in Section 3.3.2 to compute the duration (T_{90}) of the burst, using Transient-class data. We define the "LAT interval" as the time interval from T_{05} to T_{95} (of duration $T_{90} = T_{95} - T_{05}$) measured in this step. In case of a non-detection, the value of the LAT T_{90} is not available in the following steps.

2. *Time-resolved likelihood analysis*. The next step consists of time-resolved spectral analysis, which allows us to study the temporally extended emission systematically, one of the common characteristics of LAT GRBs. We analyze all data contained in GTIs within 10 ks from the GRB trigger, binning them in time. We tested several binning schemes, including linear, logarithmic, and Bayesian-blocks binning, and the resulting likelihood fit parameters were consistent among the different choices. The logarithmically spaced binning provides constant-fluence bins when applied to a signal that decreases approximately as 1/time, such as the extended GRB emission observed by the LAT. We adopt that scheme as the starting point, we start from a bin size containing at least N events, where N corresponds to the number of parameters in the model, plus 2, and then we merge consecutive time bins until we obtain a minimum TS value.

  Specifically, we divide the data into logarithmically spaced bins, truncating bins at the edges of excluded time intervals when necessary. Then, we merge bins until each of them has a number of counts at least equal to the number of parameters of the likelihood model plus 2. We then fit each bin using the maximum likelihood analysis described in Section 3.2 obtaining the likelihood and the TS value corresponding to the best-fit source model. If the resulting TS value is lower than an arbitrary threshold (TS < 16, corresponding to a pre-trials significance >$\sim$3.2–3.8σ depending on $n_{\rm dof}$), we merge the corresponding time bin with the next one and we repeat the likelihood analysis. This step is iterated until one of two conditions is satisfied: 1) we reach the end of a GTI before reaching TS = 16, in which case we compute the value of the 95% CL UL for the flux evaluated using a photon index of 2[84] or 2) we reach TS > 16, in which case we evaluate the best-fit values of the flux and the spectral index along with their 1σ errors.

The time interval between the beginning of the first and the end of the last time bin for which TS > 16, named the "LAT temporally extended time interval" (hereafter "LATTE"), constitutes a rough estimate of the time window where the GRB emission is detectable with at least a $\sim$3σ significance.

3. *Characterization of the extended emission*. After having characterized the GRB in each time bin separately, we study the light curve as a whole. Specifically, we select the events contained in an energy-dependent ROI (see Section 2.1.1) in each time bin, building a light curve of the detected counts, and we estimate the background in each time bin using the BKGE. We also compute the exposure (in cm^2 s) associated with each time bin, using the tool *gtexposure*[85] calculated in each energy-dependent ROI separately. This last step requires knowledge of the spectrum. For each time bin, we use the corresponding best-fit, PL model as found in the bin-by-bin analysis described before. We note here that in principle the uncertainty in the best-fit parameters for the PL would translate into an uncertainty in the value of the exposure, because of the energy dependence of the effective collecting area of the LAT. In our case, such an error is typically of the order of 5%, which is smaller than the systematic uncertainty in the response of the LAT and will be neglected.

  Summarizing, for each time bin i we have the observed number of counts N_i (in the energy-dependent ROI), the corresponding background estimate B_i, and the corresponding exposure A_i. Assuming a given model for the light curve $M(t)$ (for example, a PL), we compute the expected number of observed counts in the ith bin between $t_{i,1}$ and $t_{i,2}$ as

$$N_{i,\rm pred} = \left(\int_{t_{i,1}}^{t_{i,2}} M(t)dt \right) \times A_i + B_i. \qquad (9)$$

We compare $N_{i,\rm pred}$ with N_i and look for the best-fit parameters for the model $M(t)$, minimizing a Poisson log-likelihood function. We actually used the PG-stat log-likelihood function implemented in XSPEC v.12.7, which takes into account the uncertainty on B_i (see Section 3.4.2 for details). This technique, which might seem unnecessarily complex, provides a natural way of including in the fit the time intervals during which the source is barely detected or not detected at all. Indeed, they can be treated exactly like all the others, by comparing $N_{i,\rm pred}$ with N_i, even if $N_i \simeq B_i$. As a consistency check, we also have used the more conventional technique of fitting $M(t)$ to the count-flux light curve as obtained from the likelihood analysis, minimizing χ^2. To incorporate information from ULs on the flux computed from the unbinned analysis,[86] we first re-scaled the one-sided 95% CL UL to two-sided 68% CL confidence intervals under the assumption that the errors are normally distributed. Then, we replaced the value of the UL with the value of a point that would have the 68% CL correspond to the value of the UL. To obtain reliable values from the fit, we required at least one positive detection after the peak flux (in addition to ULs). The two methods gave virtually identical results and so we provide

---

[84] Conventionally the photon index for a GRB spectrum is defined as positive (i.e., $dN/dE \approx E^{-\gamma}$).

[85] http://fermi.gsfc.nasa.gov/ssc/data/analysis/scitools/help/gtexposure.txt

[86] To calculate UL, we use the *python* interface to the *Likelihood* package, as described here: http://fermi.gsfc.nasa.gov/ssc/data/analysis/scitools/python_usage_notes.html#UpperLimit.

Table 1
Definitions of Intervals Used in Time-integrated Spectral Analysis

Name	Definition	Description
GBM	GBM T_{05} – GBM T_{95}	Bulk of the GBM-detected emission
LAT	LAT T_{05} – LAT T_{95}	Bulk of the LAT-detected emission
PRE	GBM T_{05} – LAT T_{05}	Interval between GBM and LAT emission onsets
JOINT	LAT T_{05} – GBM T_{95}	Interval when both the GBM and LAT significantly detect emission
EXT	GBM T_{95} – LAT T_{95}	Interval between the end of GBM-detected and LAT-detected emissions
LATTE		Interval between the start of the first and the end of the last bins with TS > 16, as found by the time-resolved likelihood analysis

only the values from the second method, the fit of the count light curve.

We consider two models for the light curve: a simple PL model:

$$F(t) = F_0 \times (t/t_p)^{-\alpha}, \qquad (10)$$

where F_0 and α are the free parameters, and a broken PL model:

$$F(t) = F_0 \times (H(t > t_b) \times (t/t_b)^{-\alpha_1} + H(t < t_b) \times (t/t_b)^{-\alpha_2}), \qquad (11)$$

where both indices (α_1 and α_2) are left free, the normalization is F_0, and the break time is t_b. $H(x)$ is the Heaviside function whose value is 0 for $x < 0$ and 1 for $x \geqslant 0$. We measure the time t_p at which the detected flux reaches its maximum value F_p (the "peak flux") as the center of the time bin with the maximum count flux. We then consider two time intervals starting, respectively, at the peak $t \geqslant t_p$ and after the end of the prompt emission $t > $ GBM T_{95}. For each time interval, we fit the PL and the broken PL models and we compare them by performing Monte Carlo simulations similarly to the procedures described in Section 3.4.4. We consider a break significantly detected when its chance probability is smaller than 10^{-3}. In the above, all times are with respect to the GBM trigger time.

4. *Time-integrated likelihood analysis*. We now perform the likelihood analysis on different time intervals, defined in Table 1. These intervals are defined using combinations of the GBM durations reported in Paciesas et al. (2012), the Transient-class durations, and the LATTE time window. If we obtain a TS > 20 in any of these time intervals, we consider the GRB detected.

5. *Localization*. We select the interval where the GRB is detected with the largest significance among those considered in the previous step, along with the corresponding likelihood model, and we generate an improved localization using the second method described in Section 3.2.2. If the new localization has a greater significance and a smaller error than the current one, we repeat the analysis chain from the beginning, adopting the new improved value. Otherwise, we select the old localization and all the results of the last iteration of the analysis chain as the final ones and proceed to the next step. Note that we typically perform a few iterations of the whole chain.

6. *LLE analysis*. In parallel, we execute the LLE analysis, which consists of three steps. We first extract LLE data and then run the detection algorithm on LLE-class data (see Section 3.3.1). Finally, if the GRB is detected ($S_{post} > 4\sigma$), we evaluate its duration (see Section 3.3.2). Note that this part of the analysis is performed again when an improved localization is obtained using LAT Transient-class data.

7. *LAT-GBM joint spectral fits of the prompt emission*. We use the best available position to extract the spectrum of the GRB across the whole energy range covered by *Fermi*. We fit the spectrum, following the procedure described in Section 3.4. We perform a spectral analysis in two time intervals: the "GBM" time interval defined in Table 1 and the time interval starting when the first LAT photon is detected in the GRB ROI and extending up to the GBM T_{95} instant.

4. RESULTS

In this section, we describe the results from our analysis; all tables are explained in Section 7 and detailed discussions for each detected GRB are in Appendix B. According to the standard definition, GRBs with GBM $T_{90} > 2$ s are defined as long, while short-duration GRBs have GBM $T_{90} < 2$ s. Any ULs from the maximum likelihood analysis are for a 95% CL and are calculated using a photon index of 2. We quote fluences in two Earth reference frame energy ranges: 10 keV–1 MeV and 100 MeV–10 GeV, appropriate to characterize the GRB emission as measured by the GBM and the LAT, respectively. For all of the quantities, a subscript ("LAT," "GBM," or "EXT") is added to indicate the time interval used to perform the spectral analysis. Low-energy (10 keV–1 MeV) fluences of non-LAT-detected GRBs are from the GBM spectral catalog (Goldstein et al. 2012) and fluences of LAT-detected GRBs are from our joint GBM-LAT spectral analysis. A discussion on how the LAT-detected burst fluences compare with the distribution of fluences for all the GBM-detected bursts is left for the next section.

4.1. LAT Detections

We searched for high-energy emission with the LAT for the 733 GRBs described in Section 2.2 and detected 35, using the detection criteria described in Sections 3.3.1 and 3.2.1. Among them, 28 were detected by our maximum likelihood analysis at energies above 100 MeV and 21 were detected using event-counting methods applied to the LLE data. Among the GCN circulars issued by the LAT team, three GRBs (listed below) were not included in this catalog as they were below the significance threshold, while we also discovered four not previously claimed bursts (GRBs 090227B, 090531B, 100620A, and 101123A). Thirty of our detected GRBs are of the long-duration class and five are of the short-duration class (GRBs 081024B, 090227B, 090510, 090531B, and 110529A).

We list the LAT-detected GRBs in Table 2 and report their trigger times, off-axis angles at trigger time, best available localizations with errors, redshifts, and references to GCN circulars. In the table, we also report whether these GRBs were

Table 2
Sample of *Fermi*-LAT GRBs, from 2008 August to 2011 August

GRB Name	Date	GBM Trigger Time (MET[a])	R.A. Deg., J2000	Decl. Deg., J2000	θ Deg.	Loc. Err.[b]	Like.	LLE	Redshift	LAT GCN Number
080825C	2008 Aug 25 14:13:48.1	241366429.105	233.9	−4.5	60.3	0°.75$^\gamma$	1	0	. . .	8183
080916C	2008 Sep 16 00:12:45.6	243216766.614	119.85	−56.64	48.8	0″.36*	1	1	4.35	8246
081006	2008 Oct 6 14:29:34.1	244996175.173	136.32	−62.05	11.0	0°.52$^\gamma$	1	0	. . .	
081024B	2008 Oct 24 21:22:40.8	246576161.864	322.95	21.2	18.7	0°.22$^\gamma$	1	1	. . .	8407
090217	2009 Feb 17 04:56:42.5	256539404.560	204.83	−8.42	34.5	0°.35$^\gamma$	1	1	. . .	8903
090227B	2009 Feb 27 18:31:01.4	257452263.410	10.48	29.24	71.0	1°.00$^\triangle$	1	1	. . .	
090323	2009 Mar 23 00:02:42.6	259459364.630	190.71	17.053	57.2	0″.36*	1	1	3.57	9021
090328	2009 Mar 28 09:36:46.5	259925808.510	90.67	−41.715	64.6	0″.72*	1	1	0.74	9044, 9077
090510	2009 May 10 00:22:59.9	263607781.971	333.55	−26.583	13.6	1″.44*	1	1	0.90	9334, 9350
090531B	2009 May 31 18:35:56.4	265487758.490	252.07	−36.015	21.9	2′.10*	0	1	. . .	
090626	2009 Jun 26 04:32:08.8	267683530.880	170.03	−33.49	18.3	0°.22$^\gamma$	1	0	. . .	9584
090720B	2009 Jul 20 17:02:56.9	269802178.905	202.99	−54.21	56.1	0°.33$^\gamma$	1	0	. . .	
090902B	2009 Sep 2 11:05:08.3	273582310.313	264.94	27.324	50.8	3″.60*	1	1	1.82	9867, 9872
090926A	2009 Sep 26 04:20:26.9	275631628.990	353.4	−66.32	48.1	0′.60*	1	1	2.11	9934, 9972
091003	2009 Oct 3 04:35:45.5	276237347.585	251.52	36.625	12.3	1″.80*	1	0	0.90	9985
091031	2009 Oct 31 12:00:28.8	278683230.850	71.49	−57.65	23.9	0°.23$^\gamma$	1	1	. . .	10163
091208B	2009 Dec 8 09:49:57.9	281958599.956	29.392	16.89	55.6	1″.80*	1	0	1.06	
100116A	2010 Jan 16 21:31:00.2	285370262.240	305.01	14.43	26.6	0°.17$^\gamma$	1	1	. . .	10333
100225A	2010 Feb 25 02:45:31.1	288758733.147	310.3	−59.4	55.5	3°.13†	0	1	. . .	10450
100325A	2010 Mar 25 06:36:08.0	291191770.020	330.24	−26.45	7.1	0°.60$^\gamma$	1	0	. . .	10548
100414A	2010 Apr 14 02:20:21.9	292904423.990	192.11	8.693	69.0	1″.80*	1	0	1.37	10594
100620A	2010 Jun 20 02:51:29.1	298695091.100	86.9	−50.91	24.3	0°.71$^\gamma$	1	0	. . .	
100724B	2010 Jul 24 00:42:05.9	301624927.980	119.89	76.55	48.9	0°.88$^\gamma$	1	1	. . .	10978
100728A	2010 Jul 28 02:17:30.6	301976252.610	88.758	−15.255	59.9	0″.36*	1	0	. . .	
100826A	2010 Aug 26 22:58:22.8	304556304.898	279.593	−22.128	73.3	1°.20$^\triangle$	0	1	. . .	11155
101014A	2010 Oct 14 04:11:52.6	308722314.620	27.206	−50.819	54.0	1°.0†	0	1	. . .	11349
101123A	2010 Nov 23 22:51:34.9	312245496.973	135.16	1.91	78.2	3°.16†	0	1	. . .	
110120A	2011 Jan 20 15:59:39.2	317231981.230	61.5	−12.0	13.6	0°.36$^\gamma$	1	0	. . .	11597
110328B	2011 Mar 28 12:29:19.1	323008161.194	121.06	45.84	31.7	3°.23†	0	1	. . .	11835
110428A	2011 Apr 28 09:18:30.4	325675112.410	5.59	64.849	34.6	0″.04*	1	0	. . .	11982
110529A	2011 May 29 00:48:42.8	328322924.872	118.33	67.91	30.0	3°.35†	0	1	. . .	12044
110625A	2011 Jun 25 21:08:18.2	330728900.236	286.73	6.755	87.9	0″.36*	1	0	. . .	12097, 12100
110709A	2011 Jul 9 15:24:27.4	331917869.400	238.895	40.918	53.4	1″.08*	1	0	. . .	
110721A	2011 Jul 21 04:47:43.7	332916465.760	333.2	−38.5	40.7	0°.20$^\triangle$	1	1	. . .	12188
110731A	2011 Jul 31 11:09:29.9	333803371.954	280.504	−28.537	3.4	0″.36*	1	1	2.83	12218

Notes.
[a] Mission Elapsed Time: seconds since 2001-1-1 00:00:00 UTC.
[b] Uncertainties on the localizations from: $^\gamma$ *Fermi*-LAT, † *Fermi*-GBM, * *Swift*-XRT/*Swift*-UVOT, $^\triangle$ IPN.

detected by the LLE and the maximum likelihood analyses. The LLE detection significances and the likelihood TS values can be found in Table 3.

As a cross-check of our adopted detection thresholds and to estimate the rate of false detections in our sample, we repeated the analysis on a sample of "fake GBM triggers." We generated the list of fake GBM triggers by changing the real trigger times T_0 of the input list to $T_0 − 11466$ s, corresponding to approximately two orbits before the true trigger. The standard operating mode for the *Fermi* spacecraft is to change the rocking angle every orbit, viewing alternately the northern and southern orbital hemispheres. Thus, with the exception of ARRs, the "fake" sample has very similar background conditions with respect to the true sample. Excluding the ARR, for each fake GRB trigger, we computed the TS value in a series of time intervals (of 1, 3, 10, 30, 100, 300, and 1000 s duration), kept the highest TS value we obtained for each fake GRB, and compiled them into a cumulative distribution. Figure 8 compares the cumulative distribution with the same distribution for the true GBM trigger sample. Both distributions have been normalized to unity for TS = 0 [i.e., $P(\text{TS} > 0) = 1$]. For the fake triggers, we did not obtain any value for the TS greater

than $\text{TS}_{\min} = 20$ (our nominal detection threshold). The excess of the TS distribution of the true GRB sample with respect to the null distribution for TS > 20 is evident. It is important to note that the full analysis chain performed on the actual data and described in the previous section also optimizes the time window to compute the likelihood analysis, a task that is not included here.

As discussed above, in addition to the GRBs reported here, the LAT team has reported detections of three other GRBs via the GCN, but for the reasons explained below we have not included these events in the final table as they were formally below the detection threshold set for this catalog. These are:

1. GRB 081224, for which a tentative on board localization with the LAT was delivered via GCN (Wilson-Hodge et al. 2008). Further on-ground analysis did not confirm the signal excess found in the LAT data and a retraction GCN notice was issued (McEnery 2008b). Whereas the GBM light curve is a broad single pulse event lasting ~17 s, the LLE light curve shows a narrow spike at T_0 that is not associated with the main pulse in the GBM, with a low significance of 3.1σ only.

Table 3
Comparisons between Duration Estimators

GRB Name	Class[a]	GBM T_{05} (s)	GBM T_{95} (s)	LAT T_{05} (s)	LAT T_{95} (s)	LLE T_{05} (s)	LLE T_{95} (s)	Max TS	LLE Significance σ, Post Trials
080825C	L	1.22	23.4 ± 0.2	$3.3^{+0.2}_{-0.1}$	29^{+17}_{-3}	...	...	57	3.4
080916C	L	1.28	65.5 ± 0.8	$5.0^{+0.5}_{-0.3}$	210^{+60}_{-50}	$4.1^{+0.2}_{-0.1}$	80^{+30}_{-20}	1450	26.1
081006	L	-0.26	5.9 ± 0.9	>0.7	>100	...	...	72	1.1
081024B	S	-0.06	0.5 ± 0.3	>0.05	>200	$-0.1^{+0.1}_{-0.3}$	$2.1^{+0.2}_{-0.3}$	111	4.5
090217	L	0.83	34.9 ± 0.7	$6.2^{+110}_{-5.0}$	70^{+110}_{-40}	0^{+2}_{-8}	$14.0^{+7.3}_{-0.8}$	105	10.9
090227B	S	-0.06	1 ± 1	...	...	-0.01 ± 0.01	$1.6^{+0.3}_{-0.8}$	30	20.5
090323	L	8.19	152 ± 1	16^{+47}_{-5}	290^{+50}_{-30}	$6.9^{+1.0}_{-2.1}$	185^{+13}_{-6}	136	14.4
090328	L	4.35	70 ± 2	19^{+33}_{-4}	650^{+130}_{-40}	9 ± 1	90^{+10}_{-50}	107	14.2
090510	S	0.48	0.9 ± 0.1	$0.6^{+0.1}_{-0.0}$	50^{+50}_{-20}	0.630 ± 0.005	7 ± 1	1897	30.0
090531B	S	-0.20	0.8 ± 0.2	...	...	$-0.19^{+0.09}_{-0.27}$	$0.6^{+1.5}_{-0.6}$	$-$	12.9
090626	L	1.54	52 ± 3	50 ± 20	300^{+340}_{-50}	...	...	71	3.0
090720B	L	-0.26	6.4 ± 0.7	...	...	...	...	25	1.7
090902B	L	2.82	25.0 ± 0.3	>8	>800	$6.5^{+0.3}_{-0.5}$	65^{+7}_{-19}	1832	22.0
090926A	L	2.18	18.1 ± 0.3	>6	>200	4.0 ± 0.2	44^{+4}_{-9}	1983	24.0
091003	L	0.83	21.9 ± 0.4	4 ± 3	450^{+90}_{-380}	...	...	108	2.2
091031	L	1.41	36.7 ± 0.5	$3.1^{+3.4}_{-0.1}$	210^{+10}_{-40}	$-1.2^{+0.6}_{-0.3}$	17^{+2}_{-3}	44	14.4
091208B	L	0.26	15 ± 2	...	...	...	...	20	0.6
100116A	L	84.00	103 ± 2	>3	>100	$90.3^{+0.5}_{-0.2}$	114^{+12}_{-9}	77	19.3
100225A	L	-0.26	12 ± 3	...	...	3^{+1}_{-11}	17^{+1}_{-5}	7	6.0
100325A	L	-0.38	6 ± 2	...	...	...	...	40	2.4
100414A	L	1.86	30 ± 2	17^{+4}_{-5}	290^{+90}_{-110}	...	...	81	3.4
100620A	L	0.13	41.2 ± 0.7	...	...	...	...	24	0.8
100724B	L	8.96	128 ± 5	...	...	7.2 ± 0.5	104^{+24}_{-9}	93	25.9
100728A	L	14.85	192.6 ± 0.9	...	...	...	...	32	2.9
100826A	L	8.19	130 ± 10	...	...	9^{+2}_{-3}	59^{+9}_{-8}	6	19.1
101014A	L	1.41	452 ± 1	...	...	$208.5^{+0.3}_{-0.4}$	216 ± 1	$-$	15.4
101123A	L	40.26	150.8 ± 0.7	...	...	$43.4^{+0.1}_{-0.3}$	52^{+4}_{-1}	$-$	18.0
110120A	L	0.26	28 ± 10	$0.5^{+0.2}_{-0.1}$	110^{+20}_{-30}	...	...	35	3.3
110328B	L	2.05	130 ± 20	...	...	$-0.0^{+0.9}_{-1.0}$	37 ± 6	4	17.9
110428A	L	2.69	11.0 ± 0.2	11^{+4}_{-3}	410^{+90}_{-340}	...	...	53	0.0
110529A	S	0	0.41 ± 0.03	...	...	$0.0^{+0.0}_{-0.3}$	$0.4^{+0.8}_{-0.2}$	$-$	18.8
110625A	L	3.07	34 ± 1	...	...	...	...	57	0.0
110709A	L	1.10	44.3 ± 0.4	...	...	...	...	23	2.2
110721A	L	0.45	25.4 ± 0.7	>0.05	>200	-0.62 ± 0.03	20 ± 20	162	30.0
110731A	L	0.26	7.8 ± 0.3	3.0 ± 0.2	24^{+170}_{-8}	$2.5^{+0.4}_{-0.6}$	17^{+1}_{-7}	460	17.6

Notes. [a] In accordance with convention, we define as Short (S) those GRBs with GBM $T_{90} < 2$ s and those as Long (L) with $T_{90} > 2$ s. Durations of GBM bursts are from Paciesas et al. (2012).

2. GRB 100707A, which had a significance of 3.7σ using the LLE data. This result confirms the early detection (Pelassa & Pesce-Rollins 2010) obtained with a dedicated event selection that was required by the burst inclination of $\sim 90°$ at trigger time.

3. GRB 081215, which was similarly observed at a large off-axis angle and the LAT team detection for the GCN circular was by means of a dedicated event selection (McEnery 2008a). However, this burst was not detected by either of our methods here, having a very low significance in both the LLE and standard likelihood analyses.

Using matched-filter techniques, Akerlof et al. (2010, 2011) and Zheng et al. (2012a, 2012b) reported that GRBs 081006, 080905A, 090228A, 091208B, and 110709A are possibly detected by the LAT. By means of a counting method based on the LAT Diffuse class events, Rubtsov et al. (2012) also claimed the detection of four new candidates: GRBs 081009, 090720B, 100911A, and 100728A. We concur on some of these GRBs:

1. GRB 081006 is significantly detected by our likelihood analysis (with a TS of 72), although no significant emission is detected in LLE data. This burst is part of our catalog.

2. GRB 080905A (localized by *Swift;* Evans et al. 2008) corresponded to only a marginal significance (TS = 16.8), lower than our detection threshold. Additionally, no signal was detected in LLE data.

3. GRB 081009 is a GBM-detected burst, which was not detected by *Swift*. In our analysis, the final value of the TS is 14, which is below our detection threshold. Also, the GRB is not detected in the LLE data above our detection threshold of 4σ, likely due to the high inclination of $94°.5$ at the trigger time.

4. GRB 090228A has TS $\lesssim 20$ after optimization of its position and using the initial location published in Guiriec et al. (2010). There is no signal in the LLE data and the value of TS is right at our detection threshold. We did not add this GRB to the catalog. However, the photon index calculated by the likelihood analysis (~ -1.7), as well as
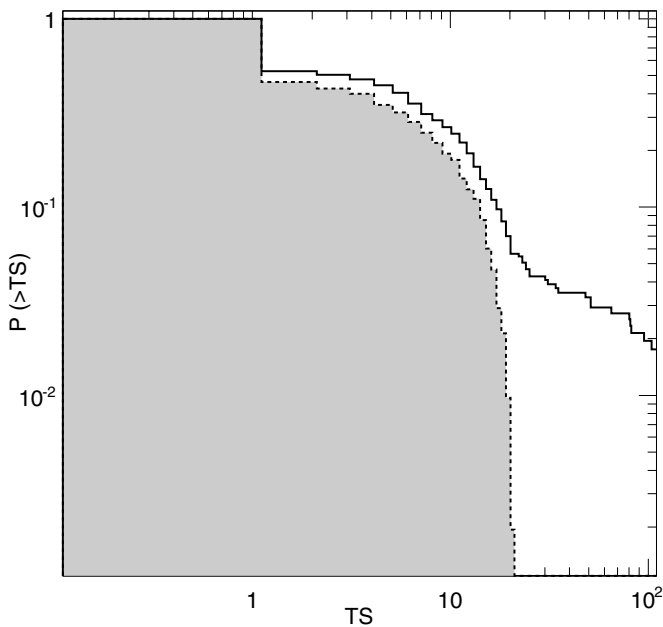
Figure 8. Normalized cumulative distribution of the maximum value of the TS obtained by performing likelihood analysis in different time windows. The dotted line with the shaded gray area is the distribution of the TS for a sample of fake GBM triggers and the solid black line is the distribution for the sample of real GBM triggers.

the TS map, are quite convincing and suggest a possible detection with the LAT, thus confirming the findings of Akerlof et al. (2010).

5. GRB 090720B is also found by our likelihood analysis, is not seen in LLE data, and will be discussed in more detail in subsequent sections.

6. GRB 091208B is localized by *Swift* and our analysis finds the maximum TS = 20. It is a marginal detection with only three events associated with the burst location. However, in this case, the TS value reaches the threshold and the spectral shape is convincing, so we consider this a detection for the catalog.

7. GRB 100728A is found by our pipeline during the LATTE time interval with a TS = 32 selecting the time interval between 5.6 and 749.9 s after the GBM trigger. In addition, a dedicated article has already been published (Abdo et al. 2011) by the LAT and GBM collaborations.

8. GRB 100911A was detected by the GBM when the direction of the burst was very close to the Earth, with an angle from the local zenith of approximately 105°. In order to minimize contamination from the bright limb of the Earth, we rejected any data taken during intervals for which the ROI intersected the Earth's limb, a cut that is more conservative than requiring that the GRB is not occulted by the Earth. As a consequence, GRB 100911A was not detected.

9. GRB 110709A is also found by our likelihood analysis and is not seen in LLE data.

4.2. Emission Onset Time and Duration in the LAT

We applied our duration measurement algorithms to all of the significantly detected GRBs, as described in Section 3.3.2. Our results are shown in Table 3.

Referring to the durations reported in the GBM GRB catalog (Paciesas et al. 2012), we report in the second column whether the GRB was categorized as long (L) or short (S), as determined

from the measured T_{90} in the 50 keV–300 keV energy bands. Our results consist of two sets of T_{05} and T_{95}, determined using the Transient event class (denoted "LAT") and the LLE event class (denoted "LLE"). We report a duration measured with an event class only if the GRB was also detected using that same event class. In several cases (e.g., GRBs 090926A and 100116A), the burst emission persisted long enough that our algorithm failed to detect a plateau before the end of the first continuous segment of observation. For these cases, we report lower limits for the LAT T_{95} and T_{05} values. This work produced the first-ever set of GRB durations measured at high (MeV/GeV) energies.

The quantities compared in Table 3 are the onset time (reported here as T_{05} and shown in Figure 9) and the duration of the GRB emission (reported here as T_{90} and shown in Figure 10). In the top panels of Figures 9 and 10, we compare the >100 MeV LAT Transient-class duration measurements with the GBM results (in the 50 keV–300 keV energy band), while in the bottom panels we compare the tens-of-MeV LLE duration measurements with the GBM results. As shown in the top panels of both figures, the LAT-detected >100 MeV emission systematically starts later and has a longer duration with respect to the GBM-detected emission. On the other hand, the bottom panels of both figures show that the durations measured using the LLE data are in better agreement with those measured by the GBM. Any deviation from the equal-duration line of the LLE versus GBM plots can be at least partially explained as due to spectral variations during the time of the GRB emission, something that can be easily observed in the light curves reported in Appendix B.

As was discussed in Section 3.3.2, the duration estimates are sensitive to the level of the background. Thus, different detectors, such as the GBM and the LAT, or different event selections, such as the LAT Transient and LLE class events, could produce different duration estimates as a consequence of their very different signal-to-noise ratios. This can partially explain the systematically longer durations (T_{90}) estimated using the LAT Transient-class events, but would not explain the systematically later onset times (T_{05}). We also note that a possible selection effect could arise owing to the typical GRB off-axis angles at the trigger time. Bursts that are initially at the edge of or outside the LAT FoV (i.e., having high (>60°) off-axis angles θ) enter the LAT FoV after some time (of the order of a few seconds), thus introducing a delay between the onset of the GBM and LAT observed signals. Even though we weight the LAT-detected signal by the inverse of the exposure to ameliorate this effect, we cannot eliminate it since the weighting is not effective for the cases in which no GRB Transient-class events are detected at all by the LAT. This effect might partially explain the delays of GRBs 090323 and 090328. For most of the other cases, however, the GRB has a small enough off-axis angle at onset to permit sufficiently sensitive prompt observations (as shown by the θ column in Table 2).

4.3. Maximum Likelihood Analysis

We split GRB observations into the six time intervals listed in Table 1 and performed a LAT-only spectral analysis using the maximum likelihood technique described in Section 3.2. Since in the "PRE" interval the GRB is not detectable (by construction), we omit reporting results from this interval and we focus on the five remaining time windows. The results of this analysis, namely the TS, the best-fit photon index, and the flux and fluence for the 100 MeV–10 GeV energy range are presented in Table 4. When possible, we also compute
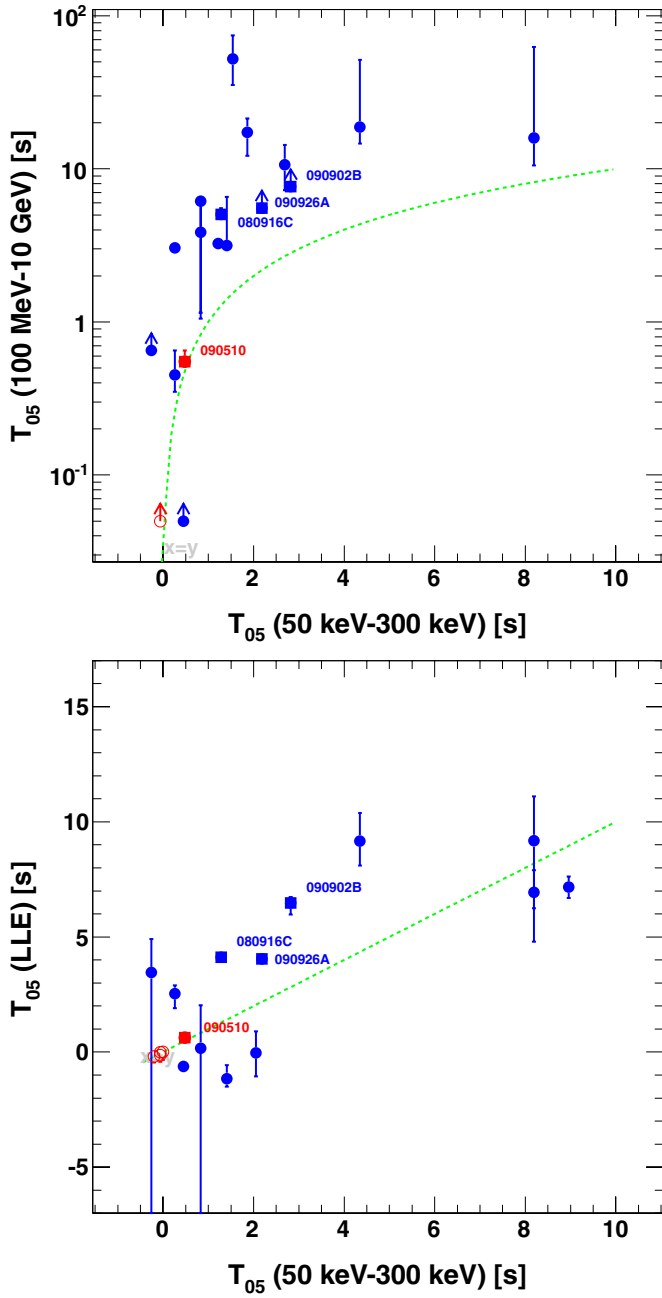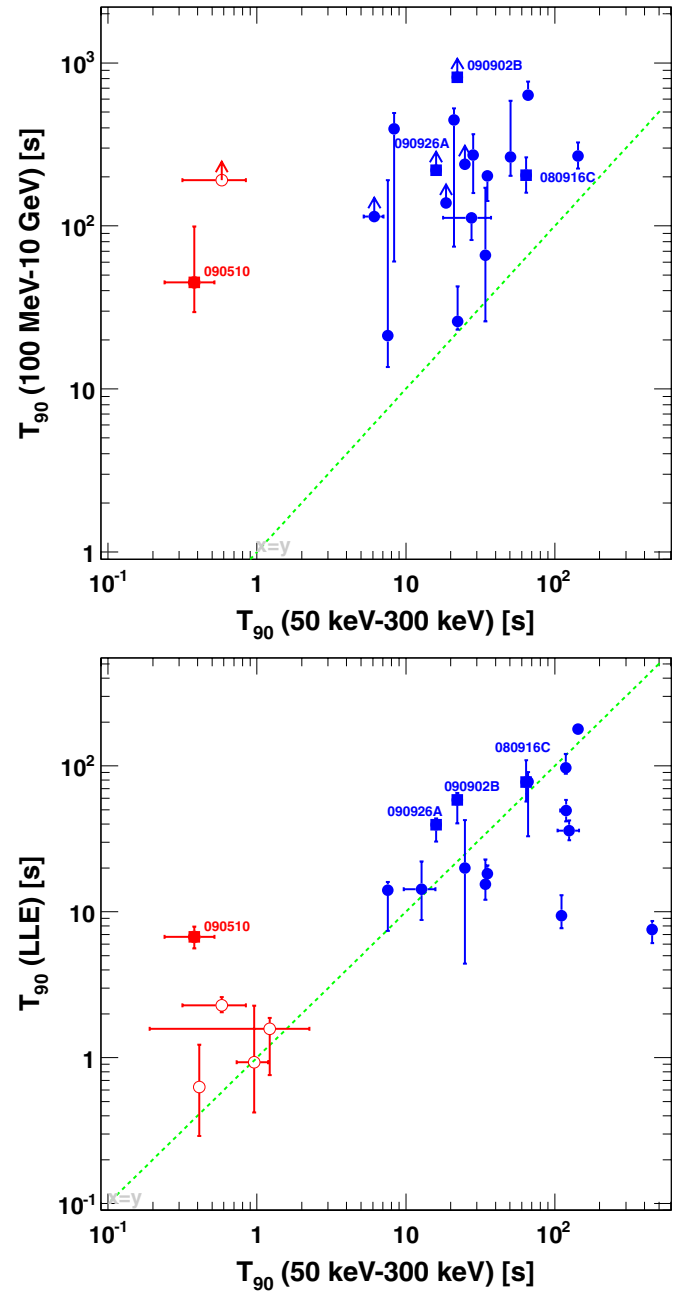
Figure 9. Top: comparison between the >100 MeV T_{05}, as measured using the LAT Transient-class events, and the 50 keV–300 keV T_{05}, as measured by the GBM (Paciesas et al. 2012). Bottom: comparison between the LLE T_{05} and GBM T_{05}. The dashed line indicates equality. Long-duration GRBs are plotted with blue symbols and short GRBs are plotted in red. The four brightest LAT-detected bursts are plotted with square symbols and labeled.

(A color version of this figure is available in the online journal.)

Figure 10. Top: comparison between the >100 MeV T_{90}, as measured using the LAT Transient-class events vs. the 50 keV–300 keV T_{90}, as measured by the GBM (Paciesas et al. 2012). Bottom: comparison between the LLE T_{90} and GBM T_{90}. The dashed lines correspond to LAT T_{90} = GBM T_{90} and LLE T_{90} = GBM T_{90}, respectively, in the top and bottom panels. The symbol convention is the same as in Figure 9.

(A color version of this figure is available in the online journal.)

the isotropic equivalent energy E_{iso} in the 100 MeV–10 GeV rest-frame energy band. In the same table, we also report the number of detected events (originating from both the GRB and any possible background components) and the number of events from the GRB as predicted by the likelihood fit. These numbers are for the 100 MeV–10 GeV energy range in the observer frame.

4.3.1. Fluxes and Fluences

Figure 11 shows the flux and fluence measured by the LAT in the "GBM" (top two panels) and "LAT" (bottom two panels)

time intervals as a function of the durations of these time intervals (i.e., GBM and LAT T_{90}, respectively). The fluxes and fluences presented in these figures are for the 100 MeV–10 GeV energy range. As can be interestingly seen in the bottom right panel of Figure 11, within the first 3 years of operations the LAT detected four very high fluence bursts (GRBs 080916C, 090510, 090902B, and 090926A) that are outliers with respect to the main distribution of the LAT-detected GRBs. We will revisit these hyper-fluent bursts in Section 5.2, where we discuss the energetics of *Fermi*-LAT detected GRBs.

Table 4
Results from Likelihood Analysis

GRB Name	Interval $(t_0 - t_1)$ (s)	Trans. Ev. in the ROI	Trans. Ev. Predicted	Test Statistic (TS)	Spectral Index	Flux (100 MeV–10 GeV) cm^{-2} s^{-1} ($\times 10^{-5}$)	Fluence (100 MeV–10 GeV) erg cm^{-2} ($\times 10^{-5}$)	E_{iso} (100 MeV–10 GeV) erg ($\times 10^{52}$)
080825C	GBM (1.2–23.4)	7	6.8	36	-3.3 ± 0.7	20 ± 10	0.16 ± 0.06	...
	LAT (3.2–29.4)	11	10.1	57	-2.7 ± 0.5	28 ± 10	0.3 ± 0.1	...
	JOINT (3.2–23.4)	7	6.8	38	-3.3 ± 0.7	30 ± 10	0.16 ± 0.06	...
	EXT (23.4–29.4)	4	3.5	25	-2.1 ± 0.5	40 ± 20	0.2 ± 0.2	...
	LATTE (3.2–56.2)	14	11.5	50	-2.7 ± 0.4	16 ± 5	0.3 ± 0.1	...
080916C	GBM (1.3–65.5)	156	150.3	1450	-2.13 ± 0.08	82 ± 7	4.3 ± 0.7	150 ± 20
	LAT (5.0–209.8)	201	180.0	1382	-2.05 ± 0.07	29 ± 2	5.7 ± 0.9	160 ± 20
	JOINT (5.0–65.5)	146	140.2	1338	-2.10 ± 0.08	81 ± 7	4.3 ± 0.8	140 ± 10
	EXT (65.5–209.8)	55	40.9	239	-1.9 ± 0.1	9 ± 2	1.6 ± 0.6	34 ± 6
	LATTE (2.4–562.3)	264	201.2	1210	-2.08 ± 0.07	11.7 ± 0.9	6.0 ± 0.9	180 ± 20
081006	GBM (−0.3–5.9)	7	7.0	72	-2.4 ± 0.5	24 ± 9	0.08 ± 0.05	...
	LAT (0.7–115.0)	42	12.6	42	-2.3 ± 0.3	2.4 ± 0.8	0.16 ± 0.09	...
	JOINT (0.7–5.9)	7	7.0	74	-2.4 ± 0.5	30 ± 10	0.08 ± 0.05	...
	EXT (5.9–115.0)	35	4.3	7	...	<2	<0.2	...
	LATTE (0.7–23.7)	13	9.8	64	-2.3 ± 0.4	9 ± 3	0.13 ± 0.08	...
081024B	GBM (−0.1–0.5)	7	7.0	111	-2.0 ± 0.4	260 ± 100	0.2 ± 0.1	...
	LAT (0.1–191.0)	40	12.2	44	-2.0 ± 0.3	1.8 ± 0.6	0.4 ± 0.3	...
	JOINT (0.1–0.5)	7	7.0	113	-2.0 ± 0.4	300 ± 100	0.2 ± 0.1	...
	EXT (0.5–191.0)	33	4.0	9	...	<2	<0.3	...
	LATTE (0.1–7.5)	12	10.9	103	-1.9 ± 0.3	31 ± 10	0.3 ± 0.2	...
090217	GBM (0.8–34.9)	17	13.5	89	-2.5 ± 0.4	11 ± 3	0.17 ± 0.08	...
	LAT (6.2–68.0)	19	15.8	105	-2.5 ± 0.3	7 ± 2	0.20 ± 0.08	...
	JOINT (6.2–34.9)	16	13.1	92	-2.5 ± 0.4	12 ± 4	0.17 ± 0.08	...
	EXT (34.9–68.0)	3	2.9	13	...	<6	<0.2	...
	LATTE (0.3–56.2)	20	15.1	94	-2.5 ± 0.3	7 ± 2	0.20 ± 0.08	...
090227B	GBM (−0.1–1.2)	3	3.0	30	-3 ± 1	500 ± 300	0.2 ± 0.1	...
090323	GBM (8.2–151.6)	20	15.1	60	-3.1 ± 0.5	6 ± 2	0.26 ± 0.08	40 ± 30
	LAT (15.9–293.9)	54	31.8	119	-2.3 ± 0.2	3.4 ± 0.7	0.6 ± 0.2	20 ± 5
	JOINT (15.9–151.6)	19	14.1	57	-3.2 ± 0.5	6 ± 2	0.23 ± 0.07	40 ± 30
	EXT (151.6–293.9)	35	16.8	73	-1.9 ± 0.2	2.4 ± 0.7	0.5 ± 0.3	7 ± 2
	LATTE (10.0–421.7)	88	41.2	136	-2.3 ± 0.2	2.7 ± 0.5	0.6 ± 0.2	24 ± 6
090328	GBM (4.3–70.4)	10	4.2	11	...	<10	<0.7	<0.4
	LAT (18.8–652.9)	192	45.6	105	-2.0 ± 0.2	1.7 ± 0.3	1.1 ± 0.4	1.1 ± 0.2
	JOINT (18.8–70.4)	6	2.5	9	...	<10	<0.6	<0.3
	EXT (70.4–652.9)	186	43.1	98	-2.1 ± 0.2	1.7 ± 0.3	0.9 ± 0.4	1.0 ± 0.2
	LATTE (13.3–1778.3)	430	61.4	107	-2.0 ± 0.1	0.8 ± 0.1	1.5 ± 0.5	1.4 ± 0.2
090510	GBM (0.5–0.9)	36	36.0	728	-1.7 ± 0.1	1800 ± 300	1.6 ± 0.6	1.3 ± 0.2
	LAT (0.6–45.6)	185	180.1	1897	-2.05 ± 0.07	80 ± 6	3.5 ± 0.6	5.5 ± 0.4
	JOINT (0.6–0.9)	36	36.0	741	-1.7 ± 0.1	2200 ± 400	1.6 ± 0.6	1.3 ± 0.2
	EXT (0.9–45.6)	149	143.6	1393	-2.16 ± 0.09	66 ± 6	2.3 ± 0.4	4.2 ± 0.4
	LATTE (0.0–177.8)	220	194.5	1529	-2.06 ± 0.07	22 ± 2	3.7 ± 0.6	5.8 ± 0.5
090626	GBM (1.5–52.0)	6	2.6	8	...	<3	<0.2	...
	LAT (52.2–299.9)	55	19.3	62	-2.3 ± 0.3	2.2 ± 0.6	0.3 ± 0.2	...
	EXT (52.0–299.9)	56	19.2	61	-2.3 ± 0.3	2.2 ± 0.6	0.3 ± 0.2	...
	LATTE (4.2–749.9)	107	28.4	71	-2.2 ± 0.2	1.3 ± 0.3	0.7 ± 0.3	...
090720B	GBM (−0.3–6.4)	3	2.5	25	-1.7 ± 0.5	10 ± 10	0.3 ± 0.4	...
	LATTE (0.2–75.0)	8	3.0	16	...	<5	<0.4	...
090902B	GBM (2.8–25.0)	158	155.4	1822	-1.96 ± 0.07	260 ± 20	7 ± 1	35 ± 3
	LAT (7.7–825.0)	438	301.1	1664	-1.95 ± 0.05	7.5 ± 0.5	8 ± 1	38 ± 2
	JOINT (7.7–25.0)	140	139.4	1824	-1.94 ± 0.07	290 ± 30	7 ± 1	32 ± 3
	EXT (25.0–825.0)	298	159.6	733	-2.02 ± 0.08	4.1 ± 0.4	3.5 ± 0.7	20 ± 2
	LATTE (2.4–749.9)	439	313.5	1832	-1.96 ± 0.05	8.6 ± 0.5	8 ± 1	40 ± 2
090926A	GBM (2.2–18.1)	152	150.7	1800	-2.29 ± 0.09	350 ± 30	3.5 ± 0.5	44 ± 4
	LAT (5.5–225.0)	246	234.1	1983	-2.12 ± 0.07	43 ± 3	8 ± 1	74 ± 5
	JOINT (5.5–18.1)	141	140.1	1755	-2.27 ± 0.09	410 ± 40	3.3 ± 0.5	41 ± 4
	EXT (18.1–225.0)	105	94.1	673	-1.94 ± 0.09	17 ± 2	5 ± 1	29 ± 3
	LATTE (3.2–294.6)	267	247.9	1954	-2.13 ± 0.07	36 ± 2	9 ± 1	83 ± 6

Table 4
(Continued)

GRB Name	Interval ($t_0 - t_1$)	Trans. Ev.	Trans. Ev.	Test Statistic	Spectral Index	Flux (100 MeV–10 GeV)	Fluence (100 MeV–10 GeV)	E_{iso} (100 MeV–10 GeV)
	(s)	in the ROI	Predicted	(TS)		cm^{-2} s^{-1} ($\times 10^{-5}$)	erg cm^{-2} ($\times 10^{-5}$)	erg ($\times 10^{52}$)
091003	GBM (0.8–21.9)	9	6.2	45	-2.0 ± 0.4	6 ± 3	0.1 ± 0.1	0.20 ± 0.09
	LAT (3.9–452.6)	99	31.3	107	-2.1 ± 0.2	1.4 ± 0.3	0.6 ± 0.2	1.0 ± 0.2
	JOINT (3.9–21.9)	8	5.2	40	-1.8 ± 0.4	6 ± 3	0.2 ± 0.2	0.18 ± 0.09
	EXT (21.9–452.6)	91	25.5	75	-2.1 ± 0.2	1.2 ± 0.3	0.4 ± 0.2	0.8 ± 0.2
	LATTE (1.0–316.2)	75	29.4	108	-2.2 ± 0.2	2.0 ± 0.4	0.5 ± 0.2	0.9 ± 0.2
091031	GBM (1.4–36.7)	15	2.2	4	$\ldots$	<5	<0.2	$\ldots$
	LAT (3.1–206.2)	64	14.8	44	-2.0 ± 0.3	1.6 ± 0.5	0.3 ± 0.2	$\ldots$
	JOINT (3.1–36.7)	14	1.0	3	$\ldots$	<4	<0.1	$\ldots$
	EXT (36.7–206.2)	50	13.7	46	-2.0 ± 0.3	1.8 ± 0.6	0.4 ± 0.2	$\ldots$
	LATTE (2.4–100.0)	34	11.2	41	-2.2 ± 0.3	2.7 ± 1.0	0.2 ± 0.1	$\ldots$
091208B	GBM (0.3–15.0)	3	3.0	20	-1.9 ± 0.5	9 ± 5	0.2 ± 0.2	0.3 ± 0.2
	LATTE (1.8–42.2)	7	4.6	17	$\ldots$	<10	<0.5	<0.5
100116A	GBM (84.0–102.6)	6	5.4	28	-2.9 ± 0.7	8 ± 4	0.05 ± 0.03	$\ldots$
	LAT (3.0–141.0)	40	14.1	60	-2.1 ± 0.3	2.3 ± 0.8	0.3 ± 0.2	$\ldots$
	JOINT (84.0–102.6)	6	5.4	28	-2.9 ± 0.7	8 ± 4	0.05 ± 0.03	$\ldots$
	EXT (102.6–141.0)	16	8.9	55	-1.9 ± 0.3	5 ± 2	0.3 ± 0.3	$\ldots$
	LATTE (1.3–177.8)	49	18.7	77	-2.2 ± 0.3	2.7 ± 0.7	0.3 ± 0.2	$\ldots$
100225A	GBM (−0.3–12.5)	2	1.8	7	$\ldots$	<20	<0.3	$\ldots$
100325A	GBM (−0.4–6.3)	4	4.0	40	-1.9 ± 0.4	11 ± 6	0.1 ± 0.1	$\ldots$
	LATTE (0.2–23.7)	7	5.2	29	-2.0 ± 0.4	4 ± 2	0.1 ± 0.1	$\ldots$
100414A	GBM (1.9–30.2)	9	6.4	27	-2.7 ± 0.6	40 ± 20	0.4 ± 0.2	4 ± 2
	LAT (17.4–288.6)	60	24.1	77	-2.0 ± 0.2	2.7 ± 0.7	0.8 ± 0.4	2.6 ± 0.6
	JOINT (17.4–30.2)	8	5.7	27	-2.4 ± 0.5	60 ± 30	0.4 ± 0.3	3 ± 1
	EXT (30.2–288.6)	52	19.6	64	-1.9 ± 0.2	2.2 ± 0.6	0.7 ± 0.4	2.1 ± 0.5
	LATTE (10.0–316.2)	65	27.0	81	-2.0 ± 0.2	2.6 ± 0.6	0.8 ± 0.4	2.8 ± 0.6
100620A	GBM (0.1–41.2)	9	4.5	19	$\ldots$	<5	<0.2	$\ldots$
	LATTE (2.4–316.2)	45	10.4	24	-3.4 ± 0.7	0.9 ± 0.3	0.07 ± 0.03	$\ldots$
100724B	GBM (9.0–127.5)	32	20.9	90	-5.0 ± 0.9	10 ± 2	0.26 ± 0.06	$\ldots$
	LATTE (5.6–100.0)	30	20.9	93	-4.8 ± 0.9	12 ± 3	0.25 ± 0.06	$\ldots$
100728A	GBM (14.8–192.6)	28	3.3	4	$\ldots$	<2	<0.5	$\ldots$
	LATTE (5.6–749.9)	136	13.0	32	-1.6 ± 0.2	0.4 ± 0.1	0.9 ± 0.6	$\ldots$
100826A	GBM (8.2–127.0)	4	2.7	6	$\ldots$	<30	<4	$\ldots$
110120A	GBM (0.3–27.8)	6	4.8	18	$\ldots$	<8	<0.2	$\ldots$
	LAT (0.5–112.8)	22	9.6	35	-1.9 ± 0.3	1.6 ± 0.6	0.3 ± 0.2	$\ldots$
	JOINT (0.5–27.8)	6	4.8	18	$\ldots$	<8	<0.2	$\ldots$
	EXT (27.8–112.8)	16	4.8	21	-1.6 ± 0.3	1.0 ± 0.5	0.3 ± 0.3	$\ldots$
	LATTE (0.6–75.0)	15	8.0	35	-1.9 ± 0.3	2.0 ± 0.8	0.2 ± 0.2	$\ldots$
110328B	GBM (2.0–127.0)	9	1.3	4	$\ldots$	<0.9	<0.1	$\ldots$
110428A	GBM (2.7–11.0)	1	0.9	3	$\ldots$	<10	<0.1	$\ldots$
	LAT (10.7–407.6)	78	16.1	53	-1.7 ± 0.2	0.8 ± 0.2	0.7 ± 0.4	$\ldots$
	EXT (11.0–407.6)	78	16.1	53	-1.7 ± 0.2	0.8 ± 0.2	0.7 ± 0.4	$\ldots$
	LATTE (5.6–177.8)	36	11.5	50	-1.7 ± 0.2	1.3 ± 0.5	0.7 ± 0.4	$\ldots$
110625A	LATTE (75.0–562.3)	121	31.0	57	-2.6 ± 0.3	3.3 ± 0.8	0.6 ± 0.2	$\ldots$
110709A	GBM (1.1–44.3)	15	8.3	21	-3.9 ± 0.9	11 ± 5	0.12 ± 0.05	$\ldots$
	LATTE (5.6–42.2)	12	7.6	23	-3.8 ± 0.9	12 ± 5	0.11 ± 0.05	$\ldots$
110721A	GBM (0.5–25.4)	21	17.7	114	-2.5 ± 0.3	21 ± 5	0.24 ± 0.09	$\ldots$
	LAT (0.1–239.0)	70	26.3	75	-2.9 ± 0.4	2.8 ± 0.6	0.22 ± 0.06	$\ldots$
	JOINT (0.5–25.4)	21	17.7	114	-2.5 ± 0.3	21 ± 5	0.24 ± 0.09	$\ldots$
	EXT (25.4–239.0)	45	3.6	3	$\ldots$	<1.0	<0.2	$\ldots$
	LATTE (0.0–23.7)	27	23.6	162	-2.9 ± 0.4	31 ± 7	0.26 ± 0.07	$\ldots$
110731A	GBM (0.3–7.8)	41	39.8	350	-2.6 ± 0.2	110 ± 20	0.37 ± 0.09	14 ± 3
	LAT (3.0–24.1)	58	55.1	460	-2.4 ± 0.2	55 ± 8	0.6 ± 0.1	17 ± 3
	JOINT (3.0–7.8)	38	37.2	357	-2.5 ± 0.2	170 ± 30	0.36 ± 0.09	13 ± 3
	EXT (7.8–24.1)	20	18.7	154	-2.3 ± 0.3	23 ± 6	0.2 ± 0.1	5 ± 1
	LATTE (1.8–562.3)	193	69.2	230	-2.4 ± 0.2	2.6 ± 0.4	0.8 ± 0.2	22 ± 4
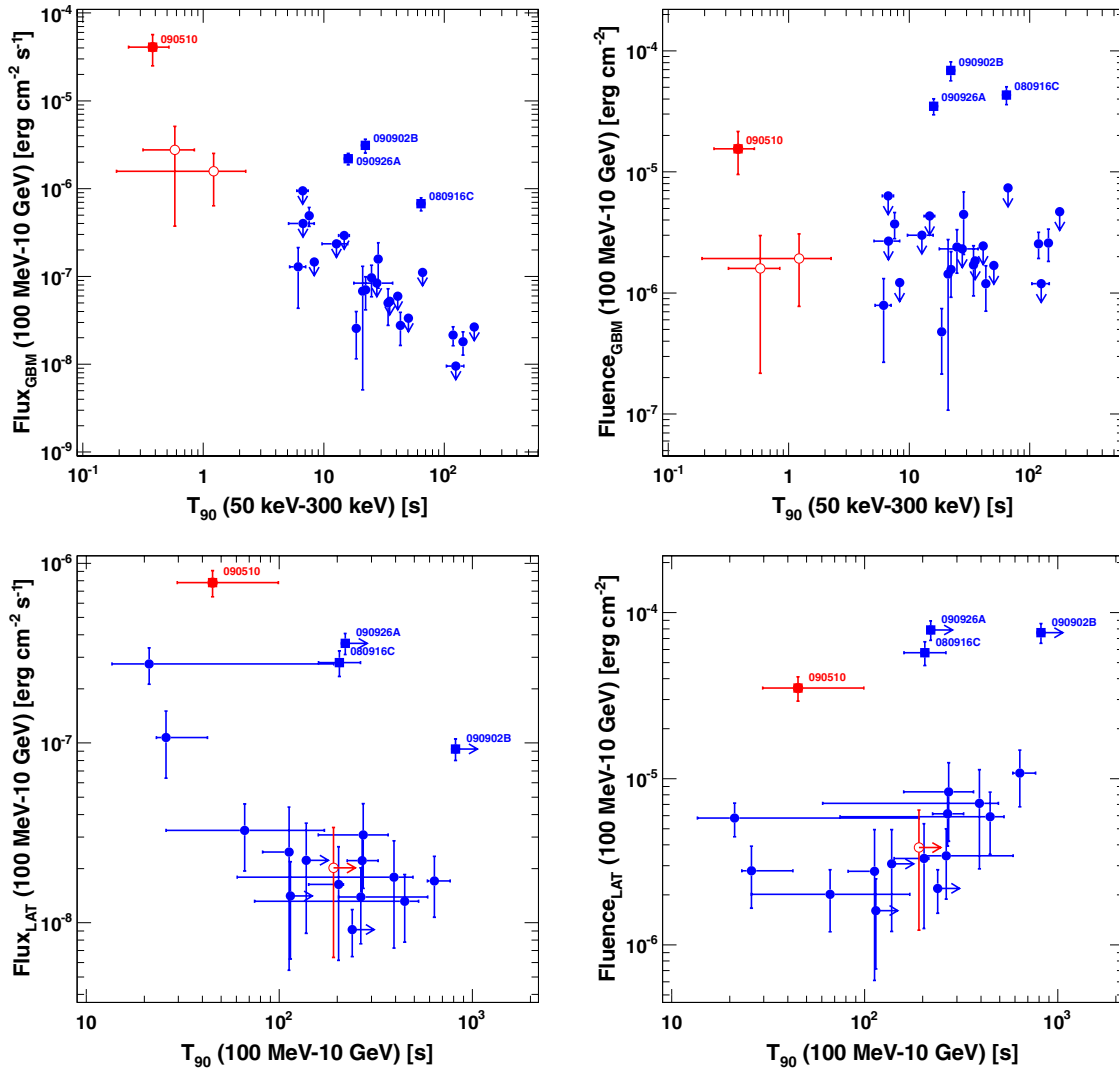
Figure 11. Flux (left-hand column) and fluence (right-hand column) in the 100 MeV–10 GeV energy range for the "GBM" (top row) and "LAT" (bottom row) time intervals as functions of the durations of these intervals. The symbol convention is the same as in Figure 9.

(A color version of this figure is available in the online journal.)

4.3.2. LAT Localizations

We evaluate localizations from the LAT for all GRBs detected by the maximum likelihood analysis by searching for the maximum of the TS map according to the procedure described in Section 3.2.2. We present our results in Table 5, in which we report the position of the maximum of the TS map (i.e., the LAT localization) along with its 68%, 90%, and 95% statistical errors.

4.3.3. High-energy Photon Events

We report the energies and arrival times of a set of interesting high-energy photons that, according to our likelihood analysis (as described in Section 3.2.3), have a high probability ($P >$ 0.9) of being associated with the GRBs. Specifically, we give information for the following events:

1. The highest energy Transient-class LAT γ-ray in the "GBM" time window (Table 6);
2. The highest energy Transient-class LAT γ-ray in the interval starting from GBM T_{95} and ending at the end of the "EXT" window (i.e., from the end of the measured

duration in the GBM data up to the end of the LAT measured duration; Table 7);
3. The highest energy Transient-class LAT γ-ray detected in the time-resolved likelihood analysis (Table 8).

The results are shown in Tables 6–8. These results show that the detection of high-energy events with GRB point source probabilities $P > 0.9$ is not strongly correlated with features in the GBM light curve. In a few cases, such as GRB 090510, such events are coincident with bright pulses in the GBM light curve, but more often the most energetic event is detected after the intense low-energy emission, as with the 33.39 GeV event detected at $T_0 + 81.75$ s from GRB 090902B, which is the highest energy ever observed from a burst. GRB 100728A is particularly interesting since a 13.54 GeV event was detected $\sim$90 minutes after the trigger time. This is the only case in which we observe such a late event and it can potentially confirm that high-energy γ-rays can arise very late in time, as observed from GRB 940217 by EGRET (Hurley et al. 1994). On the other hand, GRB 100728A is not significantly detected at the time that the highest energy event is observed (similar to GRBs 090217 and 100116A, reported in Table 8), thus the probability $P = 0.987$ that the 13.54 GeV event is associated with the burst

Table 5
Fermi-LAT Localizations

GRB Name	R.A. Deg., J2000	Decl. Deg., J2000	68% Deg.	90% Deg.	95% Deg.
080825C	233.95	−4.55	0.77	1.24	1.55
080916C	119.87	−56.58	0.07	0.10	0.12
081006	136.43	−62.10	0.51	0.76	0.89
081024B	322.94	21.05	0.29	0.46	0.56
090217	204.79	−8.41	0.35	0.51	0.59
090323	190.64	17.03	0.10	0.16	0.20
090328	90.54	−42.01	0.13	0.17	0.19
090510	333.50	−26.53	0.04	0.06	0.07
090626	169.97	−33.34	0.23	0.32	0.37
090720B	203.08	−54.26	0.33	0.53	0.65
090902B	264.99	27.32	0.04	0.05	0.06
090926A	353.57	−66.33	0.04	0.07	0.08
091003	251.40	36.57	0.15	0.22	0.25
091031	71.40	−57.70	0.24	0.35	0.41
091208B	29.02	17.74	0.88	1.47	1.76
100116A	304.96	14.48	0.17	0.25	0.29
100325A	330.18	−26.40	0.60	0.86	1.00
100414A	192.16	8.64	0.12	0.18	0.22
100620A	86.98	−50.96	0.71	1.08	1.28
100724B	120.54	76.60	1.03	1.56	1.81
100728A	88.91	−15.01	0.10	0.19	0.23
110120A	61.55	−11.95	0.35	0.53	0.62
110428A	5.47	64.80	0.16	0.23	0.27
110625A	286.68	6.81	0.27	0.42	0.51
110709A	236.28	41.74	1.51	2.37	2.99
110721A	333.49	−38.62	0.53	0.80	0.93
110731A	280.42	−28.56	0.19	0.27	0.31

Table 6
Highest Energy Events for *Fermi*-LAT GRBs: GBM Durations

GRB Name	Number of Events (>100 MeV, $P > 0.9$)	Energy (GeV)	Arrival Time (s)	Probability
080825C	7	0.29	3.25	0.9854
080916C	143	13.22	16.54	0.9999
081006	7	0.65	1.80	0.9997
081024B	7	3.07	0.49	1.0000
090217	11	0.87	14.83	0.9960
090227B	3	0.24	0.48	0.9996
090323	12	0.48	92.74	0.9682
090510	36	31.31	0.83	1.0000
090720B	2	1.45	0.22	0.9997
090902B	155	11.16	11.67	0.9999
090926A	149	3.19	9.48	0.9990
091003	6	2.83	6.47	0.9997
091208B	3	1.18	3.41	0.9958
100116A	4	0.86	101.30	0.9973
100325A	4	0.84	0.35	0.9990
100414A	4	0.64	19.89	0.9442
100620A	3	0.27	3.77	0.9886
100724B	16	0.22	61.75	0.9805
110120A	4	0.46	0.87	0.9570
110709A	3	0.17	30.63	0.9596
110721A	15	0.86	0.86	0.9937
110731A	38	0.88	5.52	0.9974

Table 7
Highest Energy Events for *Fermi*-LAT GRBs: EXT Durations

GRB Name	Number of Events (>100 MeV, $P > 0.9$)	Energy (GeV)	Arrival Time (s)	Probability
080825C	3	0.57	28.29	0.999
080916C	33	1.46	124.16	0.998
090323	11	7.50	195.42	1.000
090328	14	3.83	264.42	0.956
090510	141	3.90	1.55	1.000
090626	9	2.09	111.63	0.998
090902B	108	12.54	45.61	0.999
090926A	80	19.56	24.83	1.000
091003	11	1.79	76.78	0.993
091031	5	1.19	79.75	0.996
100116A	7	2.20	105.71	1.000
100414A	11	4.72	288.26	0.999
110120A	2	1.82	72.46	0.998
110428A	5	2.62	14.79	0.999
110731A	18	1.90	8.27	1.000

Table 8
Highest Energy Events for *Fermi*-LAT GRBs: Time Resolved Analysis

GRB Name	Number of Events (>100 MeV, $P > 0.9$)	Energy (GeV)	Arrival Time (s)	Probability
080825C	10	0.57	28.29	0.997
080916C	181	13.22	16.54	1.000
081006	10	0.79	12.08	0.955
081024B	11	3.07	0.49	1.000
090217	16	1.23	179.08	0.907
090323	28	7.50	195.42	1.000
090328	23	5.32	697.80	0.926
090510	186	31.31	0.83	1.000
090626	15	2.09	111.63	0.999
090720B	2	1.45	0.22	0.997
090902B	276	33.39	81.75	0.949
090926A	239	19.56	24.83	1.000
091003	20	2.83	6.47	1.000
091031	7	1.19	79.75	0.999
091208B	4	1.18	3.41	0.956
100116A	14	13.12	296.43	0.993
100325A	5	0.84	0.35	0.990
100414A	19	4.72	288.26	1.000
100620A	6	0.27	3.77	0.994
100724B	16	0.22	61.75	0.988
100728A	5	13.54	5461.08	0.987
110120A	6	1.82	72.46	0.999
110428A	6	2.62	14.79	1.000
110625A	6	2.42	272.44	0.986
110709A	5	0.42	41.75	0.921
110721A	22	1.73	0.74	0.998
110731A	64	3.39	435.96	0.998

shows the energies and arrival times for the highest energy γ-rays associated with LAT GRBs. The estimated errors are computed from the energy dispersion in the IRFs and are of the order of 10% for energies >1 GeV. When possible, we also indicate the source-frame energy.

4.3.4. Temporally Extended Emission

To study the temporal decay of the extended emission detected by the LAT, we utilized the time-resolved analysis described in Section 3.5. We first visualized any detected extended emission using flux light curves (shown in Appendix B) and then calculated the peak-flux value F_p and the time of the peak

must be taken with caution. Considering the trials factors, this probability would be further reduced, weakening the case for high-energy emission that persists for hours. A detailed analysis of the probability corrected by the trials factors would be non-trivial as the background strongly varies as a function of the location in orbit and is beyond the scope of this paper. Figure 12

Figure 12. Observed (upward-pointing triangles) and rest frame (downward-pointing triangles) energy and arrival time for the highest energy events associated with long (blue) and short (red) LAT-detected GRBs. Vertical dashed lines connect the observed and the rest frame energies for the same burst. Data points are from Table 8.

(A color version of this figure is available in the online journal.)

flux t_p, quantities shown in the two top panels of Figure 14. In the time-resolved analysis, we adaptively changed the size of the time bin width in order to significantly detect the source, so F_p corresponds to the average flux in the time bin of the maximum. As a result, it is more precise (i.e., with a smaller uncertainty) for bright GRBs than for faint GRBs.

The four most luminous bursts detected by the LAT have some of the highest peak fluxes in the ensemble, all exceeding 10^{-3} cm^{-2} s^{-1}. Among the rest of the bursts, GRBs 081024B and 110721A also have notably high peak fluxes. GRB 100728A was at the edge of the FoV at the time of the GBM trigger and was detected only at later times. It has by far the lowest peak flux of all GRBs, at least an order of magnitude lower than the rest of the population; however, its value is possibly affected by large systematic errors.

We also applied the methods described in Section 3.5 to the subsample of GRBs with detected extended emission. We detected temporal breaks in the decay of the extended emission of three bright GRBs: 090510, 090902B, and 090926A. In the top panel of Figure 13, we show their luminosities as a function of rest-frame time, as well as the best-fitting broken PL models. The later points in the light curves are very important to constrain the break, but they also would be the most affected by any unaccounted-for systematic uncertainties arising, for example, from the background estimation or the exposure calculation. In the bottom panel of Figure 13, we again report the luminosity as a function of the rest-frame time, but for all the GRBs in the subsample. In Table 9, we report the results of this analysis. For the three GRBs with temporal breaks, we report the decay index starting from the peak flux and before the break α_1, the decay index after the break α_2, and the break time t_b. For all other GRBs, we report the decay index for the whole extended emission starting from the peak flux and the decay index for the light curve starting from the end of the low-energy (GBM) emission.

Referring to Table 9, we also define the "late-time decay index" α_L, which corresponds to the decay index measured after the GBM T_{95} ($\alpha_L = \alpha$) for all GRBs except the three for which we detect temporal breaks, for which it corresponds to
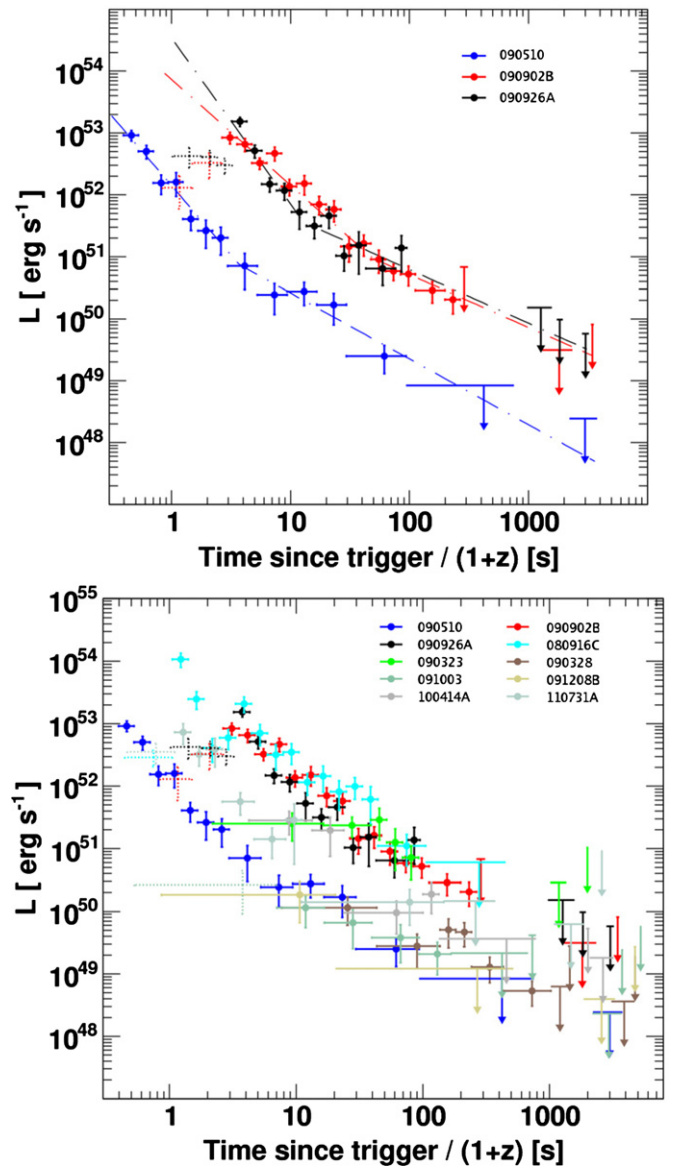
Figure 13. Top: the decay of the luminosity L with time measured in the rest frame for the three GRBs in which we detect a significant time break. Dashed–dotted lines are the best fits of the broken PL model for each GRB, while the dashed crosses are the luminosities before the peak times, which have not been used in the fits (see the text). Bottom: the same quantities for all the GRBs with detected extended emission.

(A color version of this figure is available in the online journal.)

the decay index after the break ($\alpha_L = \alpha_2$). In the third panel of Figure 14, we report α_L for all of the GRBs of the subsample.

4.4. Joint GBM-LAT Spectral Fits

For each GRB detected with the LAT, we performed joint GBM-LAT spectral analyses in two time intervals, following the procedure described in Section 3.4. We started by analyzing data taken in the "GBM" time window for all detected GRBs. The results of this analysis are presented in Tables 10 and 11. Since the emission at energies >100 MeV is delayed with respect to that at lower energies, we also performed a spectral analysis in the time interval between the first Transient-class γ-ray detected by the LAT within the energy-dependent ROI of the GRB and the GBM T_{95}, in order to maximize the signal-to-noise ratio at high energies ($E > 100$ MeV). We report the

Table 9
Temporally Extended High-energy Emission

GRB Name	Peak Flux F_p cm^{-2} s^{-1} ($\times 10^{-5}$)	Peak-Flux Time t_p (s)	α (SPL) from the Peak Flux	α (SPL) from GBM T_{95}	α_1 (BPL)	α_2 (BPL)	Break Time (BPL) t_b (s)
080916C	500 ± 100	6.6 ± 0.9	1.37 ± 0.07	**1.8 ± 0.3**	...	...	...
090323	6 ± 3	40 ± 30	1.0 ± 0.3	**0.9 ± 0.3**	...	...	...
090328	9 ± 4	40 ± 30	1.0 ± 0.3	**0.9 ± 0.2**	...	...	...
090510	3900 ± 600	0.9 ± 0.1	1.8 ± 0.2	1.82 ± 0.2	2.2 ± 0.1	**1.1 ± 0.1**	7 ± 1
090902B	600 ± 100	9 ± 1	1.56 ± 0.06	1.4 ± 0.1	1.7 ± 0.2	**0.8 ± 0.2**	130 ± 50
090926A	700 ± 100	11 ± 2	1.9 ± 0.2	1.6 ± 0.3	2.70 ± 0.09	**0.86 ± 0.07**	40 ± 5
091003	8 ± 3	22 ± 9	1.0 ± 0.2	**1.0 ± 0.2**	...	...	...
100414A	70 ± 30	20 ± 10	1.7 ± 0.3	**1.1 ± 0.4**	...	...	...
110731A	220 ± 60	4.9 ± 0.7	1.8 ± 0.2	**1.5 ± 0.2**	...	...	...

Notes. Using numbers from this table we also define the "late-time decay index" α_L, which is equal to α from GBM T_{95} for all GRBs, except the three for which we detect the break time, for which $\alpha_L = \alpha_2$. The corresponding value is also marked in bold font.
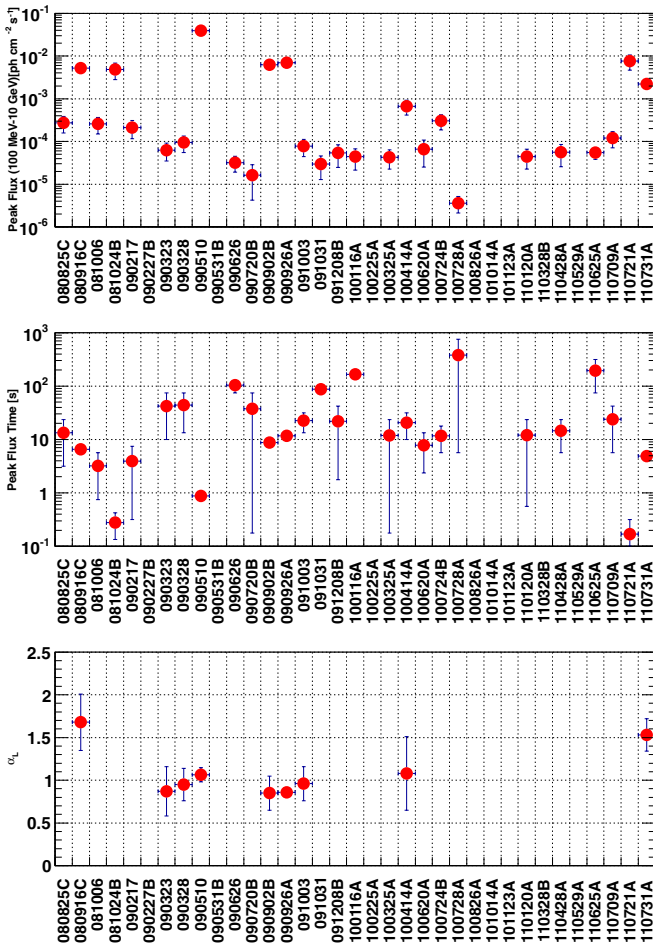
Figure 14. Quantities characterizing the extended high-energy emission detected by the LAT. Top: peak flux, middle: time of the peak flux, and bottom: temporal-decay index α_L.

(A color version of this figure is available in the online journal.)

results of this analysis for all the bursts detected by the LAT in Table 12. The first table (Table 10) summarizes the model that best fits the data for each GRB, ordered by fluence. We also report the off-axis angle, which is a proxy for the detection efficiency of the LAT for equal exposure time (high off-axis angle means low efficiency). Tables 11 and 12 contain three sets of columns: the main component section, the additional component section, and two columns with the total fluence

(in the 10 keV–10 GeV band) and the value of PG-stat (see Section 3.4.2) with the number of dof. Each spectrum is modeled by one main component (a Band model or a Comptonized model or a logarithmic parabola) and one or two additional components (PL and/or exponential cutoff) when needed (see Section 3.4.3). The SBPL model does not provide the best fit for any GRB in our sample, so we do not include it in either Table 11 or 12. Only the columns corresponding to the parameters of the components used in the best-fitting model are entered. When a spectrum requires additional components, we report separately the fluence corresponding to the main component and the fluence corresponding to the additional components.

To elaborate on the table entries, consider the results of the time-integrated analysis reported in Table 11: the first entry refers to the spectrum of GRB 080825C, which is best described by a Band model, thus only the columns referring to the parameters of the Band model are filled, and only the total fluence is reported. On the other hand, the spectrum of GRB 090926A is described by a Band model plus a PL with an exponential cutoff. Correspondingly, all columns for the parameters of those components are filled, as well as the columns for the total fluence and the fluences for the first component (Band) and the second component (PL with an exponential cutoff). The spectrum of GRB 100724B is instead described by a Band model with an exponential cutoff, so all of the corresponding columns are filled. Note that there are no partial fluences reported in this case, since the exponential cutoff is a multiplicative term. In the case of GRB 110731A, we reported in Table 11 both the Band-only fit and the Band plus PL fit, even if the extra component is not significant according to our criteria, since the PL is clearly detected in the other time interval as reported in Table 12. Thus, the Band plus PL is arguably a more accurate model for the "GBM" time window as well.

Some bursts have been detected only by the LLE photon counting analysis since they were outside the nominal LAT FoV ($\theta > 70°$; see Table 2) at the time of the trigger. These include GRBs 090227B, 100826A, 101123A, and 110625A. GRB 101014A was detected too close to the Earth's limb at the time of the trigger, resulting in a very low exposure for the LAT due to the zenith angle cut (see Section 2.1.1). For these LLE-only detections, it is not possible to obtain a spectrum from LAT standard data, and so we use only GBM data.

4.4.1. Extra Components

We found that four GRBs clearly require a PL added to the Band spectrum in both time intervals that we studied. Two

Table 10
The Best Spectral Model for the GRB During the GBM Interval, Ordered by Fluence

GRB Name	Fluence 10 keV–10 GeV (10^{-7} erg cm^{-2})	Best Model	θ (deg)
100724B	4665^{-76}_{+78}	Band with exponential cutoff	48.9
090902B	4058^{-24}_{+25}	Comptonized + power law	50.8
090926A	2225^{-48}_{+50}	Band + power law with exponential cutoff	48.1
080916C	1795^{-39}_{+41}	Band + power law	48.8
090323	1528^{-44}_{+44}	Band	57.2
100728A	1293^{-27}_{+28}	Comptonized	59.9
100414A	1098^{-27}_{+35}	Comptonized + power law	69.0
090626	927^{-16}_{+17}	Logarithmic parabola	18.3
110721A	876^{-28}_{+28}	Logarithmic parabola	40.3
090328	817^{-33}_{+34}	Band	64.6
100116A	638^{-25}_{+26}	Band	26.6
110709A	518^{-27}_{+28}	Band	53.4
080825C	517^{-20}_{+21}	Band	60.3
090217	512^{-15}_{+16}	Band	34.5
091003	461^{-14}_{+15}	Band	21.3
110120A	422^{-22}_{+23}	Band	13.6
110328B	417^{-37}_{+47}	Comptonized	31.7
110731A	379^{-21}_{+20}	Band + power law	3.4
090510	360^{-16}_{+18}	Band + power law	13.6
091031	288^{-10}_{+10}	Band	23.9
110428A	255^{-9}_{+10}	Band	34.6
090720B	185^{-11}_{+13}	Band	56.1
100225A	101^{-7}_{+7}	Band	55.5
091208B	93^{-11}_{+13}	Band	55.6
100620A	84^{-9}_{+9}	Band	24.3
081006	56^{-9}_{+10}	Band	11
110529A	49^{-6}_{+6}	Band	30
100325A	46^{-4}_{+4}	Band	7.1
090531B	38^{-5}_{+5}	Comptonized	21.9
081024B	30^{-5}_{+6}	Band	18.7

Note. We exclude from this table all GRBs outside the nominal LAT FoV (with $\theta > 70°$) and GRB 101014A, which was detected too close to the Earth's limb.

cases, GRB 090510 and GRB 090902B, are already known (Ackermann et al. 2010b; Abdo et al. 2009a). The two additional cases are GRB 080916C and GRB 110731A. During the "GBM" interval for GRB 080916C, we obtain a value of PG-stat $S = 519$ (with 356 dof) with the Band model alone, while we obtain $S = 485$ (with 354 dof) adding an extra PL. The value $\Delta S = 34$ is well above our detection threshold of 25 (see Section 3.4.4). It corresponds to a chance probability of $\simeq 1 \times 10^{-5}$ or possibly lower (see Figure 6). The possibility for an extra component was already considered in our first publication on this GRB (Abdo et al. 2009d), but the significance of the PL was not high enough to claim a firm detection. Now, thanks to a better understanding of the background in the LAT with the use of the BKGE and a better calibration of the GBM instrument, we obtained convincing evidence for such a claim. We also detect an extra component in GRB 110731A, as published in Ackermann et al. (2013). In the "GBM" time interval, the significance of this component is below our threshold, but in the LAT time interval, with a better signal-to-noise ratio, we obtain $\Delta S = 42$. This result is fully consistent with what we already published.

We also find an extra component in GRB 100414A, but in this case we highlight some possible problems with the analysis. We refer to Figure 15 that shows the off-axis angle of the GRB as a function of the time since the GBM trigger. During the GRB prompt emission, this GRB was at the edge of the FoV of the LAT, where the effective area is small. In addition, the ARR maneuver was particularly fast in terms of angular speed for this GRB and happened during the GBM T_{90}, resulting in rapidly changing backgrounds and effective area at the source location, which could create large and difficult to evaluate systematic uncertainties. Indeed, in the "GBM" time interval, the spectrum is better described by a Comptonized model with an additional PL, while in the LAT time interval the statistically preferred model is a Band function. In this case, we cannot firmly claim the detection of the extra PL component.

We confirm the detection of a cutoff around 1.5 GeV in the extra component of GRB 090926A, as previously published by Ackermann et al. (2011), and we also significantly detect a new cutoff at lower energies in GRB 100724B. For the latter, considering again the "GBM" time interval, we find

Table 11
Results for the Joint Fit Over the Interval GBM T_{05}–GBM T_{95}

| GRB | Main Component | | | | | | | | Additional Components | | | Total Fluence | Statistic |
| | Band | | | Comptonized | | Log. Parabola | | Fluence | Power Law | CutOff | Fluence | | |
	E_0 (keV)	α	β	E_0 (keV)	α	b	E_p (keV)	10 keV–10 GeV (10^{-7} erg cm^{-2})	α	E_c (MeV)	10 keV–10 GeV (10^{-7} erg cm^{-2})	10 keV–10 GeV (10^{-7} erg cm^{-2})	Stat./Dof
080825C	141^{-5}_{+5}	$-0.65^{-0.02}_{+0.02}$	$-2.40^{-0.04}_{+0.03}$									517^{-20}_{+21}	1002.2/821
080916C	269^{-19}_{+21}	$-0.65^{-0.06}_{+0.05}$	$-2.22^{-0.04}_{+0.02}$					1614^{-12}_{+12}	$2.01^{-0.07}_{+0.15}$		181^{-102}_{+114}	1795^{-39}_{+41}	485.1/354
081006	496^{-197}_{+394}	$-0.48^{-0.26}_{+0.34}$	$-2.30^{-0.10}_{+0.08}$									56^{-9}_{+10}	477.3/478
081024B	1313^{-580}_{+1196}	$-0.93^{-0.13}_{+0.16}$	$-2.12^{-0.13}_{+0.10}$									30^{-5}_{+6}	354.3/357
090217	504^{-27}_{+30}	$-0.86^{-0.02}_{+0.02}$	$-2.56^{-0.05}_{+0.05}$									512^{-15}_{+16}	495.7/358
090227B	1300^{-68}_{+76}	$-0.49^{-0.02}_{+0.03}$	$-3.20^{-0.32}_{+0.23}$									325^{-16}_{+17}	516.1/462
090323	440^{-20}_{+21}	$-1.01^{-0.01}_{+0.01}$	$-2.70^{-0.07}_{+0.06}$									1528^{-44}_{+44}	963.9/357
090328	769^{-49}_{+54}	$-1.07^{-0.02}_{+0.02}$	$-2.61^{-0.09}_{+0.07}$									817^{-33}_{+34}	713.2/471
090510	2578^{-222}_{+240}	$-0.61^{-0.05}_{+0.05}$	$-2.98^{-0.23}_{+0.16}$					275^{-14}_{+15}	$1.61^{-0.04}_{+0.03}$		84^{-17}_{+19}	360^{-16}_{+18}	704.9/707
090531B				1233^{-231}_{+270}	$0.58^{-0.10}_{+0.08}$							38^{-5}_{+5}	696.2/587
090626						$0.34^{-0.01}_{+0.01}$	300^{-11}_{+12}					927^{-16}_{+17}	993.4/593
090720B	817^{-74}_{+85}	$-0.88^{-0.03}_{+0.03}$	$-2.60^{-0.13}_{+0.10}$									185^{-11}_{+13}	431.8/470
090902B	524^{-9}_{+10}	$-0.61^{-0.01}_{+0.01}$	$-4.26^{-0.57}_{+0.29}$					3116^{-31}_{+21}	$1.94^{-0.01}_{+0.01}$		985^{-55}_{+58}	4101^{-31}_{+32}	627.5/477
090926A	204^{-6}_{+6}	$-0.65^{-0.02}_{+0.02}$	$-2.60^{-0.05}_{+0.04}$					1739^{-49}_{+53}	$1.73^{-0.04}_{+0.03}$	1533^{-408}_{+665}	486^{-43}_{+44}	2225^{-48}_{+50}	709.0/470
091003	430^{-18}_{+19}	$-1.02^{-0.01}_{+0.01}$	$-2.66^{-0.07}_{+0.06}$									461^{-14}_{+15}	1139.8/710
091031	450^{-29}_{+33}	$-0.91^{-0.03}_{+0.03}$	$-2.66^{-0.12}_{+0.09}$									288^{-10}_{+10}	400.4/356
091208B	153^{-30}_{+38}	$-1.29^{-0.07}_{+0.08}$	$-2.28^{-0.08}_{+0.07}$									93^{-11}_{+13}	538.9/355
100116A	1133^{-82}_{+91}	$-1.02^{-0.01}_{+0.01}$	$-3.00^{-0.13}_{+0.10}$									638^{-25}_{+26}	381.2/356
100225A	254^{-21}_{+23}	$-0.57^{-0.06}_{+0.05}$	$-2.49^{-0.17}_{+0.11}$									101^{-7}_{+7}	499.5/470
100325A	92^{-9}_{+10}	$-0.33^{-0.11}_{+0.12}$	$-2.34^{-0.09}_{+0.07}$									46^{-4}_{+4}	485.0/468
100414A				365^{-13}_{+13}	$0.46^{-0.03}_{+0.02}$			998^{-15}_{+16}	$1.75^{-0.09}_{+0.06}$		100^{-34}_{+43}	1098^{-27}_{+35}	504.1/354
100620A	360^{-77}_{+113}	$-1.10^{-0.09}_{+0.09}$	$-2.39^{-0.11}_{+0.08}$									84^{-9}_{+9}	814.0/710
100724B	263^{-4}_{+4}	$-0.73^{-0.00}_{+0.01}$	$-2.00^{-0.01}_{+0.01}$							40^{-3}_{+3}		4665^{-76}_{+78}	734.7/468
100728A				270^{-13}_{+14}	$0.79^{-0.02}_{+0.02}$							1293^{-27}_{+28}	391.5/242
100826A[a]	323^{-12}_{+12}	$-1.00^{-0.01}_{+0.01}$	$-2.03^{-0.02}_{+0.02}$									6030^{-372a}_{+403}	636.8/350
101014A						$0.27^{-0.01}_{+0.01}$	340^{-12}_{+13}					3882^{-53}_{+54}	778.0/349
101123A[a]	427^{-20}_{+21}	$-0.96^{-0.01}_{+0.01}$	$-2.04^{-0.03}_{+0.03}$									5355^{-586a}_{+647}	619.7/348

28

Table 11
(Continued)

GRB	Main Component								Additional Components			Total Fluence	Statistic
	Band			Comptonized		Log. Parabola		Fluence	Power Law	CutOff	Fluence		
	E_0 (keV)	α	β	E_0 (keV)	α	b	E_p (keV)	10 keV–10 GeV (10^{-7} erg cm^{-2})	α	E_c (MeV)	10 keV–10 GeV (10^{-7} erg cm^{-2})	10 keV–10 GeV (10^{-7} erg cm^{-2})	Stat./Dof
110120A	609^{-60}_{+70}	$-0.65^{-0.04}_{+0.04}$	$-2.94^{-0.17}_{+0.11}$									422^{-22}_{+23}	385.2/357
110328B				1210^{-220}_{+322}	$1.23^{-0.03}_{+0.03}$							417^{-37}_{+47}	539.7/358
110428A	105^{-3}_{+3}	$-0.28^{-0.03}_{+0.03}$	$-2.90^{-0.13}_{+0.10}$									255^{-9}_{+10}	531.4/470
110529A	882^{-159}_{+226}	$-0.80^{-0.06}_{+0.06}$	$-2.75^{-0.34}_{+0.19}$									49^{-6}_{+6}	450.0/470
110625A[a]	165^{-5}_{+5}	$-0.85^{-0.02}_{+0.02}$	$-2.44^{-0.06}_{+0.05}$									$964^{-48\,a}_{+54}$	773.8/462
110709A	352^{-26}_{+29}	$-0.81^{-0.04}_{+0.04}$	$-2.54^{-0.07}_{+0.06}$									518^{-27}_{+28}	599.4/355
110721A						$0.29^{-0.01}_{+0.01}$	1491^{-92}_{+99}					876^{-28}_{+28}	1112.3/701
110731A	264^{-16}_{+18}	$-0.82^{-0.03}_{+0.03}$	$-2.32^{-0.03}_{+0.02}$									400^{-16}_{+17}	413.8/354
	172^{-15}_{+16}	$-0.40^{-0.10}_{+0.10}$	$-2.48^{-0.24}_{+0.13}$					286^{-47}_{+56}	$1.95^{-0.04}_{+0.08}$		93^{-42}_{+31}	379^{-21}_{+20}	397.1/352

Notes. Each GRB is modeled by one main component and eventually one or more additional components. So, for example, the spectrum of GRB 080825C is well described by a Band model, thus only the corresponding columns are filled. The spectrum of GRB 090926A is instead modeled by a Band model plus a power law times an exponential cutoff (see the main text).

[a] These GRBs have such a large off-axis angle that the corresponding effective area for the LAT (Transient class) is negligible. Accordingly, only GBM data have been used during the spectral analysis and the fluence has been computed extrapolating the best-fit model up to the LAT energy range.

Table 12
Results for the Joint Fit Over the Interval between the First Photon Detected by the LAT Inside the Energy-dependent ROI and the GBM T_{95}

| GRB | Main Component | | | | | | | Additional Components | | | Total Fluence | Statistic |
| | Band | | | Comptonized | | Log. Parabola | | Fluence | Power Law | CutOff | Fluence | | |
	E_0 (keV)	α	β	E_0 (keV)	α	b	E_p (keV)	10 keV–10 GeV (10^{-7} erg cm^{-2})	α	E_c (MeV)	10 keV–10 GeV (10^{-7} erg cm^{-2})	10 keV–10 GeV (10^{-7} erg cm^{-2})	Stat./Dof
080825C	126^{-5}_{+5}	$-0.65^{-0.02}_{+0.02}$	$-2.43^{-0.05}_{+0.04}$									358^{-17}_{+18}	975.9/821
080916C	260^{-17}_{+22}	$-0.65^{-0.06}_{+0.05}$	$-2.20^{-0.04}_{+0.02}$					1498^{-11}_{+12}	$2.00^{-0.06}_{+0.12}$		191^{-98}_{+107}	1689^{-36}_{+38}	474.6/354
081006						$0.25^{-0.05}_{+0.05}$	6765^{-1598}_{+2309}					46^{-9}_{+11}	461.7/479
081024B						$0.13^{-0.03}_{+0.03}$	46287^{-22078}_{+69759}					22^{-4}_{+5}	338.9/358
090217	526^{-29}_{+32}	$-0.88^{-0.02}_{+0.02}$	$-2.57^{-0.05}_{+0.05}$									500^{-15}_{+16}	497.7/358
090323	436^{-20}_{+21}	$-1.01^{-0.01}_{+0.01}$	$-2.69^{-0.07}_{+0.06}$									1492^{-44}_{+44}	965.4/357
090510	2734^{-243}_{+261}	$-0.67^{-0.05}_{+0.05}$	$-3.04^{-0.30}_{+0.19}$					263^{-14}_{+15}	$1.60^{-0.05}_{+0.04}$		89^{-17}_{+18}	352^{-17}_{+19}	668.6/707
090720B	915^{-119}_{+145}	$-1.03^{-0.04}_{+0.04}$	$-2.59^{-0.20}_{+0.13}$									114^{-9}_{+9}	440.7/470
090902B				531^{-10}_{+10}	$0.62^{-0.01}_{+0.01}$			3057^{-24}_{+25}	$1.94^{-0.01}_{+0.01}$		1007^{-57}_{+59}	4063^{-24}_{+24}	628.5/478
090926A	188^{-7}_{+7}	$-0.64^{-0.03}_{+0.03}$	$-2.63^{-0.06}_{+0.05}$					1276^{-42}_{+45}	$1.76^{-0.03}_{+0.02}$	1513^{-381}_{+617}	543^{-41}_{+42}	1818^{-45}_{+46}	685.9/467
091003	425^{-18}_{+19}	$-1.02^{-0.01}_{+0.01}$	$-2.65^{-0.07}_{+0.06}$									457^{-14}_{+15}	1133.5/710
091208B	157^{-34}_{+45}	$-1.29^{-0.08}_{+0.09}$	$-2.26^{-0.08}_{+0.07}$									80^{-10}_{+12}	514.2/355
100116A	1117^{-136}_{+163}	$-1.08^{-0.03}_{+0.03}$	$-2.80^{-0.10}_{+0.08}$									660^{-37}_{+40}	512.2/356
100325A	88^{-9}_{+10}	$-0.30^{-0.12}_{+0.14}$	$-2.32^{-0.09}_{+0.07}$									42^{-4}_{+4}	458.8/468
100414A	401^{-16}_{+16}	$-0.63^{-0.02}_{+0.02}$	$-2.68^{-0.10}_{+0.08}$									792^{-38}_{+41}	418.7/355
100724B	265^{-4}_{+4}	$-0.72^{-0.00}_{+0.01}$	$-2.00^{-0.01}_{+0.01}$							40^{-3}_{+3}		4856^{-78}_{+79}	745.6/468
110709A	474^{-46}_{+53}	$-0.97^{-0.04}_{+0.04}$	$-2.50^{-0.07}_{+0.06}$									426^{-25}_{+26}	575.0/355
110721A						$0.28^{-0.01}_{+0.01}$	1847^{-107}_{+114}					1041^{-31}_{+31}	1101.0/701
110731A	144^{-14}_{+18}	$0.05^{-0.14}_{+0.15}$	$-2.41^{-0.11}_{+0.07}$					324^{-44}_{+40}	$2.00^{-0.05}_{+0.08}$		75^{-31}_{+32}	399^{-18}_{+19}	409.8/352

Notes. Each GRB is modeled by one main component and eventually one or more additional components. So, for example, the spectrum of GRB 080825C is well described by a Band model, thus only the corresponding columns are filled. The spectrum of GRB 090926A is instead modeled by a Band model plus a power law times an exponential cutoff (see the main text).

Figure 15. Position of GRB 100414A in the FoV as a function of the time since the GBM trigger. The y-axis is the off-axis angle. The green box is the GBM T_{90} while the red dashed line represents the edge of the FoV.

(A color version of this figure is available in the online journal.)

$S = 977$ with 469 dof using the Band model, while adding an exponential cutoff we find $S = 734$ with 468 dof. The value $\Delta S = 243$ is well above our threshold $\Delta S = 28$. Discussion of the physical implications of these findings is beyond the scope of the present paper. Finally, the spectral analysis of GRB 110731A by Ackermann et al. (2013) revealed a hint of another cutoff at high energy with a significance of $\sim 4\sigma$ in the time interval starting from the LAT T_{05} and ending at the GBM T_{95}. We refer the reader to that paper for details.

5. DISCUSSION

In this section, we describe the emergent properties of LAT-detected GRBs revealed by this study.

5.1. Broadband Spectroscopy

5.1.1. A Band Model Crisis?

Before the launch of *Fermi*, GRBs were mainly studied in the energy range from a few keV to a few MeV, with the catalog of BATSE (Kaneko et al. 2006, 2008) constituting the largest sample available to date. Several spectroscopic analyses have been performed on that sample, showing that most of the GRB spectra are well described by a Band model, a Comptonized model, or an SBPL model (Preece et al. 2000). LAT-detected GRBs are bright in the GBM energy band, which is very similar to the BATSE band, and thus we can compare our detection statistics with those found in the bright BATSE sample by Kaneko et al. (2006). In Table 10, we report all LAT-detected GRBs, ordered by fluence, and the model that best describes the spectrum over the GBM time interval. For convenience, we also report their off-axis angles θ at the trigger times. We exclude GRBs outside of the nominal FoV ($\theta > 70°$). We also exclude GRB 101014A, which was too close to the Earth's limb to allow a spectroscopic study.

Kaneko et al. (2006) found that the spectra of $\sim 85\%$ of the brightest 350 BATSE GRBs are well described by a Band function, while we find that 70% of LAT-detected GRBs are well described by either a Band model or a Comptonized model, which is similar to a Band model with a very soft value of β. Given the small size of our sample, the two fractions are very similar. Additionally, Kaneko et al. (2006) found that 5% of BATSE GRBs require the more complex SBPL model, while no LAT-detected GRB requires it. Again, this is very likely to be due just to the small size of our sample.

On the other hand, Table 10 shows that the spectra of all of the brightest bursts inside the LAT FoV present significant devi-

ations from a Band function, requiring additional components. Other GRBs, observed with low θ angles and correspondingly high effective areas, show deviations as well. The phenomenological Band model, implemented for BATSE GRB observations up to a few MeV, does not seem to describe bright or well-observed LAT-detected GRBs sufficiently.

For each GRB with a very high signal-to-noise ratio in the LAT data, we find that the Band model needs to be supplemented with additional components or modified with a cutoff. There is no common recipe to fit all *Fermi* GRBs: for the bright GRBs 090510 and 090902B, an additional PL component, extending from low to high energies, is required; for GRB 100724B, a cutoff in the high-energy spectrum is needed in order to explain the rapid drop-off of the flux at high energies; the case of GRB 090926A is even more complex, with both a PL and an exponential cutoff required to describe the spectrum. Other works (Guiriec et al. 2011; Zhang et al. 2011) use a thermal component added to the Band function. This difficulty arises thanks to the wider energy coverage provided by *Fermi* with respect to BATSE; accurate GRB spectroscopy in the *Fermi* era requires improved broadband modeling.

5.2. Energetics

Cenko et al. (2011) and Racusin et al. (2011) studied the energetics of the afterglows of LAT-detected GRBs and concluded that they are among the most luminous afterglows observed by *Swift*. We start our analysis by examining the properties of LAT-detected GRBs in the context of the prompt emission and compare the high-energy properties measured by the LAT to the low-energy properties measured by the GBM.

5.2.1. Prompt Phase Energetics

We first study the fluence and then continue with the sub-sample of GRBs that have a measured redshift and examine intrinsic GRB quantities. Even though intrinsic properties are, by far, more interesting for understanding the physics, properties measured in the observer's frame (such as the fluence or the peak flux) are sometimes more instructive from the experimental point of view, as they can reveal observational biases and selection effects.

In Figure 16, we compare the fluence measured by the GBM in the 10 keV–1 MeV energy band for the full GBM spectral catalog (Goldstein et al. 2012) with the 10 keV–1 MeV fluence of LAT-detected GRBs. Since the LAT observations are photon-limited, the detection efficiency is directly related to the source fluence (Band et al. 2009). This is in contrast to the GBM data, which are background dominated and where the peak flux is a better proxy for the detection efficiency.

In general, LAT detected GRBs are among the brightest detected by the GBM, populating the right-hand side of the fluence distribution. The brightest GRB in the GBM catalog is GRB 090618 (McBreen 2009a), also detected by *AGILE* (MINICAL and Super-*AGILE*) (Longo et al. 2009b) and *Swift*-BAT (Schady et al. 2009), but not detected by the LAT because it occurred outside its FoV ($\theta = 132°$). The second brightest GRB in the GBM catalog is the LAT-detected GRB 090902B. More interestingly, there are a few cases of bursts that were not particularly bright in the GBM, yet were detected by the LAT, namely short GRBs 081024 and 090531, which have a relatively small fluences compared with the rest of the GBM catalog bursts, mainly because of their short durations ($<20\%$ and $<30\%$ quantile of the distribution). The former was detected by the LAT up to $\sim$GeV energies (Abdo et al. 2010b), while the
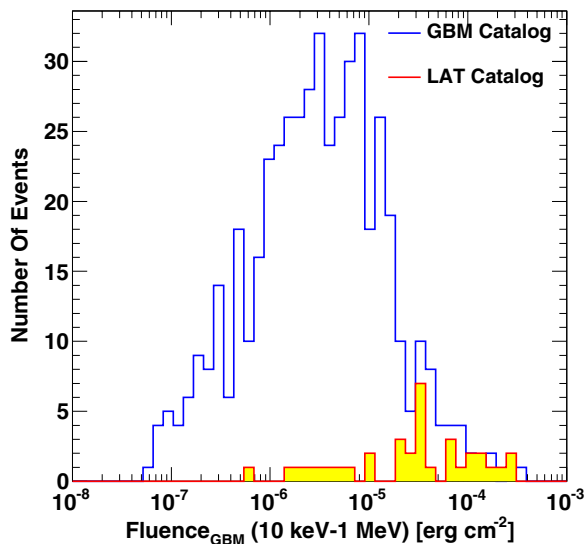
Figure 16. Distribution of the energy fluences in the 10 keV–1 MeV energy range for the bursts detected by the LAT compared with the fluences in the same energy band for the entire sample of GRBs in the GBM spectral catalog (Goldstein et al. 2012).

(A color version of this figure is available in the online journal.)

latter was detected only at low energies by the LLE analysis. Note, however, that the published GBM catalog includes bursts only up to the beginning of 2010 July. Thus, it does not contain a significant part of our sample, and in particular GRB 100724B, which has the highest fluence in the GBM energy range in our sample (see Table 10).

The top panel of Figure 17 shows the fluence measured by the LAT versus the fluence measured by the GBM in the "GBM" time window. The plotted GBM fluences were produced by the joint GBM-LAT spectral analysis in this study, in accordance with the best-fit spectral model described in Table 11. LAT fluences calculated from the LAT-only maximum-likelihood analysis and from the joint GBM-LAT spectral fits are both shown in the figure. Generally speaking, the agreement is good, however, for bright bursts the two methods produce results that are in slight disagreement. This arises because we use a two-component model in joint GBM-LAT spectral fits, with the low-energy component (a Band model or a Comptonized model) having a non-negligible contribution at high energy. Thus, both the photon index and the normalization of the PL component are different with respect to the maximum-likelihood analysis, which uses a PL only.

The bulk of the LAT GRB population, primarily composed of long GRBs, has a ratio of high- (100 MeV–10 GeV) to low-energy (10 keV–1 MeV) fluence $\lesssim 20\%$. It is interesting to note that the three short LAT-detected bursts (red symbols in Figure 17) have a greater ratio of high- to low-energy fluence than the bulk of the long-GRB population (blue symbols). Two short bursts, GRBs 080825C and 090510, have the two highest ratios (over 100%) and the short burst GRB 090227B also has a relatively high ratio ($\sim$10%). This reflects the well-known fact that short GRBs have harder spectra than long-duration bursts. On the other hand, since the high-energy emission typically lasts longer than the low-energy emission, and since in this plot the integration time is the same (the GBM T_{90}) for both axes, only part of the emission at high energies is included in the calculation of the fluence. For this reason, we also integrate the fluence between 100 MeV and 10 GeV over the full LAT T_{90} time window and in the bottom panel we compare this quantity
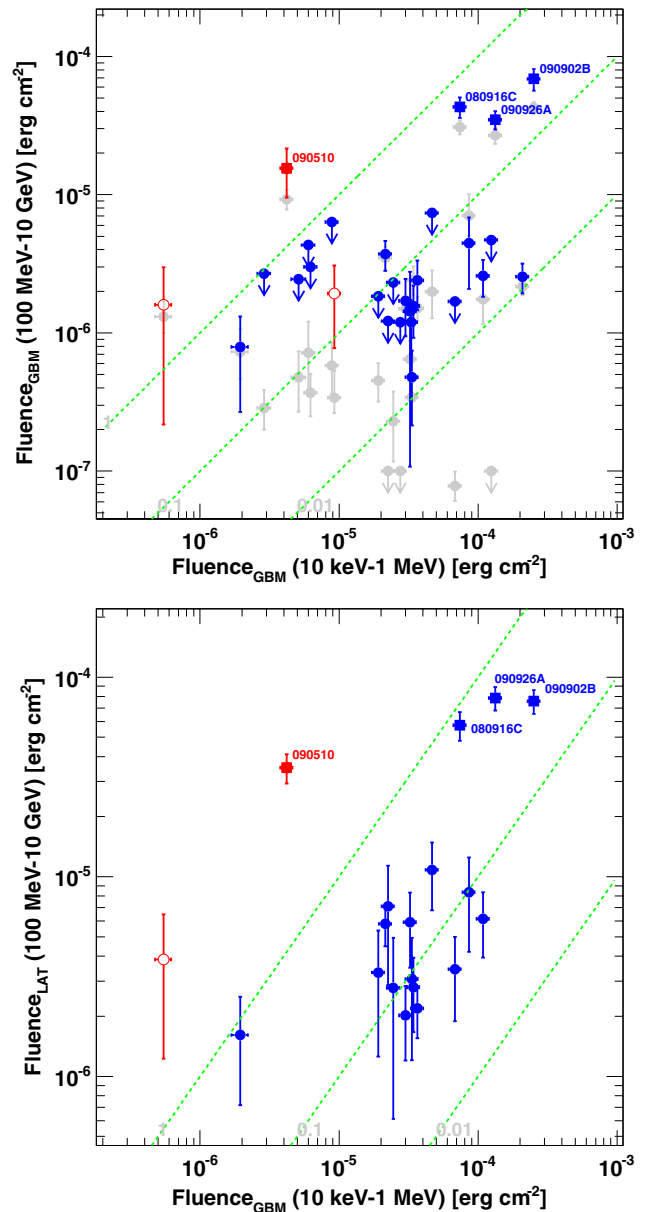
Figure 17. Fluence measured by the LAT vs. the fluence measured by the GBM in the "GBM" time window (top panel) and in the "LAT" time window (bottom panel). The three dashed lines denote the 100%, 10%, and 1% fluence ratios. Colored symbols follow the convention of Figure 9. Additionally, we use gray circles for the joint-fit results.

(A color version of this figure is available in the online journal.)

with the fluence as measured by the GBM during the GBM time window. In this way, we better account for the energetics in the LAT energy range. The LAT measurements in this panel were all derived from the likelihood analysis of this study. Because we were not able to measure durations in the LAT energy range for all bursts, this panel has fewer entries than in the top panel. Similarly to the above, short GRBs appear considerably more efficient at radiating at high energies than at low energies.

In both panels of Figure 17, we can see that the four hyper-fluent LAT bursts, GRBs 080916C, 090510, 090902B, and 090926A, have evidently greater emission in the LAT energy range compared with the rest of the GRB population. The discrepancy increases when comparing the high-energy emission measured in the generally longer LAT time window with the low-energy emission measured in the GBM time
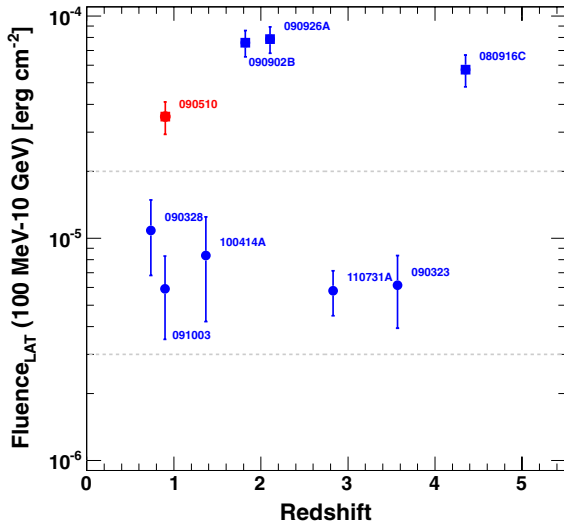
Figure 18. Fluence measured by the LAT during the "LAT" time interval vs. redshift. The two dashed lines in this figure denote a fluence of 3×10^{-6} erg cm^{-2} and 2×10^{-5} erg cm^{-2}, with the first number corresponding to an approximate empirical LAT detection threshold and the second simply denoting a minimum fluence for the four hyper-fluent bursts. The symbol convention is the same as in Figure 9.

(A color version of this figure is available in the online journal.)

Figure 19. Isotropic energy in the 1 keV–10 MeV energy range of LAT-detected GRBs (blue/red symbols) compared with *Swift* GRBs (Butler et al. 2007; gray symbols) and GBM GRBs (Goldstein et al. 2012; green symbols). The blue and red squares denote the LAT-detected GRBs (with a measured redshift).

(A color version of this figure is available in the online journal.)

window, which is a result of the bright extended high-energy emission of these four bursts.

It is worth examining whether the four brightest LAT bursts appear bright because they are systematically closer to us compared with the rest of the GRB population. As can be seen in Figure 18, which shows the fluence in the LAT energy range and the LAT time window versus redshift, this is not the case. In the figure, we denote an empirical LAT-detection threshold. We caution the reader that since the minimum fluence at which the LAT can detect a GRB depends on the position of the GRB in the LAT FoV, as well as on the intrinsic properties of the GRB (photon index, duration, etc.), this threshold is just a crude estimate for reference.

To quantify the energy release at the source in some source-frame energy range E_1–E_2, we compute the isotropic equivalent energy E_{iso} as

$$E_{iso} = 4 \pi \, d_L(z)^2 \, \frac{S(E_1, E_2, z)}{1+z}, \qquad (12)$$

where $d_L(z)$ is the luminosity distance of a source at redshift z and $S(E_1, E_2, z)$ is the fluence of the source integrated in the source frame energy range E_1 and E_2:

$$S(E_1, E_2, z) = \int_{E_1/(1+z)}^{E_2/(1+z)} E \, \frac{dN(E)}{dE} dE, \qquad (13)$$

where $dN(E)/dE$ describes the spectral model. The choice of the energy band used to compute the isotropic energy is important and requires some discussion. In order to calculate the bolometric isotropic energy, the energy band must be as broad as possible. On the other hand, the calculation in principle should include only the portion of the spectrum that has been directly measured (i.e., constrained by the data) or a potentially inaccurate extrapolation would be required. Considering the spectral coverage of the two instruments on board *Fermi*, we chose to integrate between the $E_1 = 1$ keV and $E_2 = 10$ GeV source-frame energies. We start at 1 keV

source frame, which corresponds to a few keV in the observer frame and is slightly outside of the GBM energy band, to make comparisons with some studies already in the literature. In addition, we compute the isotropic equivalent energy in a narrower band (1 keV–10 MeV), covering mainly the energy range of the GBM detectors. The latter choice allows us to directly compare our results with those of previous works, namely Amati et al. (2002) and Racusin et al. (2011), who adopted a source-frame range between 10 keV and 10 MeV, Amati (2006) and Butler et al. (2007), who adopted a slightly broader source-frame range extending from 1 keV to 10 MeV, and Cenko et al. (2011), who used an observer-frame range between 1 keV and 10 MeV.

In Figure 19, we plot E_{iso} in the 1 keV–10 MeV energy range versus redshift in the prompt ("GBM") time interval. The energy range matches that of previous works (Butler et al. (2007) for *Swift* bursts and Goldstein et al. (2012) for GBM bursts), allowing direct comparisons of E_{iso}. For a given redshift, LAT-detected GRBs are generally brighter than the average burst, in agreement with the findings from other works (Cenko et al. 2011; Racusin et al. 2011). We note that although GRBs 110731A and 090510 have a moderate 1 keV–10 MeV E_{iso}, they have been detected by the LAT. For these two bursts, the observational conditions were very favorable for detection, since they were nearly on-axis for the LAT at the times of the GBM triggers (off-axis angles of 13°.6 for GRB 090510 and 3°.4 for GRB 110731A).

Before proceeding, we would like to make an important point concerning the definition of "bolometric" luminosity of the prompt phase for GRBs. Before *Fermi*, the properties of prompt spectra of GRBs were known up to ∼MeV energies and there was no way to account for the higher energy portion of the spectrum (>10 MeV) in the total energy budget. This is reasonable as long as the high-energy emission does not constitute a significant part of the total emitted energy. Using LAT detections of GRBs, it has been discovered that extra PL components are more common in GRBs compared with what

Figure 20. Top: isotropic equivalent energy in the 100 MeV–10 GeV energy range vs. the 1 keV–10 GeV energy range. Bottom: radiated energy corresponding to the PL spectral component vs. that corresponding to the Band component. The symbol convention is the same as in Figure 9.

(A color version of this figure is available in the online journal.)

Table 13
Isotropic Equivalent Energy by Component

GRB Name	Best Model	$E_{\rm iso}$ (10^{52} erg)	$E_{\rm iso}^{\rm Band}$ (10^{52} erg)	$E_{\rm iso}^{\rm PL}$ (10^{52} erg)
GRB080916C	BP	$647.2^{+12.8}_{-12.3}$	$564.6^{+38.1}_{-4.1}$	$82.69^{+29.42}_{-24.24}$
GRB090323	B	$411.7^{+11.7}_{-11.7}$	$411.7^{+11.7}_{-11.7}$	...
GRB090328	B	$11.7^{+0.5}_{-0.5}$	$11.7^{+0.5}_{-0.5}$	...
GRB090510	BP	$7.3^{+0.3}_{-0.3}$	$5.9^{+0.3}_{-0.3}$	$1.41^{+0.30}_{-0.27}$
GRB090902B	BP	$343.6^{+2.6}_{-2.6}$	$259.2^{+2.6}_{-2.6}$	$84.46^{+3.90}_{-3.75}$
GRB090926A	BC	$242.0^{+5.1}_{-5.0}$	$199.1^{+6.5}_{-6.1}$	$46.74^{+4.48}_{-4.61}$
GRB091003	B	$9.9^{+0.3}_{-0.3}$	$9.9^{+0.3}_{-0.3}$	...
GRB091208B	B	$3.0^{+0.4}_{-0.3}$	$3.0^{+0.4}_{-0.3}$	...
GRB100414A	CP	$52.5^{+1.2}_{-1.0}$	...	...
GRB110731A	B BP	$71.7^{+2.8}_{-2.7}$	$51.4^{+9.8}_{-8.3}$	$17.72^{+4.25}_{-6.03}$

Note. The best fit models are Band (B), Band + Powerlaw (BP), Band + Comptonized (BC), and Comptonized + Powerlaw (CP).

radiated during the prompt phase. The short GRB 090510 has an especially high fraction of ∼50%.

For the few bursts for which we can significantly separate the contributions from the extra component (PL) and the main component (the "Band" model), we can calculate the fraction of the energy during the prompt emission that is associated with each of these two spectral components. In the bottom panel of Figure 20, we show the emitted energy corresponding to each component for the "GBM" time interval. As shown, the energy radiated during the prompt emission by the PL component is between 10% and 50% of the energy radiated by the Band component. The numerical results of this analysis can be found in Table 13.

5.2.2. The Highest Energy Photons

Events with source-frame-corrected energies up to 50–100 GeV have been measured in GRBs by the LAT, including from high-redshift sources (up to $z = 4.35$ from GRB 080916C; Greiner et al. 2009). In order to produce γ-rays of such high energies within the first few seconds of the burst, particle acceleration must be efficient in a GRB. Internal-opacity constraints also indicate that these high-energy photon detections require large bulk Lorentz factors for the jet. Moreover, high-energy γ-rays from high-redshift GRBs offer a valuable tool for measuring the opacity of the universe due to the interaction of >10 GeV γ-rays with optical and UV photons from the extragalactic background light (Abdo et al. 2010a). Finally, the short time delay observed in LAT GRBs between low- and high-energy events can be used to place tight constraints on any energy dependence of the speed of light in vacuum, as postulated by some quantum gravity theories (Abdo et al. 2009b).

Figure 21 shows the source-frame-corrected energy of the highest energy events with a high probability (>0.9) of being associated with the GRB, detected in the time-resolved likelihood analysis, versus $E_{\rm iso}$. For long bursts, the most energetic photons appear in the brightest GRBs. Interestingly, our only short GRB with a measured redshift, GRB 090510, does not follow the correlation pattern followed by LAT detected long bursts. More statistics are needed to determine whether this pattern is significant.

5.2.3. Extended Phase Energetics

We have explored the energy budget of the highly energetic GRBs during the prompt phase. Now we focus on the temporally

was previously thought. More importantly, even if the high-energy emission can last longer than the usual keV-to-MeV emission, in some cases (GRBs 090510, 090902B, 090926A) it contributes significantly during the prompt phase. These two considerations suggest that the total energy budget at high energies can be an important fraction of the total energy reservoir.

In Figure 20 (top panel), we try to address this issue by plotting the amount of energy radiated by the source between 100 MeV and 10 GeV during the temporal extended emission compared with that radiated in the wider 1 keV–10 GeV energy range in the "GBM" time interval. As can be seen, the fraction of energy radiated in the form of high-energy γ-rays during the temporal extended phase is typically $\lesssim$10% of the total energy

Figure 21. Rest-frame-corrected energy of the highest energy event recorded during the time resolved analysis vs. E_{iso}. Data points are from Table 8. The symbol convention is the same as in Figure 9.

(A color version of this figure is available in the online journal.)
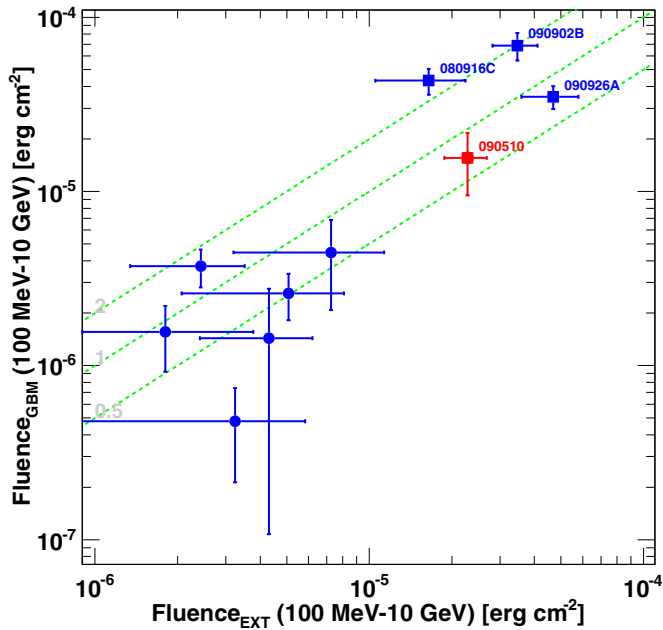
Figure 22. Fluence in the 100 MeV–10 GeV energy range measured in the "GBM" vs. the "EXT" time intervals. The dashed lines correspond to ratios of 0.5, 1, and 2. The symbol convention is the same as in Figure 9.

(A color version of this figure is available in the online journal.)

Figure 23. Ratio of the 100 MeV–10 GeV fluence measured in the "EXT" time intervals over that measured in the "GBM" time intervals plotted for each burst that has significant extended emission in the LAT data.

(A color version of this figure is available in the online journal.)

extended phase. First, we compare the energy radiated above 100 MeV during the prompt and temporally extended phases. Since we are comparing energies in the same band, we increase the statistics of our sample by comparing fluences, a quantity that does not require knowing the redshift. Figure 22 shows the 100 MeV–10 GeV fluence measured during the "GBM" time interval versus the fluence measured in the "EXT" time interval and Figure 23 shows the ratio of these quantities for all GRBs with a LAT detection in both time intervals. We note that most of the ratios are consistent with unity. This implies that the energy

released above 100 MeV during the prompt emission is similar to the energy released during the temporally extended emission.

To study the relative efficiencies of the Band and extra PL components during the prompt and temporally extended emission phases, we calculate the ratio of the source-frame isotropic equivalent energy, as measured by the LAT above 100 MeV in the temporally extended phase (the "EXT" time window), to the same quantity measured during the GBM time window. This quantity is what we display on the y-axis of Figure 24. We now know that high-energy emission can be produced during both the prompt and the temporally extended phases and the y-axis of Figure 24 shows the relative importance
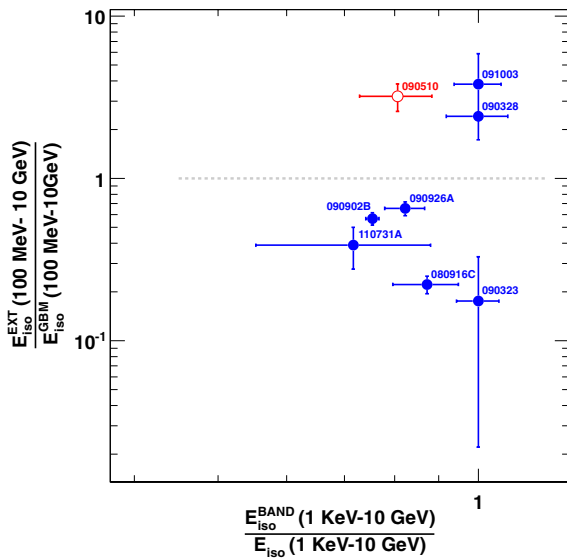
Figure 24. γ-ray efficiency of the temporally extended emission phase vs. the efficiency of the prompt Band component. The y-axis shows the ratio between the energy released during the temporally extended emission phase and the energy released during the prompt GBM phase and the x-axis shows the ratio between the bolometric isotropic equivalent energy radiated by the Band component over the total radiated energy during the prompt emission. The symbol convention is the same as in Figure 9.

(A color version of this figure is available in the online journal.)

of these two phases. The GRBs in the plot occupy two regions: "γ-ray-afterglow dominated" GRBs, with $E_{\rm iso}^{\rm EXT} > E_{\rm iso}^{\rm GBM}$, like GRBs 090510, 091003, and 090328 and "prompt-γ-ray dominated" GRBs, for which $E_{\rm iso}^{\rm EXT} < E_{\rm iso}^{\rm GBM}$.

The "γ-ray-afterglow dominated" GRBs in our sample (GRBs 090510, 091003, and 090328) do not necessarily have a dominant PL component in the prompt phase. This could imply that the energy radiated by the extra component during the prompt phase can be dominated by the energy radiated by the main prompt component described by a Band function. Note that the LAT sensitivity to GRB 090328 at the time of the GBM trigger was not optimal and part of the emission may not have been detected. This is certainly true for long bursts, such as GRBs 091003 and 090328, while it is not true for GRB 090510, for which a PL component has been detected. The majority of LAT-detected bursts radiate more efficiently at high energies during the prompt GBM phase (GRBs below the horizontal line in Figure 24). We define such bursts as "prompt-γ-ray dominated" GRBs. The five such bursts follow an expected trend: the more important the PL component in the prompt emission phase, the brighter the late-time emission becomes compared with the prompt high-energy γ-ray emission. As already noted, each of the four hyper-fluent GRBs shows evidence of an extra component, as does GRB 110731A.

5.3. High-energy Spectral Properties

In the previous section, we discussed the energetics of *Fermi*-LAT GRBs and we now consider their spectral properties. Since our primary interest is reporting observations related to *Fermi*-LAT data, we focus on the spectral properties at high energies, with special emphasis on the role of the extra component. We start from the LAT-only analysis. Figure 25 shows the photon indices of all GRBs detected by the likelihood analysis as measured in three different time windows. Almost all photon index values are consistent with a value of -2 for all three time
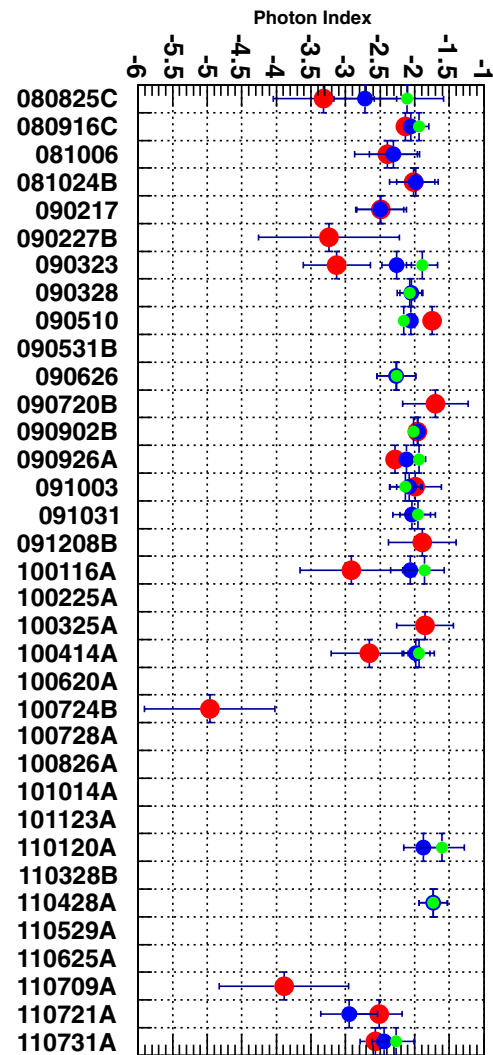
Figure 25. Photon index Γ of the likelihood-detected bursts as measured in three time windows: "GBM" (red), "LAT" (blue), and "EXT" (green).

(A color version of this figure is available in the online journal.)

windows; we obtain the average values $\langle \gamma_{\rm GBM} \rangle = -2.08 \pm 0.04$ in the "GBM" time window, $\langle \gamma_{\rm LAT} \rangle = -2.05 \pm 0.03$ in the "LAT" time window, and $\langle \gamma_{\rm EXT} \rangle = -2.00 \pm 0.04$, in the "EXT" time window using the estimated errors as weights. There is a selection effect such that any bursts with a photon index considerably softer than ~ -2 are less detectable by the LAT. Interestingly, GRB 100724B, which has the steepest photon index during the "GBM," has the second largest GBM-measured duration, while the GRB with the shortest duration, GRB 090510, has one of the hardest photon indices.

To further explore whether the photon indices depend on duration, we plot in Figure 26 the value of the photon index of the extra PL as measured in the "GBM" time window $\Gamma_{\rm GBM}$ (top panel) and in the "EXT" time window $\Gamma_{\rm EXT}$ (bottom panel) versus the GBM T_{90}. The photon index has a weak inverse correlation with the duration of the burst (top panel), in agreement with our results above and previous findings that the spectra of short-duration GRBs tend to be harder (Piran 2004). On the other hand, when the spectral analysis is performed during the "EXT" time window (bottom panel), during which the signal from the GRB is no longer detected by the GBM but is still bright in the LAT energy window, this weak correlation

Figure 27. Red/blue symbols: photon index Γ_{EXT} of the PL spectrum as measured by the LAT during the "EXT" time interval. The x-axis is the value of the β parameter of the Band function. Gray symbols: photon index α of the extra PL component obtained by our joint GBM-LAT fits as measured in the "GBM" time window. The symbol convention is the same as in Figure 9.

(A color version of this figure is available in the online journal.)

fit the LAT-GBM data. An important selection effect must be kept in mind: distinguishing an extra PL spectral component is difficult when it is softer than the high-energy component of the Band function. As can be seen in Figure 27, the PL component described by Γ_{EXT} is typically harder than the high-energy emission measured during the prompt phase by GBM, described by β. Furthermore, the two quantities do not seem to be correlated. The most extreme case, GRB 090902B, is shown in the inset of that figure, together with GRB 100414A, for which we detect the temporally extended emission, while the β index of the Band function is only an UL. In fact, for these bursts, the best-fit models found by our procedure were the Comptonized + power law and the Comptonized alone, respectively. Therefore, it is very reasonable that when we replace the Comptonized model with a Band function, the resulting β parameter is very steep and not constrained toward lower values.

In two cases, GRBs 090510 and 090926A, the extra PL component that is significantly detected during the prompt emission is harder than the PL of the extended emission. For the first case, this is probably caused by the hard-to-soft spectral evolution of the extra component, as demonstrated by the results of the time-resolved likelihood analysis shown in Figure 53. For the case of GRB 090926A, the extra PL component during the prompt emission is significantly attenuated at high energies and the model that best fits the emission during the "GBM" time window consists of a Band function plus a Comptonized model and has a very high peak energy. The (exponential) spectral cutoff of GRB 090926A is not significantly detected at later times. Overall, the temporal evolution of the extra PL component of this GRB can be described as very soft/weak at the start, progressively becoming harder but also demonstrating a roll-off at around 10 GeV, and then becoming softer again with an index of $\Gamma_{EXT} \sim -2$.

In the other three cases for which we significantly detect the extra PL component during the prompt phase (GRBs 080916C, 090902B, and 110731A; see Section 3.4.4), the photon index of the extra PL in the prompt "GBM" time interval γ is consistent with the index of the PL in the LAT energy range measured during the temporally extended emission Γ_{EXT}.

Figure 26. Top: power-law photon index measured in the GBM time window and (bottom) in the EXT time window. The symbol convention is the same as in Figure 9.

(A color version of this figure is available in the online journal.)

disappears. Note that some of the GRBs (like GRB 100724B) do not have detected extended emission and are reported only in the top panel.

To further investigate this, we show in Figure 27 the PL photon index Γ_{EXT} of the GRB emission in the LAT energy range as measured during the "EXT" time interval versus the value of the high-energy PL index β of the Band function as measured in the prompt "GBM" time interval. The value Γ_{EXT} was obtained by our LAT-only likelihood analysis and the β value was obtained by our joint GBM-LAT spectral fits. We measured β using either a Band-only or a Band-plus-power-law spectral model. For the cases where the more complex Band-plus-power-law spectral model also provided a good fit (i.e., when all the parameters were constrained and the fit converged), we selected the β value found for the more complex model. For those cases, in addition to Γ_{EXT} we also plot the fitted values of the extra PL component photon index α versus β. Table 11 summarizes the numerical values of the parameters of the model that best

Figure 28. Value of the "late-time decay index" α_L as a function of the fluence between 100 MeV and 10 GeV in the "GBM" time interval (top) and the isotropic luminosity between 1 keV–10 GeV in the source frame (bottom). The value of α_L is ∼1, except for GRB 080916C and GRB 110731A, which notably have the shortest durations when measured in the source frame (see the text). The symbol convention is the same as in Figure 9.

(A color version of this figure is available in the online journal.)

The picture emerging from the analyses described in this subsection suggests that the high-energy (>GeV) emission is dominated by a single long-lasting component, well described by a PL function of a photon index typically near −2, independent of burst properties such as the duration, the brightness, or the spectral properties of the lower energy prompt emission.

5.4. Extended Emission Temporal Decay

In Figure 28, we report the "late-time decay index" α_L as a function of the fluence measured by the LAT in the GBM interval (top panel) and the luminosity in the "GBM" time interval (lower panel). The values of α_L seem to cluster around 1, which, in the context of the fireball model, indicates an adiabatic expansion of the fireball (see Section 6.2). There are two exceptions: GRB 080916C and GRB 110731A. To investigate this a little further, we plot in Figure 29 the values of α_L as a function of the intrinsic duration of the GRBs at high energy. Both GRB 080916C and GRB 110731A have the shortest intrinsic LAT T_{90} among long GRBs. This suggests that we have probably
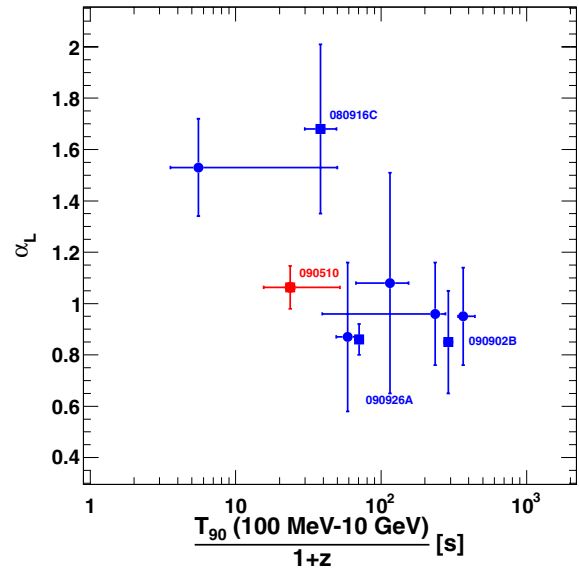
Figure 29. Value of the "late-time decay index" α_L as a function of the LAT T_{90} in the source reference frame. The symbol convention is the same as in Figure 9.

(A color version of this figure is available in the online journal.)

observed only the first steep part of the decay after the prompt phase and that we cannot exclude the existence of a flattening or a break at later times that would reconcile them with the other bursts.

5.5. LAT Detection Rate

Band et al. (2009) reported the number of expected GRBs per year detectable by the LAT as a function of the number of excess events. This rate was estimated with Monte Carlo simulations using the predicted pointing history for the first year of observations. This calculation was performed using a standard survey profile without any pointed-mode observations (due to a positive response to ARR or planned Target Of Opportunity (TOO)). The spectral model was a simple Band function, with parameters distributed according to the sample of bright BATSE GRBs (Kaneko et al. 2008). The all-sky burst rate was assumed to be 50 GRB yr^{-1} over the full sky (above the peak flux in 256 ms of 10 ph s^{-1} cm^{-2} in the 50–300 keV band or with an energy flux greater than 2×10^{-5} erg cm^{-2}) in the 20–2000 keV band, derived from the BATSE catalog of bright bursts. Band et al. (2009) calculated the number of expected γ-rays using the bright BATSE GRB sample and also repeated the calculation with the hardest spectrum (index $\beta > -2$) GRBs removed as the numbers of γ-rays at high energies would have been unphysically large.

In addition, Band et al. (2009) used simplified detection criteria based entirely on the numbers of detected photons assuming a negligible contribution from the background. These authors also used a semi-analytical model to compute the value of the TS. For the latter, an isotropic background was assumed, but no additional sources were added to the simulation, including the Earth's bright limb. The results of these simulations, taken from Band et al. (2009), are shown in Figure 30. We compare these results with the numbers of events above 100 MeV predicted by the best-fit model, including all bursts from Table 4. In this comparison, we use the values obtained both by integrating the spectrum in the GBM time window and in the LAT time window. Several interesting features are evident
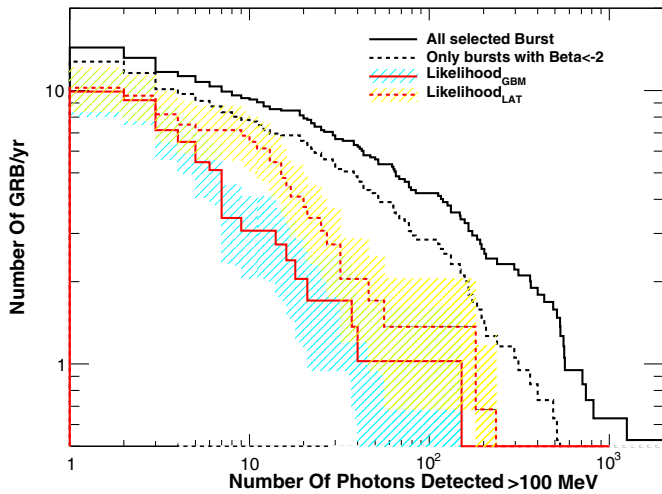
Figure 30. Comparison between the observed yearly rate of LAT GRB detections and the pre-launch expectations. Black lines are taken from Band et al. (2009) for an energy threshold of 100 MeV, using the bright BATSE GRB sample from Kaneko et al. (2008) as input. The dashed black line corresponds to an input distribution from which hard bursts with $\beta \geqslant -2$ have been removed. The red lines indicate the observed number of GRBs as a function of the number of events predicted by the best-fit model. The hatched regions correspond to the statistical uncertainties assuming Poisson statistics.

(A color version of this figure is available in the online journal.)

from this plot. First of all, the number of detected GRBs is somewhat less than expected. Additionally, the differences between the predicted and observed numbers of GRBs increase for bursts with many γ-rays in the LAT data. The absence of very bright bursts (with several hundreds of γ-rays detected above 100 MeV) could be due to the systematic uncertainties that are propagated in the simulation when extrapolating the Band function fits to high energies over a very large lever arm. Especially when the high-energy photon index is close to -2, a small change of the flux value could create large uncertainties in the number of detected events at high energies, when extrapolated. This has been specifically tested using bright GBM bursts that were not detected by the LAT and the bias introduced by fitting GBM-only data for bursts has been estimated by adding LAT ULs in the spectral fit (Ackermann et al. 2012b). On the other hand, intrinsic deviations from a pure Band function, such as spectral cutoffs, spectral breaks, or curvature in the spectra, could influence the number of predicted LAT detected GRBs.

5.6. Detectability of GBM Bursts

Although many observed properties may be considered in classifying the detectability of GBM GRBs by the LAT, we limit the current analysis to the competing effects that the effective area decreases with increasing off-axis angle θ while the solid angle increases with θ.

It follows that there are more GRBs at large θ, although the LAT can detect only the brightest. Figure 31 shows the fluence in the GBM energy band as a function of θ. Using the sample of GRBs through 2011 August that is available at the HEASARC web site,[87] we display both the LAT- and LLE-detected GRBs. For LAT detections, we use the fluence computed by our analysis, while for GBM-detected GRBs, we

---
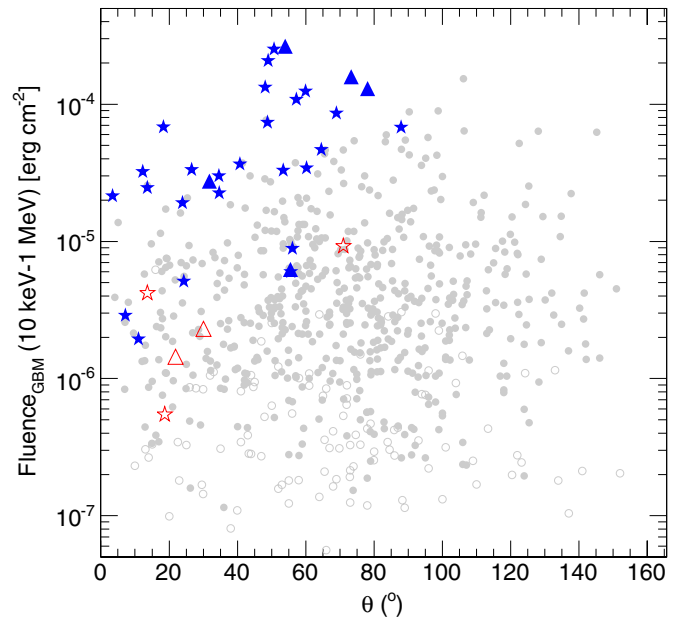
Figure 31. Sensitivity plot for GBM GRBs showing the fluence in the 10 keV–1 MeV energy band as a function of the LAT off-axis position (θ). Filled symbols indicate long-duration bursts while empty symbols denote short bursts. Gray circles denote GBM bursts that were not detected by the LAT, stars denote LAT bursts detected using the standard likelihood analysis, and triangles denote bursts detected by the LLE analysis only. For clarity, long-duration LAT-detected GRBs are plotted in blue, while short-duration, LAT-detected GRBs are plotted in red.

(A color version of this figure is available in the online journal.)

use the value obtained from the GBM Burst Catalog. Generally speaking, the LAT-detected GRBs are among the brightest GBM GRBs occurring in the LAT FoV. On the other hand, there are some exceptions where GRBs with a modest energy fluence or with a suboptimal viewing angle have still been detected by the LAT. These cases highlight the importance of secondary considerations other than θ or fluence. In terms of GBM fluence, short bursts are easier to detect. Also, we note that the location of the GRB in the FoV at the time of the GBM trigger is not always representative of the quality of the exposure obtained during the burst. For example, GRB 110625A was far off-axis at the time of the trigger (87°), but the high-energy emission was detected by the likelihood analysis a few hundred seconds after the GBM trigger when the GRB was well inside the FoV of the LAT. LLE bursts (triangles in Figure 31) occur typically at larger incidence angles, indicating that the FoV of the LAT is larger for the LLE data sample than when using standard event classification. There is also one case of a relatively bright GBM burst (GRB 110328B) where the off-axis angle was relatively small (∼32°) but the GRB was detected only using LLE analysis. This is explained by the results of the combined spectral analysis (summarized in Table 11), which show that the best-fit spectral model is a Comptonized model cutting off approximately at 1.2 MeV, implying suppression of high-energy emission.

6. INTERPRETATION

In this study, we have characterized the high-energy emission observed from 35 GRBs detected by the LAT. While the number of LAT GRBs is a small fraction of the number detected by the GBM (Paciesas et al. 2012; Goldstein et al. 2012), there are a

few emission features that show up only at high energies and distinguish the LAT GRBs:

1. high fluence and energy release,
2. temporally extended emission lasting longer than the GBM-detected emission,
3. delayed onset with respect to the GBM-detected emission, and
4. presence of an extra PL component in the spectrum.

Here, we discuss plausible interpretations of the emission properties observed with the LAT, the salient features of these models, and possible issues.

6.1. Fluence and Energetics of LAT Bursts

The distribution of fluences of LAT GRBs (see Figure 17) provides hints of two classes: a hyper-fluent class currently comprising four members, GRBs 080916C (Abdo et al. 2009d), 090510 (Abdo et al. 2009b; Ackermann et al. 2010b; Giuliani et al. 2010a), 090902B (Abdo et al. 2009a), and 090926A (Ackermann et al. 2011), which have a typical 100 MeV–10 GeV fluence of $\sim(3\text{–}8) \times 10^{-5}$ erg cm^{-2}, and a larger class with a lower typical fluence of $\sim(2\text{–}10) \times 10^{-6}$ erg cm^{-2}. The GBM fluences for the hyper-fluent class are also higher, ~1.3 times the LAT fluence for the short burst GRB 090510 and $\sim3\text{–}10$ times the LAT fluences for the three long bursts (see Figure 17, bottom panel). For comparison, we note that the typical fluence for the GBM long bursts is $\sim2 \times 10^{-6}$ erg cm^{-2} in the 8 keV–1 MeV range and $\sim10^{-5}$ erg cm^{-2} in the 8 keV–40 MeV range, based on Band function fits to the spectra (Goldstein et al. 2012). It is evident that most of the LAT bursts do seem to be very bright in the GBM, especially when comparing their 10 keV–1 MeV fluences (see Figures 31 and 16) to the 8 keV–1 MeV fluence of the typical GBM bursts (Goldstein et al. 2012).

In the cases of the nine LAT bursts for which redshift information is available, the isotropic equivalent energy $E_{\rm iso}$ in the LAT energy range (100 MeV–10 GeV) is also higher for the three hyper-fluent long bursts (see Figures 18 and 20, top panels). The ratio of the $E_{\rm iso}$ (100 MeV–10 GeV) to the total γ-ray energy $E_{\rm iso}$ (1 keV–10 GeV) for the long bursts is $\sim(5\text{–}25)\%$. Interestingly, in the case of GRB 090510, the only short LAT burst with a known redshift, this ratio is $\sim70\%$ and is clearly distinct from the long bursts. The bottom panel of Figure 20 shows that for the bright bursts, including GRB 090510 with its additional PL spectral component, the ratio of isotropic equivalent energies in the PL and Band components is concentrated at $\sim25\%$. Thus, the high ($\sim70\%$) LAT-to-GBM $E_{\rm iso}$ ratio for GRB 090510 is a combination of high Band $E_{\rm pk}$, typical for the short, hard class, and a very hard (-1.61) PL photon index that must cut off at high energies. The bursts with $\lesssim10\%$ LAT-to-GBM $E_{\rm iso}$ ratios do not allow for the detection of an additional PL spectral component, although it could still be present. The additional PL spectral component is most likely responsible for the high fluence detected by the LAT, as also indicated in Figure 24 for five of the eight brightest bursts.

The isotropic-equivalent energies of the LAT bursts calculated here are largely consistent with the energies calculated by Cenko et al. (2011) and show that LAT bursts possibly compose the most energetic sub-sample of GRBs (see Figure 19). The range of $E_{\rm iso}$ for short bursts in the pre-*Fermi* era was $(0.0033\text{–}10.2) \times 10^{52}$ erg (Ghirlanda et al. 2010). GRB 090510 is clearly at the high end of that range with $E_{\rm iso} \simeq 7 \times 10^{52}$ erg. Although the sample is rather small, the detected redshifts of LAT bursts do not show a concentration of bursts at any particular range

(see Figure 19). Racusin et al. (2011) showed that the redshift distributions are statistically consistent for *Swift*-BAT-detected GRBs, those detected by both GBM and BAT, and the small sample of LAT-detected bursts with measured redshifts. The only redshifts available for the GBM sample are for those bursts that also triggered BAT or LAT. Therefore, whether LAT-detected GRBs follow the redshift distribution of the rest of GBM-detected bursts is still an open question.

Another interesting feature of the LAT emission is that the 100 MeV–10 GeV fluences in the "GBM" and "EXT" time intervals are within a factor ~2 of each other for a handful of bursts with high-significance detections (see Figure 22). This may indicate an approximately equal efficiency of the GRB fireball to produce high-energy emission during the coasting (prompt) and deceleration (afterglow) phases, in the context of the early-afterglow model as the origin of LAT emission.

6.2. Temporally Extended Emission

The flux of LAT-detected emission at late times decays rather smoothly and can generally be fit with a PL $F_\nu \propto t^{-\alpha_L}$ (see Section 4.3.4 and Figures 13 and 14). Such behavior also is typically observed in X-ray, UV, and optical wavelengths after the prompt γ-ray emission and is attributed to the afterglow emission. The apparent constancy of the photon index for individual bursts (see Figure 25) in the "EXT" time interval as compared with the "LAT" time interval also suggests that the temporally extended LAT emission resembles afterglow rather than prompt emission, for which the photon index is likely to vary with time. The burst-averaged values for the photon index in these two intervals ($\Gamma_{\rm EXT} = -2.00 \pm 0.04$ and $\Gamma_{\rm LAT} = -2.05 \pm 0.03$) are also very similar. The slightly larger values for the burst-averaged photon index in the earlier "GBM" time interval ($\Gamma_{\rm GBM} = -2.08 \pm 0.04$) could be due to plausible contamination by the prompt emission in the LAT. Indeed, the high-energy photon index of the Band function, $\beta_{\rm Band}$, is systematically softer than $\Gamma_{\rm EXT}$ in the joint fit to the GBM and LAT data (Figure 27), suggesting that the hard spectral component becomes dominant at late times.

Remarkably, the "late-time decay index" is always close to $\alpha_L = 1$ (see Figures 14 and 28), except in two cases, GRBs 080916C and 110731A, which could be affected by an observational bias (see Section 5.4). The clustering around $\alpha_L = 1$ suggests a common emission mechanism, even though our limited sample does not allow firm conclusions. In the context of afterglow emission, the bolometric flux decays as $\propto t^{-\alpha}$, with $\alpha = 1$ and $\alpha = 10/7$ for an adiabatic fireball and a radiative fireball in a constant density environment (Sari 1997; Katz & Piran 1997; Ghisellini et al. 2010), respectively. The flux decay in a particular energy band is more complicated and depends on the fast- or slow-cooling spectral models (Sari et al. 1998), as well as on the surrounding environment (i.e., whether it is a uniform density interstellar medium (ISM) or whether a wind-type density profile is present (Sari et al. 1998; Chevalier & Li 2000; Panaitescu & Kumar 2000)). In particular, the relation between the flux-decay slope α and spectral index β for the flux density $F_\nu(t) \propto t^{-\alpha}\nu^{-\beta}$ varies between different parts of the spectrum. LAT-detected $\gtrsim100$ MeV emission is likely to be from the fast-cooling part of the spectrum for which $\alpha = (12\beta - 2)/7$ for a radiative fireball and $\alpha = (3\beta - 1)/2$ for an adiabatic fireball, both for the ISM and wind environments (Sari et al. 1998; Granot & Sari 2002). In the LAT data, $\beta = -\Gamma_{\rm EXT} - 1 = 1.00 \pm 0.04$ and $\alpha_{\rm adiabatic} = 1$ and $\alpha_{\rm radiative} = 10/7$, both of which are equal to their respective

bolometric flux-decay indices. Thus, a simple interpretation of the $\alpha_L \approx 1$ flux-decay index for most LAT bursts indicates that the $\gtrsim 100$ MeV emission is more likely from an adiabatic fireball (Kumar & Barniol Duran 2009; De Pasquale et al. 2010; Razzaque 2010) rather than from a radiative fireball, as Ghisellini et al. (2010) suggested.

For three bright bursts (GRBs 090510, 090902B, and 090926A), a broken PL fits the LAT data better than a single PL (see Section 4.3.4). After the time of peak flux, the initial flux decay is much steeper than the later decay. The initial steep-decay phase is likely due to a transition from the prompt to afterglow emission. An additional short-lived emission component, such as the high-latitude emission from the fireball that decays quickly (Kumar & Panaitescu 2000) and dominates the underlying afterglow emission, may in principle explain the initial steep decay.

6.3. Delayed Onset of LAT-detected Emission

For most bursts, the onset of the LAT-detected emission, as measured by LAT T_{05} (100 MeV–10 GeV), is delayed with respect to the onset of the GBM-detected emission, measured by GBM T_{05} (50 keV–300 keV; see Figure 9). Delays of up to 40 s have been detected in long bursts, with a few seconds being a typical value. The delay is ~ 0.5 s for GRB 090510 and $\gtrsim 0.05$ s for GRB 081024B, both of which are short bursts. The origin of the delayed onset of the LAT emission is poorly understood. Meszaros & Rees (1994) predicted that delayed emission at GeV energies should arise due to the reverse shock of the decelerating blast wave in the external medium and, more recently, the delayed onset measured by the LAT is interpreted in the context of the early afterglow model for the temporally extended emission in the LAT energy range (Kumar & Barniol Duran 2009; Ghisellini et al. 2010; De Pasquale et al. 2010; Razzaque 2010). The bolometric flux from a coasting fireball increases as $\propto t^2$ (Sari 1997), both for an adiabatic and a radiative fireball, before it decelerates and enters a self-similar phase (Blandford & McKee 1976; Rees & Meszaros 1994). The time required for the flux to increase and be detected by the LAT corresponds to the delayed onset of the LAT emission in this scenario. It also implies that the peak-flux time of the LAT is of the order of the fireball deceleration time. The corresponding jet bulk Lorentz factor can be estimated for an ISM of constant density $n = 1$ cm^{-3} as (Blandford & McKee 1976; Sari et al. 1998; Ghisellini et al. 2010)

$$\Gamma_0 = \left[\frac{3E_{k,\mathrm{iso}}(1+z)^3}{32\pi n m_p c^5 t_{\mathrm{peak}}^3}\right]^{1/8} \times \begin{cases} a^{-1/8}; a = 4 & \text{(adiabatic)} \\ a^{-5/32}; a = 7 & \text{(radiative)}, \end{cases}$$
(14)

where $E_{k,\mathrm{iso}}$ is the isotropic-equivalent jet kinetic energy immediately before deceleration.

In the case of a wind environment, with the wind parameter $A = 3.02 \times 10^{35} A_\star$ cm^{-1} for a $10^{-5} M_\odot$ yr^{-1} mass-loss rate in the wind of velocity 10^3 km s^{-1} and $A_\star \sim 1$ (Chevalier & Li 2000), the jet bulk Lorentz factor can be estimated as (Chevalier & Li 2000; Panaitescu & Kumar 2000)

$$\Gamma_0 = \left[\frac{E_{k,\mathrm{iso}}(1+z)}{16\pi A m_p c^3 t_{\mathrm{dec}}}\right]^{1/4},$$
(15)

where $t_{\mathrm{peak}} \approx t_{\mathrm{dec}}$ for the adiabatic and radiative fireballs.

Figure 32 illustrates the range of the bulk Lorentz factors calculated using Equations (14) and (15) for the nine LAT bursts
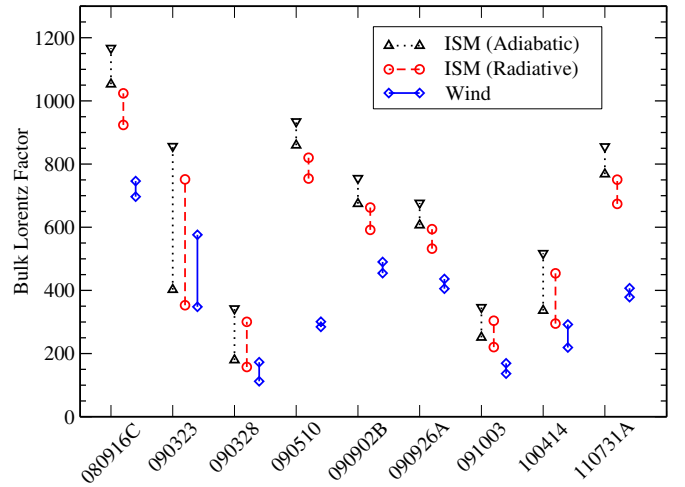
Figure 32. Bulk Lorentz factors of the LAT bursts derived on the assumption that the peak flux time in the LAT (Figure 14) represents the fireball deceleration time through Equations (14) and (15). We also assumed a constant ISM density of $n = 1$ cm^{-3}, a wind parameter with $A_\star = 0.1$, and a kinetic energy four times the γ-ray energy, $E_{k,\mathrm{iso}} = 4 \times E_{\gamma,\mathrm{iso}}$, for this illustrative plot. The range of Γ_0 in each case represents the 1σ error on t_{peak}.

(A color version of this figure is available in the online journal.)

with known redshifts. The range depends on the uncertainty of the measurement of the peak flux time in the LAT (see Figure 14). We assumed $n = 1$ cm^{-3}, $A_\star = 0.1$, and $E_{k,\mathrm{iso}}$ four times larger than the isotropic-equivalent γ-ray energy $E_{\gamma,\mathrm{iso}}$ in the Band or Comptonized (in the case of GRB 100414A) component. The dependence of Γ_0 on the ISM density ($\propto n^{-1/8}$) is rather weak. Thus, the dominant uncertainty of Γ_0 in the ISM environment comes from the peak-flux time. Note that Γ_0 needs to be large in order to explain the delayed onset and peak of the LAT emission as results of the early afterglow. These estimates of Γ_0 are similar to $\Gamma_{\min}$ values calculated from $\gamma\gamma$ pair production opacities for the four brightest LAT bursts (Abdo et al. 2009d; Ackermann et al. 2010b; Abdo et al. 2009a; Ackermann et al. 2011) and are significantly larger than the characteristic value estimated in Ghirlanda et al. (2013), suggesting that *Fermi*-LAT GRBs have exceptionally fast jets. For GRB 110731A, detailed multiwavelength modeling suggests a wind environment. In the case of a wind environment, Γ_0 is usually smaller with a weaker $t_{\mathrm{dec}}^{-1/4}$ dependence.

The temporal variability of >100 MeV emission in GRBs 090902B (Abdo et al. 2009a) and 090926A (Ackermann et al. 2011) argues against a simple forward shock interpretation in the prompt phase, since such variability is characteristic of internal shocks. However, an energy-dependent transition between the prompt and afterglow contributions in the LAT flux is possible.

In the context of the internal shock scenario, the delayed onset of the LAT-detected emission could arise from late internal shocks produced via inverse Compton (IC) scattering with plausible evolution of the microphysical parameters from the early internal shocks (Wang et al. 2006; Bošnjak et al. 2009; Toma et al. 2011). Hadronic emission such as proton/ion synchrotron radiation and/or photopion-induced cascade radiation could also account for this delay based on the time required for proton/ion acceleration and cooling as well as the formation of cascades (Asano et al. 2009; Razzaque et al. 2010; Wang et al. 2006). However, a challenge for the internal shocks scenario is explaining the temporally extended LAT-detected

emission often lasting $\sim 10^2$–10^3 s (see Figure 10) without associated detectable keV– MeV emission.

6.4. Spectral Models of LAT-detected Emission

A PL spectral component that dominates LAT-detected emission has been detected in the brightest LAT bursts: GRBs 080916C, 090510, 090902B, 090926A, and 110731A. This component is in addition to the Band function or the Comptonized model that typically describes the keV–MeV emission. The top panel of Figure 26 shows that this PL component is hard in the prompt phase ($\Gamma_{GBM} \sim -2$), allowing for a high-significance detection. In other bursts it can be softer and consequently not easily detectable. In the "EXT" time window, however, the PL component is hard (Figure 26, bottom panel) without any contamination from the keV–MeV photons. Whether or not the same hard PL component in the prompt phase evolves into the PL in the "EXT" time window is a central issue in GRB science.

Early afterglow models for the temporally extended LAT-detected emission (Kumar & Barniol Duran 2009; Ghisellini et al. 2010; De Pasquale et al. 2010; Razzaque 2010) imply that a PL component from the forward shock that propagates into the external medium surrounding the GRB (Meszaros & Rees 1997; Sari et al. 1998) arises early in the prompt phase when the fireball is still coasting. A high jet bulk Lorentz factor seems to be required in this scenario, as discussed earlier. IC scattering of soft target photons, either synchrotron or photospheric, by relativistic electrons can also produce an additional PL component (Wang et al. 2006; Bošnjak et al. 2009; Ackermann et al. 2010b; Toma et al. 2011). The IC component contributes most significantly in the $\gg 1$ GeV range. Hadronic emission models, either proton/ion synchrotron radiation or photopion-induced cascade radiation, can produce an additional spectral component as well that is able to dominate the LAT-detected emission in the prompt phase (Asano et al. 2009; Razzaque et al. 2010; Wang et al. 2006). However, these models require a much larger total energy budget than the leptonic models, especially if the jet bulk Lorentz factor is high, which seems to be the case for LAT bursts.

Finally, significant cutoffs in the additional PL component have been detected in the time-integrated prompt spectra of GRBs 090926A and 110731A. Electron-positron pair production by high-energy photons with keV–MeV photons is a plausible origin of these multi-GeV cutoffs (Krolik & Pier 1991; Fenimore et al. 1993; Baring & Harding 1997; Lithwick & Sari 2001). The detection of such cutoffs in some future LAT bursts will be helpful in determining the bulk Lorentz factors of the jets, as well as in answering whether $\gamma\gamma$ opacity plays a role in the observed low detection rate of LAT bursts.

6.5. Summary and Conclusions

We have compiled a catalog of all GRBs significantly detected by the *Fermi*-LAT. For each of these bursts, we have examined the spectral and temporal behavior of its high-energy emission. In this ensemble of bursts, we have searched for common patterns in flux behavior in order to obtain an unbiased view of high-energy emission from GRBs. We have also compared the LAT-detected emission with the lower energy emission detected by the GBM for a much greater number of bursts and sought theoretical interpretations of the LAT observations.

In general, LAT bursts are also among the brightest bursts seen by GBM. They are also the most energetic when redshift measurements allow the determination of their total luminosities. There seems to be an emergent class of hyper-fluent LAT GRBs, although our conclusion is only based on four bursts.

A common characteristic of the LAT-detected emission is that it is delayed with respect to the GBM emission. This delay is longer for long bursts, with some indications that the onset time increases with energy. LAT bursts also generally have longer durations in the LAT energy range than in the GBM energy range for the same bursts.

LAT GRBs exhibit a temporally extended phase during which the LAT flux decays following a single or broken PL. The photon index in this phase is also distributed in a relatively narrow range. The index of PL flux decay (the later index in the case of broken PL fits) is typically close to $F_\nu \propto t^{-1}$, with only a few exceptions.

The temporally extended LAT-detected emission is consistent with that expected from afterglow (forward shock) emission from a relativistic blast wave. An adiabatic fireball model is favored over a radiative fireball model by the measured $\propto t^{-1}$ LAT flux-decay behavior in the majority of bursts.

The spectra of LAT GRBs are typically well described by a PL with a fairly narrow distribution of indices, centered at -2.0 although deviations (spectral cutoffs) from a pure PL have been detected in GRBs 090926A and 110731A in the GeV range. Joint GBM-LAT spectral fits require an additional PL component in all bright LAT bursts, indicating that the Band function alone is inadequate to fit the spectra of these bursts.

Several models exist in the literature for the delayed onset of LAT-detected emission and the additional PL component. The early afterglow model for temporally extended LAT-detected emission can explain both the delayed onset and the additional component, but other models involving internal shocks cannot be ruled out. The detection of additional bright LAT bursts will help to characterize and explain cutoffs in the PL spectra, determine the bulk Lorentz factors, and constrain the GRB energetics.

7. TABLES

In the following section, we present the results of our catalog in tabular form. Additionally, we provide all the numbers shown here in an electronic FITS[88] file format.

Table 1 summarizes the intervals in which we performed the time-integrated spectral analysis described in Section 3.5 on page 40.

Table 2 contains the list of LAT-detected GRBs, including the trigger time and position information used as input to our analysis pipeline. The initial position used in the analysis is the best localization available at the time we completed our analysis (2011 August); we note that in few cases, the localization was subsequently improved using Interplanetary Network data (Hurley et al. 2013) and would have reduced the radius for the initial searching window but would not have significantly changed our final results.

Each GRB was detected using the standard likelihood analysis (denoted by "Like=1" in the table) and/or the LLE analysis (denoted using "LLE=1"). We also list the redshift (errors are omitted) and the reference number of the LAT GCN circular, if one was issued. Since the LAT localizations are obtained iteratively, we report only the final localization.

Table 3 shows a comparison between the various duration estimates obtained using the standard LAT data and the LLE

---

[88] http://fits.gsfc.nasa.gov/

analysis. We also report the duration of the bursts as reported in the GBM catalog (Paciesas et al. 2012), indicating whether the burst is classified as short (S) or long (L). The final two columns report the maximum significance of the source in the likelihood analysis (Max TS) and the post-trials detection significance obtained by the LLE analysis.

Likelihood analysis results are summarized in Table 4, where we report the number of events actually detected inside the ROI, the predicted number of events from the source, the detection significance, and the values of the measured photon flux, energy fluence, and isotropic equivalent energy (if a redshift is available) for each interval and for each GRB. For the cases where the significance is below our detection threshold, we report ULs. Three bursts detected by the LLE analysis are included in this table, while the other four bursts (GRBs 090531B, 101014A, 101123A, and 110529A) had too few events to even compute an UL during the "GBM" time interval.

Table 5 shows our best reconstructed direction with associated errors.

The highest energy events associated with each GRB are summarized in Tables 6–8. In these tables, we used different time windows to perform the analysis and we indicate the number of events associated with the GRB, the energy, and the arrival time of the highest energy event. We also report the probability of the event being associated with the GRB, computed as described in Section 3.2.3.

The temporally extended high-energy emission is systematically studied in this paper and the relative quantities are summarized in Table 9. We report the results obtained by fitting the photon flux light curves with simple PLs starting from the position of the peak flux and from the position of the GBM T_{95}. When the statistics allow, we also perform a broken PL fit. Bold letters indicate the parameters that best reproduce the late time decay of the γ-ray flux.

Next, we summarize the results of our joint spectral-fit analyses. In Table 10, we report the spectral model that best fits the data during the "GBM" time interval. Then, we present the entire range of results from the joint-fit spectral analyses as obtained in the "GBM" time interval (Table 11) and in the interval extending from the first detection of a GRB photon by the LAT up to the GBM T_{95} (Table 12). Only bursts detected by the LAT (TS > 20; see Section 3.5) in the "GBM" time interval are included in Table 12. In these two tables, we display the parameters of the main component and the parameters of any additional components required to describe the spectrum. For the cases where more than one component is needed, we compute the energy fluence for each spectral component separately. In Table 13, we report the isotropic equivalent energy in aggregate and also per spectral component for the best-fit spectral model.

Finally, we address the systematic uncertainties of our results by using a different set of data-selection cuts and we compare our standard results obtained with the Pass 6 event selection with the results obtained with the new Pass 7 data selection. This is summarized in Table 14 and described in Appendix A.

APPENDIX A

SYSTEMATIC ERRORS

In this appendix, we report possible sources of systematic uncertainties in our results and how we estimate or ameliorate them.

The most important source of systematic errors arises from potentially inaccurate descriptions of the responses of the GBM and the LAT. The parameterization of the response of the LAT to incident γ-rays is tabulated in IRFs, produced using Monte Carlo simulations and subsequently refined based on in-flight data. Even though the results of these simulations have been verified extensively against flight data and also pre-launch using calibrated sources (Abdo et al. 2009c), any imperfections in the simulation model or in the simulation procedure can propagate in the IRFs, affecting all of our results.

Additionally, any relative calibration errors between the GBM and the LAT and any errors in the description of the response of the GBM can affect the joint spectral fits, manifesting as distortions in the spectral shapes and biases in the measured parameters.

Finally, the results of joint spectral fits also can be affected by the motion of the GRB in the instruments' FoVs, which creates variations in their responses over time. These effects are minimized by producing response matrices that accurately describe the response of the instruments at any instant of the observation (see Section 3.4).

Another source of systematic uncertainty is the background estimates. For Transient-class events, background estimation is performed using a procedure that has an estimated systematic uncertainty of 10%–15% and negligible statistical errors (as described in Section 3.1.1). For LLE and GBM data, the backgrounds are estimated using interpolations of the event rate before and after the burst, the uncertainty of which primarily arises from limited statistics and is estimated to be ∼10% for LLE and less for the GBM data. For observations involving large variations in an instrument's pointing (e.g., in ARRs) or observations of locations near the Earth's limb, the systematic errors can increase possibly up to the magnitude of the statistical errors. Any misestimates of the LAT backgrounds can affect the final results, especially those for longer time scales such as duration estimates. The maximum likelihood analyses are not particularly sensitive to errors in the background estimates since the background level is a loosely constrained parameter in the fitting; thus, any systematic errors are partially "fit out."

In order to evaluate the impact of the above uncertainties on the maximum likelihood analysis results, we repeated the analysis using different sets of cuts. The magnitude of the difference between the results obtained with these alternative

Table 14
Systematic Uncertainties

		A: CATALOG	B: Pass7	$\frac{A-B}{\sqrt{\sigma_A^2+\sigma_B^2}}$	C: DIFF	$\frac{A-C}{\sqrt{\sigma_A^2+\sigma_C^2}}$	D: DIFF-F	$\frac{A-D}{\sqrt{\sigma_A^2+\sigma_D^2}}$	E: DIFF-B	$\frac{A-E}{\sqrt{\sigma_A^2+\sigma_E^2}}$
080825C	Flux ($\times 10^{-5}$ m^{-2} s^{-1})	20 ± 10	27 ± 10	-0.5	<20	...	<70	...	...	...
	Spectral idx	-3.3 ± 0.7	-3.1 ± 0.6	-0.2	...	...	...	...	...	...
	Temporal idx	...	...	...	...	...	...	...	...	...
	Loc. err. (deg.)	0.77	0.85	-0.08	0.77	0.01	0.85	-0.08	1.65	-0.87
080916C	Flux ($\times 10^{-5}$ m^{-2} s^{-1})	82 ± 7	84 ± 7	-0.2	100 ± 10	-1.5	100 ± 20	-0.8	90 ± 20	-0.4
	Spectral idx	-2.13 ± 0.08	-2.21 ± 0.08	0.7	-2.2 ± 0.1	0.5	-2.2 ± 0.2	0.3	-2.2 ± 0.1	0.5
	Temporal idx	1.8 ± 0.3	1.26 ± 0.07	1.8	1.28 ± 0.08	1.7	1.4 ± 0.1	1.3	1.3 ± 0.1	1.6
	Loc. err. (deg.)	0.07	0.07	-0.00	0.07	-0.00	0.10	-0.03	0.08	-0.01
081006	Flux ($\times 10^{-5}$ m^{-2} s^{-1})	24 ± 9	20 ± 8	0.3	30 ± 20	-0.3	40 ± 30	-0.5	<50	...
	Spectral idx	-2.4 ± 0.5	-2.2 ± 0.4	-0.3	-3.2 ± 0.9	0.8	-2.7 ± 0.8	0.3	...	...
	Temporal idx	...	...	...	...	...	...	...	...	...
	Loc. err. (deg.)	0.51	0.44	0.08	0.49	0.03	0.53	-0.02	0.62	-0.10
081024B	Flux ($\times 10^{-5}$ m^{-2} s^{-1})	260 ± 100	190 ± 80	0.5	200 ± 200	0.3	500 ± 300	-0.8	...	...
	Spectral idx	-2.0 ± 0.4	-1.8 ± 0.3	-0.4	-2.5 ± 0.7	0.6	-2.5 ± 0.7	0.6	...	...
	Temporal idx	...	...	...	...	...	...	...	...	...
	Loc. err. (deg.)	0.29	0.21	0.07	0.32	-0.03	0.29	-0.00	1.65	-1.36
090217	Flux ($\times 10^{-5}$ m^{-2} s^{-1})	11 ± 3	13 ± 3	-0.5	10 ± 5	0.2	20 ± 10	-0.9	<10	...
	Spectral idx	-2.5 ± 0.4	-2.5 ± 0.3	0.0	-2.4 ± 0.4	-0.2	-2.6 ± 0.5	0.2	...	...
	Temporal idx	...	1.1 ± 0.2	-1.1	...	...	...	...	...	...
	Loc. err. (deg.)	0.35	0.32	0.03	0.31	0.04	0.39	-0.04	0.80	-0.44
090227B	Flux ($\times 10^{-5}$ m^{-2} s^{-1})	500 ± 300	500 ± 300	0.0	<2000	...	...	...	<2000	...
	Spectral idx	-3 ± 1	-2.8 ± 0.8	-0.2	...	...	...	...	...	...
	Temporal idx	...	...	...	...	...	...	...	...	...
	Loc. err. (deg.)	...	...	...	...	...	...	...	...	...
090323	Flux ($\times 10^{-5}$ m^{-2} s^{-1})	6 ± 2	4 ± 1	0.9	<6	...	<6	...	<9	...
	Spectral idx	-3.1 ± 0.5	-2.8 ± 0.5	-0.4	-2.7 ± 0.6	-0.5	...	...	...	...
	Temporal idx	0.9 ± 0.3	0.8 ± 0.1	0.3	0.8 ± 0.2	0.3	...	...	...	...
	Loc. err. (deg.)	0.10	0.10	-0.00	0.10	0.00	0.08	0.02	0.30	-0.20
090510	Flux ($\times 10^{-5}$ m^{-2} s^{-1})	1800 ± 300	2000 ± 300	-0.5	2100 ± 500	-0.5	2200 ± 700	-0.5	2000 ± 700	-0.3
	Spectral idx	-1.7 ± 0.1	-1.8 ± 0.1	0.7	-1.8 ± 0.2	0.4	-1.8 ± 0.2	0.4	-1.9 ± 0.2	0.9
	Temporal idx	1.1 ± 0.1	1.29 ± 0.09	-1.4	1.3 ± 0.1	-1.4	1.42 ± 0.08	-2.5	1.9 ± 0.2	-3.6
	Loc. err. (deg.)	0.04	0.04	0.00	0.06	-0.02	0.07	-0.02	0.12	-0.08
090720B	Flux ($\times 10^{-5}$ m^{-2} s^{-1})	10 ± 10	30 ± 10	-1.4	<60	...	<100	...	...	...
	Spectral idx	-1.7 ± 0.5	-2.1 ± 0.5	0.6	...	...	...	...	...	...
	Temporal idx	...	...	...	...	...	...	...	...	...
	Loc. err. (deg.)	0.33	0.30	0.04	1.02	-0.69	1.02	-0.69	...	0.33
090902B	Flux ($\times 10^{-5}$ m^{-2} s^{-1})	260 ± 20	280 ± 20	-0.7	220 ± 30	1.1	220 ± 40	0.9	220 ± 40	0.9
	Spectral idx	-1.96 ± 0.07	-1.93 ± 0.06	-0.3	-2.0 ± 0.1	0.3	-1.9 ± 0.1	-0.5	-2.0 ± 0.1	0.3
	Temporal idx	1.4 ± 0.1	1.1 ± 0.1	2.1	1.4 ± 0.1	0.0	1.1 ± 0.2	1.3	1.37 ± 0.09	0.2
	Loc. err. (deg.)	0.04	0.06	-0.02	0.04	0.00	0.04	-0.00	0.11	-0.08
090926A	Flux ($\times 10^{-5}$ m^{-2} s^{-1})	350 ± 30	390 ± 30	-0.9	400 ± 50	-0.9	420 ± 90	-0.7	380 ± 70	-0.4
	Spectral idx	-2.29 ± 0.09	-2.36 ± 0.09	0.5	-2.4 ± 0.1	0.8	-2.6 ± 0.2	1.4	-2.3 ± 0.2	0.0
	Temporal idx	1.1 ± 0.1	1.2 ± 0.2	-0.4	1.4 ± 0.1	-2.1	1.4 ± 0.1	-2.1	1.2 ± 0.2	-0.4
	Loc. err. (deg.)	0.04	0.04	0.00	0.04	-0.00	0.04	-0.00	0.20	-0.15
091003	Flux ($\times 10^{-5}$ m^{-2} s^{-1})	6 ± 3	6 ± 3	0.0	6 ± 3	0.0	9 ± 6	-0.4	<20	...
	Spectral idx	-2.0 ± 0.4	-2.0 ± 0.4	0.0	-1.8 ± 0.4	-0.4	-2.0 ± 0.5	0.0	...	...
	Temporal idx	1.0 ± 0.2	0.8 ± 0.2	0.7	0.9 ± 0.2	0.4	...	...	...	...
	Loc. err. (deg.)	0.15	0.15	0.00	0.15	0.00	0.15	-0.00	0.55	-0.40
091208B	Flux ($\times 10^{-5}$ m^{-2} s^{-1})	9 ± 5	<20	...	<30	...	...	...	<50	...
	Spectral idx	-1.9 ± 0.5	...	...	...	...	...	...	...	...
	Temporal idx	...	...	...	...	...	...	...	...	...
	Loc. err. (deg.)	0.88	...	0.88	...	0.88	...	0.88	...	0.88
100116A	Flux ($\times 10^{-5}$ m^{-2} s^{-1})	8 ± 4	<10	...	<10	...	<20	...	...	...
	Spectral idx	-2.9 ± 0.7	...	...	...	...	...	...	...	...
	Temporal idx	...	...	...	...	...	...	...	...	...
	Loc. err. (deg.)	0.17	0.18	-0.02	0.06	0.10	0.04	0.12	1.21	-1.05
100325A	Flux ($\times 10^{-5}$ m^{-2} s^{-1})	11 ± 6	10 ± 5	0.1	14 ± 9	-0.3	<40	...	<60	...
	Spectral idx	-1.9 ± 0.4	-2.0 ± 0.5	0.2	-2.0 ± 0.5	0.2	...	...	...	...
	Temporal idx	...	...	...	...	...	...	...	...	...
	Loc. err. (deg.)	0.60	0.54	0.06	0.61	-0.02	0.67	-0.07	0.73	-0.13
100414A	Flux ($\times 10^{-5}$ m^{-2} s^{-1})	40 ± 20	40 ± 20	0.0	<80	...	...	...	<100	...
	Spectral idx	-2.7 ± 0.6	-2.9 ± 0.6	0.2	...	...	...	...	...	...
	Temporal idx	1.1 ± 0.4	1.4 ± 0.4	-0.5	1.2 ± 0.7	-0.1	...	...	...	...
	Loc. err. (deg.)	0.12	0.12	0.00	0.12	0.00	0.13	-0.01	0.28	-0.17

Table 14
(Continued)

	A: CATALOG	B: Pass7	$\frac{A-B}{\sqrt{\sigma_A^2+\sigma_B^2}}$	C: DIFF	$\frac{A-C}{\sqrt{\sigma_A^2+\sigma_C^2}}$	D: DIFF-F	$\frac{A-D}{\sqrt{\sigma_A^2+\sigma_D^2}}$	E: DIFF-B	$\frac{A-E}{\sqrt{\sigma_A^2+\sigma_E^2}}$
100620A Flux ($\times 10^{-5}$ m^{-2} s^{-1})	<5	<6	...	<6	...	<10	...	...	...
Spectral idx	-2.5 ± 0.6	-2.5 ± 0.6	0.0	-4 ± 1	1.3	-4 ± 1	1.3	...	...
Temporal idx	...	...	...	...	...	...	...	...	...
Loc. err. (deg.)	0.71	0.72	-0.01	0.80	-0.09	1.00	-0.28	...	0.71
100724B Flux ($\times 10^{-5}$ m^{-2} s^{-1})	10 ± 2	9 ± 2	0.4	<4	...	<8	...	<4	...
Spectral idx	-5.0 ± 0.9	-5.3 ± 1.0	0.2	...	...	...	...	...	...
Temporal idx	...	0.9 ± 0.1	-0.9	...	...	...	...	...	...
Loc. err. (deg.)	1.03	1.19	-0.17	1.56	-0.54	1.50	-0.48	...	1.03
110120A Flux ($\times 10^{-5}$ m^{-2} s^{-1})	<8	<6	...	<9	...	<10	...	<9	...
Spectral idx	-2.4 ± 0.6	...	...	...	...	...	...	...	...
Temporal idx	...	...	...	...	...	...	...	...	...
Loc. err. (deg.)	0.35	0.27	0.08	0.24	0.11	0.24	0.11	...	0.35
110709A Flux ($\times 10^{-5}$ m^{-2} s^{-1})	11 ± 5	11 ± 4	0.0	<8	...	<20	...	<10	...
Spectral idx	-3.9 ± 0.9	-2.7 ± 0.6	-1.1	...	...	...	...	...	...
Temporal idx	...	...	...	...	...	...	...	...	...
Loc. err. (deg.)	1.39	0.60	0.79	...	1.39	...	1.39	...	1.39
110721A Flux ($\times 10^{-5}$ m^{-2} s^{-1})	21 ± 5	22 ± 5	-0.1	30 ± 10	-0.8	<20	...	40 ± 20	-0.9
Spectral idx	-2.5 ± 0.3	-2.2 ± 0.2	-0.8	-2.9 ± 0.5	0.7	...	...	-2.9 ± 0.6	0.6
Temporal idx	...	1.00 ± 0.10	-1.0	...	...	...	...	...	...
Loc. err. (deg.)	0.53	0.11	0.41	0.56	-0.03	0.91	-0.38	0.72	-0.20
110731A Flux ($\times 10^{-5}$ m^{-2} s^{-1})	110 ± 20	100 ± 20	0.4	100 ± 20	0.4	70 ± 30	1.1	130 ± 40	-0.4
Spectral idx	-2.6 ± 0.2	-2.5 ± 0.2	-0.4	-2.4 ± 0.3	-0.6	-2.5 ± 0.5	-0.2	-2.4 ± 0.3	-0.6
Temporal idx	1.5 ± 0.2	1.1 ± 0.2	1.4	2.3 ± 0.3	-2.2	1.8 ± 0.3	-0.8	...	...
Loc. err. (deg.)	0.19	0.48	-0.29	0.11	0.08	0.12	0.08	0.42	-0.22

datasets and the standard one can be used as an order-of-magnitude estimate of the systematic uncertainties in our (standard) results.

First, we repeated the maximum-likelihood analysis using Diffuse-class events ("Pass 6 V7 Diffuse Class"), adopting the standard isotropic template available at the FSSC web site[89] as a representation of the non-rejected charged particle background. Because the Diffuse class has significantly less background contamination than the Transient class, any uncertainties in the background estimates are minimal. Thus, a comparison against this set of results can reveal the uncertainties arising from any inaccuracy in the background estimates for our standard set of results. Furthermore, because the two analyses employ different sets of IRFs, this test is also sensitive to systematics of the IRFs in general.

We continued by splitting the Diffuse-class data sample into two independent datasets depending on which portion of the tracker each event was converted from (front versus back). Events produced by photons converting in the first 12 layers of the tracker ("front") suffer on average fewer multiple scatterings than those converting at the next 4 layers of the tracker ("back") since the front layers have thinner converter foils (see Section 1 for a description of the instrument). The decreased magnitude of multiple scattering for front-converting events provides significantly better angular resolution. In addition, the front-converting events have a significantly smaller fraction of their energy measured by the calorimeter than back-converting events, which results in lower energy (<few GeV) front-converting events being reconstructed with a worse energy resolution than back-converting events. A comparison against this sample can be sensitive to systematics of the IRFs associated with the particular properties of front- versus back-converted events.

Finally, we repeated the analysis using a more recent iteration of the set of event selection cuts for the LAT data, specifically the "Pass 7 Transient V6" selection, which benefits from more robust and accurate classification algorithms and increased refinement using flight data. Again, a comparison of our results from this dataset can reveal differences affecting any parts of the IRFs.

We refer to the standard configuration as "CATALOG," to the Diffuse class as "DIFF," to the front and back as "DIFF:F" and "DIFF:B," respectively, and to the "Pass 7 Transient V6" as "Pass7." Table 14 summarizes the results of the above tests, quoting for each analysis the photon flux, the spectral index, the index of the temporal-decay PL along with their statistical errors, and the estimated localization error. We also report the absolute difference between the CATALOG and each of the test configurations. In Figure 33, we compare the results between the Pass7 and CATALOG results. The quantities compared (clockwise from top left) are the LAT T_{90}, the fluence in the 100 MeV–10 GeV energy range during the "LAT" time interval, the index of the PL temporal decay, and the photon index of the emission detected by the LAT. As can be seen, there are no discernible differences within the errors.

We also estimated the error in the localizations obtained with the LAT. For 13 of the GRBs localized by the LAT, a *Swift* XRT position is also available. For those cases, we calculated the quantity $\rho = \delta/\epsilon$, which is the ratio between the angular separation (δ) between the LAT and the XRT position over the estimated LAT 1σ localization error ϵ. In Figure 34, we plot the cumulative distribution of the number of GRBs against ρ. The number of GRBs in this sample is very limited and thus we cannot draw any firm conclusions, but we note that, as expected, the 68% quantile of the distribution is consistent with the 68% (1σ) estimated error.

To estimate the effects arising from relative miscalibrations between the GBM and the LAT in the joint-spectral fit results,

[89] fermi.gsfc.nasa.gov/ssc/data/access/lat/BackgroundModels.html
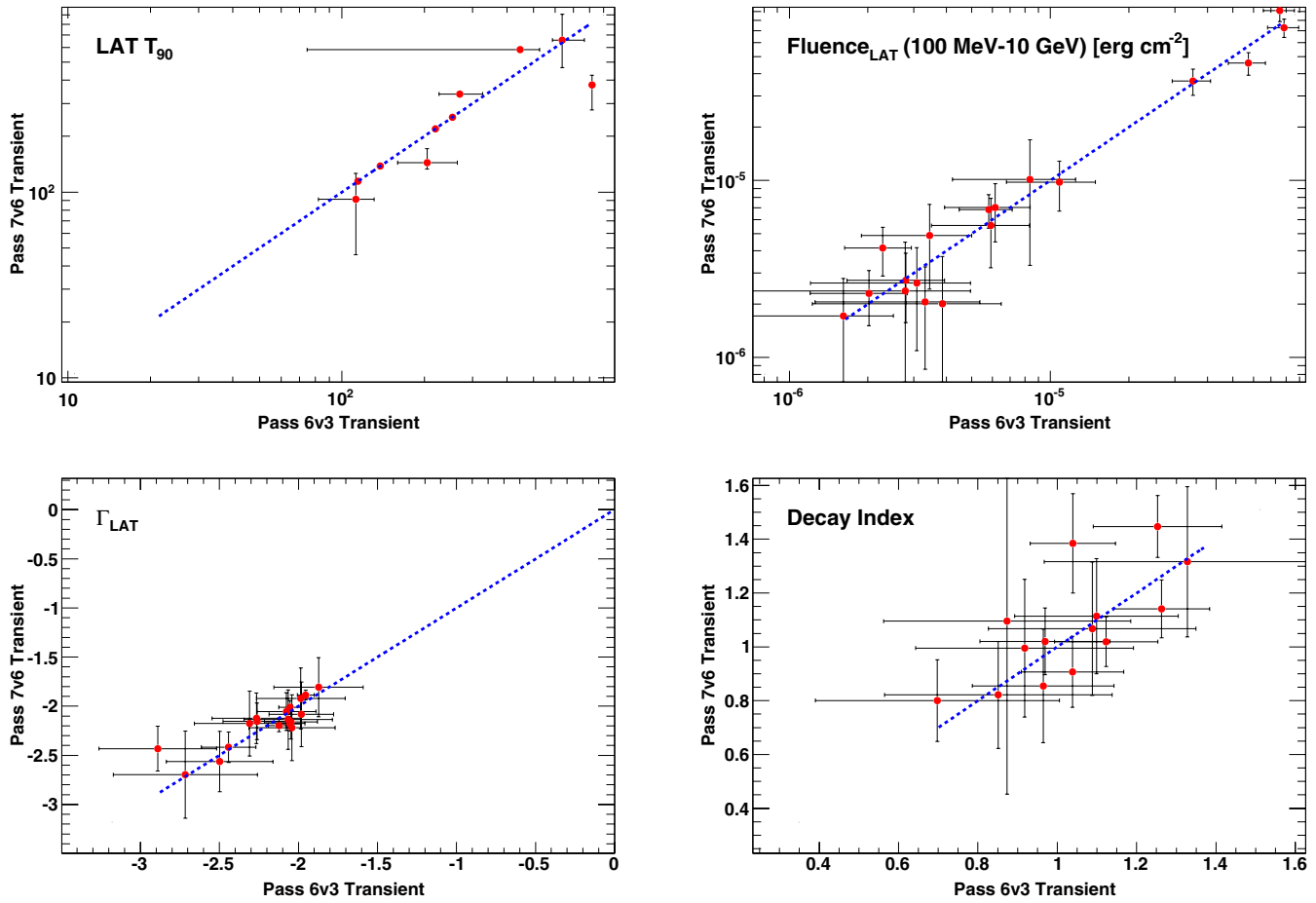
Figure 33. Comparison between our standard results produced with the "Pass6 V3 Transient" set of cuts vs. the results obtained with the more recent "Pass7 V6 Transient" set of cuts. Clockwise from top left: LAT T_{90}, fluence in the 100 MeV–10 GeV energy range during the "LAT" time interval, index of the PL temporal decay, and photon index of the emission detected by the LAT.

(A color version of this figure is available in the online journal.)
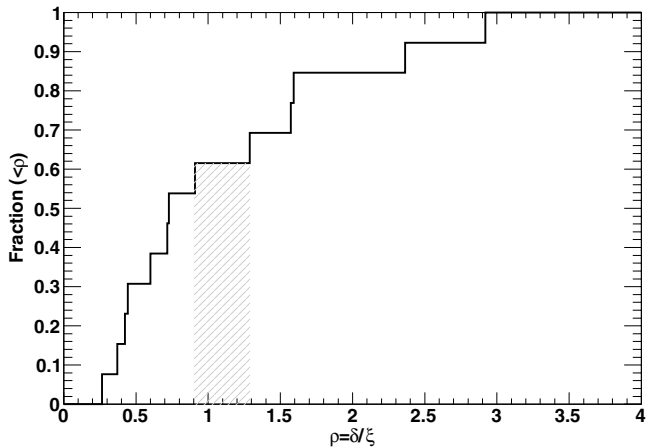
Figure 34. Cumulative distribution of the number of GRBs (with good X-ray localizations) over some ρ, defined as the ratio between the angular separation of the best LAT localization and the X-ray position over the 1σ statistical error of the LAT localization. The vertical dashed area below the curve highlights the range where the cumulative distribution reaches the 68% level.

we introduced a flux normalization factor for each detector, letting all but one such factor be free to vary during the fit. This is basically equivalent to a rigid effective area correction across the entire bandpass of each instrument, relative to one detector chosen as a reference (we chose the LAT). This

procedure could give spurious results if the model used for the fit contains localized features or components, which is not the case for the models we used. We introduced these factors for the brightest GRBs of our sample: GRBs 080916C, 090323, 090328, 090510, 090902B, 090926A, 100724B, 100826A, 100414A, and 110731A. For all other GRBs, the factors were effectively unconstrained by the fit because the inter-calibration systematic errors were small compared with the statistical errors or because the systematic errors were dominated by other components. The resulting correction was less than 5% for the NaI detectors and less than 15% for the BGO detectors. According to these initial tests, the relative inter-calibration uncertainties are important only in the case of bright GRBs, for which statistical errors are small.

We also tested our GBM background estimation procedure. We first considered real spectra from time intervals well outside any GRB emission. For each of these intervals $I_{\rm fake}$, the actually observed spectrum was compared with the spectrum predicted by a background model obtained from the fit of two intervals surrounding $I_{\rm fake}$, obtained with the procedure described in Section 3.1.2. We selected a couple of GRBs and we defined different background models by selecting different time intervals around the GRB times. These validation studies showed that the procedure has, under normal circumstances, a systematic error of $\sim$3%, which we have added to all of our predicted background spectra.
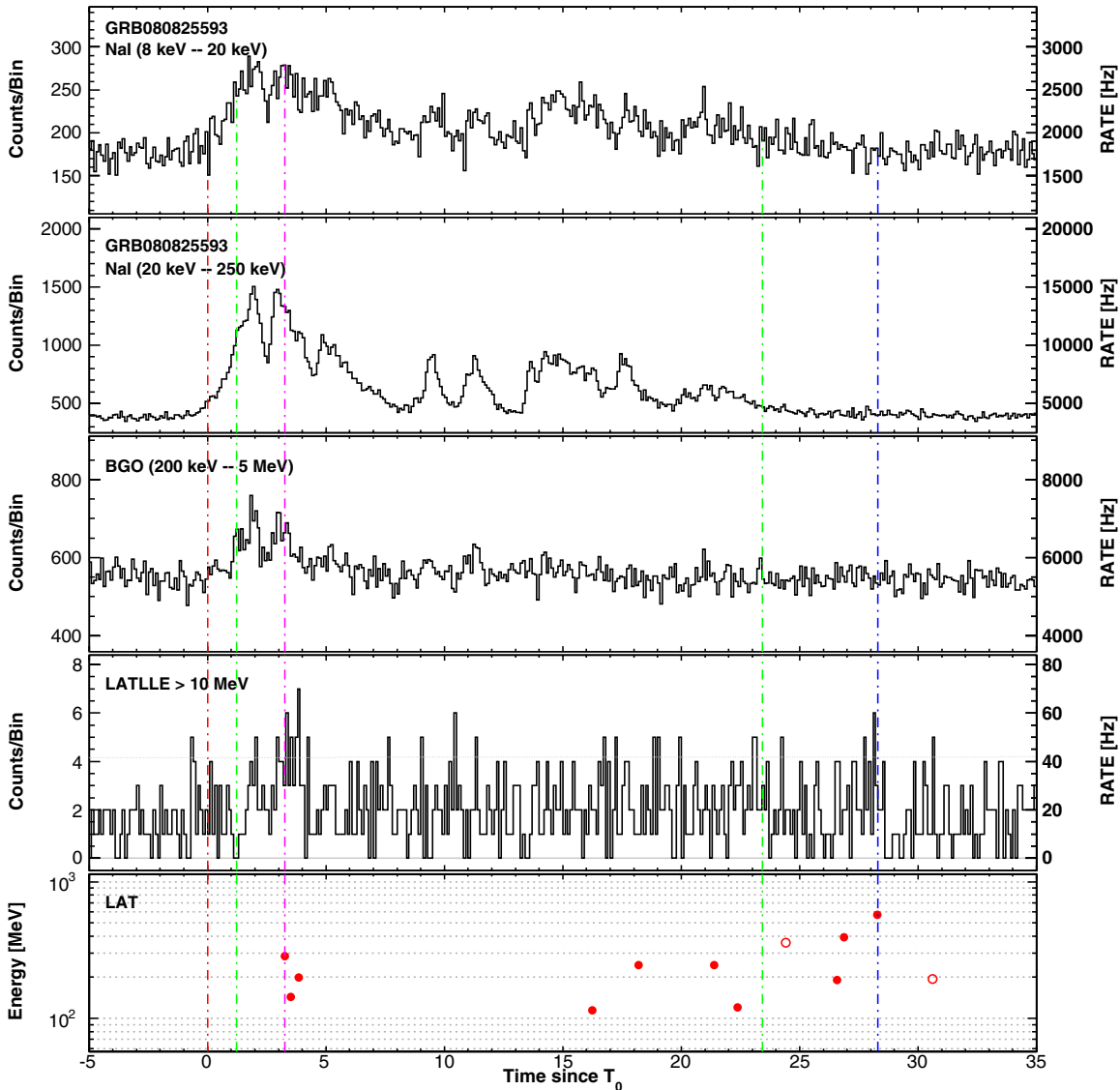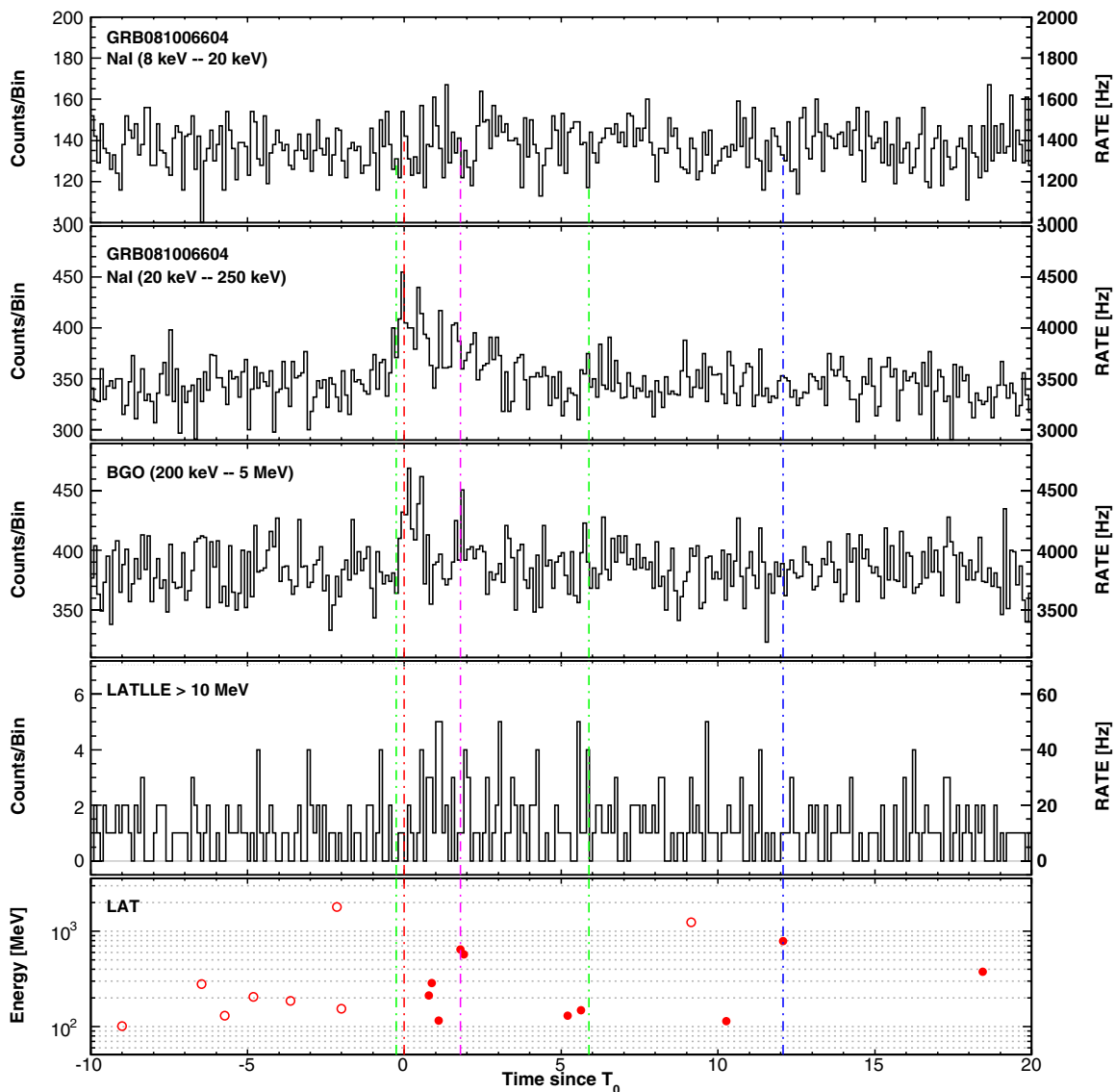
Figure 35. Composite light curve for GRB 080825C: summed GBM/NaI detectors (first two panels), GBM/BGO (third panel), LLE (fourth panel), and LAT Transient-class events above 100 MeV within a 12° ROI (bottom panel). See Appendix B.1 for more information on the lines and symbols in the LAT panels.

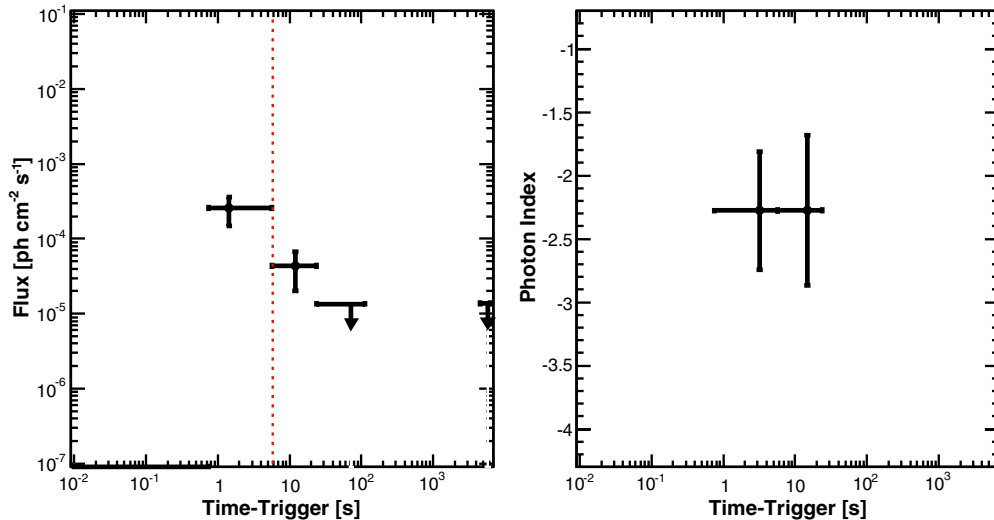(A color version of this figure is available in the online journal.)

APPENDIX B

FERMI LAT GAMMA-RAY BURSTS

In this appendix, we give detailed information on individual LAT-detected GRBs. We summarize the information previously published in refereed papers and GCN circulars. We also include figures showing the GBM/LAT composite light curves as well as, when possible, the results of the LAT time-resolved spectral analyses.

B.1. Conventions and Styles for Figures

Each composite light curve consists of either 4 or 5 panels, showing the emission (in counts) recorded by the GBM NaI detectors (the first two panels from the top) and the GBM BGO detector (third panel), the LAT within the LLE event selection (fourth panel) and, if any, the selected LAT Transient-class events above 100 MeV (bottom panel).

1. The GBM NaI light curves were obtained by summing all the NaI detectors (typically 2 or 3) for which the

GRB position was within 50° from the detector normal pointing axis. We also selected the BGO detector that faces the burst. We used GBM TTE data and selected the channels corresponding to the energy ranges of 8–20 keV and 20–250 keV for the NaI detectors and 0.2–5 MeV for the BGO detector.

2. The LLE light curve corresponds to the selection cuts discussed in Section 2.1.1, which were applied to LAT events with energies above 10 MeV. As the γ-ray signal in the LAT is proportional to the LAT effective area, it depends strongly on the GRB off-axis angle θ (and spectrum) at any time. In order to reflect the amplitude of this modulation, the gray curve displayed in the LLE panel shows the $\cos[\theta(t)]$ function (ranging from 0 to 1 over the full extent of the panel).

3. In the last light curve, we selected the LAT Transient-class events in a 12° ROI that have a reconstructed energy above 100 MeV. We represent, as filled circles, the events that also have a probability >0.9 of being associated with the GRB (see Section 3.2.3).
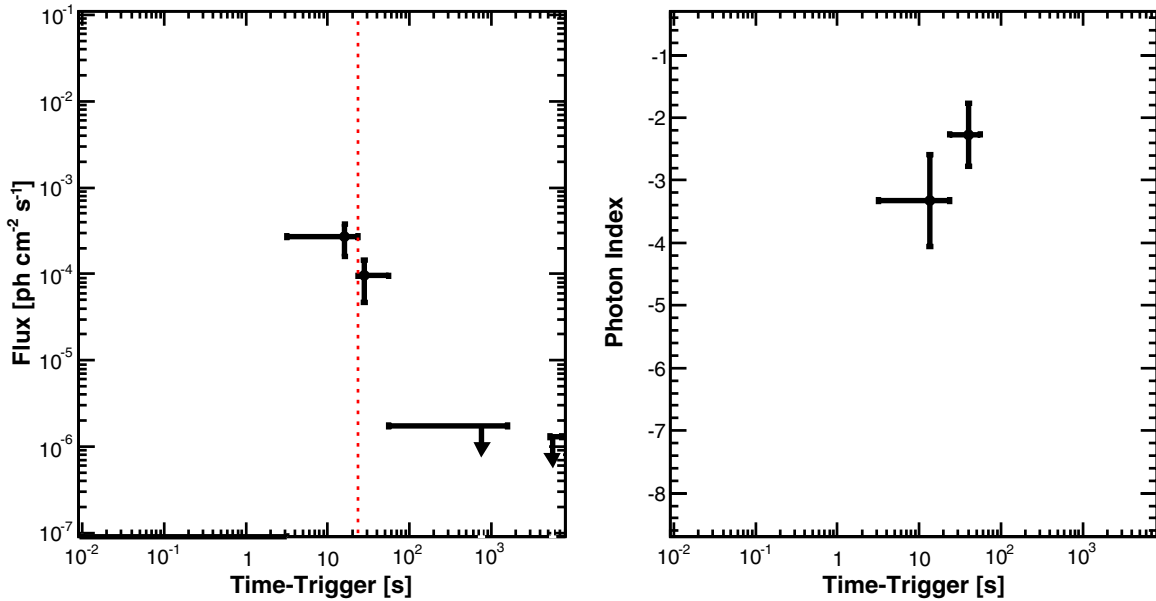
Figure 36. Likelihood light curve for GRB 080825C (flux above 100 MeV on the left, photon index on the right). See Appendix B.1 for more information on lines and symbols.

(A color version of this figure is available in the online journal.)

4. In each panel, vertical dashed lines indicate the GBM trigger time (in red, at $T = 0$), the GBM T_{05}, and the GBM T_{95} (both in green). Other lines indicate the time of the LAT highest energy event associated with the GRB within the GBM T_{90} (in magenta, from Table 6) and during the LAT emission (in blue, from Table 8). If the two events are identical, then only the blue line is displayed.

When possible, we add a figure for the >100 MeV flux light curve, showing how the temporally extended emission develops and then decays as a function of time $F(t)$.

1. The GBM T_{95} is indicated by a vertical red dashed line.
2. For each time bin where the GRB was significantly detected (i.e., TS > 16; see step 2 in Section 3.5), we also show the value of the photon index (we use here the convention $N(E) \propto E^{\beta}$, where N is the fitted photon flux and β is typically negative).
3. For the bins with no detection, we fixed the PL index to $\beta = -2.0$ and then report the value of the flux UL.
4. When the statistics are sufficient, we give the decay indices from the fit $F(t) \propto t^{-\alpha}$ of a PL (starting from the latest time between the peak flux time t_p and the time of the GBM T_{95}) and a broken PL (starting from t_p). If a significant break is found in the latter fit, the broken PL is displayed as a filled gray line and the PL is shown as a dashed gray line. The line styles are reversed in the opposite case.

In two cases (GRBs 090323 and 090328) where the ARR maneuver caused a particularly bright increase of the background during the GBM prompt emission, we also show the LLE light curve and the relative background estimation.

B.2. GRB 080825C

The long GRB 080825C triggered the GBM flight software at $T_0 = 14:13:48$ UT on 2008 August 25 (trigger 241366429; van der Horst & Connaughton 2008). Although this faint burst had an off-axis angle of 60°.3 at the trigger time, where the effective area is a factor ~ 3 less than on-axis, the LAT detected it significantly

and the LAT preliminary localization was delivered via GCN (Bouvier et al. 2008) with a statistical error of 0°.95. A detailed analysis was published by the *Fermi*-LAT collaboration in Abdo et al. (2009e). The composite light curve (Figure 35) shows a multi-peak structure in the GBM signal, while the number of counts is not large enough at high energy to study the temporal profile in detail. The LAT emission, especially above 100 MeV, seems to coincide with the second bright pulse in the GBM. The high-energy emission is also clearly visible at later times and the highest energy event (0.57 GeV) is detected at $T_0+28.29$ s, i.e., after the end of the GBM emission. However, as the temporally extended, high-energy emission is faint, the LAT time-resolved likelihood analysis returned a significant flux in two time bins only (Figure 36).

Note that an LLE light curve of GRB 080825C was reported in the paper on GRB 090217 published by the *Fermi*-LAT collaboration (Ackermann et al. 2010a), which indicated a $\sim 5\sigma$ signal after integration over the first ~ 4 s, slowly increasing to $\sim 9\sigma$ after ~ 30 s. We could not confirm this signal excess in LLE data as our analysis is based on a different detection algorithm, which is not tuned to slowly accumulating signals. This algorithm is mostly sensitive to short variability time scales as it looks for the highest significant excess among all considered time bins in the LLE light curve (see Section 3.3.1). A 3.2σ post-trial significance (4.2σ pre-trial) was found, thus no LLE results are reported for this burst in the catalog.

B.3. GRB 080916C

The long, bright GRB 080916C triggered the GBM at $T_0 = 00:12:46$ UT on 2008 September 16 (trigger 243216766; Goldstein & van der Horst 2008). This burst would have been bright enough to trigger an ARR of the *Fermi* spacecraft, but the repointing capability of the spacecraft was enabled only a few weeks later, on 2008 October 8. GRB 080916C was easily detected by the LAT, which delivered a localization via GCN (Tajima et al. 2008) with a statistical error of 0°.09. It had an off-axis angle of 48°.8 at the trigger time and it exited the FoV of the LAT after ~ 3000 s. *Swift* TOO observations
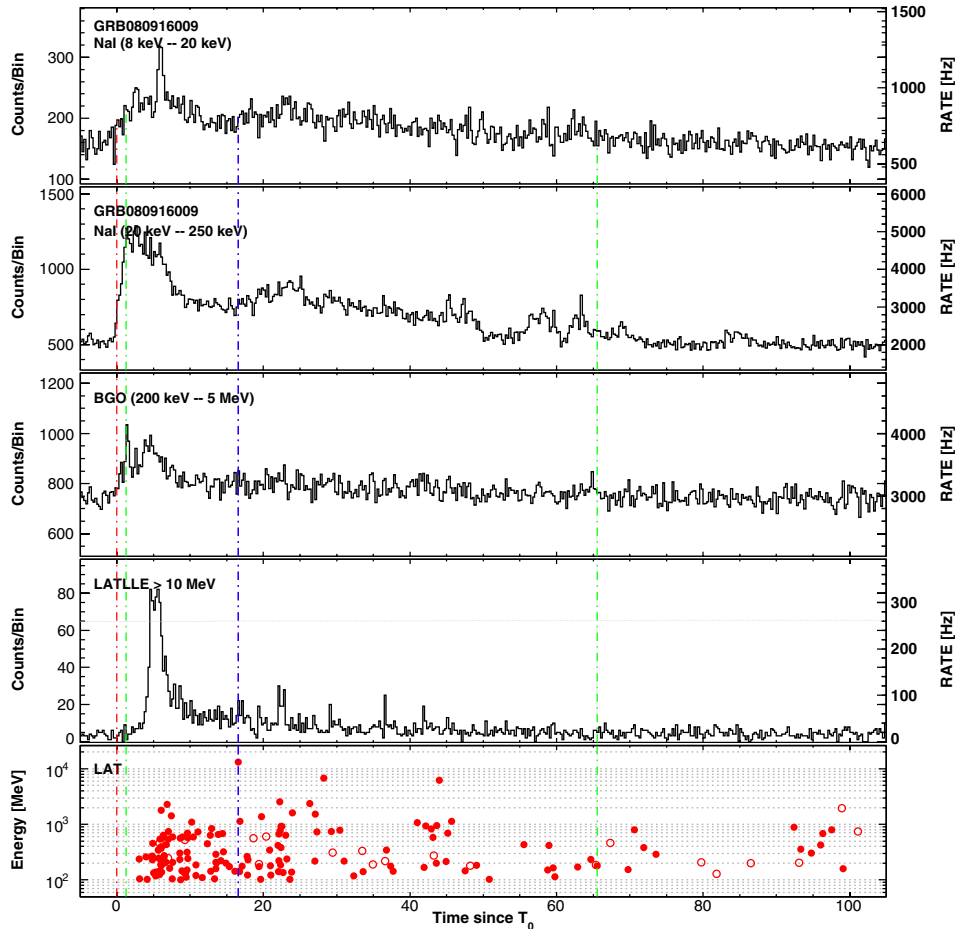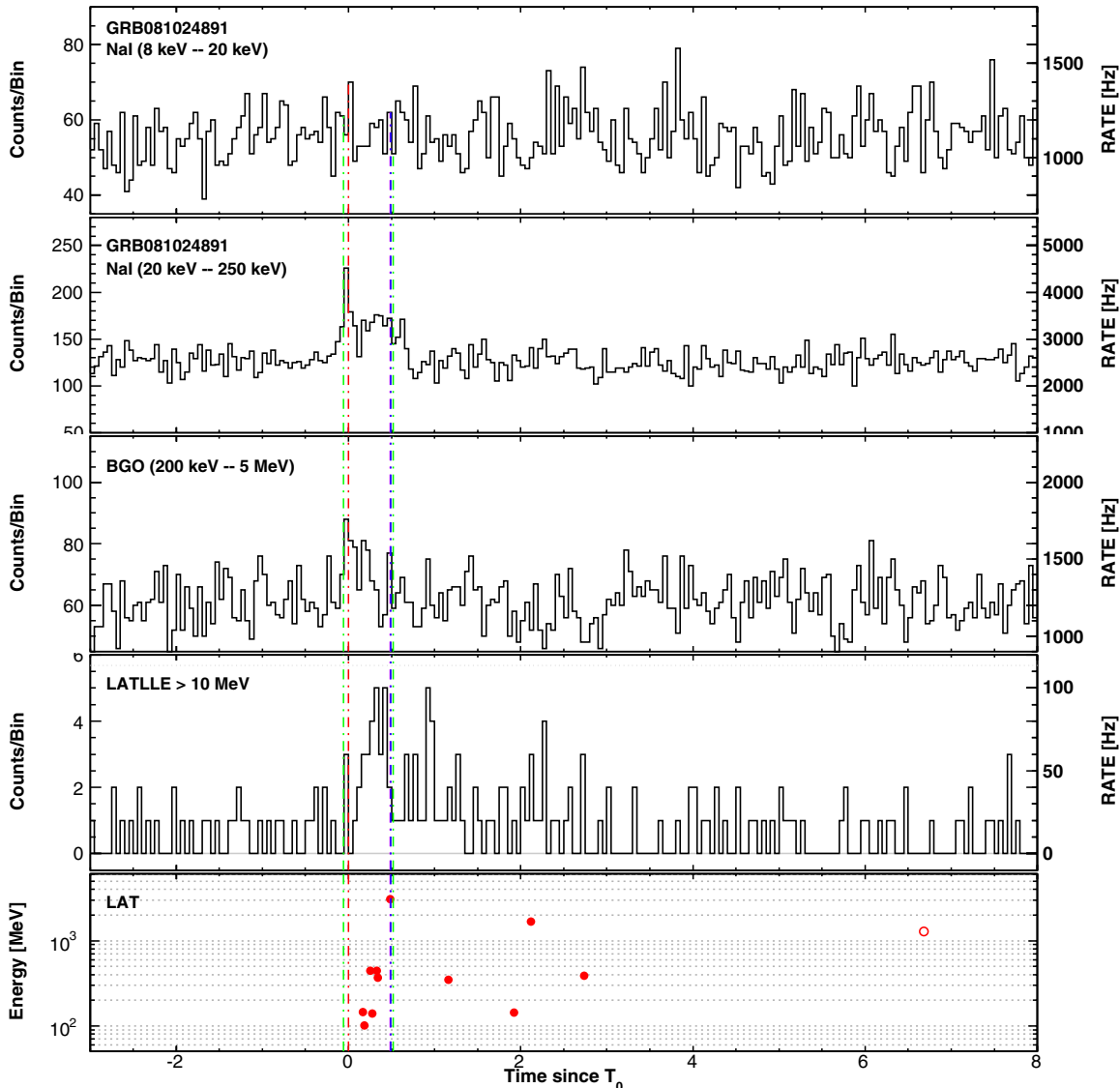
Figure 37. Composite light curve for GRB 080916C: summed GBM/NaI detectors (first two panels), GBM/BGO (third panel), LLE (fourth panel), and LAT Transient-class events above 100 MeV within a 12° ROI (bottom panel). See Appendix B.1 for more information on lines and symbols in the LAT panels.
(A color version of this figure is available in the online journal.)

started ~17 hr after the trigger time (Stratta et al. 2008). A possible X-ray counterpart was found by *Swift*-XRT 3.1 arcmin away from the LAT position (Kennea 2008) and further observations confirmed the existence of a fading source (Perri et al. 2008). Follow-up observations with the Gamma-Ray Burst Optical/Near-infrared Detector (GROND) yielded a high photometric redshift of $z = 4.35 \pm 0.15$ (Greiner et al. 2009) which, combined with its brightness, makes GRB 080916C the most energetic burst ever detected, with an isotropic equivalent energy $E_{iso} \simeq 6.5 \times 10^{54}$ erg (1 keV–10 GeV, within the GBM T_{90}).

The LAT emission peaked ~5 s after the trigger time, coinciding with the second GBM bright pulse (Figure 37). Approximately 180 Transient-class events are recorded above 100 MeV within the LAT $T_{90} \sim 210$ s, including many GeV events. The highest energy event (13.22 GeV), which is detected at $T_0+16.54$ s, does not coincide with any noticeable feature in the GBM light curve. In the first paper published by the *Fermi*-LAT collaboration (Abdo et al. 2009d), the prompt emission spectrum of GRB 080916C was fit over six decades in energy by the empirical Band function. This previous analysis also searched for possible deviations from the Band function and did not provide any evidence for a deficit or a signal excess at the highest energies in the LAT. In particular, the significance for an additional PL component was found to be small, ~2σ. We repeated the analysis and found that an additional PL is actually required (4–5σ; see Section 4.4.1). It is worth stressing the

improvements that have been brought to the analysis procedure since the first post-launch GRB studies and which support this new result. First of all, we now use the Background Estimator tool (see Section 3.1.1), which provides a much more accurate description of the backgrounds in the spectral fits. In addition, we benefit from a better calibration of both the GBM and the LAT instruments. Finally, we base our assessment of the significance of any new spectral feature on dedicated and extended Monte Carlo simulations. These improvements, along with a new choice of the time intervals (based on our estimates for the durations of the emission in the GBM and the LAT), as well as a different spectral shape, also explain the differences in our results (Tables 11 and 12) with respect to the original publication.

The high-energy emission of GRB 080916C lasts much longer than the GBM estimated duration. The LAT time-resolved likelihood analysis resulted in a well sampled light curve of the high-energy flux up to ~560 s (Figure 38). Its first point suggests that the spectrum is significantly softer than the LAT emission at later times, where the photon index fluctuates consistently around $\beta = -2$. The decay of the flux as a function of time follows a simple PL starting from the GBM T_{95}, with a decay index $\alpha = 1.78 \pm 0.33$.

This steep decay is similar to the first part of the decay observed in GRBs 090510, 090902B, and 090926A (Table 9), for which a significant break was found in the flux light curve. This suggests that GRB 080916C was observed during the
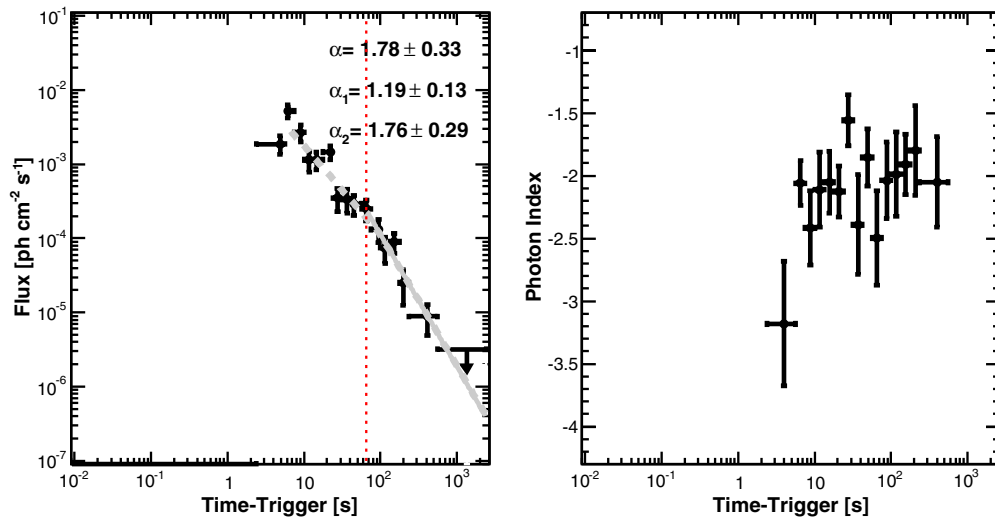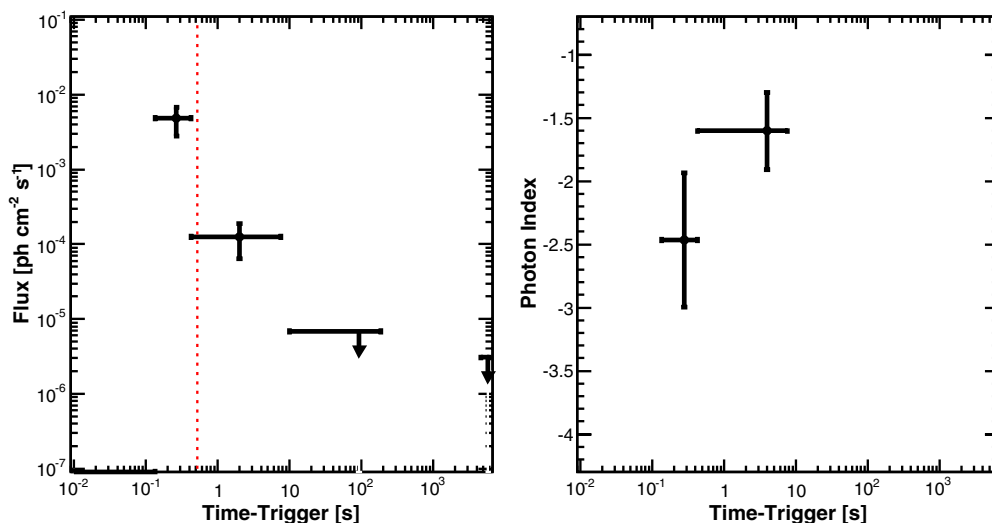
Figure 38. Likelihood light curve for GRB 080916C (flux above 100 MeV on the left, photon index on the right). See Appendix B.1 for more information on lines and symbols.

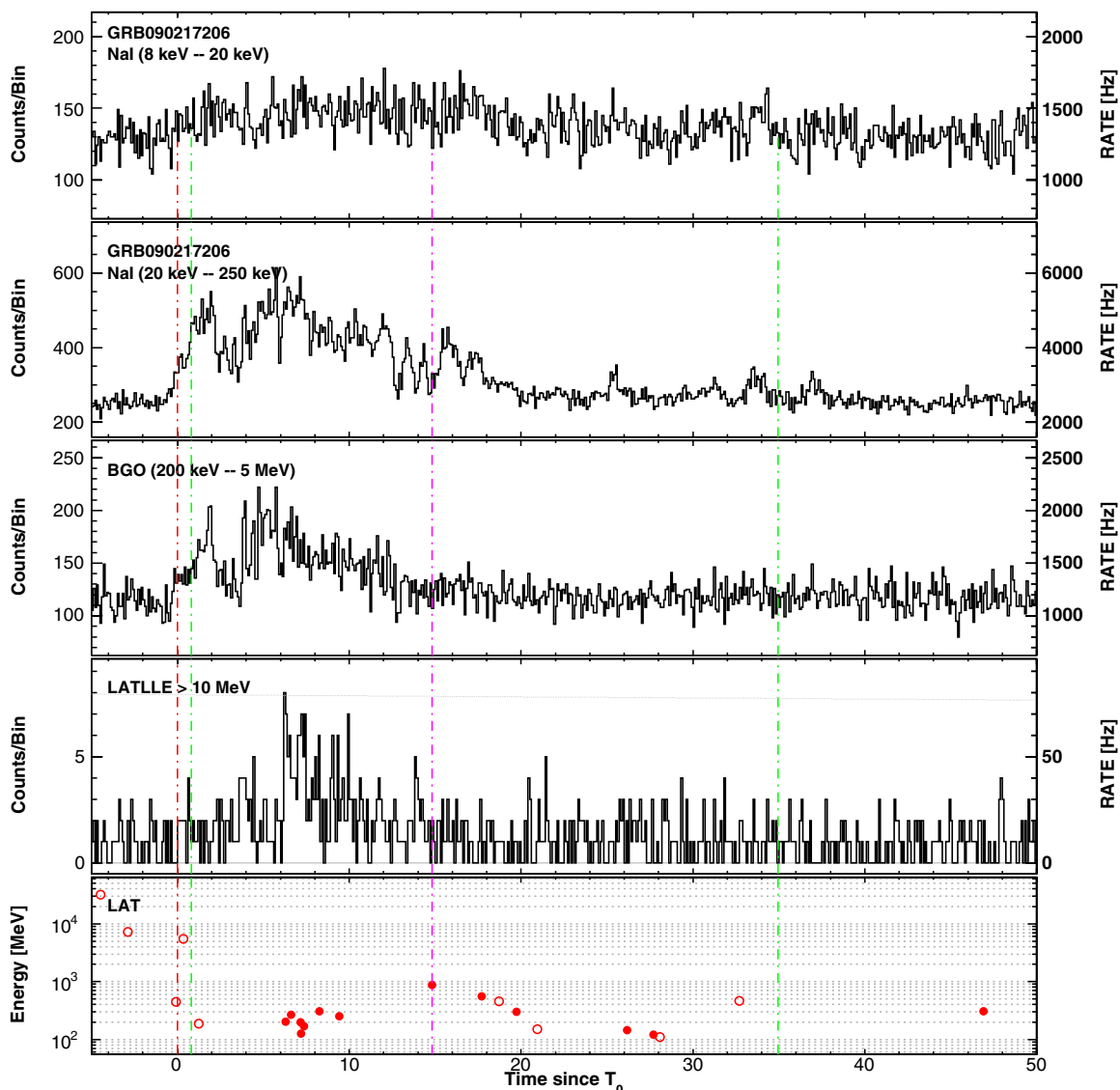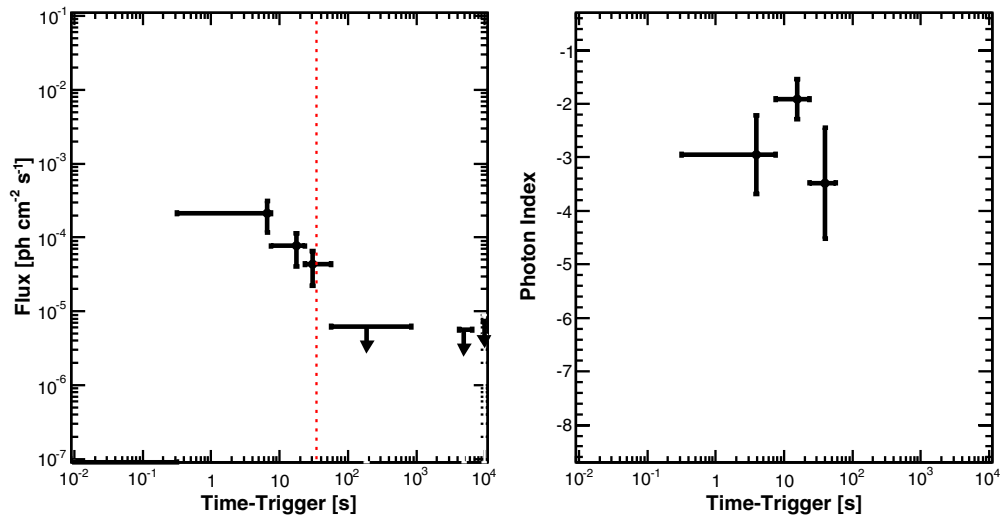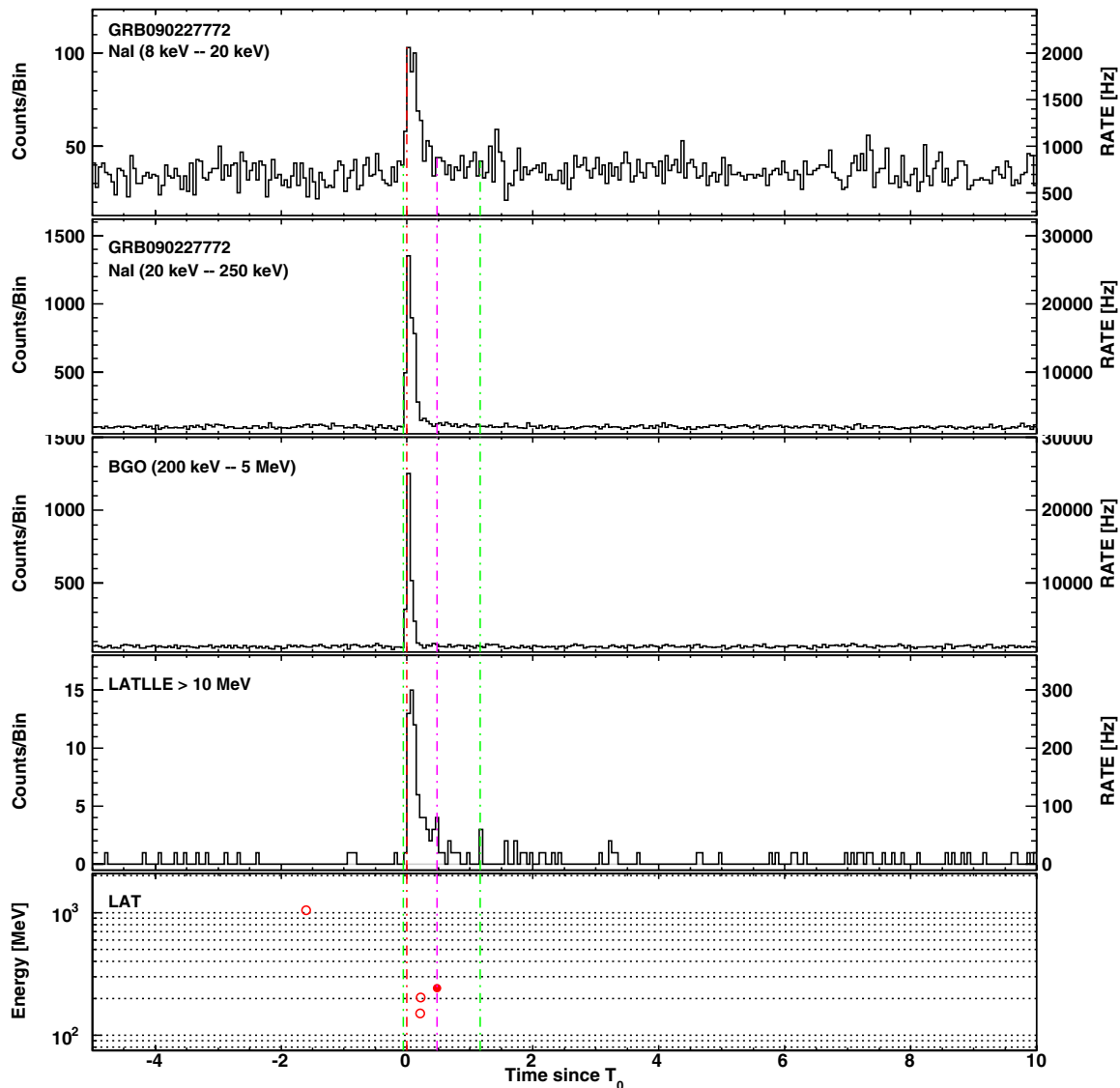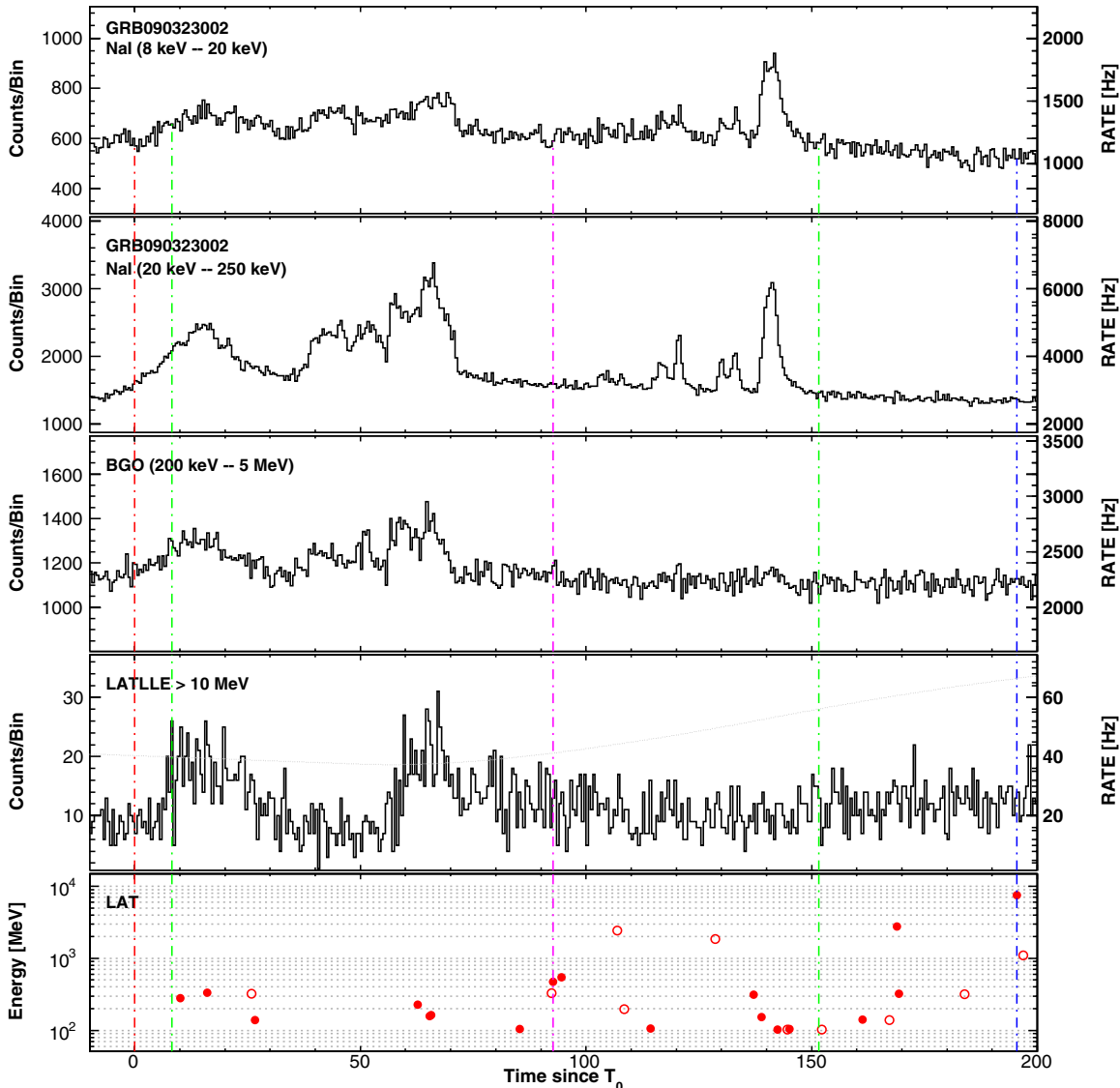(A color version of this figure is available in the online journal.)

Figure 39. Composite light curve for GRB 081006: summed GBM/NaI detectors (first two panels), GBM/BGO (third panel), LLE (fourth panel), and LAT Transient-class events above 100 MeV within a 12° ROI (bottom panel). See Appendix B.1 for more information on lines and symbols in the LAT panels.

(A color version of this figure is available in the online journal.)

49

Figure 40. Likelihood light curve for GRB 081006 (flux above 100 MeV on the left, photon index on the right). See Appendix B.1 for more information on lines and symbols.

(A color version of this figure is available in the online journal.)

transition from the prompt phase to the afterglow phase, as discussed in Section 6.2.

B.4. GRB 081006

The long GRB 081006 triggered the GBM at $T_0 = $ 14:29:34 UT on 2008 October 6 (trigger 244996175; van der Horst 2008). It was a faint burst, both in the GBM and in the LAT (despite an initial off-axis angle of 11°). No significant emission was detected in the LLE light curve (Figure 39) despite a 2.7σ fluctuation observed shortly after the trigger time. More interestingly, this burst was detected and localized by the LAT likelihood analysis using Transient-class events above 100 MeV, with a maximum TS $\sim$ 72 (see Table 4). Taking into account uncertainties in the calculation of the LAT T_{90}, the high-energy emission could be simultaneous with the low-energy emission (i.e., happening on very similar time scales) or it could last much longer as a significant signal excess is detected above the estimated background up to $\sim T_0 + 115$ s. This time corresponds to the entrance of the LAT in the SAA and was thus reported as a lower limit to the duration in Table 3. In spite of this hint of temporally extended high-energy emission, the LAT likelihood analysis did not find any significant signal in the "EXT" time interval and could not provide good time-resolved spectral measurements (Figure 40).

B.5. GRB 081024B

GRB 081024B triggered the GBM at $T_0 = $ 21:22:41 UT on 2008 October 24 (trigger 246576161; Connaughton & Briggs 2008) and it was the first LAT detection of a short burst. The LAT preliminary localization was delivered via GCN (Omodei 2008), with a statistical error of 0°.16. Follow-up observations by *Swift* and ground-based telescopes did not find any conclusive evidence for an afterglow counterpart (Guidorzi et al. 2008). Historically, GRB 081024B represents the first clear detection of temporally extended emission from a short GRB at GeV energies (Abdo et al. 2010b; Corsi et al. 2010). Whereas the low-energy emission observed by the GBM lasts $\sim$0.5 s, the high-energy emission is visible up to $\sim$3 s after the trigger time (Figure 41). The highest energy event (3.07 GeV) is detected at $T_0 + 0.49$ s, i.e., very close in time to the end of the GBM

emission. A LAT T_{90} could not be derived due to the small number of Transient-class events above 100 MeV, however the LLE duration ($\sim$2.3 s) indicates a significantly longer duration of the LAT emission at energies of tens of MeV. Due to the low photon statistics, the LAT likelihood analysis did not find any significant signal in the "EXT" interval and could not provide good time-resolved spectral measurements (Figure 42).

B.6. GRB 090217

The long GRB 090217 triggered the GBM at $T_0 = $ 04:56:42.56 UT on 2009 February 17 (trigger 256539404; von Kienlin 2009a). The LAT preliminary localization was delivered via GCN (Ohno et al. 2009b), with a statistical error of 0°.36. A detailed analysis was published by the *Fermi*-LAT collaboration in Ackermann et al. (2010a). No X-ray counterpart was found in *Swift* TOO observations of the LAT preliminary localization that covered only the center of the LAT error circle (Godet 2009) and therefore no redshift is available for this burst. GRB 090217 is a bright burst both in LLE and in LAT Transient-class data above 100 MeV. The LLE light curve shows a series of pulses coincident with the GBM emission (Figure 43). The highest energy event (0.87 GeV) during this prompt emission is detected at $T_0 + 14.83$ s and is not associated with any noticeable structure of the GBM light curve. The LAT $T_{95} = 68^{+109}_{-40}$ s is not accurate enough to conclude if the high-energy emission extends later than the low-energy emission (GBM $T_{95} \sim 35$ s). The off-axis angle of GRB 090217 remained below 60° until $T_0 + 500$ s, but no additional signal was found and ULs are reported up to 10 ks (Figure 44).

B.7. GRB 090227B

The short GRB 090227B triggered the GBM at $T_0 = $ 18:31:01.41 UT on 2009 February 27 (trigger 257452263; Guiriec 2009a). It is one of the brightest short GRBs observed with GBM and time-resolved spectroscopy at timescales as short as 2 ms was performed by Guiriec et al. (2010), revealing a significant deviation from a Band function and suggesting the presence of an extra PL at both low and high energies. GRB 090227B had an initial off-axis angle of 71° from the LAT boresight and the ARR triggered by the GBM brought it down to $\sim$20°
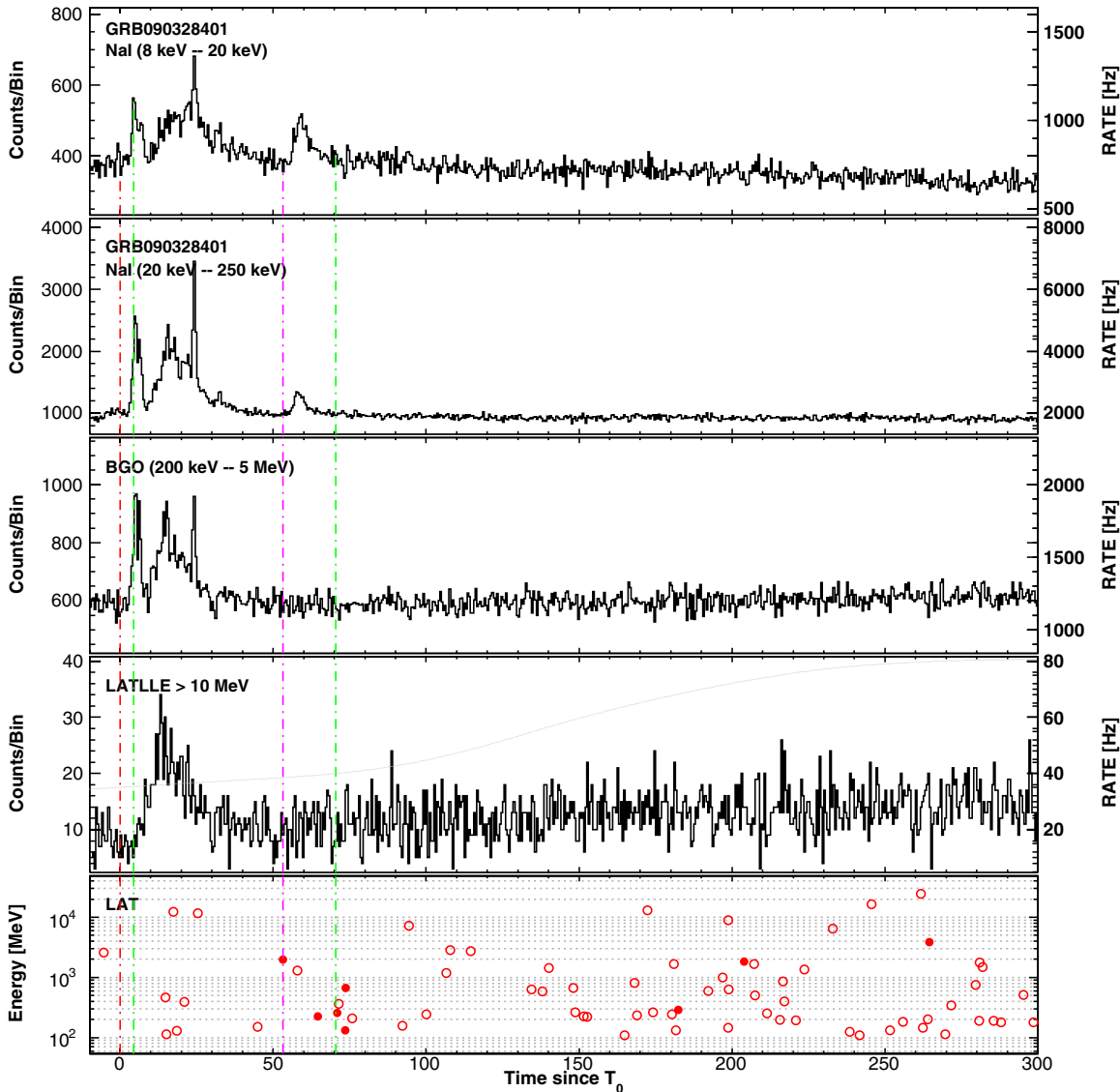
Figure 41. Composite light curve for GRB 081024B: summed GBM/NaI detectors (first two panels), GBM/BGO (third panel), LLE (fourth panel), and LAT Transient-class events above 100 MeV within a 12° ROI (bottom panel). See Appendix B.1 for more information on lines and symbols in the LAT panels.

(A color version of this figure is available in the online journal.)

after ~300 s. The triangulation of the burst by the Interplanetary Network (IPN) provided a position with a 3σ error box area of 1.5 deg^2 (Golenetskii et al. 2009), which we used in our analysis. The GBM light curve of GRB 090227B consists of one single episode that was also significantly detected in the LLE data, with a comparable duration (Figure 45). A TS $\sim$ 30 was obtained by the LAT likelihood analysis based on the three Transient-class events recorded above 100 MeV during the GBM time window, thus the burst is included in the catalog. However, due to the position of the burst in the LAT FoV during the main emission, no LAT T_{90} could be derived due to the paucity of events. We also could not improve on the IPN localization as no reliable TS map could be obtained. For the same reason, no time-resolved likelihood analysis could be performed with the LAT.

B.8. GRB 090323

The long, bright GRB 090323 triggered the GBM at $T_0 =$ 00:02:42.63 UT on 2009 March 23 (trigger 259459364; Ohno et al. 2009a). It had an initial off-axis angle of 57°.2, where

the LAT effective area is low, but it triggered an ARR of the *Fermi* spacecraft that allowed the LAT to detect its late-emission phase and to localize it with a statistical error of 0°.09 (Ohno et al. 2009a). Specifically, GRB 090323 was detected by the LAT on-ground ASP, which searches for LAT counterparts to known GRBs. *Swift* TOO observations started ~19.5 hr after the trigger time. A possible X-ray counterpart was found by *Swift*-XRT 1.9 arcmin away from the LAT position (Kennea et al. 2009a) and further observations confirmed the existence of a fading source (Perri & Stratta 2009). Follow-up observations of the X-ray afterglow with GROND in 7 bands started ~27 hr after the trigger time, providing a preliminary photometric redshift of $z = 4.0 \pm 0.3$ (Updike et al. 2009c). Chornock et al. (2009) reported a spectroscopic redshift of $z =$ 3.57 based on observations of the optical afterglow using the Gemini Multi-Object Spectrograph (GMOS) mounted on the Gemini South Telescope. Combined with its brightness, this makes GRB 090323 the second most energetic LAT-detected burst after GRB 080916C, with an isotropic equivalent energy $E_{iso} \simeq 4.1 \times 10^{54}$ erg (1 keV–10 GeV, within the GBM T_{90}). The
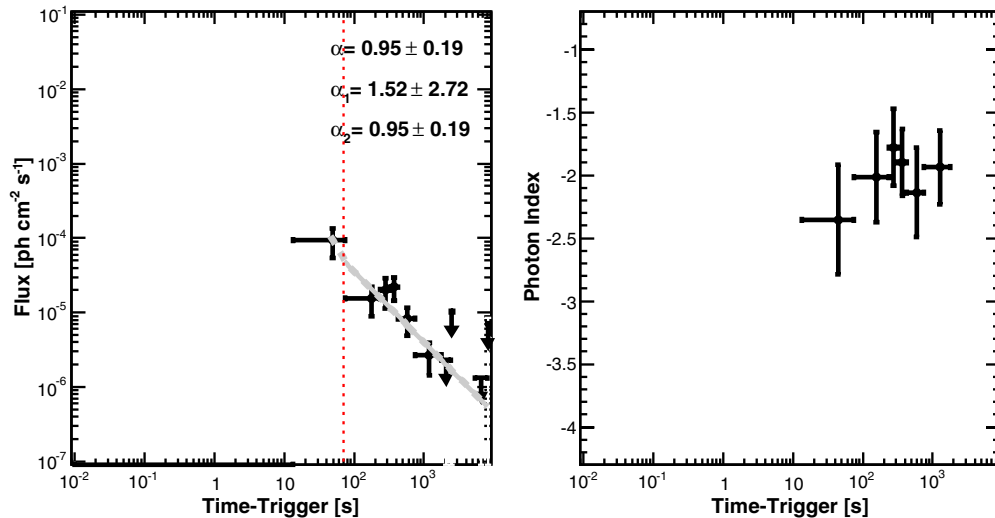
Figure 42. Likelihood light curve for GRB 081024B (flux above 100 MeV on the left, photon index on the right). See Appendix B.1 for more information on lines and symbols.

(A color version of this figure is available in the online journal.)

Figure 43. Composite light curve for GRB 090217: summed GBM/NaI detectors (first two panels), GBM/BGO (third panel), LLE (fourth panel), and LAT Transient-class events above 100 MeV within a 12° ROI (bottom panel). See Appendix B.1 for more information on lines and symbols in the LAT panels.

(A color version of this figure is available in the online journal.)

Figure 44. Likelihood light curve for GRB 090217 (flux above 100 MeV on the left, photon index on the right). See Appendix B.1 for more information on lines and symbols.

(A color version of this figure is available in the online journal.)

Figure 45. Composite light curve for GRB 090227B: summed GBM/NaI detectors (first two panels), GBM/BGO (third panel), LLE (fourth panel), and LAT Transient-class events above 100 MeV within a 12° ROI (bottom panel). See Appendix B.1 for more information on lines and symbols in the LAT panels.

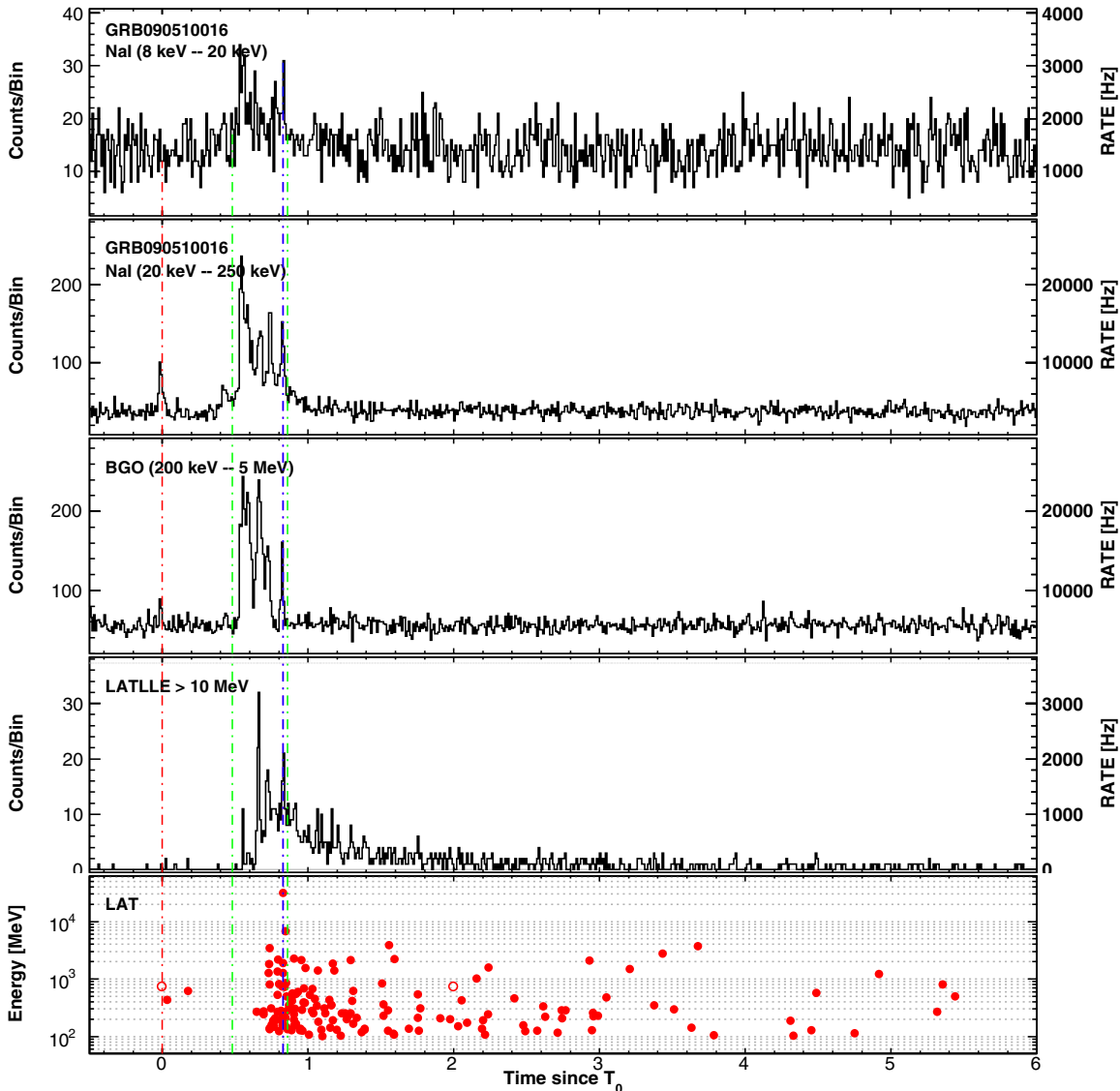(A color version of this figure is available in the online journal.)

Figure 46. Composite light curve for GRB 090323: summed GBM/NaI detectors (first two panels), GBM/BGO (third panel), LLE (fourth panel), and LAT Transient-class events above 100 MeV within a 12° ROI (bottom panel). See Appendix B.1 for more information on lines and symbols in the LAT panels.

(A color version of this figure is available in the online journal.)

burst was also detected in the radio band (Harrison et al. 2009; van der Horst 2009). A dedicated analysis of the near-infrared (NIR) and optical follow-up observations of GRB 090323 is presented in McBreen et al. (2010).

The GBM light curve of GRB 090323 consists of several pulses and lasts ∼150 s (Figure 46). The LLE light curve shows two bright long pulses that somehow coincide with two broad pulses observed in the GBM light curve. The ARR caused the GBM and LAT orientations to change very rapidly with time, requiring a careful evaluation of the instruments' responses and backgrounds as the spacecraft is slewing. In particular, the burst zenith angle increased from $67°$ at T_0 to $84°$ at T_0+300 s, causing a rise in the LAT count rate due to the entrance of the Earth's limb in the instrument's FoV. As illustrated in Figure 47, the analysis of LLE data accounts for this effect, following the background estimation method discussed in Section 3.1. In the LAT likelihood analysis, we reduced the contamination from the Earth's limb by simply rejecting the time intervals in which the burst zenith angle was larger than $105°$. Indications of long-lasting, high-energy emission are seen in the LAT

Transient-class data where multi-GeV events were recorded well after the GBM emission, similar to the 7.50 GeV event detected at $T_0+195.42$ s. The LAT $T_{95} = 294^{+55}_{-25}$ s confirms the temporal extension of the high-energy emission and the LAT time-resolved likelihood analysis returned a significant signal up to T_0+422 s, with a temporal decay index $\alpha = 0.85 \pm 0.29$ (Figure 48). GRB 090323 became occulted after ∼570 s and, in the next orbit, the spacecraft entered the SAA only ∼50 s after the burst exited occultation, thus only ULs are reported at later times, up to ∼10 ks.

B.9. GRB 090328

The long, bright GRB 090328 triggered the GBM at $T_0 =$ 09:36:46 UT on 2009 March 28 (trigger 259925808; McEnery et al. 2009b). GRB 090328 had an initial off-axis angle of $64°6$ in the LAT and the ARR triggered by the GBM brought it down to ∼10° after ∼300 s. The LAT preliminary localization was delivered via GCN (McEnery et al. 2009b), with a statistical error of $0°11$. *Swift* TOO observations started ∼16 hr after the
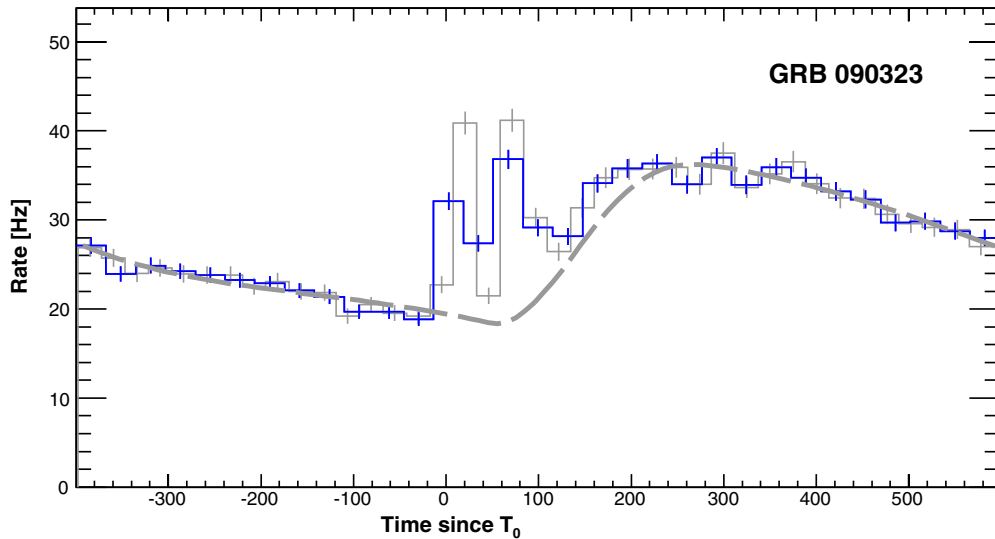
Figure 47. Background estimation in the LLE light curve of GRB 090323. Gray and blue histograms are the count rates in the LAT detector for two different time binnings. The dashed gray line is the best-fit background.

(A color version of this figure is available in the online journal.)
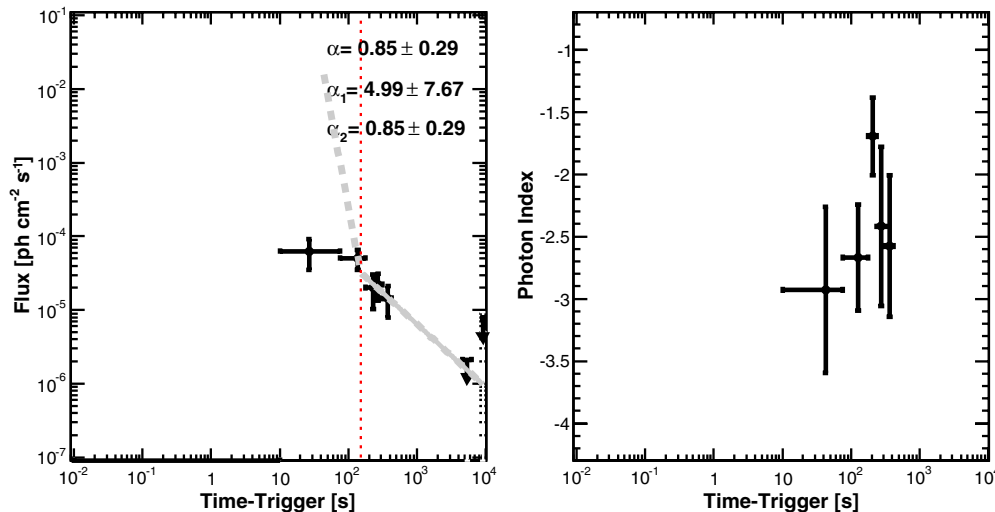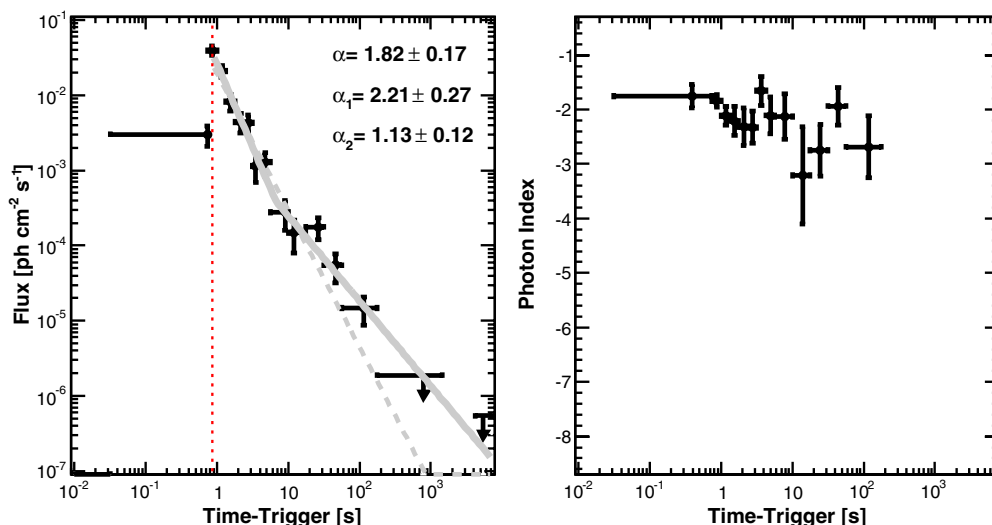

Figure 48. Likelihood light curve for GRB 090323 (flux above 100 MeV on the left, photon index on the right). See Appendix B.1 for more information on lines and symbols.

(A color version of this figure is available in the online journal.)

trigger time (Marshall et al. 2009). A possible X-ray counterpart was found by *Swift*-XRT ∼10 arcmin away from the LAT position (Kennea 2009) and further observations confirmed the existence of a fading source (Rowlinson & Page 2009). Observations of a candidate optical afterglow were also reported by Kennea et al. (2009b) and Oates (2009). More observations of the afterglow were conducted in the optical (Allen et al. 2009), in the optical/NIR with GROND (Updike et al. 2009a), and in the radio band (Frail et al. 2009). Cenko et al. (2009) reported a spectroscopic redshift of $z = 0.736$ based on observations of the optical afterglow using GMOS stated previously. A dedicated analysis of the NIR and optical follow-up observations of GRB 090328 is presented in McBreen et al. (2010).

The GBM light curve of GRB 090328 consists of several pulses and lasts ∼70 s (Figure 49). The LLE light curve shows one single, long bright pulse that coincides with the second broad pulse observed in the GBM light curve. In addition, the first narrow spike in the GBM light curve has no LLE

counterpart, indicating an initially soft spectrum. The ARR caused an increase in the background rate in the LLE light curve as the burst off-axis angle was decreasing (third panel of Figure 49). Figure 50 shows the results of the background estimation in the analysis of LLE data.

In the preliminary analysis of LAT data, Cutini et al. (2009) reported that GRB 090328 high-energy emission lasted until ∼900 s post trigger. Our analysis of the LAT Transient-class data above 100 MeV provided a LAT $T_{95} = 653^{+134}_{-45}$ s, which confirms the temporal extension of the burst emission in the LAT. We could also confirm that the highest energy events detected by the LAT, which are spatially coincident with the burst position, arrived hundreds of seconds after the trigger time. Multi-GeV events were recorded well after the GBM emission, in particular two 3.83 GeV and 5.32 GeV events detected at $T_0+264.42$ s and $T_0+697.80$ s, respectively. Unlike GRB 090323, the ARR for GRB 090328 was excellent and started just after the burst exited occultation. During the next two orbits, observations were only

Figure 49. Composite light curve for GRB 090328: summed GBM/NaI detectors (first two panels), GBM/BGO (third panel), LLE (fourth panel), and LAT Transient-class events above 100 MeV within a 12° ROI (bottom panel). See Appendix B.1 for more information on lines and symbols in the LAT panels.
(A color version of this figure is available in the online journal.)

interrupted by occultations, with no passage through the SAA. As a result, the LAT time-resolved likelihood analysis detected a significant signal up to $T_0+1.78$ ks, with a temporal decay index $\alpha = 0.95 \pm 0.19$ (Figure 51).

B.10. GRB 090510

The short, bright GRB 090510 is the only burst detected so far by the LAT on board flight software (trigger 263607783). The LAT on board localization was delivered via GCN (Ohno & Pelassa 2009), with a statistical error of 7 arcmin. Combined with an initial off-axis angle of 13°.6, GRB 090510 caused exceptionally bright emission in the LAT, as reported in the follow-up analysis by Omodei et al. (2009), and it triggered an ARR of the *Fermi* spacecraft. GRB 090510 was also significantly ($>5\sigma$) detected by the *AGILE*-GRID above 100 MeV (Longo et al. 2009a; Giuliani et al. 2010a). At lower energies, GRB 090510 triggered both the *Swift*-BAT (Hoversten et al. 2009a, 2009b) and the GBM (trigger 263607781, at $T_0 = 00:22:59.97$ UT on

2009 May 10; Guiriec et al. 2009) instruments. Both the *Swift*-XRT and GBM positions were consistent with the LAT on board localization. Follow-up observations of the candidate optical afterglow found by *Swift*-UVOT (Marshall & Hoversten 2009) were conducted with the Nordic Optical Telescope (Malesani 2009) and in the optical/NIR with GROND (Olivares et al. 2009b). Rau et al. (2009) reported a spectroscopic redshift of $z = 0.903 \pm 0.003$ based on observations with the Very Large Telescope (VLT)/FORS2 instrument. A dedicated analysis of the NIR and optical follow-up observations of GRB 090510 is presented in McBreen et al. (2010) and analysis of the broadband observations including γ-ray, X-ray, and optical are presented in De Pasquale et al. (2010).

As shown in Figure 52, the GBM triggered on a precursor in the GRB 090510 light curve. The main emission in the GBM consists of several pulses, with a maximum at $T_0+0.6$ s and a duration of $\sim$0.6 s. The temporal structure of the LAT emission shows fast variability on timescales as short as 20 ms. The LLE light curve shows a series of short spikes coinciding
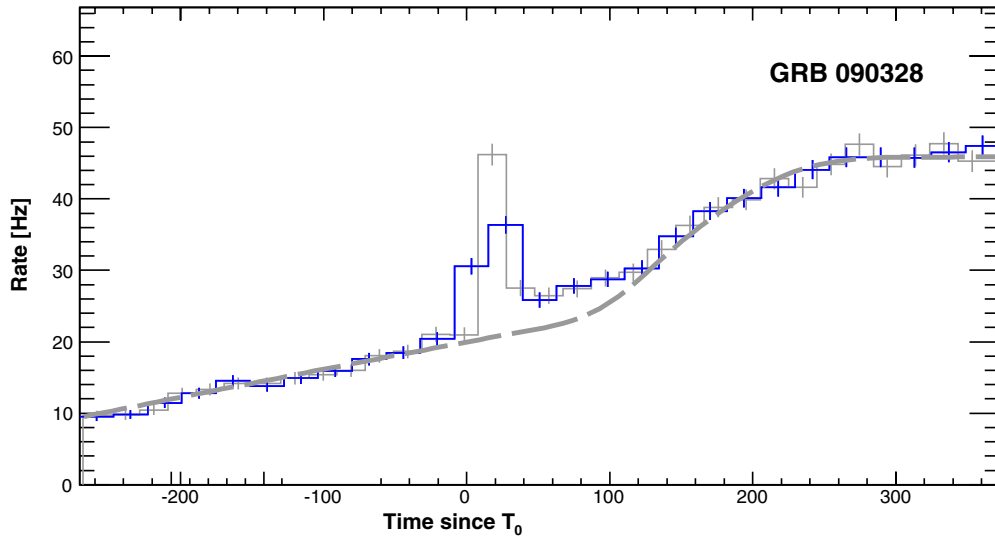
Figure 50. Background estimation in the LLE light curve of GRB 090328401. Gray and blue histograms are the count rates in the LAT detector for two different time binnings. The dashed gray line is the best-fit background.

(A color version of this figure is available in the online journal.)
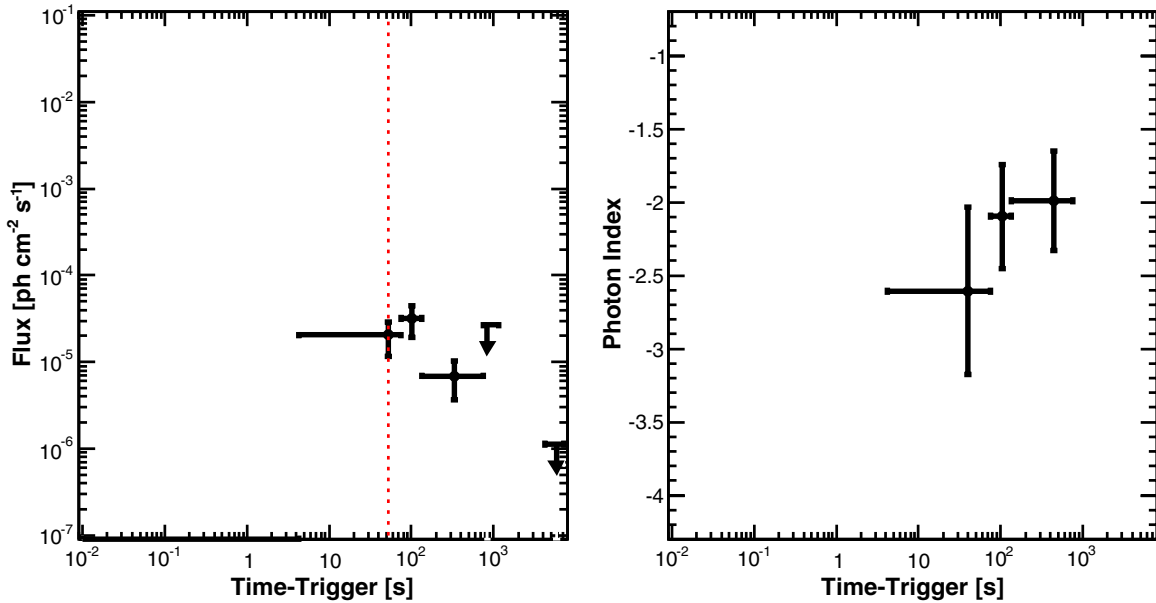

Figure 51. Likelihood light curve for GRB 090328 (flux above 100 MeV on the left, photon index on the right). See Appendix B.1 for more information on lines and symbols.

(A color version of this figure is available in the online journal.)

with the GBM pulses and appearing on top of a smoother and longer single pulse. Two of the three LAT Transient-class events recorded above 100 MeV at the time of the precursor (between T_0 to $T_0+0.2$ s) have high probabilities of being associated with the burst. The main emission in the LAT starts at $T_0+0.6$ s and lasts much longer than the GBM estimated duration, with 180 Transient-class events recorded above 100 MeV within the LAT $T_{90} \sim 45$ s (see Table 4). Many GeV events are recorded during and well after the GBM emission, similar to the 31.31 GeV event detected at $T_0+0.83$ s, coinciding with a short bright spike in the GBM light curve. This photon candidate has been used by the *Fermi*-LAT collaboration to set the best lower limit on the energy scale at which postulated quantum-gravity effects create violations of Lorentz invariance, disfavoring models that predict a linear variation of the speed of light with photon energy below the Planck energy scale $E_{\mathrm{Planck}} = 1.22 \times 10^{19}$ GeV (Abdo et al. 2009b). It should be noted that Troja et al. (2010) detected an additional precursor $\sim$13 s before the GBM trigger

using *Swift* data. The existence of this second precursor could in principle considerably weaken one of the constraints on Lorentz invariance reported in Abdo et al. (2009b). However, the exceptional spectral softness of this additional precursor and the absence of detection by the GBM or the LAT imply that it is very unlikely that this precursor is associated with the 31 GeV photon. Thus, the considerations and results of the original *Fermi* publication remain unaffected.

In the time-resolved spectral analysis published by the *Fermi*-LAT collaboration (Ackermann et al. 2010b), the prompt emission spectrum of GRB 090510 was fit over more than six decades in energy by the combination of an empirical Band function with a high-energy PL. The hard PL is detected from the onset of the main emission in the LAT and it dominates the Band function not only at high energy but also below $\sim$20 keV. Our GBM-LAT joint spectral analysis in the GBM time window confirms these results, yielding a peak energy $E_p \sim 3.6$ MeV for the Band function and a spectral slope of 1.60 ± 0.04 for

Figure 52. Composite light curve for GRB 090510: summed GBM/NaI detectors (first two panels), GBM/BGO (third panel), LLE (fourth panel), and LAT Transient-class events above 100 MeV within a 12° ROI (bottom panel). See Appendix B.1 for more information on lines and symbols in the LAT panels.

(A color version of this figure is available in the online journal.)

the additional PL component. The total isotropic equivalent energy is $(7.3 \pm 0.3) \times 10^{52}$ erg (1 keV–10 GeV, within the GBM T_{90}).

The LAT time-resolved likelihood analysis resulted in a well sampled light curve of the high-energy flux up to T_0+178 s (Figure 53). No significant spectral evolution was detected. The decay of the flux as a function of time can be fit with a simple PL starting from the GBM T_{95}, with a decay index $\alpha = 1.82 \pm 0.17$, somewhat steeper than the index of 1.38 ± 0.07 reported in De Pasquale et al. (2010). However, the fit of the flux light curve with a broken PL from the peak flux time $t_p = T_0$+0.9 s up to T_0+ $\sim$ 8 ks (including flux ULs after T_0+178 s) returned a significant break at $t_b = 7.0 \pm 1.5$ s, along with a steeper initial decay ($\alpha_1 = 2.21 \pm 0.27$) and a smoother decay ($\alpha_2 = 1.13 \pm 0.12$) at later times.

B.11. GRB 090531B

The short GRB 090531B triggered the GBM at $T_0 =$ 18:35:56.49 UT on 2009 May 31 (trigger 265487758, Guiriec

2009b) and it was also detected by the *Swift*-BAT (Cummings et al. 2009) and *Swift*-XRT (Sbarufatti et al. 2009) instruments. It is a relatively faint burst, both in the GBM and in the LAT (despite an initial off-axis angle of 21°.9). Only a few LAT Transient-class events above 100 MeV are consistent with the *Swift* localization, therefore no significant emission was found in the likelihood analysis. GRB 090531B was detected in the LLE data only and the LLE light curve shows a significant signal excess that is temporally coincident with the first pulse detected by the NaI and BGO detectors (Figure 54).

B.12. GRB 090626

The long GRB 090626 triggered the GBM at $T_0 =$ 04:32:08.88 UT on 2009 June 26 (trigger 267683530; von Kienlin 2009b). It was also detected by the LAT on-ground ASP, which searches for LAT counterparts to known GRBs, and the LAT preliminary localization was delivered via GCN (Piron et al. 2009), with a statistical error of 0°.32 (95% CL). The GBM light curve of GRB 090626 consists of several bright pulses

Figure 53. Likelihood light curve for GRB 090510 (flux above 100 MeV on the left, photon index on the right). See Appendix B.1 for more information on lines and symbols.

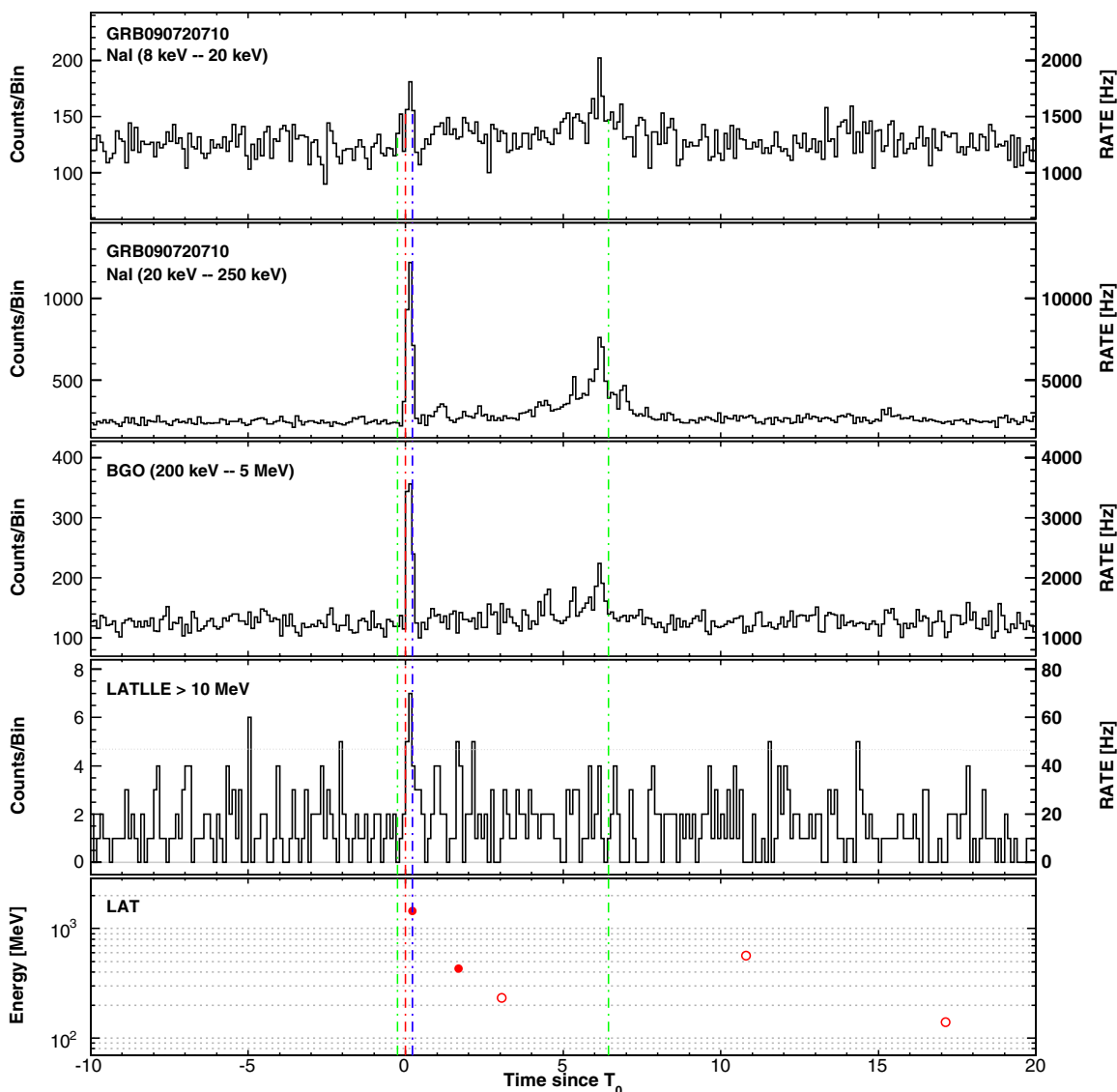(A color version of this figure is available in the online journal.)
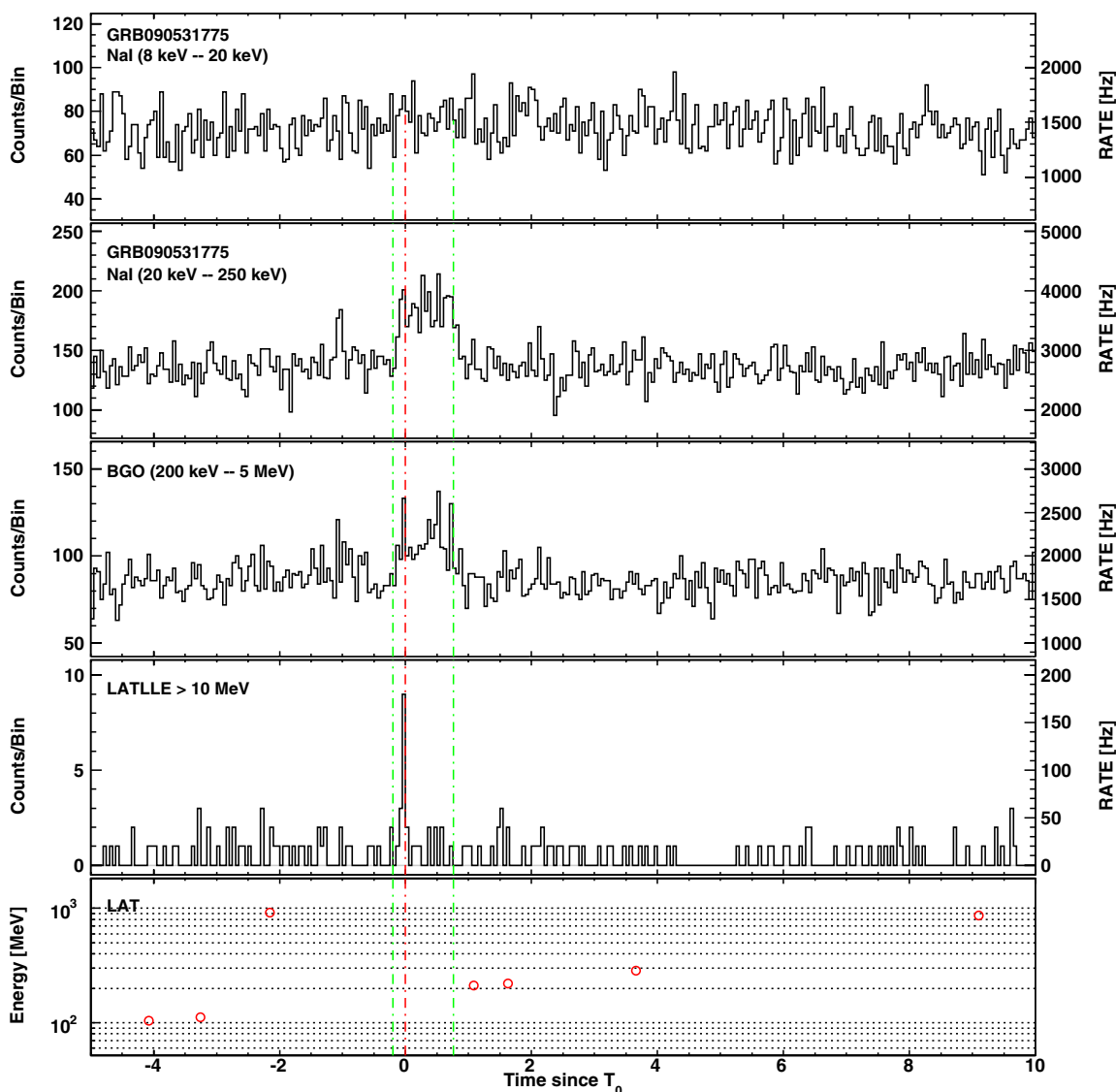
Figure 54. Composite light curve for GRB 090531B: summed GBM/NaI detectors (first two panels), GBM/BGO (third panel), LLE (fourth panel), and LAT Transient-class events above 100 MeV within a 12° ROI (bottom panel). See Appendix B.1 for more information on lines and symbols in the LAT panels.

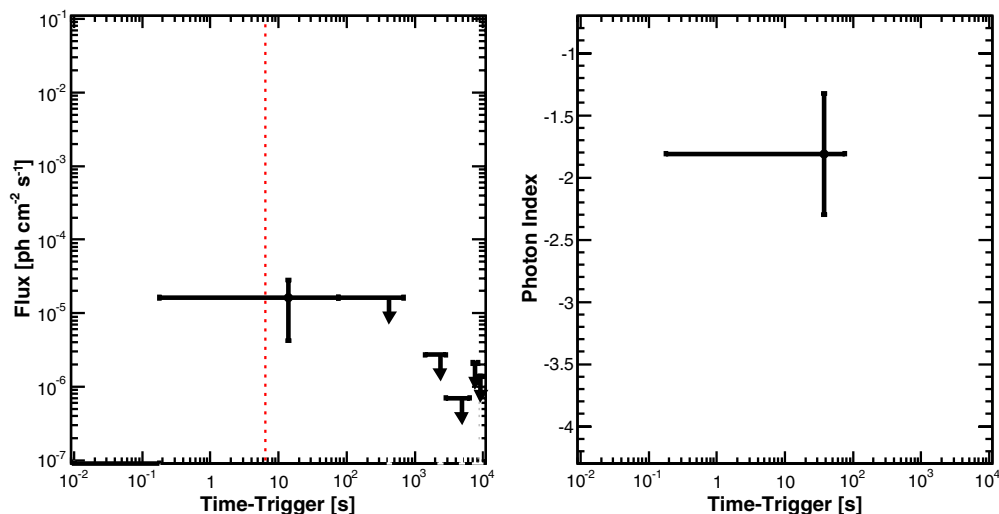(A color version of this figure is available in the online journal.)
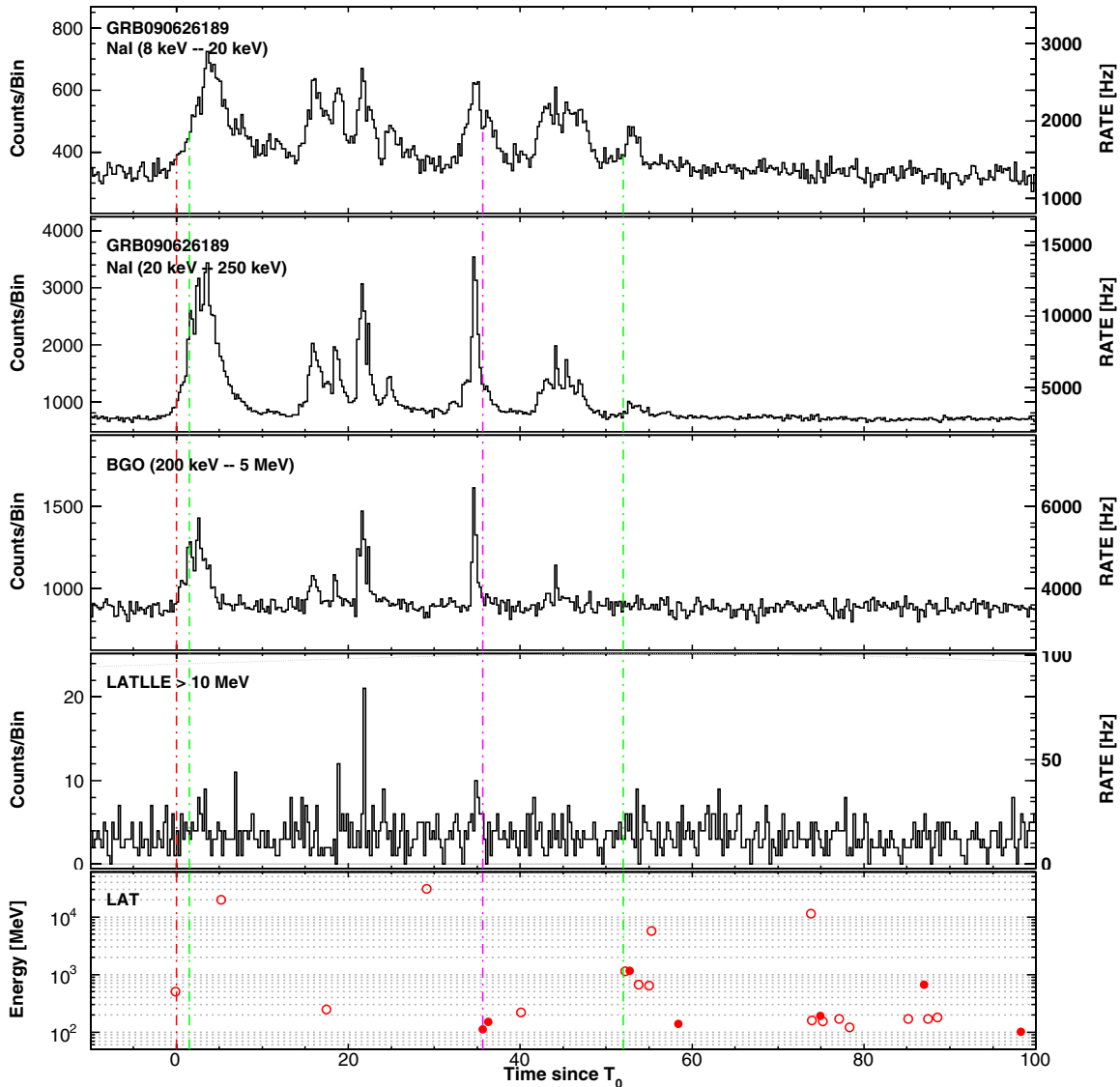
Figure 55. Composite light curve for GRB 090626: summed GBM/NaI detectors (first two panels), GBM/BGO (third panel), LLE (fourth panel), and LAT Transient-class events above 100 MeV within a 12° ROI (bottom panel). See Appendix B.1 for more information on lines and symbols in the LAT panels.

(A color version of this figure is available in the online journal.)

and lasts ∼55 s (Figure 55). The LLE light curve shows one single, faint short pulse that coincides with the second bright pulse observed in the BGO light curve. However, this signal excess was not significant enough to claim an LLE detection (see Table 2). In the preliminary analysis of LAT data, Piron et al. (2009) reported that GRB 090626 high-energy emission lasted until $T_0+ \sim 250$ s. Our analysis of the LAT Transient-class data above 100 MeV provided a LAT $T_{95} = 300^{+338}_{-53}$ s, which confirms the temporal extension of the burst emission in the LAT. In addition, a 2.09 GeV event is recorded at $T_0+111.63$ s. The LAT time-resolved likelihood analysis returned a significant flux in three time bins only up to T_0+750 s (Figure 56).

B.13. GRB 090720B

The long GRB 090720B triggered the GBM at $T_0 = $ 17:02:56.91 UT on 2009 July 20 (trigger 269802178; Burgess et al. 2009). The GBM light curve consists of one short, hard pulse followed by a wider pulse (Figure 57). GRB 090720B had an off-axis angle of 56°.1 in the LAT at the trigger time, where the effective area is a factor ∼3 less than on axis. The burst was not

significantly detected in the LLE data and the LAT likelihood analysis returned a TS ∼ 25 based on the three Transient-class events recorded above 100 MeV during the GBM time window, including a 1.45 GeV event at $T_0+0.22$ s. No LAT T_{90} could be derived due to the large zenith angle of the burst. The LAT time-resolved likelihood analysis returned a marginal detection in one time bin only, ending at T_0+75 s (Figure 58).

B.14. GRB 090902B

The long, bright GRB 090902B triggered the GBM at $T_0 = $ 11:05:08.31 UT on 2009 September 2 (trigger 273582310; Bissaldi & Connaughton 2009). In spite of an initial off-axis angle of 50°.8, GRB 090902B caused exceptionally bright emission in the LAT and it triggered an ARR of the *Fermi* spacecraft. The LAT preliminary localization was delivered via GCN (de Palma et al. 2009b), with a statistical error of 0°.04. *Swift* TOO observations started ∼12.5 hr after the trigger time (Stratta et al. 2009b). A possible X-ray counterpart was found by *Swift*-XRT 3.2 arcmin away from the LAT position (Kennea & Stratta 2009) and further observations confirmed

Figure 56. Likelihood light curve for GRB 090626 (flux above 100 MeV on the left, photon index on the right). See Appendix B.1 for more information on lines and symbols.

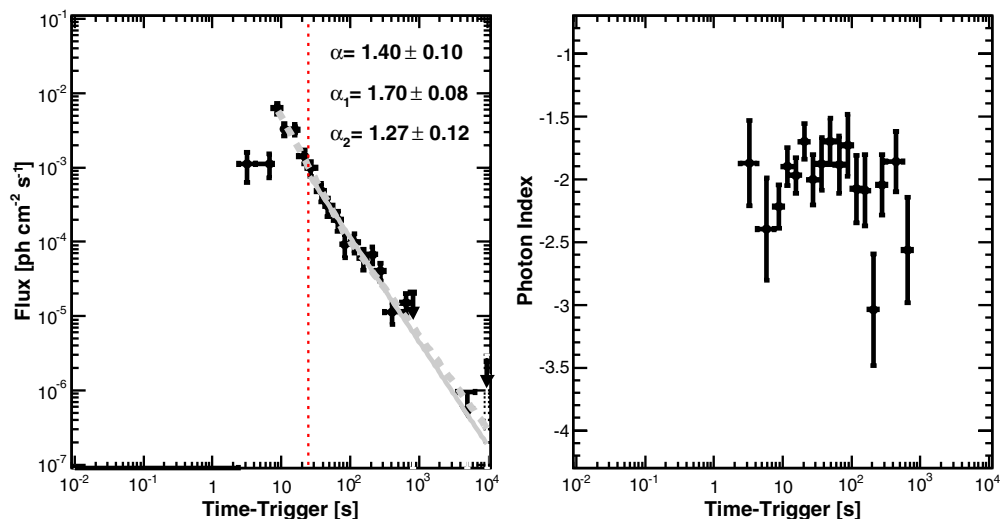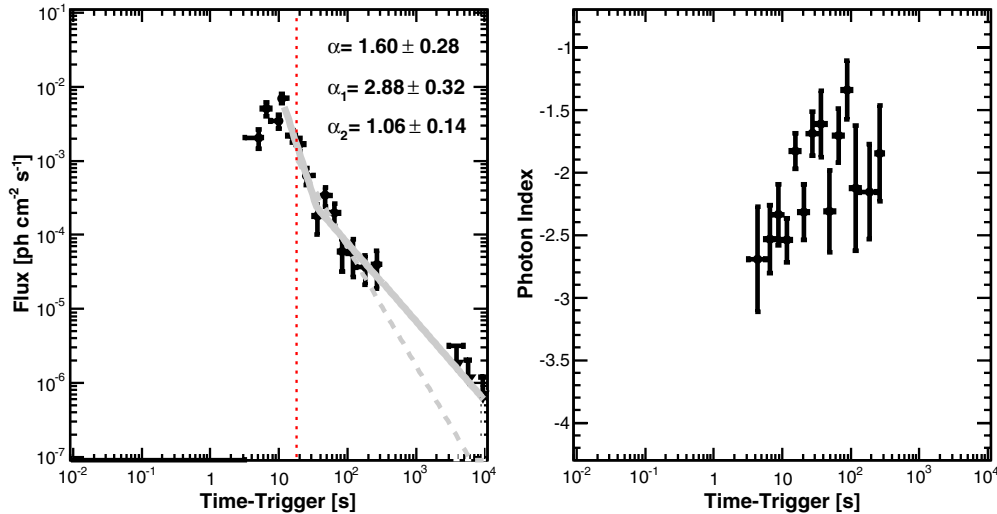(A color version of this figure is available in the online journal.)

the existence of a fading source (Stratta et al. 2009a). Follow-up detections in the optical were reported by the *Swift*-UVOT team (Swenson & Siegel 2009; Swenson & Stratta 2009) and by several observers operating ground-based telescopes (Perley et al. 2009a; Guidorzi et al. 2009; Pandey et al. 2009). GRB 090902B was also detected in the optical/NIR (Olivares et al. 2009a) and in the radio band (van der Horst et al. 2009; Chandra & Frail 2009). Cucchiara et al. (2009b) reported a spectroscopic redshift of $z = 1.822$ based on observations of the optical afterglow using GMOS. Combined with its brightness, this makes GRB 090902B the third most energetic LAT-detected burst after GRB 080916C and GRB 090323, with an isotropic equivalent energy $E_{iso} \simeq 3.4 \times 10^{54}$ erg (1 keV–10 GeV, within the GBM T_{90}). A dedicated analysis of the NIR and optical follow-up observations of GRB 090902B is presented in McBreen et al. (2010).

As shown in Figure 59, the GBM light curve of GRB 090902B is complex both in the NaI and BGO detectors, probably resulting from the overlap of many small pulses. After a plateau phase of ∼6 s, similar to what is observed at lower energies, the LLE light curve shows a series of short spikes on top of two broad and partially overlapping pulses, which seem to coincide with two distinct emission episodes visible in both the NaI and BGO light curves. The temporal structure of the LAT emission shows fast variability on timescales as short as ∼100 ms. In the first paper published by the *Fermi*-LAT collaboration (Abdo et al. 2009a), the prompt emission spectrum of GRB 090902B was fit over more than six decades in energy by the combination of an empirical Band function with a high-energy PL. The hard PL is detected from the trigger time and it dominates the Band function not only at high energies but also below ∼50 keV, as already reported in the preliminary joint analysis of GBM and LAT data (de Palma et al. 2009a). Our GBM-LAT joint spectral analysis in the GBM time window confirms these results, yielding similar parameters for the Band function and a spectral slope of 1.94 ± 0.01 for the additional PL component. Note that alternative spectral models have been studied in detail (Ryde et al. 2010; Liu & Wang 2011) and that the peculiar

spectrum of GRB 090902B has also been used to constrain several theoretical models (Barniol Duran & Kumar 2011; Pe'er et al. 2012).

The LAT emission contains many GeV events during and well after the GBM emission, similar to the 33.39 GeV event detected at $T_0+81.75$ s. This photon candidate has the highest energy ever observed from a burst and it has been used by the *Fermi*-LAT collaboration to probe the extragalactic background light as a function of redshift in the optical-UV range (Abdo et al. 2010a). The temporally extended high-energy emission reaches at least the end of the first GTI (LAT $T_{95} > 825$ s) and ∼300 Transient-class events are recorded above 100 MeV until this time (see Table 4). The LAT time-resolved likelihood analysis resulted in a well sampled light curve of the high-energy flux up to T_0+750 s (Figure 60). No significant spectral evolution was detected. The decay of the flux as a function of time can be fit with a simple PL starting from the GBM T_{95}, with a decay index $\alpha = 1.40 \pm 0.10$, in agreement with the result reported by Abdo et al. (2009a). Similar to GRB 090510, however, the fit of the flux light curve with a broken PL from the peak flux time $t_p = T_0+8.7$ s up to $T_0+ \sim 8$ ks (including flux ULs after T_0+750 s) returned a significant break at $t_b = 130 \pm 50$ s, along with a steeper initial decay ($\alpha_1 = 1.70 \pm 0.19$) and a smoother decay ($\alpha_2 = 1.27 \pm 0.12$) at later times.

B.15. GRB 090926A

The long, bright GRB 090926A triggered the GBM at $T_0 = 04{:}20{:}26.99$ UT on 2009 September 26 (trigger 275631628; Bissaldi 2009). In spite of an initial off-axis angle of 48°.1, GRB 090926A caused exceptionally bright emission in the LAT and it triggered an ARR of the *Fermi* spacecraft. The spacecraft initially remained in survey mode as long as the Earth avoidance angle condition was not satisfied and GRB 090926A became occulted by the Earth ∼500 s after the trigger time. At $\sim T_0 + 3$ ks, the LAT resumed observations and the spacecraft slewed to the burst position, keeping it in the LAT FoV until 5 hr post trigger. The LAT preliminary localization was delivered via GCN (Uehara et al. 2009), with a statistical error of 0°.04.

Figure 57. Composite light curve for GRB 090720B: summed GBM/NaI detectors (first two panels), GBM/BGO (third panel), LLE (fourth panel), and LAT Transient-class events above 100 MeV within a 12° ROI (bottom panel). See Appendix B.1 for more information on lines and symbols in the LAT panels.

(A color version of this figure is available in the online journal.)

Figure 58. Likelihood light curve for GRB 090720B (flux above 100 MeV on the left, photon index on the right). See Appendix B.1 for more information on lines and symbols.

(A color version of this figure is available in the online journal.)
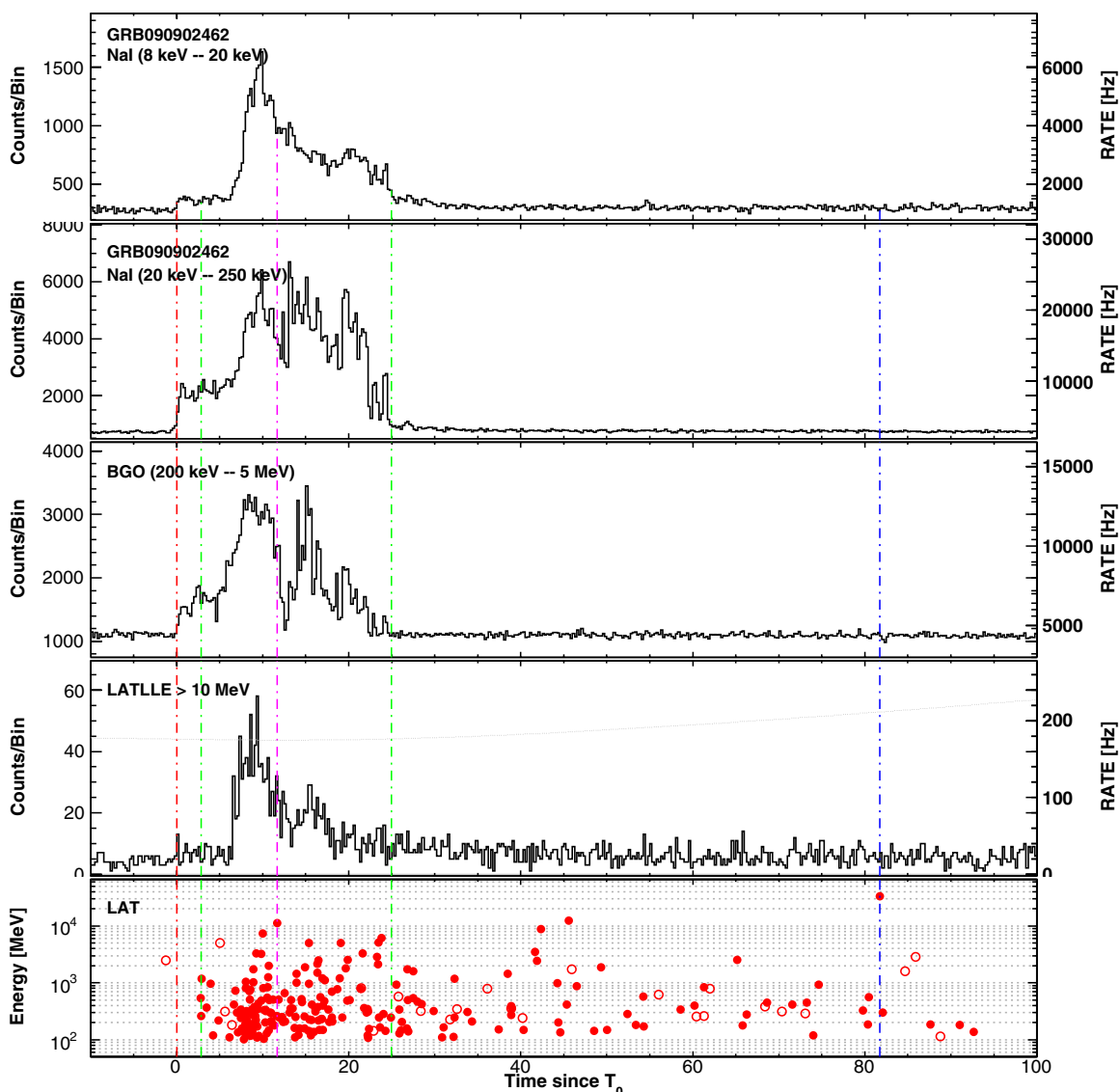
Figure 59. Composite light curve for GRB 090902B: summed GBM/NaI detectors (first two panels), GBM/BGO (third panel), LLE (fourth panel), and LAT Transient-class events above 100 MeV within a 12° ROI (bottom panel). See Appendix B.1 for more information on lines and symbols in the LAT panels.

(A color version of this figure is available in the online journal.)

Figure 60. Likelihood light curve for GRB 090902B (flux above 100 MeV on the left, photon index on the right). See Appendix B.1 for more information on lines and symbols.

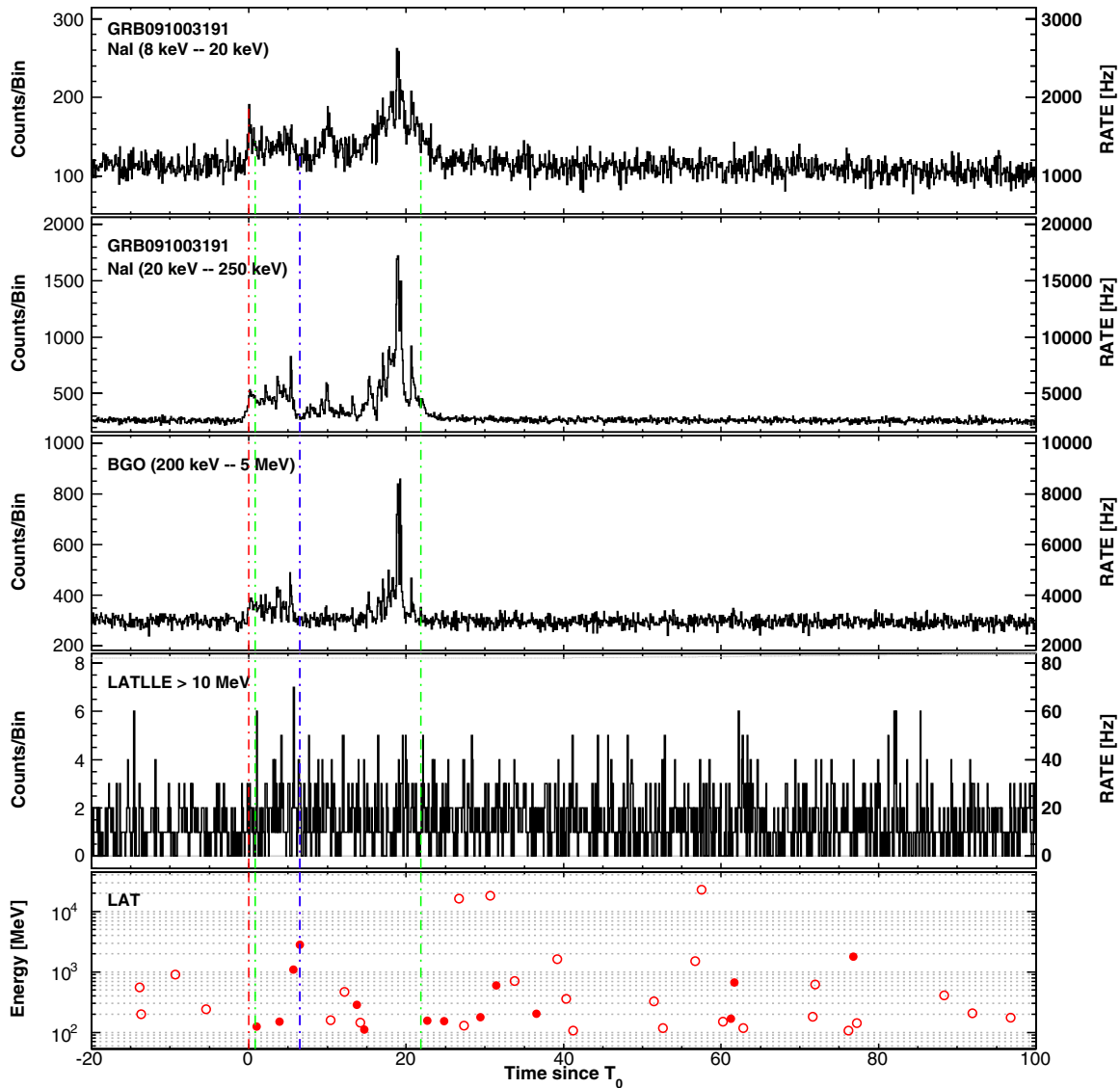(A color version of this figure is available in the online journal.)
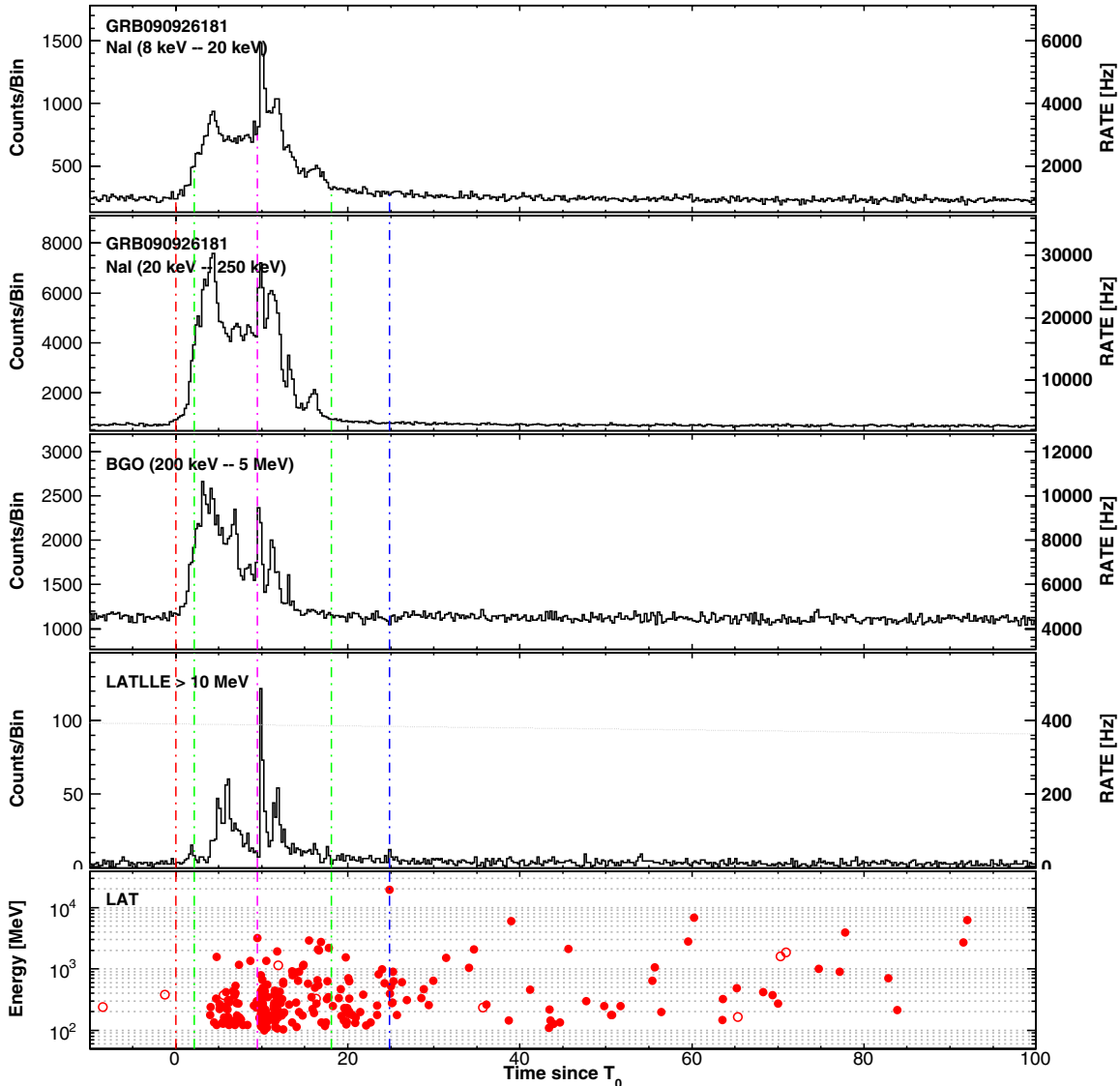
Figure 61. Composite light curve for GRB 090926A: summed GBM/NaI detectors (first two panels), GBM/BGO (third panel), LLE (fourth panel), and LAT Transient-class events above 100 MeV within a 12° ROI (bottom panel). See Appendix B.1 for more information on lines and symbols in the LAT panels.
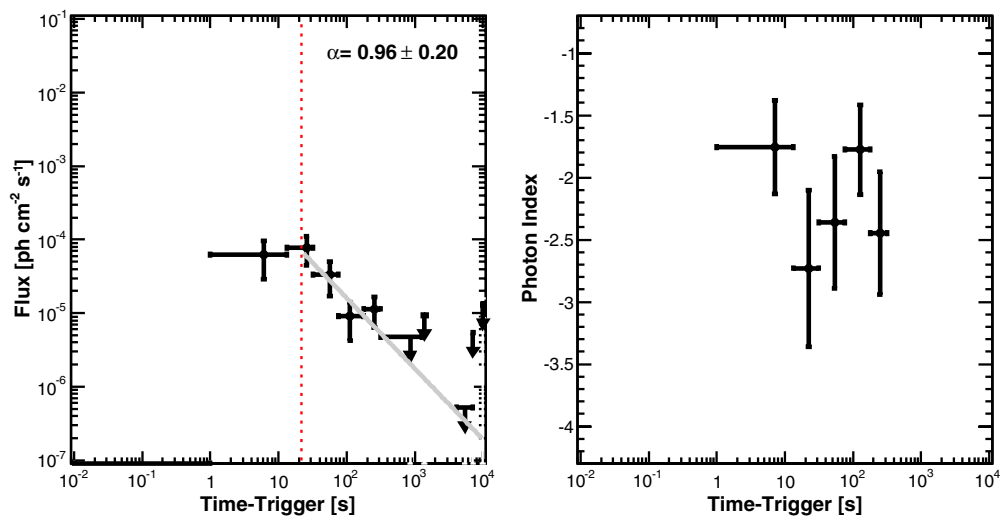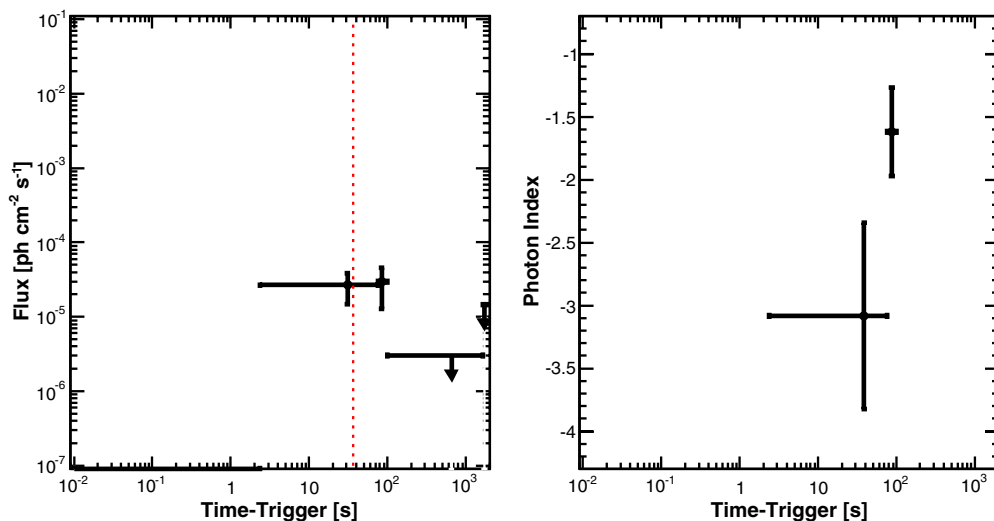(A color version of this figure is available in the online journal.)

Swift TOO observations started ∼13 hr after the trigger time (Vetere et al. 2009b; Swenson et al. 2010). An X-ray counterpart was found by *Swift*-XRT 4 arcmin away from the LAT position (Vetere et al. 2009a) and further observations confirmed the existence of a fading source with some flaring activity (Vetere 2009). The optical afterglow of GRB 090926A was discovered by the Skynet-PROMPT telescopes (Haislip et al. 2009b, 2009a, 2009e, 2009c, 2009d) and also detected by *Swift*-UVOT (Gronwall & Vetere 2009; Oates & Vetere 2009). Malesani et al. (2009) reported a spectroscopic redshift of $z = 2.1062$ based on observations of the optical afterglow using the XSHOOTER spectrograph mounted on the ESO-VLT UT2. Combined with its brightness, this makes GRB 090926A the fourth most energetic LAT-detected burst, with an isotropic equivalent energy $E_{iso} \simeq 2.4 \times 10^{54}$ erg (1 keV–10 GeV, within the GBM T_{90}).

As shown in Figure 61, the light curve of GRB 090926A exhibits a bright, short pulse at $\sim T_0 + 10$ s in all energy bands covered by the GBM and the LAT. In the preliminary analysis of GBM and LAT data, Bissaldi et al. (2009) fit the emission spectrum of this pulse with the combination of an empirical Band function and a high-energy PL. In the time-resolved spectral analysis published by the *Fermi*-LAT collaboration (Ackermann et al. 2011), the high-energy, PL component was found to start at the time of the bright pulse and persist until $\sim T_0 + 22$ s. In this study, a spectral break was also found at the highest energies, with a cutoff energy $E_c \sim 400$ MeV during the bright pulse and $E_c \sim 1.4$ GeV for the time-integrated spectrum. Our GBM-LAT joint spectral analysis in the GBM time window confirms these results, yielding $E_c \sim 1.5$ GeV and a similar spectral slope of 1.73 ± 0.03 for the high-energy, PL component (Table 11).

The LAT emission contains many GeV events during and well after the GBM emission, similar to the 19.56 GeV event detected at $T_0 + 24.83$ s. The temporally extended high-energy emission reaches at least $T_0 + 225$ s and ∼230 Transient-class events are recorded above 100 MeV until this time (see Table 4). The LAT time-resolved likelihood analysis resulted in a well sampled light curve of the high-energy flux up to $T_0 + 295$ s (Figure 62). The decay of the flux as a function of time can

Figure 62. Likelihood light curve for GRB 090926A (flux above 100 MeV on the left, photon index on the right). See Appendix B.1 for more information on lines and symbols.

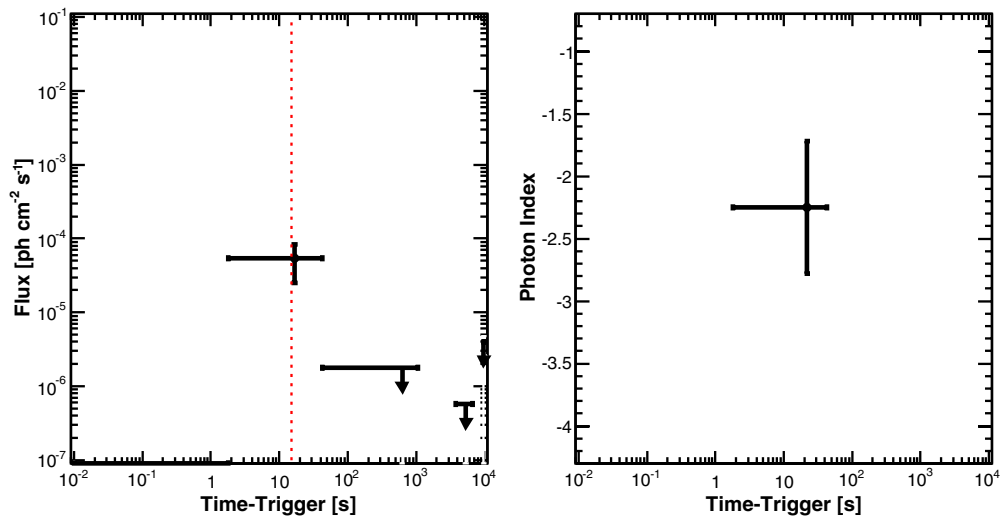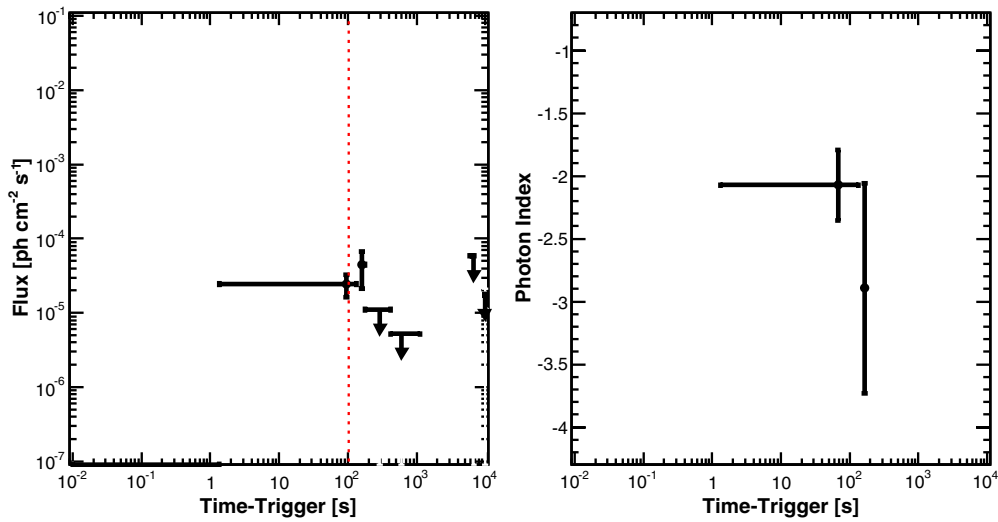(A color version of this figure is available in the online journal.)

be fit with a simple PL starting from the GBM T_{95}, with a decay index $\alpha = 1.60 \pm 0.28$, in agreement with the result reported by Ackermann et al. (2011). Similar to GRB 090510 and GRB 090902B, however, the fit of the flux light curve with a broken PL from the peak flux time $t_p = T_0 + 11.7$ s up to $T_0 + \sim 8$ ks (including flux ULs after $T_0 + 295$ s) returned a significant break at $t_b = 40 \pm 5$ s, along with a steeper initial decay ($\alpha_1 = 2.88 \pm 0.32$) and a smoother decay ($\alpha_2 = 1.06 \pm 0.14$) at later times. The right hand plot of Figure 62 also suggests that the photon index in the first phase is steeper than the one in the final decay part.

B.16. GRB 091003

The long GRB 091003 triggered the GBM at $T_0 = $ 04:35:45.5 UT on 2009 October 3 (trigger 276237347; Rau 2009). The LAT preliminary localization was delivered via GCN (McEnery et al. 2009a), with a statistical error of 0°.15. *Swift* TOO observations started ∼15.5 hr after the trigger time (Starling et al. 2009). A fading source was detected in X-rays by *Swift*-XRT (Starling & Beardmore 2009; Page et al. 2009) and an UV/optical afterglow candidate was found by *Swift*-UVOT (Gronwall & Starling 2009; Pritchard et al. 2009). The optical afterglow was also detected by the William Herschel Telescope (Wiersema et al. 2009a) and a possible low redshift host galaxy was found by the Lick Observatory (Perley et al. 2009b). A spectroscopic redshift measurement of $z = 0.8969$ was obtained using GMOS (Cucchiara et al. 2009a).

No significant emission was detected in the LLE light curve (Figure 63). The highest energy event (2.8 GeV) is detected at $T_0 + 6.47$ s and does not coincide with any noticeable feature in the GBM light curve. Although the LAT $T_{95} = 453^{+86}_{-376}$ s suffers from a large uncertainty due to the relatively small number statistics (∼30 events), the burst was detected up to this time with high significance by the LAT likelihood analysis of the Transient-class data above 100 MeV. The LAT time-resolved likelihood analysis returned a significant flux up to $T_0 + 316$ s, with a temporal decay index $\alpha = 0.96 \pm 0.20$ (Figure 64).

B.17. GRB 091031

The long GRB 091031 triggered the GBM at $T_0 = $ 12:00:28.85 UT on 2009 October 31 (trigger 278683230;

McBreen & Chaplin 2009). The LAT preliminary localization was delivered via GCN (de Palma et al. 2009c), with a statistical error of 0°.2. This burst was significantly detected in the LLE light curve (Figure 65) and above 100 MeV by the likelihood analysis up to the LAT $T_{95} = 206^{+12}_{-43}$ s. The LAT time-resolved likelihood analysis returned a significant flux up to $T_0 + 100$ s (Figure 66). The highest energy event (1.19 GeV) is detected with two other high-energy events at $T_0 + 79.75$ s, well after the end of the GBM emission.

B.18. GRB 091208B

The long GRB 091208B triggered the GBM at $T_0 = $ 09:49:57.96 UT on 2009 December 8 (trigger 281958599; McBreen 2009b) and the *Swift*-BAT at 09:49:57 UT (Pagani et al. 2009). *Swift*-XRT observations started 115.2 s after the BAT trigger (Pagani et al. 2010). A fading and uncataloged X-ray source was found and *Swift*-UVOT detected a bright afterglow candidate consistent with the XRT localization (de Pasquale & Pagani 2009; Pagani et al. 2009). Several telescopes detected the bright optical transient (Xin et al. 2009; Kinugasa et al. 2009; Andreev et al. 2009; Updike et al. 2009b; Xu et al. 2009; Cano et al. 2009; Nakajima et al. 2009; Yoshida et al. 2009; de Ugarte Postigo et al. 2009). A spectroscopic redshift measurement of $z = 1.063$ was obtained using GMOS (Wiersema et al. 2009b), later confirmed by the HIRES-r spectrometer mounted on the 10 m Keck I telescope (Perley et al. 2009c). Using the XRT refined position (Osborne et al. 2009), the LAT likelihood analysis found a marginal detection (TS = 20) during the GBM T_{90}, based on three Transient-class events associated with the burst. The highest energy event (1.18 GeV) is detected at $T_0 + 3.41$ s. Due to the paucity of events (Figure 67), no LAT T_{90} could be derived and the LAT time-resolved likelihood analysis returned a significant flux in one time bin only, ending at $T_0 + 42$ s (Figure 68).

B.19. GRB 100116A

The long GRB 100116A triggered the GBM at $T_0 = $ 21:31:00.24 UT on 2010 January 16 (trigger 285370262; Briggs & Connaughton 2010). The LAT preliminary localization was delivered via GCN (McEnery et al. 2010), with a statistical error of 0°.17. As shown in Figure 69, the GBM triggered on a

Figure 63. Composite light curve for GRB 091003: summed GBM/NaI detectors (first two panels), GBM/BGO (third panel), LLE (fourth panel), and LAT Transient-class events above 100 MeV within a 12° ROI (bottom panel). See Appendix B.1 for more information on lines and symbols in the LAT panels.

(A color version of this figure is available in the online journal.)

Figure 64. Likelihood light curve for GRB 091003 (flux above 100 MeV on the left, photon index on the right). See Appendix B.1 for more information on lines and symbols.

(A color version of this figure is available in the online journal.)
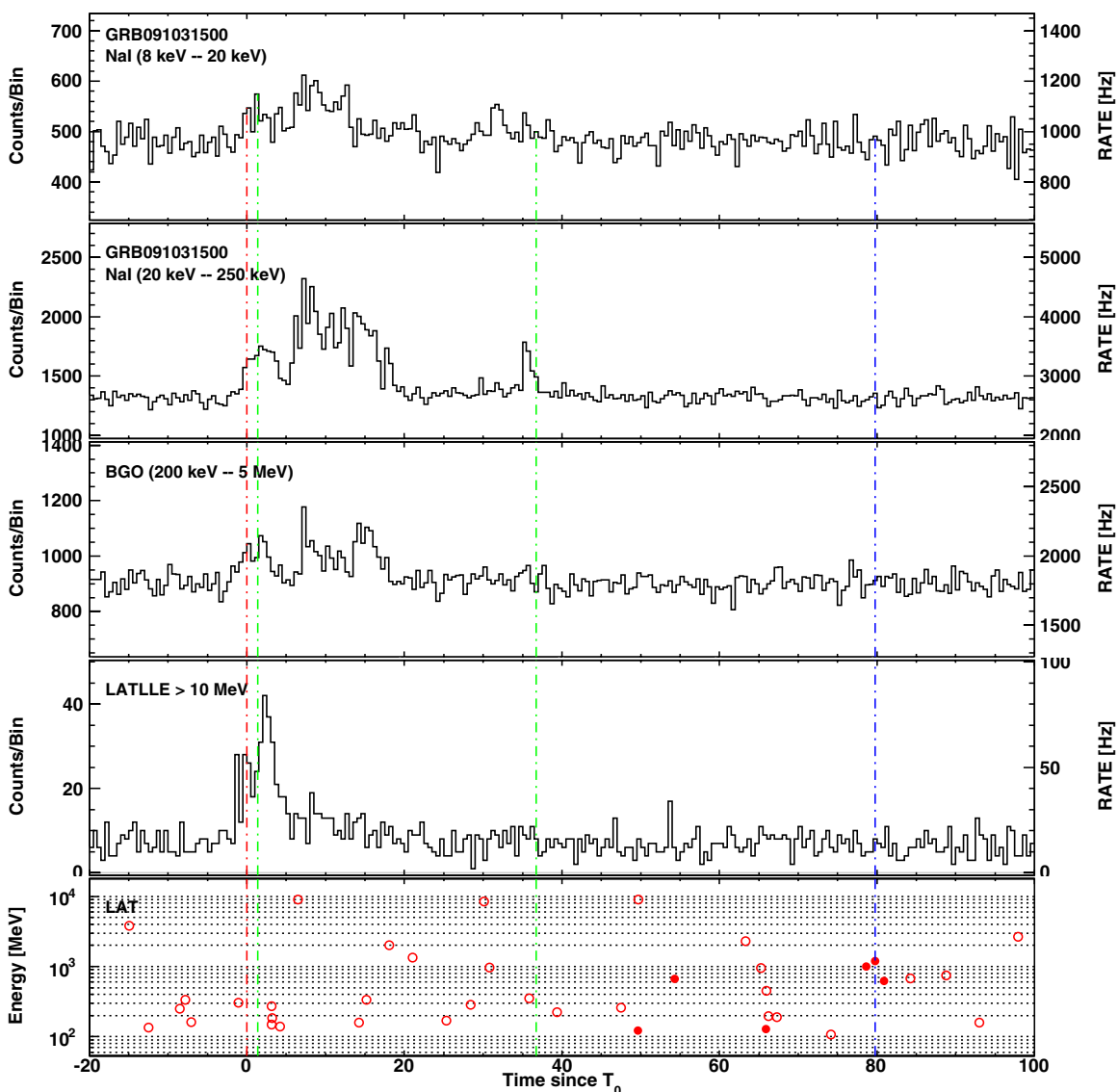
Figure 65. Composite light curve for GRB 091031: summed GBM/NaI detectors (first two panels), GBM/BGO (third panel), LLE (fourth panel), and LAT Transient-class events above 100 MeV within a 12° ROI (bottom panel). See Appendix B.1 for more information on lines and symbols in the LAT panels.

(A color version of this figure is available in the online journal.)

Figure 66. Likelihood light curve for GRB 091031 (flux above 100 MeV on the left, photon index on the right). See Appendix B.1 for more information on lines and symbols.

(A color version of this figure is available in the online journal.)
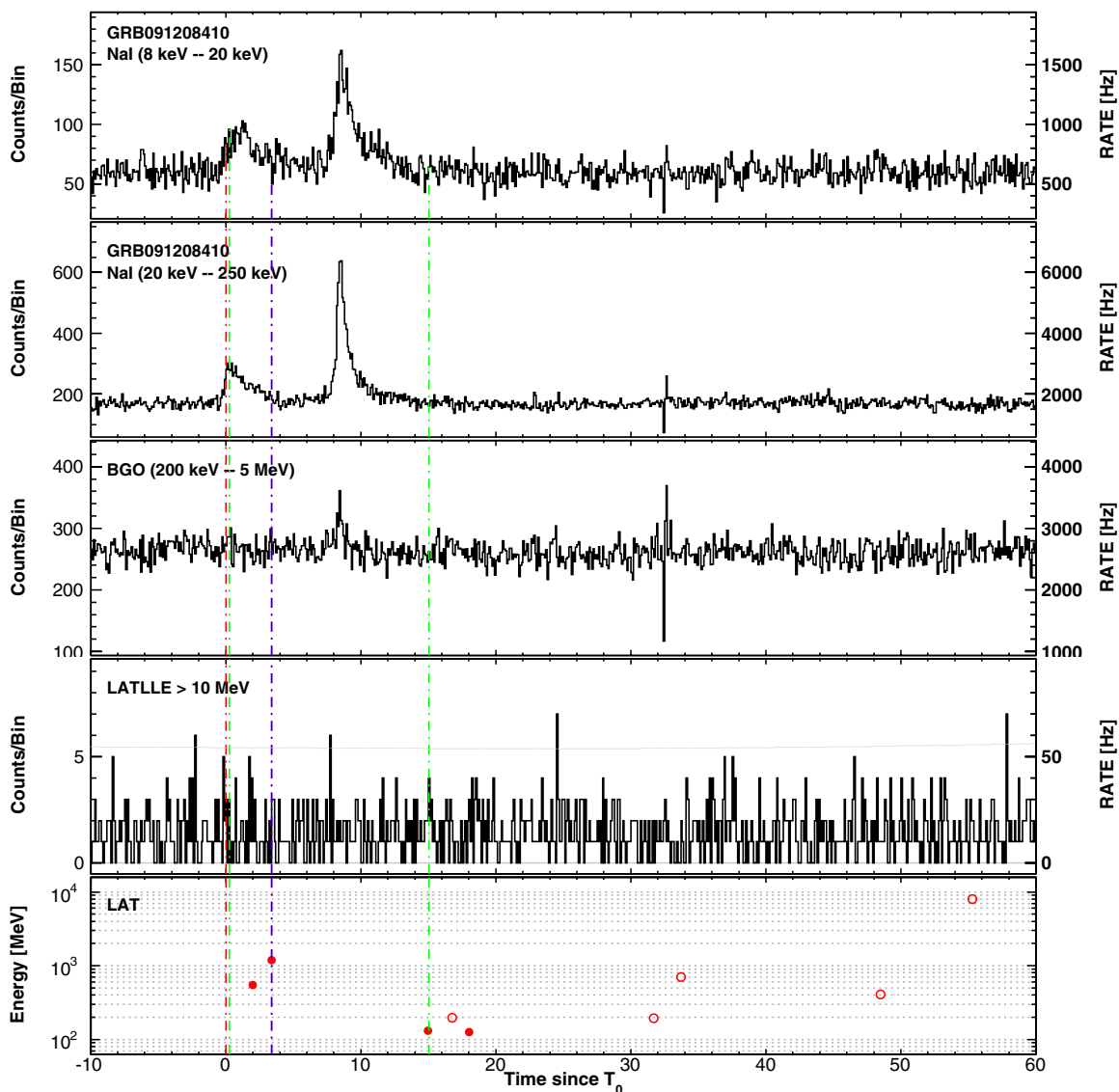
Figure 67. Composite light curve for GRB 091208B: summed GBM/NaI detectors (first two panels), GBM/BGO (third panel), LLE (fourth panel), and LAT Transient-class events above 100 MeV within a 12° ROI (bottom panel). See Appendix B.1 for more information on lines and symbols in the LAT panels.

(A color version of this figure is available in the online journal.)
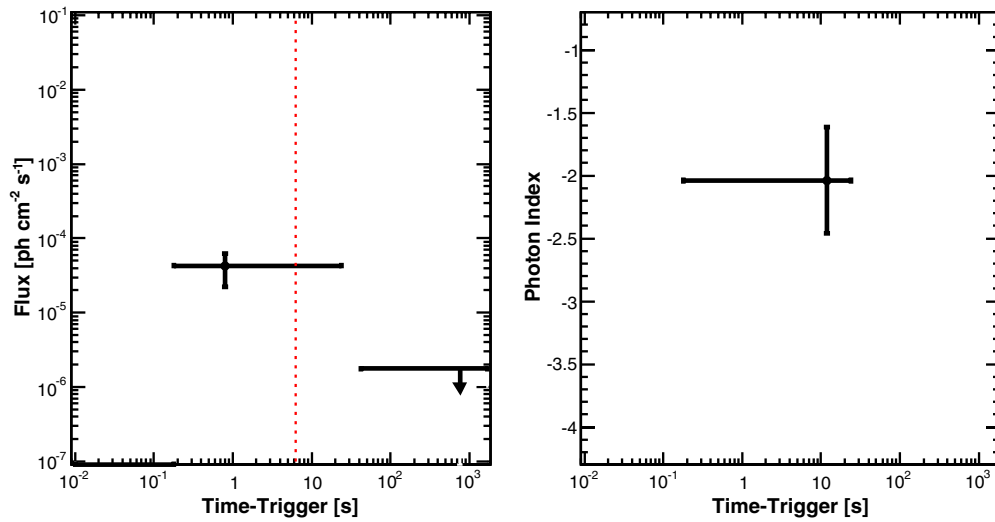

Figure 68. Likelihood light curve for GRB 091208B (flux above 100 MeV on the left, photon index on the right). See Appendix B.1 for more information on lines and symbols.

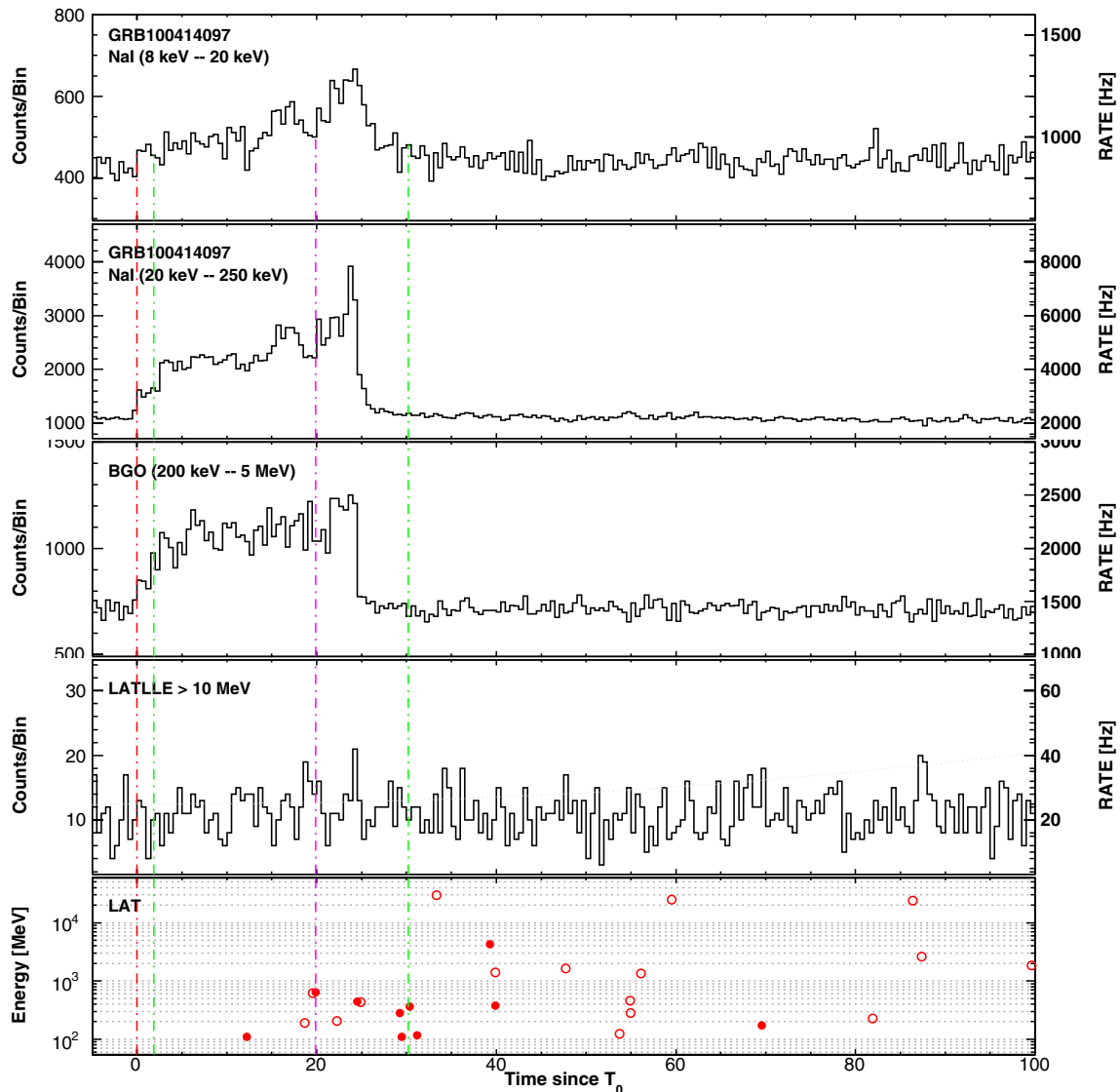(A color version of this figure is available in the online journal.)
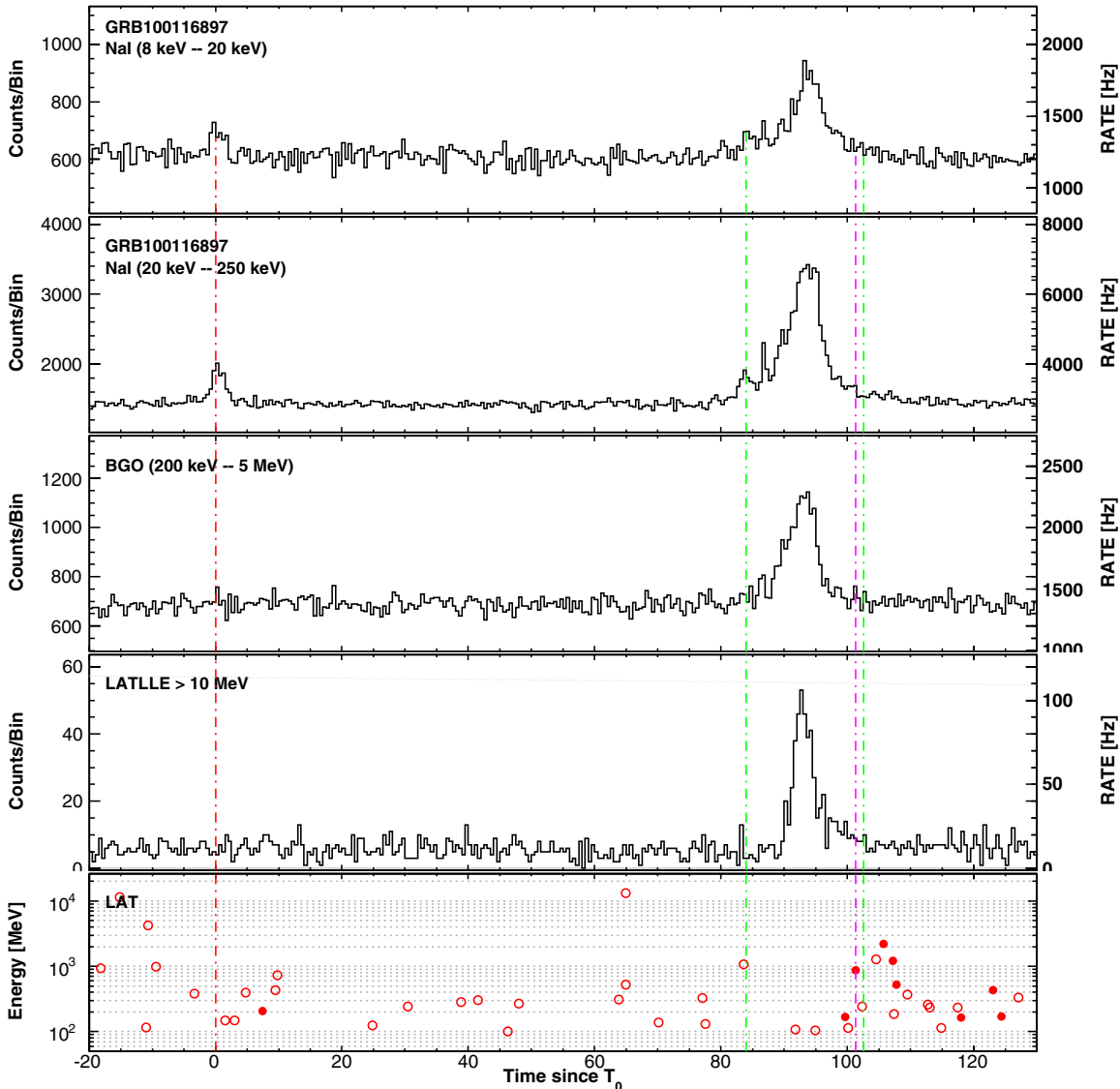
Figure 69. Composite light curve for GRB 100116A: summed GBM/NaI detectors (first two panels), GBM/BGO (third panel), LLE (fourth panel), and LAT Transient-class events above 100 MeV within a 12° ROI (bottom panel). See Appendix B.1 for more information on lines and symbols in the LAT panels.

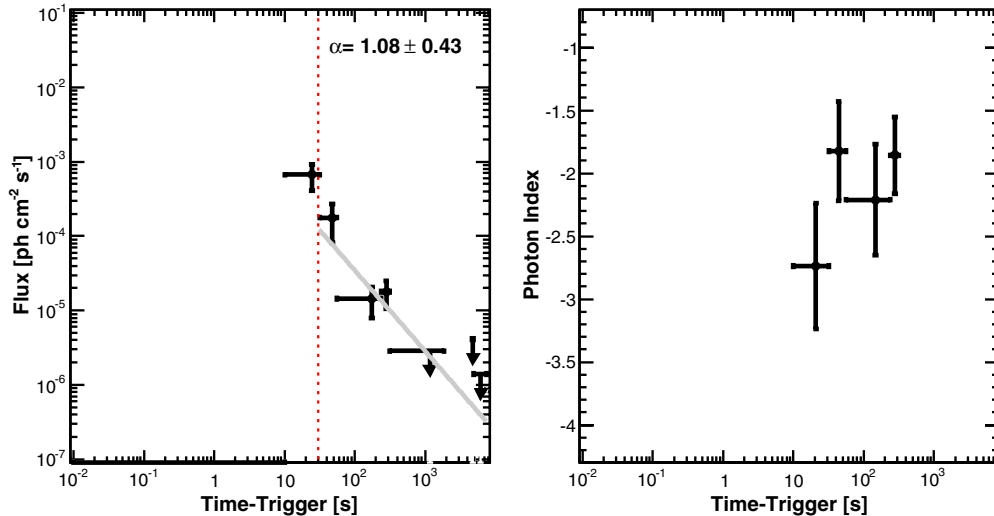(A color version of this figure is available in the online journal.)

precursor in GRB 100116A light curve. A very intense pulse is observed at $\sim T_0+90$ s, with a slow rise and a fast decay, probably due to the overlap of many smaller pulses during the rising part. LAT low-energy events are recorded in temporal coincidence with this bright GBM pulse. More interestingly, the Transient-class events above 100 MeV that are consistent with the burst position appear to be slightly delayed (~ 20 s) with respect to both the LLE and GBM emission and the highest energy event (2.2 GeV) is detected at $T_0+105.71$ s, right at the end of the GBM emission. This temporally extended high-energy emission reaches at least the end of the first GTI (LAT $T_{95} > 141$ s). The LAT time-resolved likelihood analysis returned a significant flux up to T_0+178 s (Figure 70). A 13.12 GeV event with a probability higher than 99% of being associated with the burst is detected at $\sim T_0+296$ s (see the discussion in Section 4.3.3).

B.20. GRB 100225A

The long GRB 100225A triggered the GBM at $T_0 = 02\text{:}45\text{:}31.15$ UT on 2010 February 25 (trigger 288758733;

Foley & McBreen 2010). This faint burst had an off-axis angle of 55.5 at the trigger time, where the LAT effective area is low. A tentative localization with the LAT was delivered via GCN (Piron et al. 2010), with a statistical error of 0.9. Only a few LAT Transient-class events above 100 MeV are actually consistent with the burst position, therefore no LAT T_{90} could be derived and no significant emission was found in the likelihood analysis. GRB 100225A was detected in the LLE data only. The LLE light curve consists of a long-duration pulse that mimics the light curve seen in the NaI detectors (Figure 71).

B.21. GRB 100325A

The long GRB 100325A triggered the GBM at $T_0 = 06\text{:}36\text{:}08.02$ UT on 2010 March 25 (trigger 291191770; von Kienlin 2010a). The LAT preliminary localization was delivered via GCN (de Palma et al. 2010), with a statistical error of 0.6. The light curve in the NaI detectors consists of several overlapping pulses, whereas the burst is not visible in the BGO light curve and only marginally detected in the LLE light

Figure 70. Likelihood light curve for GRB 100116A (flux above 100 MeV on the left, photon index on the right). See Appendix B.1 for more information on lines and symbols.

(A color version of this figure is available in the online journal.)
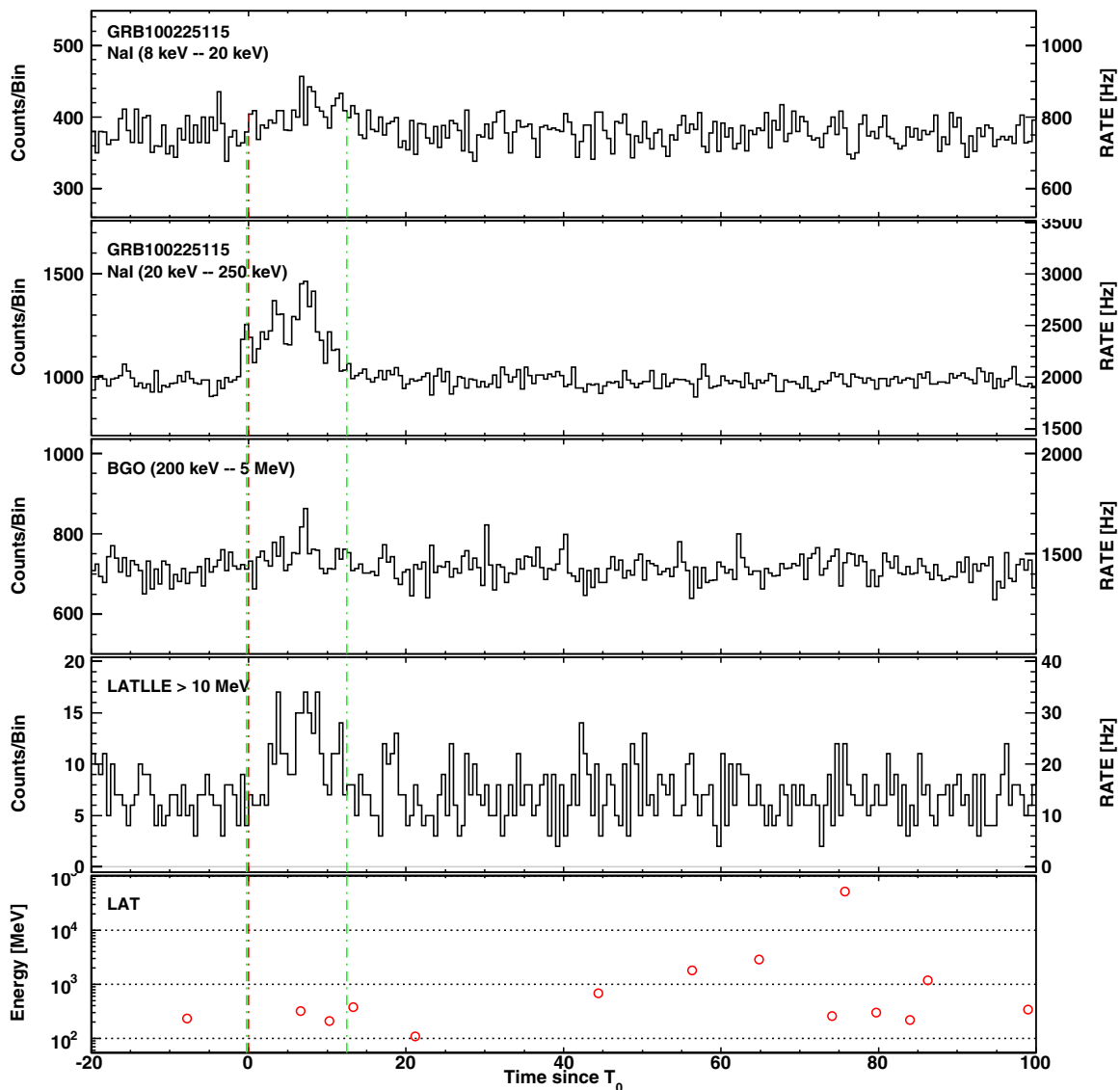
Figure 71. Composite light curve for GRB 100225A: summed GBM/NaI detectors (first two panels), GBM/BGO (third panel), LLE (fourth panel), and LAT Transient-class events above 100 MeV within a 12° ROI (bottom panel). See Appendix B.1 for more information on lines and symbols in the LAT panels.

(A color version of this figure is available in the online journal.)
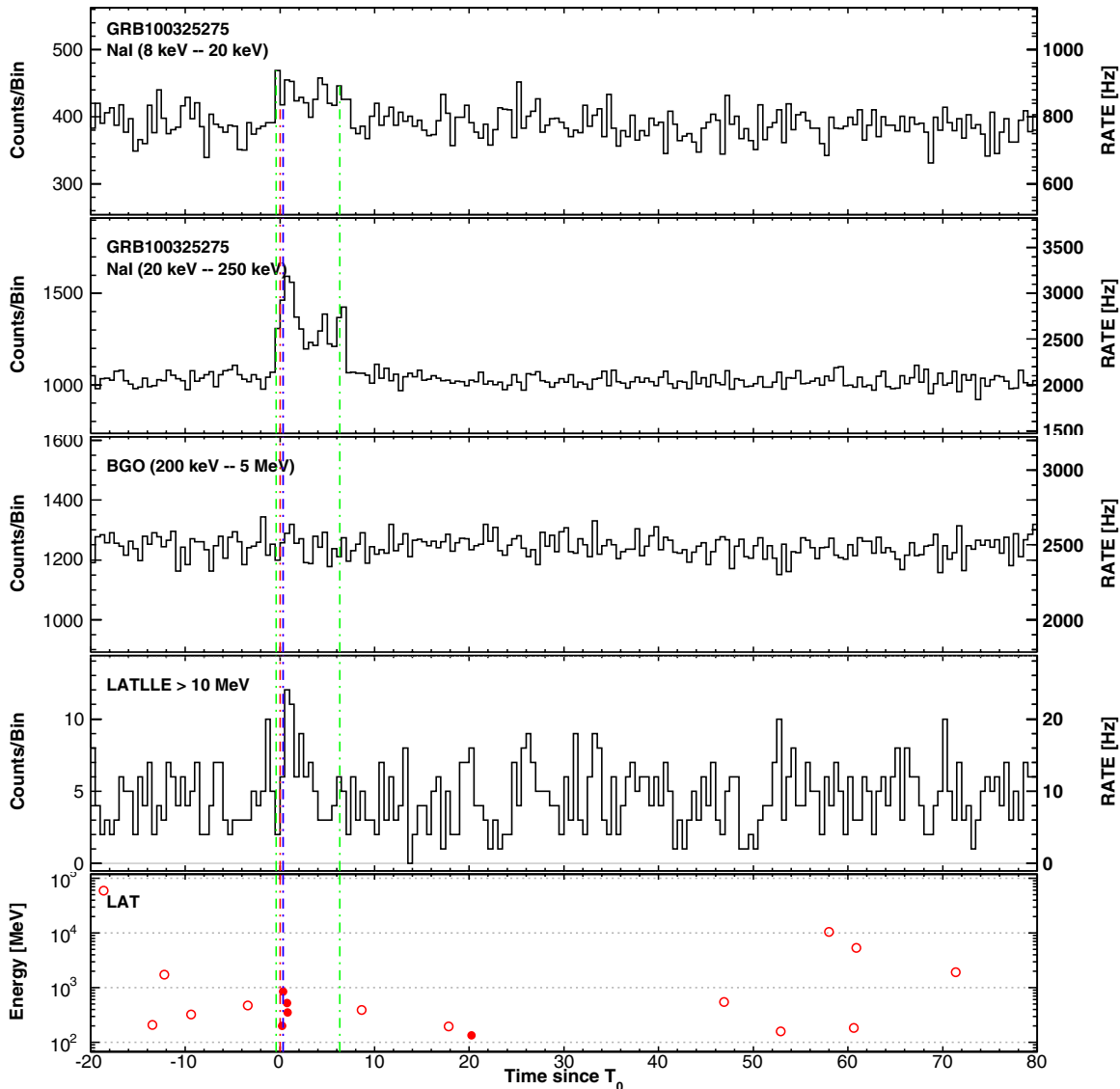
Figure 72. Composite light curve for GRB 100325A: summed GBM/NaI detectors (first two panels), GBM/BGO (third panel), LLE (fourth panel), and LAT Transient-class events above 100 MeV within a 12° ROI (bottom panel). See Appendix B.1 for more information on lines and symbols in the LAT panels.

(A color version of this figure is available in the online journal.)

curve (Figure 72). Due to the paucity of events, no LAT T_{90} could be derived. A cluster of four Transient-class events above 100 MeV are recorded within 0.57 s right after the trigger time and the LAT time-resolved likelihood analysis returned a significant flux up to $T_0+23.7$ s (Figure 73). More interestingly, the time-integrated spectrum of GRB 100325A during the GBM T_{90} is best represented by a Band function, with a hard value for the low-energy spectral slope, $\alpha = -0.33 \pm 0.11$.

B.22. GRB 100414A

The long GRB 100414A triggered the GBM at $T_0 =$ 02:20:21.99 UT on 2010 April 14 (trigger 292904423; Foley 2010). It had an initial off-axis angle of 69° in the LAT and the ARR triggered by the GBM brought it down to ~10° after ~250 s. The LAT preliminary localization was delivered via GCN (Takahashi et al. 2010), with a statistical error of 0°.14. *Swift* TOO observations started ~48 hr after the trigger time and a possible X-ray counterpart was found by *Swift*-XRT (Page et al. 2010b, 2010a). Further observations confirmed the exis-

tence of a fading source (Page & Cannizzo 2010). Follow-up detections in the optical were reported by the *Swift*-UVOT team (Landsman & Cannizzo 2010) and by other observers operating ground-based telescopes (Moskvitin et al. 2010; Urata & Huang 2010). GRB 100414A was also detected in the optical/NIR (Filgas et al. 2010) and in the radio band (Kamble et al. 2010; Frail et al. 2010). Cucchiara & Fox (2010) reported a spectroscopic redshift of $z = 1.368$ based on observations of the optical afterglow using GMOS.

The GBM light curve of GRB 100414A consists of a single slowly rising pulse that ends abruptly after culminating at T_0+23 s (Figure 74). No significant emission was detected in the LLE light curve. Although the LAT $T_{95} = 289^{+90}_{-111}$ s suffers from a large uncertainty due to the relatively small number statistics (~20 events), the burst was detected up to this time with high significance by the LAT likelihood analysis of the Transient-class data above 100 MeV. The LAT time-resolved likelihood analysis returned a significant flux up to T_0+316 s, with a temporal decay index $\alpha = 1.08 \pm 0.43$ (Figure 75). More interestingly, the time-integrated spectrum of GRB 100414A

Figure 73. Likelihood light curve for GRB 100325A (flux above 100 MeV on the left, photon index on the right). See Appendix B.1 for more information on lines and symbols.

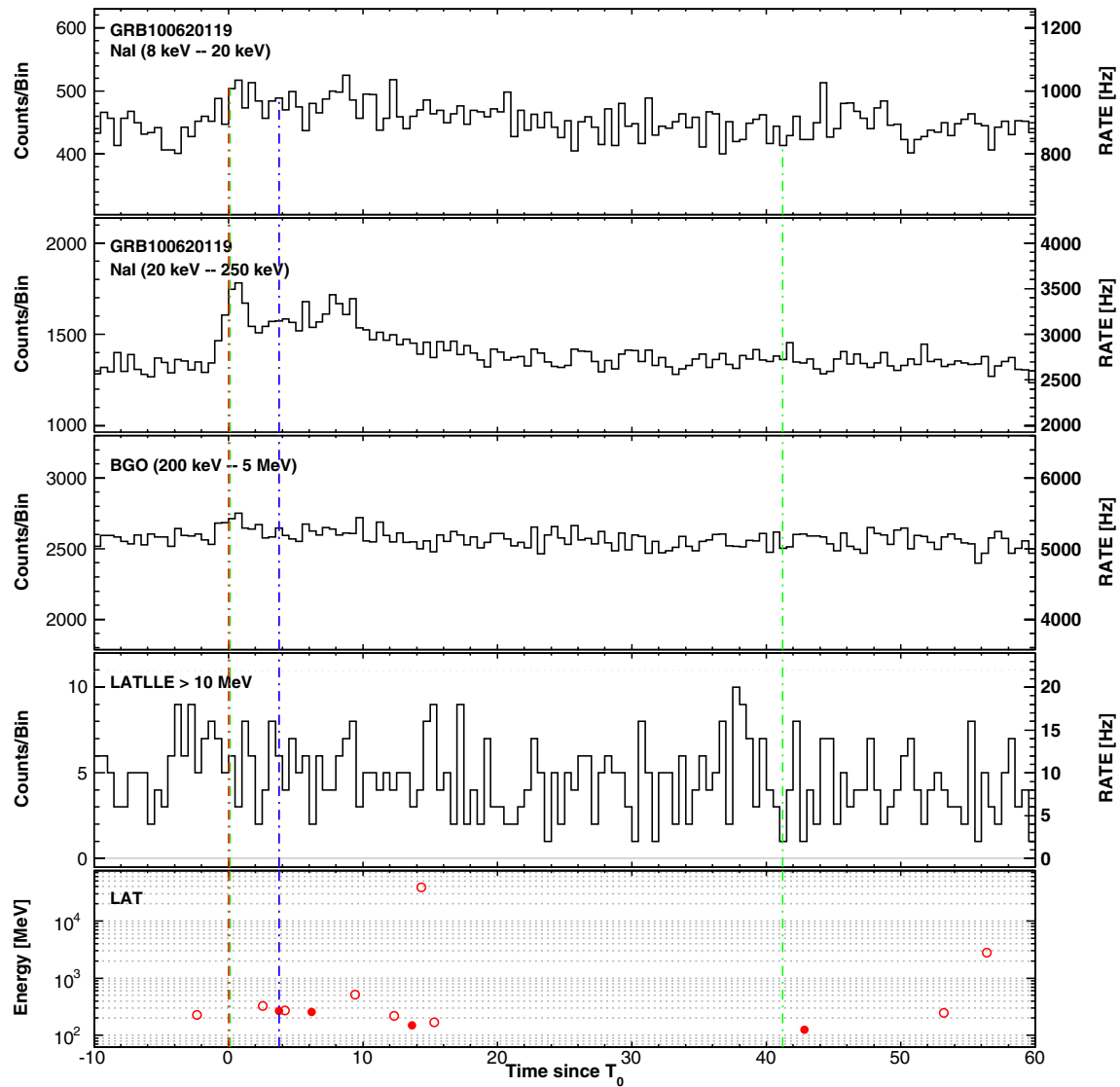(A color version of this figure is available in the online journal.)

Figure 74. Composite light curve for GRB 100414A: summed GBM/NaI detectors (first two panels), GBM/BGO (third panel), LLE (fourth panel), and LAT Transient-class events above 100 MeV within a 12° ROI (bottom panel). See Appendix B.1 for more information on lines and symbols in the LAT panels.

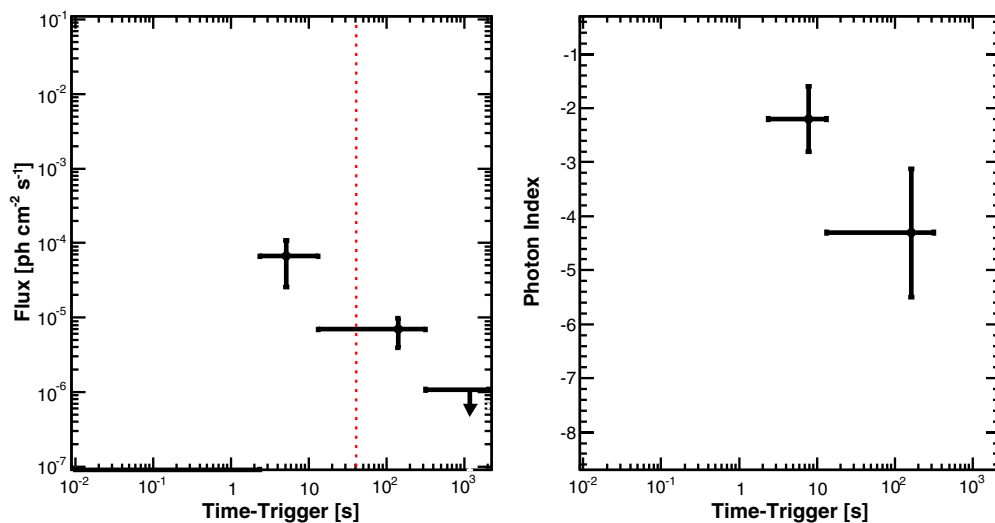(A color version of this figure is available in the online journal.)

Figure 75. Likelihood light curve for GRB 100414A (flux above 100 MeV on the left, photon index on the right). See Appendix B.1 for more information on lines and symbols.

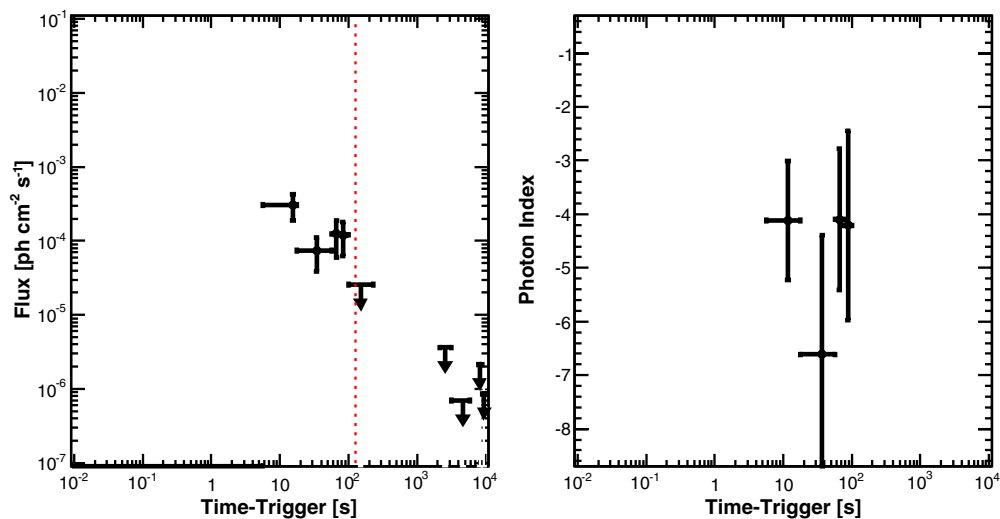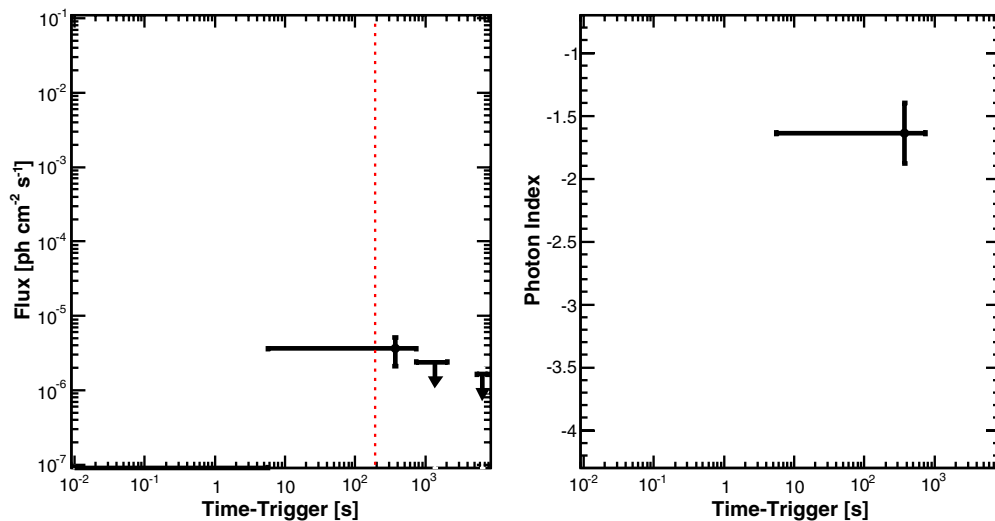(A color version of this figure is available in the online journal.)

during the GBM T_{90} is best represented by a Comptonized model with an additional PL component with a spectral slope of 1.75 ± 0.07. However, as discussed in Section 4.4.1, this additional component is seen in the "GBM" time interval only (Tables 11 and 12) and its existence is uncertain due to possible systematic effects in the GBM-LAT joint spectral analysis during the ARR maneuver.

B.23. GRB 100620A

The long GRB 100620A triggered the GBM at $T_0 = 02:51:29.1134$ UT on 2010 June 20 (trigger 298695091). The best localization reported in the GBM catalog (Paciesas et al. 2012) was used as an initial seed for our analysis. Using LAT Transient-class events above 100 MeV, we could improve upon the GBM localization. The LAT localization, which has a statistical error of $0°.71$ (Table 5), is the final best position. GRB 100620A is a faint burst in the GBM, with no emission in the BGO detector nor in the LLE data (Figure 76). No LAT T_{90} could be derived due to the paucity of events, but accumulating signal in the LAT time-resolved likelihood analysis allowed us to detect a significant flux up to T_0+316 s (Figure 77).

B.24. GRB 100724B

The long GRB 100724B triggered the GBM at $T_0 = 00:42:05.98$ UT on 2010 July 24 (trigger 301624927; Bhat 2010). Its off-axis angle in the LAT was $48°.9$ at the trigger time and remained greater than $40°$ for 2700 s despite the ARR triggered by the GBM, as the *Fermi* spacecraft remained in survey mode as long as the Earth avoidance angle condition was not satisfied. The LAT preliminary localization was delivered via GCN (Tanaka et al. 2010b), with a statistical error of $0°.6$. The burst was also significantly detected by both the *AGILE*-GRID and the *AGILE*-MCAL (Marisaldi et al. 2010; Giuliani et al. 2010b).

GRB 100724B is very bright in the GBM and LLE data, with two main emission episodes (Figure 78). Surprisingly, it is not exceptionally bright in LAT Transient-class data above 100 MeV and the highest energy event (0.22 GeV) is detected at $T_0+61.75$ s, during the second episode. No LAT T_{90} could be derived due to the large zenith angle of the burst, but the

burst was detected up to T_0+125 s with high significance by the LAT likelihood analysis above 100 MeV. This analysis actually revealed a fairly steep high-energy spectrum, with a photon index of -4.96 ± 0.94 during the GBM T_{90} and -4.85 ± 0.92 in the LATTE time interval. Similar indices were measured in the LAT time-resolved likelihood analysis (Figure 79). More interestingly, the time-integrated spectrum of GRB 100724B during the GBM T_{90} is best represented by a Band function with a hard value for the high-energy spectral slope $\beta = -2.00 \pm 0.01$ and with an exponential cutoff at $E_c = 40 \pm 3$ MeV (Tables 11 and 12). The spectral analysis performed by Guiriec et al. (2011) was based on GBM data only and yielded similar results except for the spectral break, whose detection requires the addition of LAT data. Conversely, our analysis is not in agreement with the results reported by Del Monte et al. (2011), who found a single PL spectral shape extending up to 100 MeV with a photon index $\beta = -2.13^{+0.05}_{-0.04}$. This difference could be explained by the larger effective area and the deeper calorimeter of the *Fermi*-LAT (Atwood et al. 2009), which provides more sensitive spectral measurements than the *AGILE* instruments. Owing to its long duration (~120 s in the GBM) and despite the relatively low peak energy $E_p = 263 \pm 4$ keV and the spectral break at MeV energies, GRB 100724B is the most fluent burst in the catalog, with a fluence of $(4.66\pm0.08)\times10^{-4}$ erg cm^{-2} (10 keV–10 GeV, within the GBM T_{90}).

B.25. GRB 100728A

The long GRB 100728A triggered the GBM at $T_0 = 02:17:30.61$ UT on 2010 July 28 (trigger 301976252; von Kienlin 2010b) and the *Swift*-BAT at 02:18:24 UT (Cannizzo et al. 2010a). *Swift*-XRT observations started 76.7 s after the BAT trigger and a bright, uncataloged X-ray source was immediately located (Cannizzo et al. 2010b). The enhanced *Swift*-XRT position (Beardmore et al. 2010) enabled the detection of the optical/NIR afterglow (Perley et al. 2010; Ivarsen et al. 2010; Olivares et al. 2010), but no redshift could be measured.

The GBM light curve of GRB 100728A shows a multi-peaked structure lasting approximately ~190 s (Figure 80). Most of the emission is detected at low energy and the time-integrated spectrum of the burst during the GBM T_{90} is best
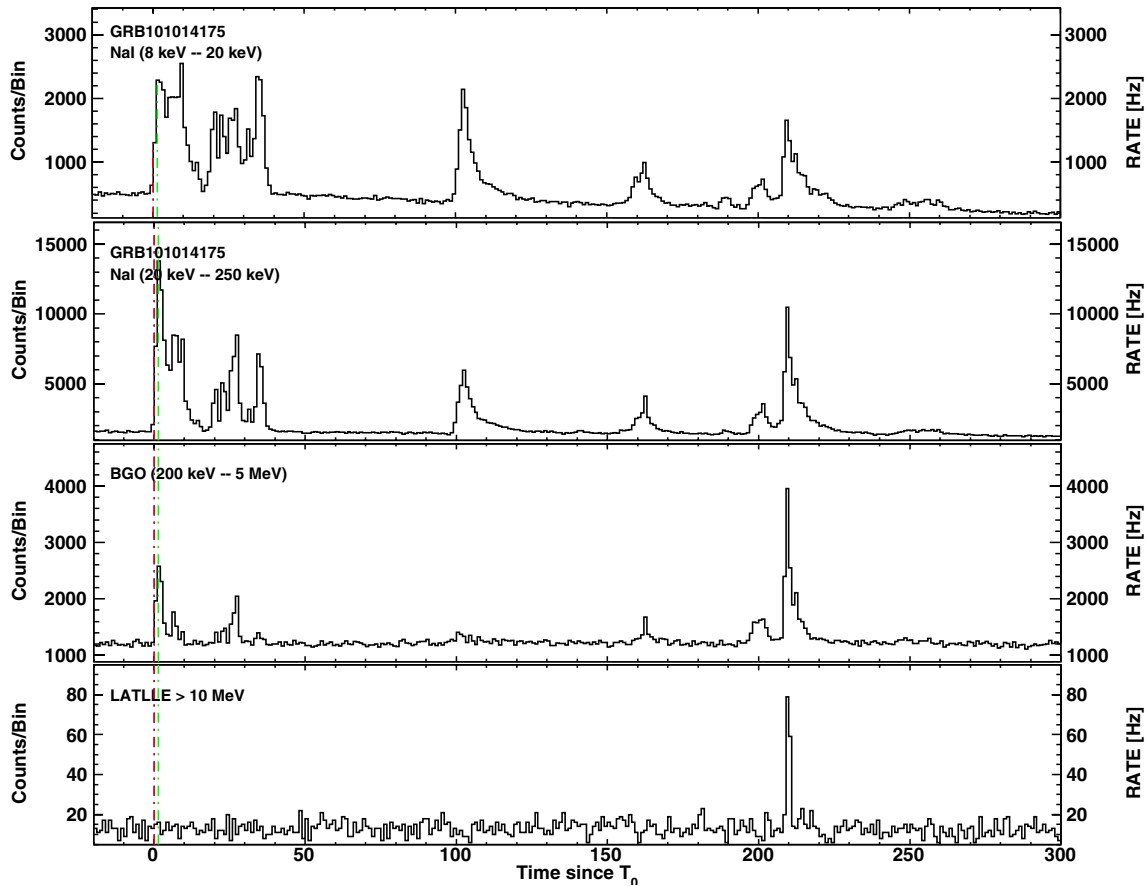
Figure 76. Composite light curve for GRB 100620A: summed GBM/NaI detectors (first two panels), GBM/BGO (third panel), LLE (fourth panel), and LAT Transient-class events above 100 MeV within a 12° ROI (bottom panel). See Appendix B.1 for more information on lines and symbols in the LAT panels.

(A color version of this figure is available in the online journal.)

Figure 77. Likelihood light curve for GRB 100620A (flux above 100 MeV on the left, photon index on the right). See Appendix B.1 for more information on lines and symbols.

(A color version of this figure is available in the online journal.)
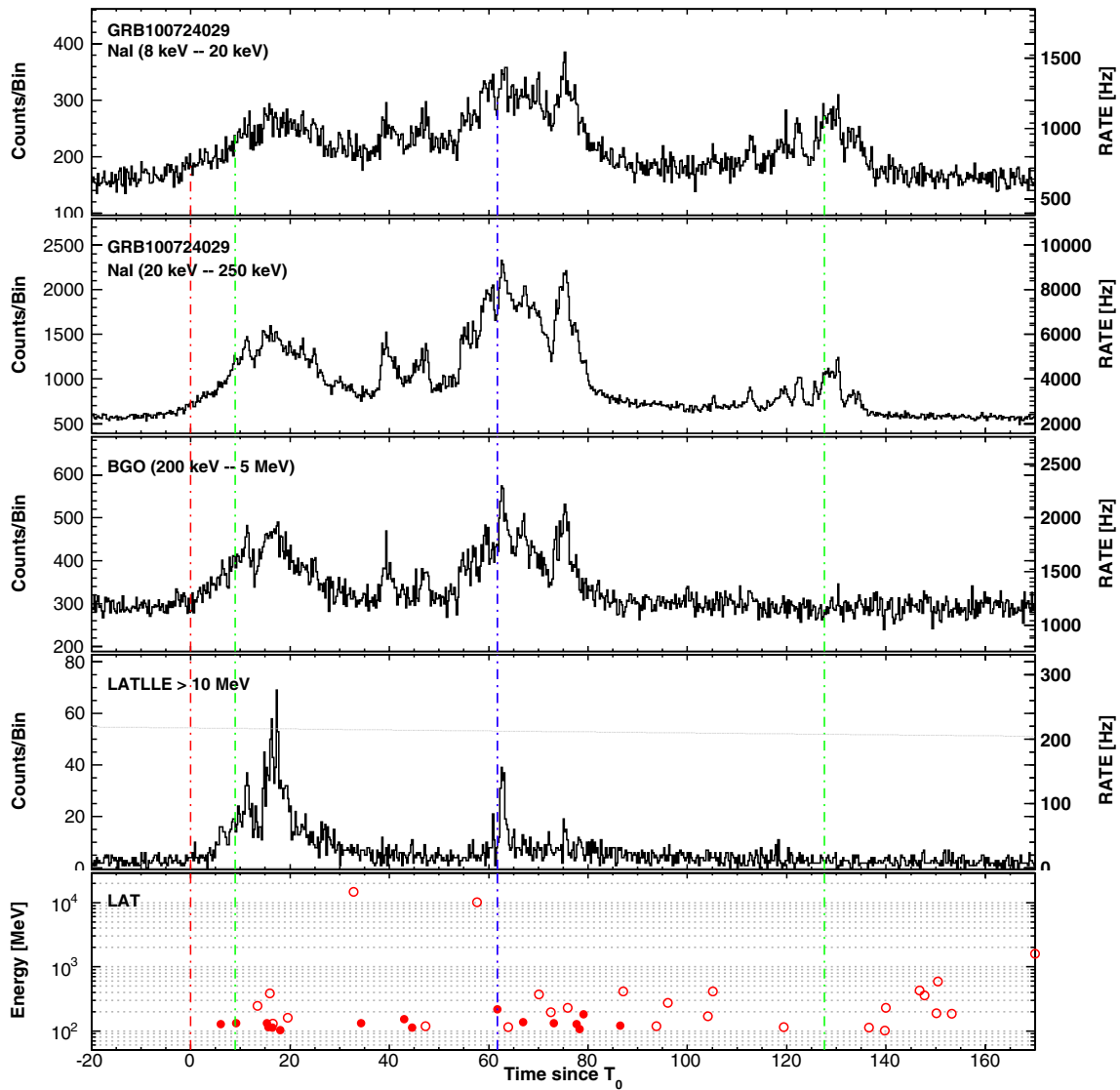
Figure 78. Composite light curve for GRB 100724B: summed GBM/NaI detectors (first two panels), GBM/BGO (third panel), LLE (fourth panel), and LAT Transient-class events above 100 MeV within a 12° ROI (bottom panel). See Appendix B.1 for more information on lines and symbols in the LAT panels.

(A color version of this figure is available in the online journal.)

Figure 79. Likelihood light curve for GRB 100724B (flux above 100 MeV on the left, photon index on the right). See Appendix B.1 for more information on lines and symbols.

(A color version of this figure is available in the online journal.)
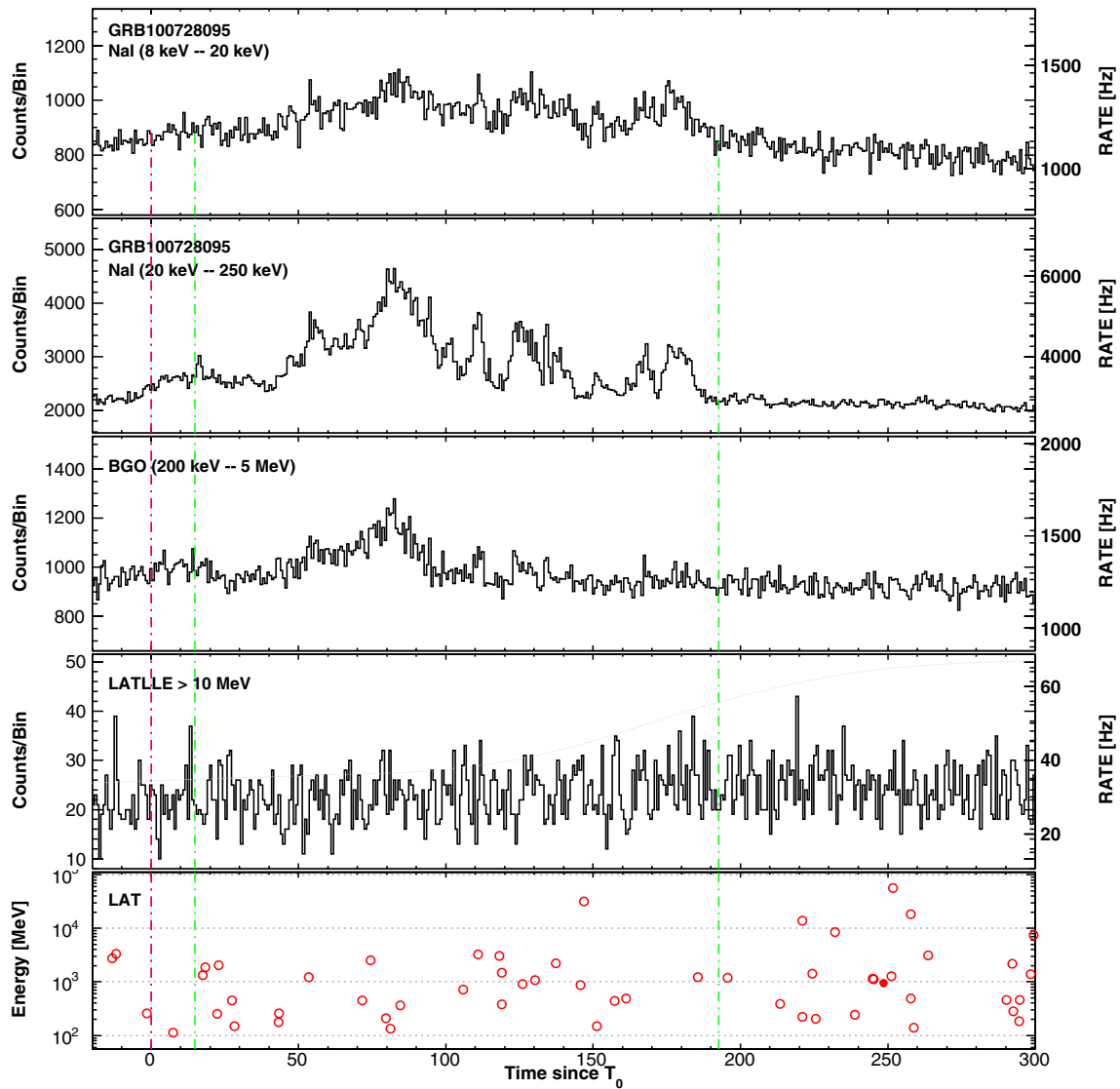
Figure 80. Composite light curve for GRB 100728A: summed GBM/NaI detectors (first two panels), GBM/BGO (third panel), LLE (fourth panel), and LAT Transient-class events above 100 MeV within a 12° ROI (bottom panel). See Appendix B.1 for more information on lines and symbols in the LAT panels.

(A color version of this figure is available in the online journal.)

Figure 81. Likelihood light curve for GRB 100728A (flux above 100 MeV on the left, photon index on the right). See Appendix B.1 for more information on lines and symbols.

(A color version of this figure is available in the online journal.)
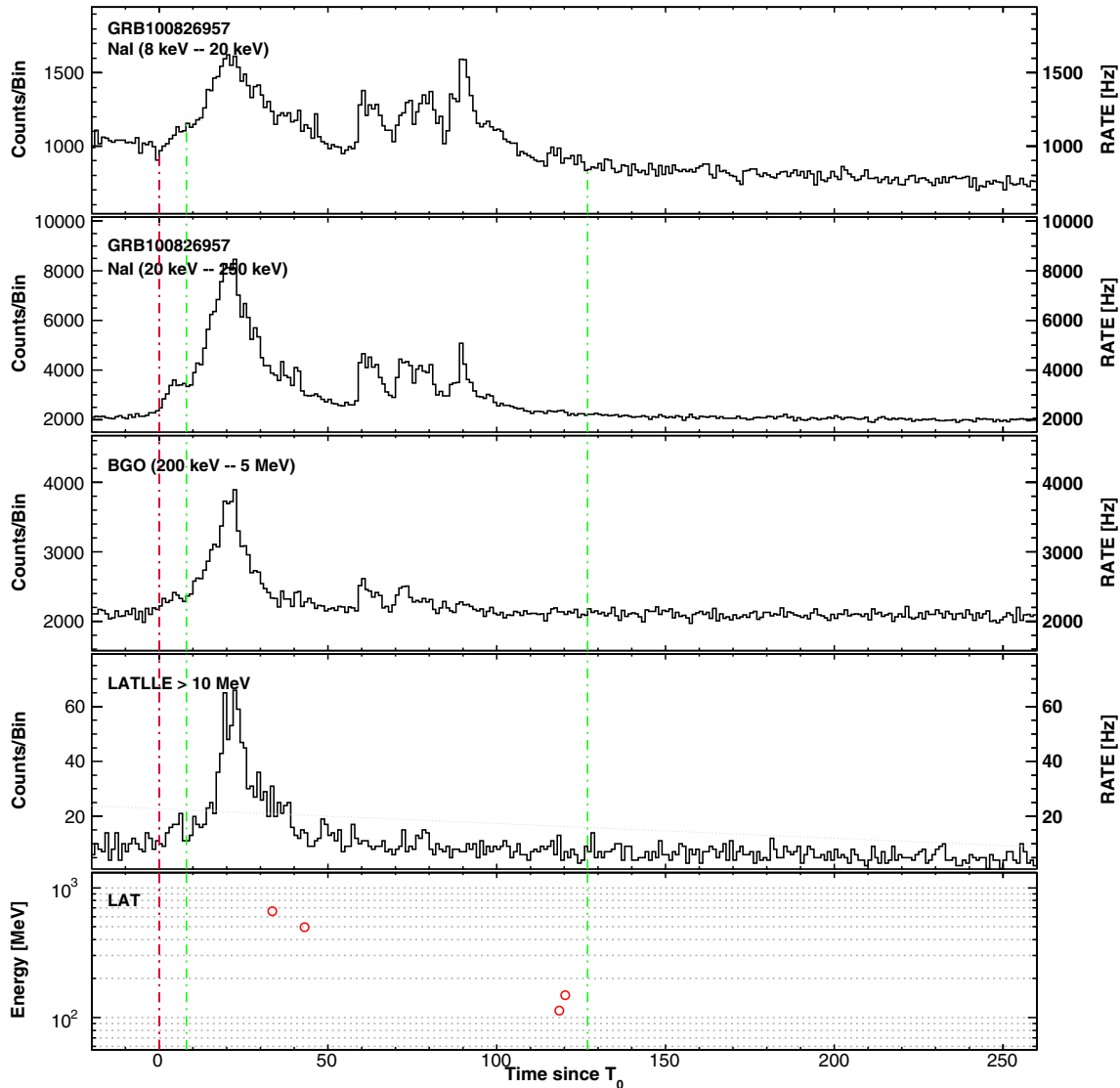
Figure 82. Composite light curve for GRB 100826A: summed GBM/NaI detectors (first two panels), GBM/BGO (third panel), LLE (fourth panel), and LAT Transient-class events above 100 MeV within a 12° ROI (bottom panel). See Appendix B.1 for more information on lines and symbols in the LAT panels.
(A color version of this figure is available in the online journal.)

represented by a Comptonized model. GRB 100728A had an initial off-axis angle of 59°.9 in the LAT and the ARR triggered by the GBM brought it down to ~10° after ~300 s. Only a few LAT Transient-class events above 100 MeV are consistent with the burst position, therefore no LAT T_{90} could be derived and no significant emission was found in the likelihood analysis. Accumulating signal in the LAT time-resolved likelihood analysis allowed us to detect a significant flux in one time bin, ending at T_0+750 s (Figure 81). This detection confirms the temporal coincidence of the high-energy emission of GRB 100728A with its flaring activity in X-rays, as published in Abdo et al. (2011). The implications of the *Fermi*-LAT observation and the possible connection between the γ-ray emission and the X-ray activity of GRB 100728A have also been discussed in He et al. (2012) and Mao & Wang (2012). A 13.54 GeV event with a probability higher than 98% of being associated with the burst is detected ~90 minutes after the trigger time (see the discussion in Section 4.3.3). This represents the only evidence in our catalog that high-energy events (>10 GeV) can arrive very late in time, confirming the

results from Hurley et al. (1994) and suggesting that such events are rare.

B.26. GRB 100826A

The long GRB 100826A triggered the GBM at $T_0 =$ 22:58:22.89 UT on 2010 August 26 (trigger 304556304; McEnery & Omodei 2010). The triangulation of the burst by the IPN provided a position with a 3σ error box area of 1.5 deg^2 (Hurley et al. 2010), which we used in our analysis. Only a few LAT Transient-class events above 100 MeV are consistent with the burst position, therefore no LAT T_{90} could be derived and no significant emission was found in the likelihood analysis. GRB 100826A was detected in the LLE data only (McEnery & Omodei 2010). The LLE light curve has a very similar structure to the GBM broad peak, with the maximum count rate occurring at ~T_0+22 s (Figure 82). The burst is bright in the GBM and its time-integrated spectrum during the GBM T_{90} is best represented by a Band function, with a hard value for the high-energy spectral slope, $\beta = -2.03 \pm 0.02$.
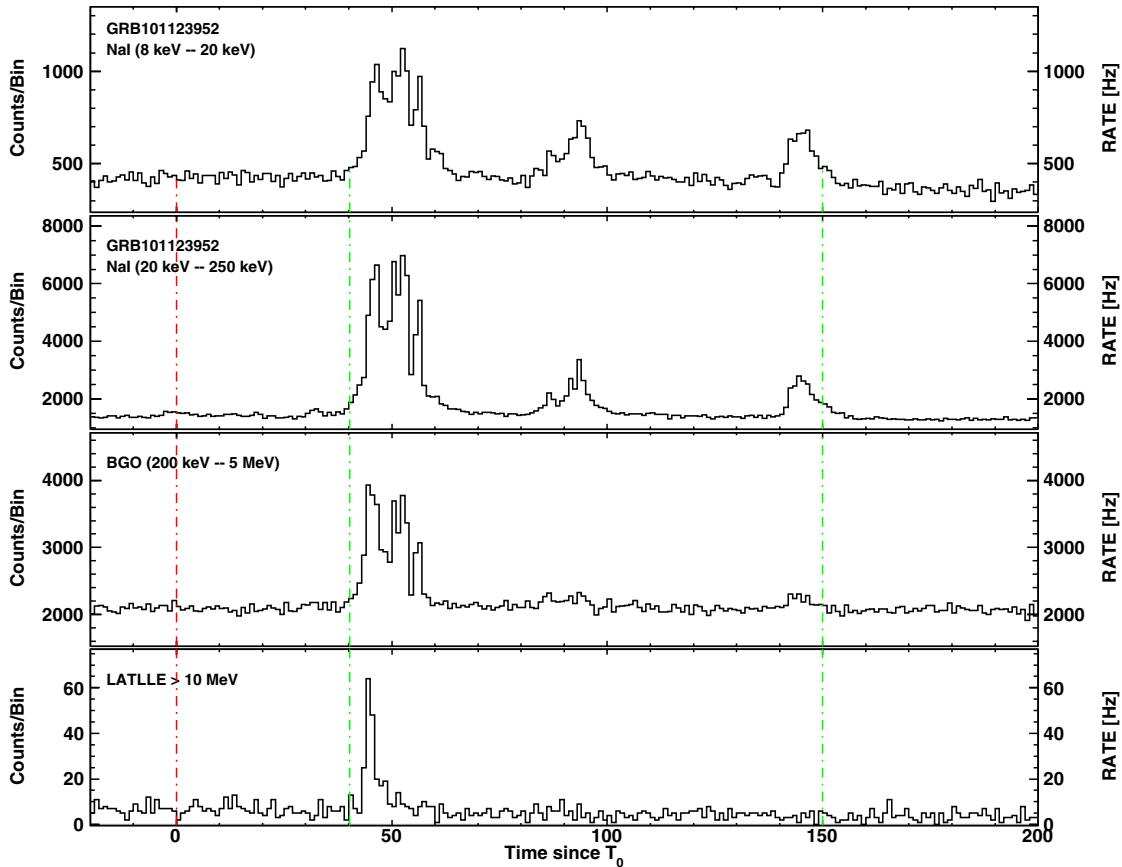
Figure 83. Composite light curve for GRB 101014A: summed GBM/NaI detectors (first two panels), GBM/BGO (third panel) and LLE (bottom panel). See Appendix B.1 for more information on lines.

(A color version of this figure is available in the online journal.)

B.27. GRB 101014A

The long GRB 101014A triggered the GBM at $T_0 = $ 04:11:52.62 UT on 2010 October 14 (trigger 308722314; Tierney & Goldstein 2010) and it has the longest GBM duration ($T_{90} \sim 450$ s) in the catalog. It had an initial off-axis angle of $54°$ in the LAT and the ARR triggered by the GBM brought it down to $\sim 10°$ after ~ 200 s. Because of the burst's proximity to the orbital pole, there was substantial contamination in the surrounding region owing to γ-ray emission from the Earth's limb (Tanaka et al. 2010a). As a result, no LAT Transient-class events are left above 100 MeV after our selection cuts (Section 2.1.1). We could thus not improve upon the GBM localization and no likelihood analysis was possible. GRB 101014A was detected in the LLE data only. Whereas the GBM light curve exhibits several emission episodes, the LLE light curve consists of a single, narrow pulse at $\sim T_0 + 210$ s (Figure 83).

B.28. GRB 101123A

The long GRB 101123A triggered the GBM at $T_0 = $ 22:51:34.97 UT on 2010 November 23 (trigger 312245496; Guiriec 2010). It had an initial off-axis angle of $78°2$ in the LAT and a large zenith angle, thus no LAT Transient-class events are left above 100 MeV after our selection cuts (Section 2.1.1). We could thus not improve upon the GBM localization and no likelihood analysis was possible. GRB 101123A was detected in the LLE data only. The LLE light curve consists of a single, narrow pulse at $\sim T_0 + 45$ s, in temporal coincidence with the

first pulse of the first bright emission episode observed in the GBM light curve (Figure 84) The burst is relatively bright in the GBM and its time-integrated spectrum during the GBM T_{90} is best represented by a Band function, with a hard value for the high-energy spectral slope, $\beta = -2.04 \pm 0.03$.

B.29. GRB 110120A

The long GRB 110120A triggered the GBM at $T_0 = $ 15:59:39.23 UT on 2011 January 20 (trigger 317231981; Lin 2011). In spite of an initial off-axis angle of $13°6$, GRB 110120A was relatively faint in the LAT. The LAT preliminary localization was delivered via GCN (Omodei et al. 2011), with a statistical error of $0°4$. The GBM light curve of GRB 110120A consists of two overlapping pulses (Figure 85). The LLE light curve shows a small signal excess that coincides with the GBM emission, but this excess was not significant enough to claim an LLE detection (see Table 2). Our analysis of the LAT Transient-class data above 100 MeV provided a LAT $T_{95} = 113^{+21}_{-30}$ s, which indicates the temporal extension of the burst emission in the LAT. In addition, a 1.82 GeV event is recorded at $T_0 + 72.46$ s. The LAT time-resolved likelihood analysis returned a significant flux in two time bins only, up to $T_0 + 75$ s (Figure 86).

B.30. GRB 110328B

The long GRB 101123A triggered the GBM at $T_0 = $ 12:29:19.19 UT on 2011 March 28 (trigger 323008161; von Kienlin 2011). Only a few LAT Transient-class events above 100 MeV are consistent with the burst position, therefore no
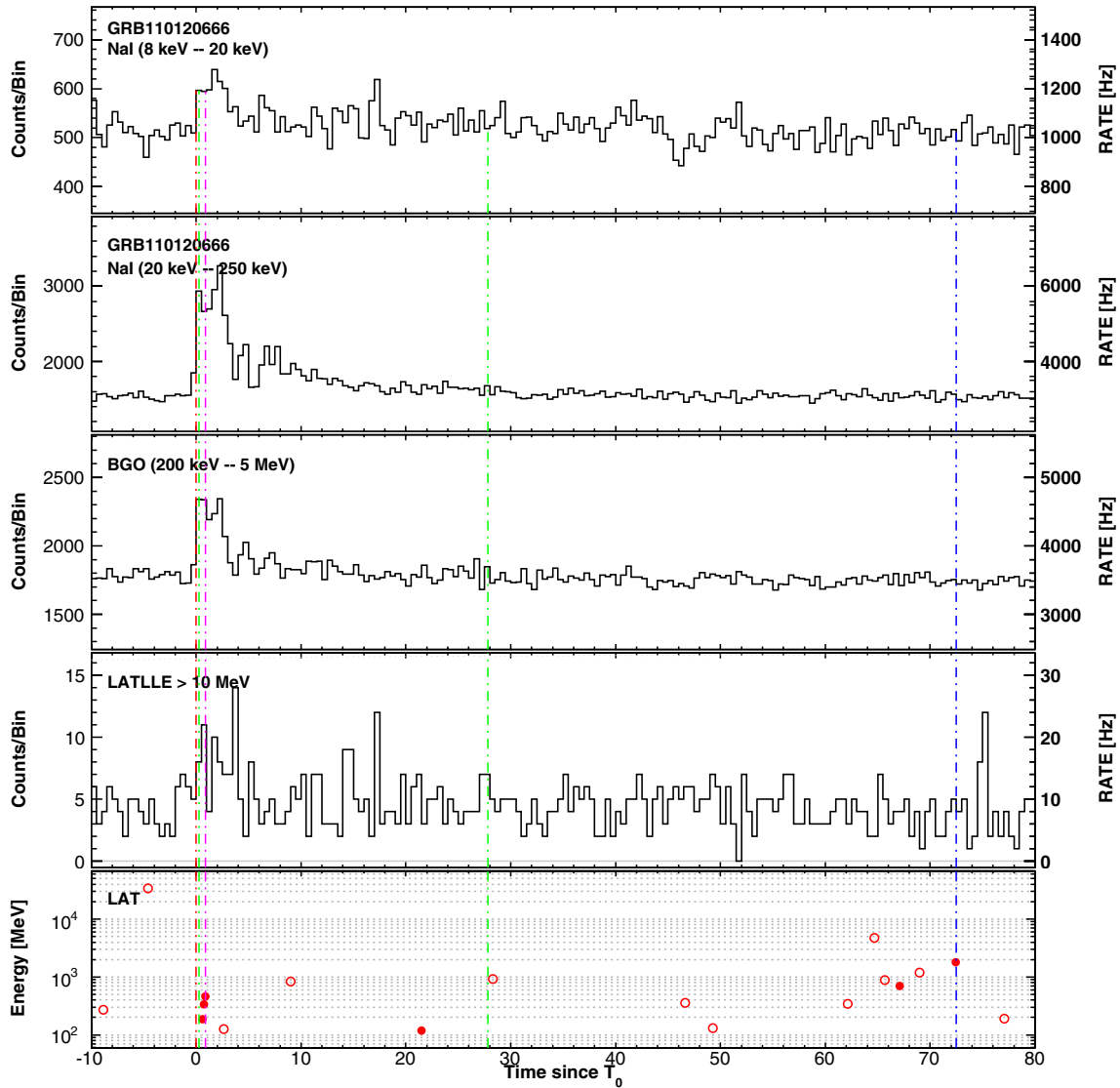
Figure 84. Composite light curve for GRB 101123A: summed GBM/NaI detectors (first two panels), GBM/BGO (third panel) and LLE (bottom panel). See Appendix B.1 for more information on lines.

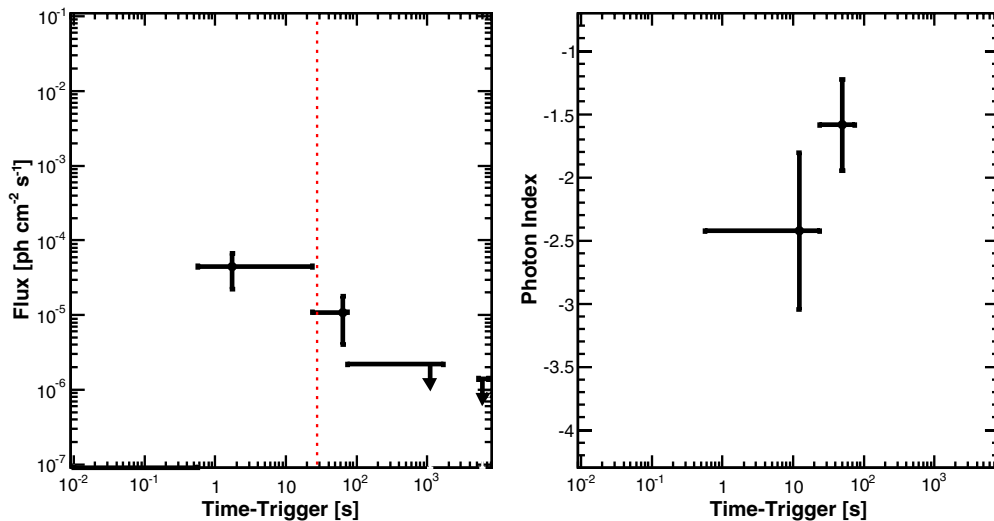(A color version of this figure is available in the online journal.)

LAT T_{90} could be derived and no significant emission was found in the likelihood analysis. Using a lower energy threshold of 50 MeV, a tentative localization with the LAT was delivered via GCN (Vasileiou et al. 2011a), consistent with the GBM localization and with a statistical error of 1°.7. GRB 110328B was detected in the LLE data only. The LLE light curve consists of a single pulse that starts approximately at the time of the GBM trigger and mimics the light curve seen in the NaI and BGO detectors (Figure 87).

B.31. GRB 110428A

The long GRB 110428A triggered the GBM at $T_0 = $ 09:18:30.41 UT on 2011 April 28 (trigger 325675112; Tierney & Fitzpatrick 2011). It had an initial off-axis angle of 34°.6 in the LAT and the ARR triggered by the GBM brought it down to $\sim 5°$ after ~ 200 s. The LAT preliminary localization was delivered via GCN (Vasileiou et al. 2011b), with a statistical error of 0°.15. *Swift* TOO observations started ~ 55.6 ks after the trigger time and a possible X-ray counterpart was found by *Swift*-XRT (Melandri et al. 2011b). Further observations confirmed the existence of a fading source (Melandri et al. 2011a).

The GBM light curve of GRB 110428A consists of several overlapping pulses (Figure 88). No significant emission was detected in the LLE light curve. The highest energy event (2.62 GeV) is detected at $T_0 + 14.79$ s and does not coincide with any noticeable feature in the GBM light curve. Although the LAT $T_{95} = 408^{+93}_{-336}$ s suffers from a large uncertainty due to the relatively small number statistics (~ 16 events),

the burst was detected up to this time with high significance by the LAT likelihood analysis of the Transient-class data above 100 MeV. The LAT time-resolved likelihood analysis returned a significant flux in two time bins only, up to $T_0 + 178$ s (Figure 89). More interestingly, the time-integrated spectrum of GRB 110428A during the GBM T_{90} is best represented by a Band function, with a steep value for the high-energy spectral slope, $\beta = -2.90 \pm 0.10$. This value is very different from the hard photon index of -1.73 ± 0.20, which is found by the likelihood analysis at late times (Figure 89). In the catalog, GRB 110428A is thus among the bursts that show the strongest spectral evolution between the prompt and late emission phases.

B.32. GRB 110529A

The short GRB 110529A triggered the GBM at $T_0 = $ 00:48:42.87 UT on 2011 May 29 (trigger 328322924; Burgess & Guiriec 2011). Only a few LAT Transient-class events above 100 MeV are consistent with the burst position, therefore no significant emission was found in the likelihood analysis. The burst was detected in the LLE data only (McEnery et al. 2011) and the light curve consists of a short spike coincidental with the GBM emission (Figure 90).

B.33. GRB 110625A

The long GRB 110625A triggered the GBM at $T_0 = $ 21:08:18.24 UT on 2011 June 25 (trigger 330728900; Gruber et al. 2011) and the *Swift*-BAT at 21:08:28 UT (Page et al. 2011a). *Swift*-XRT observations started 140.3 s after the
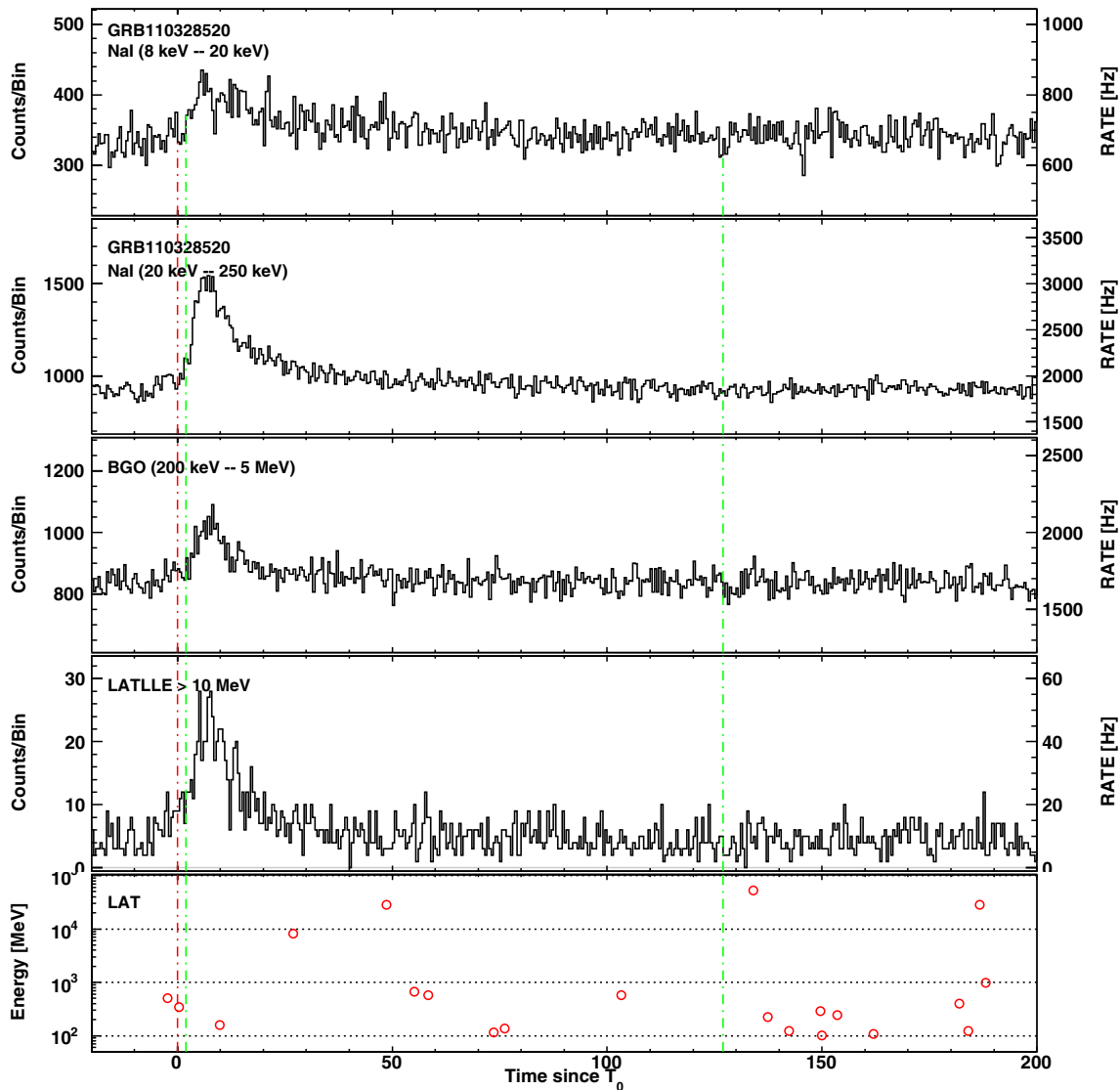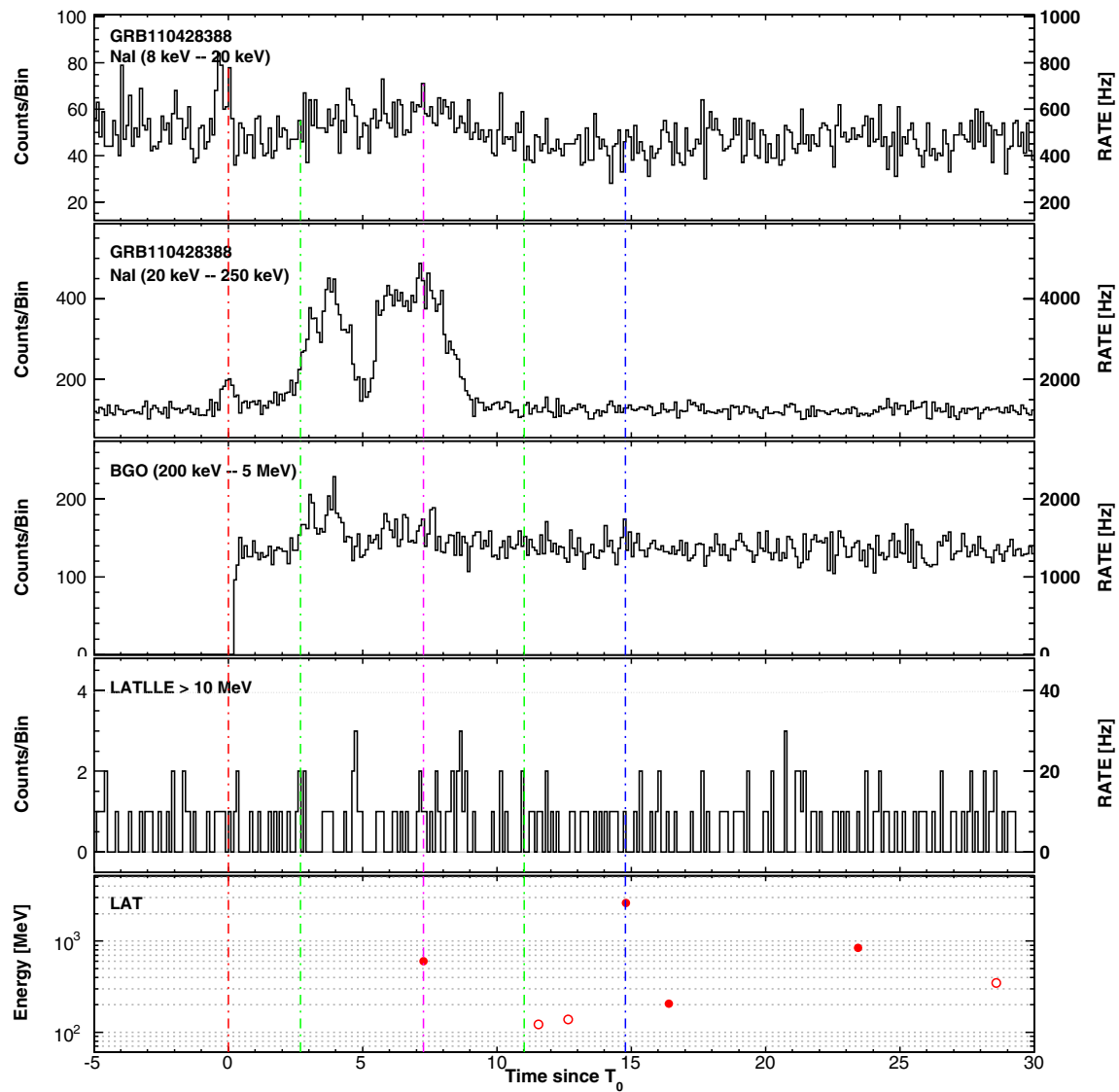
Figure 85. Composite light curve for GRB 110120A: summed GBM/NaI detectors (first two panels), GBM/BGO (third panel), LLE (fourth panel), and LAT Transient-class events above 100 MeV within a 12° ROI (bottom panel). See Appendix B.1 for more information on lines and symbols in the LAT panels.

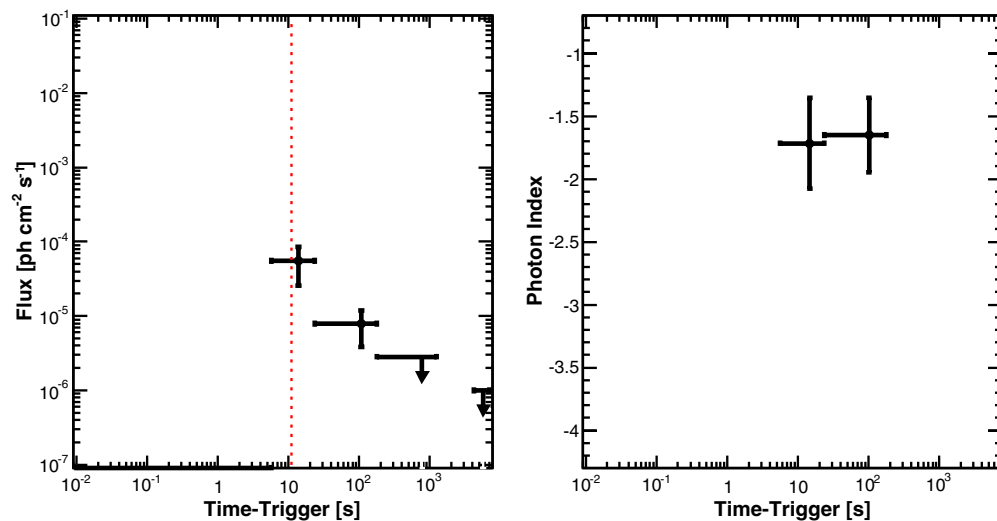(A color version of this figure is available in the online journal.)

Figure 86. Likelihood light curve for GRB 110120A (flux above 100 MeV on the left, photon index on the right). See Appendix B.1 for more information on lines and symbols.

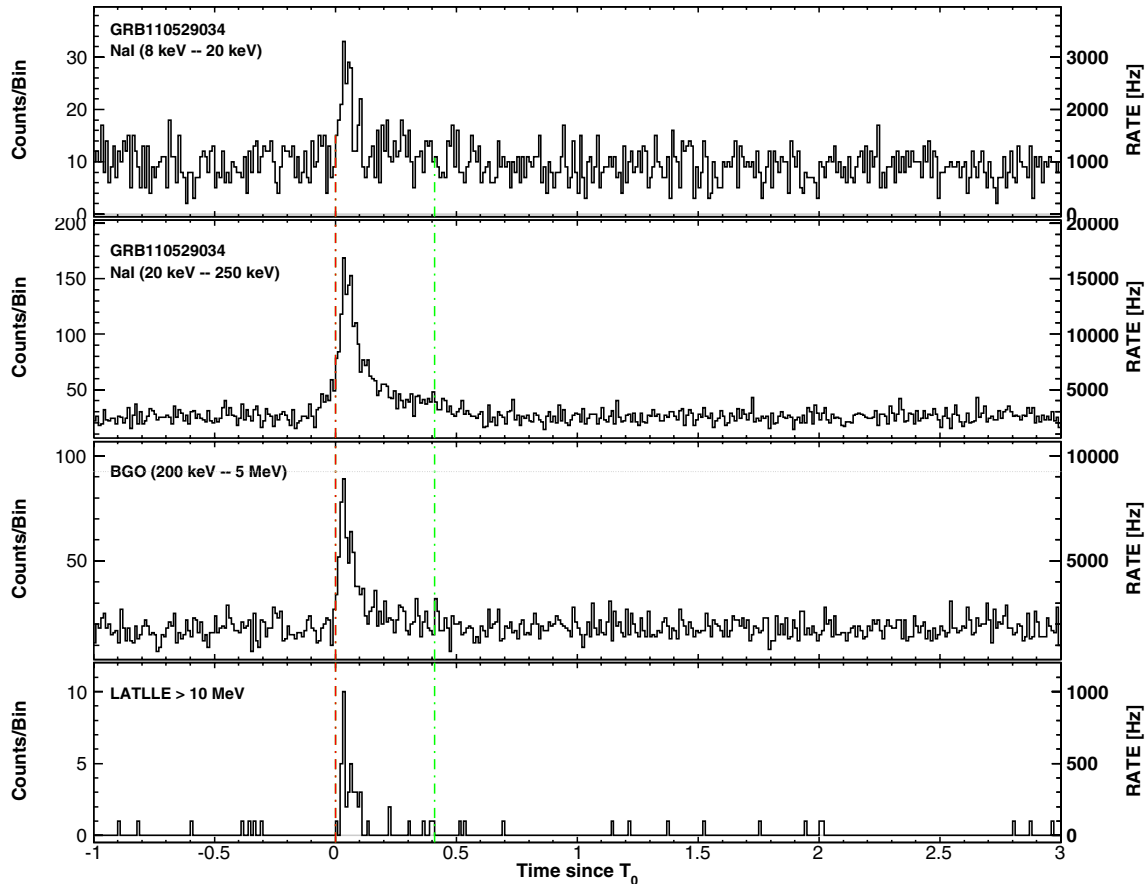(A color version of this figure is available in the online journal.)

Figure 87. Composite light curve for GRB 110328B: summed GBM/NaI detectors (first two panels), GBM/BGO (third panel), LLE (fourth panel), and LAT Transient-class events above 100 MeV within a 12° ROI (bottom panel). See Appendix B.1 for more information on lines and symbols in the LAT panels.

(A color version of this figure is available in the online journal.)

BAT trigger and a bright, fading, and uncataloged X-ray source was immediately located (Page et al. 2011b). Further analysis refined the position of the X-ray source (Palmer et al. 2011; Page 2011), enabling optical follow-up observations (Kelemen 2011a; Im et al. 2011; Filgas et al. 2011; Gorosabel et al. 2011; Holland & Page 2011; Golovnya 2011), but no redshift could be measured. GRB 110625A was bright enough to trigger an ARR of the *Fermi* spacecraft. However, its initial off-axis angle of 87°9 in the LAT resulted in a very poor photon statistics above 100 MeV (Figure 91) and no LAT T_{90} could be derived. In addition, the *Fermi* spacecraft continued its maneuver toward the GBM flight software reconstructed position, which was off by 68° from the enhanced *Swift*-XRT position (Page 2011), providing non-optimal exposure for LAT follow-up observations. Accumulating signal in the LAT time-resolved likelihood analysis allowed us to detect a significant flux in two time bins, up to T_0+562 s (Gruber et al. (2011) and Figure 92), confirming the earlier detection by Tam & Kong (2011). The highest energy event (2.42 GeV) is detected at T_0+272.44 s.

B.34. GRB 110709A

The long GRB 110709A triggered the GBM at T_0 = 15:24:27.37 UT on 2011 July 9 (trigger 331917869; Connaughton 2011) and the *Swift*-BAT at 15:24:29 UT (Holland et al. 2011a). *Swift*-XRT observations started 65.6 s after the BAT trigger and a bright, uncataloged X-ray source was immediately located (Holland et al. 2011b). Further analysis refined the position of the X-ray source (Evans 2011; Osborne et al. 2011). In spite of numerous follow-up observations (Ivanov et al. 2011; Xin et al. 2011; Tello et al. 2011; Kuroda et al. 2011; Kelemen 2011b; Holland 2011), no optical afterglow was detected. GRB 110709A was bright enough to trigger an ARR of the *Fermi* spacecraft. However, its initial off-axis angle of 53°4 in the LAT resulted in a very poor photon statistics above 100 MeV (Figure 93). The LAT time-resolved likelihood analysis returned a significant flux in one time bin only, ending at T_0+42 s (Figure 94). In addition, no LAT T_{90} could be derived due to the large zenith angle of the burst.

Figure 88. Composite light curve for GRB 110428A: summed GBM/NaI detectors (first two panels), GBM/BGO (third panel), LLE (fourth panel), and LAT Transient-class events above 100 MeV within a 12° ROI (bottom panel). See Appendix B.1 for more information on lines and symbols in the LAT panels.

(A color version of this figure is available in the online journal.)

Figure 89. Likelihood light curve for GRB 110428A (flux above 100 MeV on the left, photon index on the right). See Appendix B.1 for more information on lines and symbols.

(A color version of this figure is available in the online journal.)

Figure 90. Composite light curve for GRB 110529A: summed GBM/NaI detectors (first two panels), GBM/BGO (third panel) and LLE (bottom panel). See Appendix B.1 for more information on lines.

(A color version of this figure is available in the online journal.)

B.35. GRB 110721A

The long GRB 110721A triggered the GBM at $T_0 = $ 04:47:43.75 UT on 2011 July 21 (trigger 332916465; Tierney & von Kienlin 2011). It had an initial off-axis angle of $40°3$ in the LAT and the ARR triggered by the GBM brought it down to $\sim 10°$ after ~ 240 s. The LAT preliminary localization was delivered via GCN (Vasileiou et al. 2011c), with a statistical error of $0°51$. A low-significance faint candidate afterglow was found by Greiner et al. (2011) analyzing the *Swift*-XRT and GROND data. Using GMOS, Berger (2011) found two clear absorption features at 5487 and 5436 Å, matching Ca II H&K at a redshift of $z = 0.382$, with a significant decline in flux at shorter wavelengths, but to a non-zero level. However, the triangulation of the burst by the IPN provided a position with a 3σ error box area of 2250 arcmin², excluding the position of the candidate afterglow (Hurley et al. 2011). Moreover, further observations with *Swift*-XRT did not confirm the afterglow detection (Grupe et al. 2011) and radio observations with the Expanded Very Large Array suggested that the X-ray candidate was instead associated with the radio-loud Active Galactic Nucleus; PKS 2211-388 (Chandra et al. 2011). As a result, we used the IPN position in our analysis and we did not assume any redshift for this burst.

A dedicated analysis of the prompt emission spectrum of GRB 110721A is presented in Axelsson et al. (2012). The NaI light curve of GRB 110721A consists of two overlapping pulses. Whereas only the first pulse is visible in the BGO and LLE light curves, the second pulse is much softer and is detected down to

8–20 keV (Figure 95). The LLE pulse starts and peaks earlier than the GBM emission. It appears narrower and the highest energy event (1.73 GeV) is detected at $T_0+0.74$ s. However, the LAT emission above 100 MeV could last longer, potentially up to T_0+239 s or later. Due to the large zenith angle of the burst after this time and the paucity of events after the end of the GBM emission, we could not perform a good measurement of the LAT T_{95}, however. The LAT time-resolved likelihood analysis actually returned a significant signal up to T_0+24 s only (Figure 96).

B.36. GRB 110731A

The long GRB 110731A triggered the GBM at $T_0 = $ 11:09:29.94 UT on 2011 July 31 (trigger 333803371; Gruber 2011) and the *Swift*-BAT at 11:09:30 UT (Oates et al. 2011a). The LAT preliminary localization was delivered via GCN (Bregeon et al. 2011), with a statistical error of $0°2$. GRB 110731A was bright enough to trigger an ARR of the *Fermi* spacecraft. Its initial off-axis angle was $3°4$ in the LAT, thus the repointing had little impact on the prompt emission phase observations and permitted excellent observations of the extended emission for 2.5 hr after the trigger time. High quality, continuous observations of the burst are available until the first *Fermi* passage into the SAA at $\sim T_0+1400$ s. The ARR continued for another 90 minutes after *Fermi* had exited the SAA. *Swift*-XRT observations started 56 s after the BAT trigger (Oates et al. 2011b). A bright, uncataloged X-ray source was found and
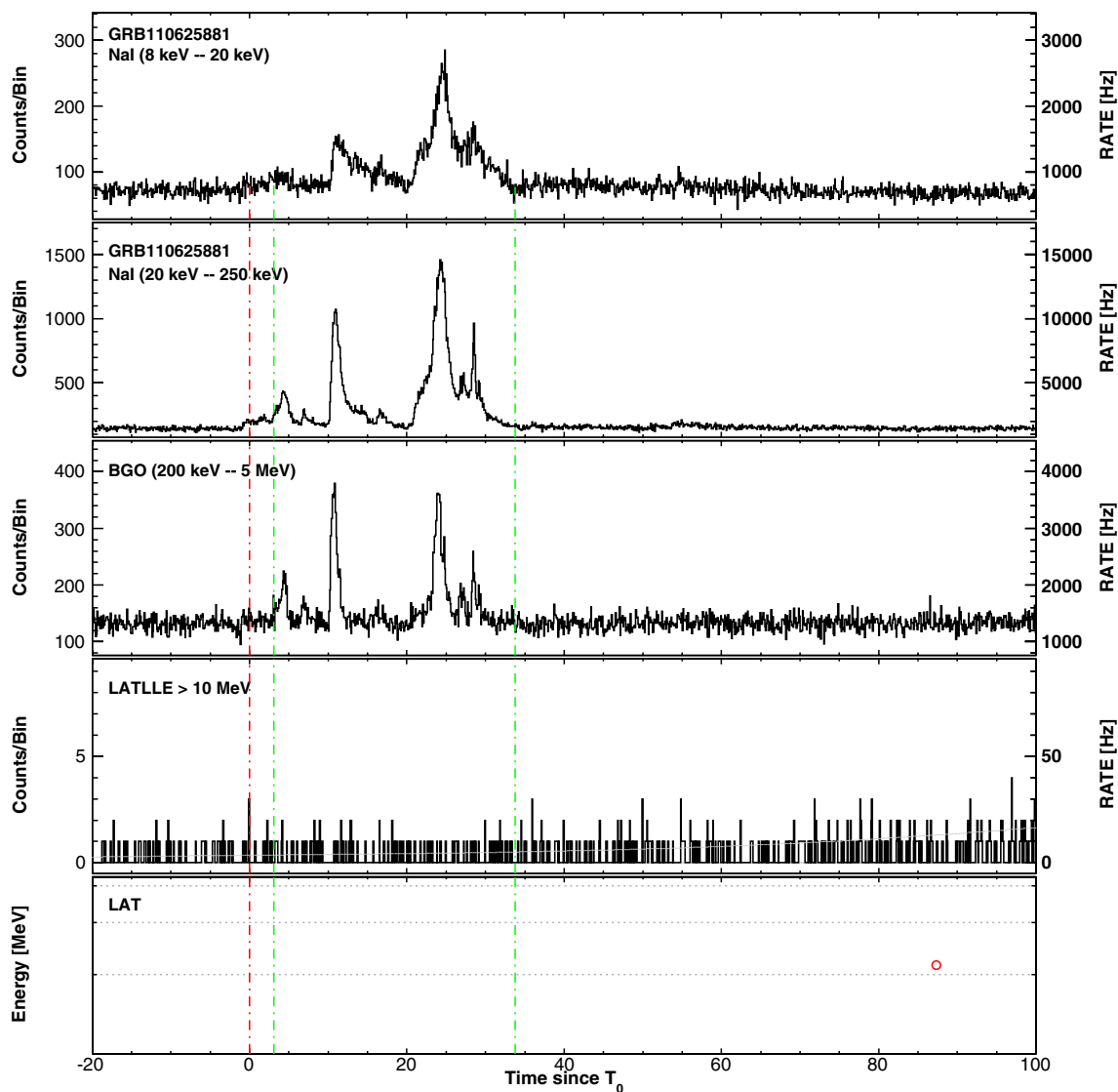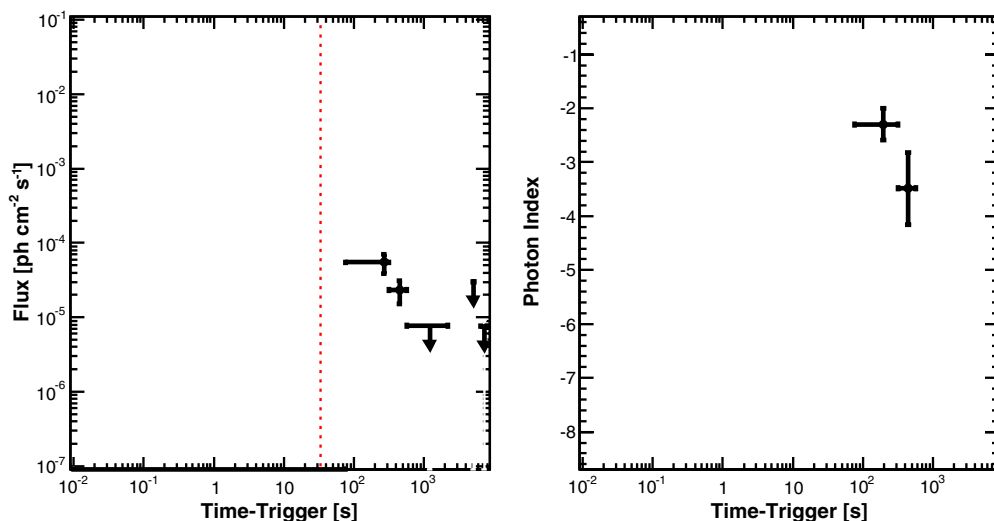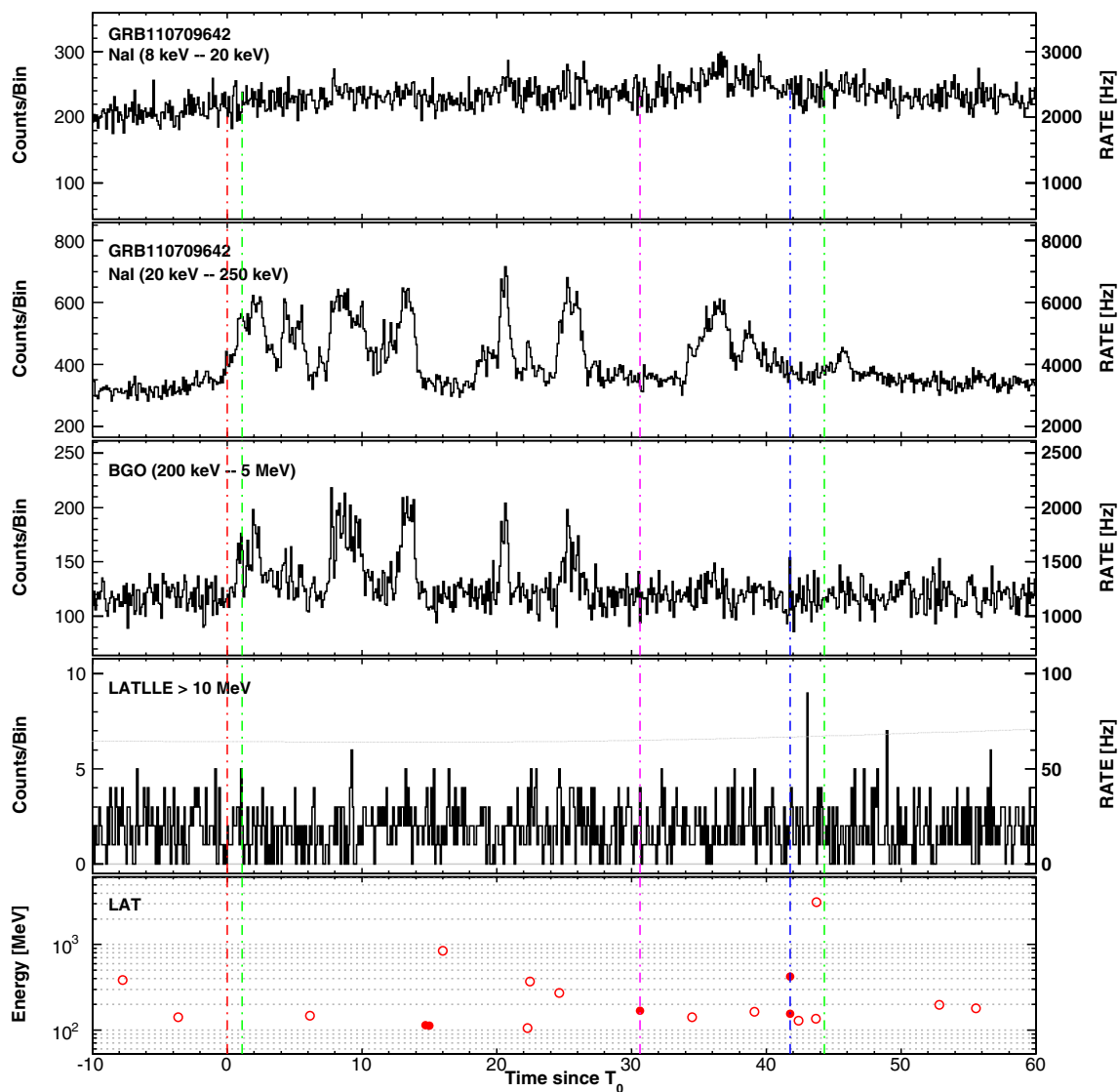
Figure 91. Composite light curve for GRB 110625A: summed GBM/NaI detectors (first two panels), GBM/BGO (third panel), LLE (fourth panel), and LAT Transient-class events above 100 MeV within a 12° ROI (bottom panel). See Appendix B.1 for more information on lines and symbols in the LAT panels.

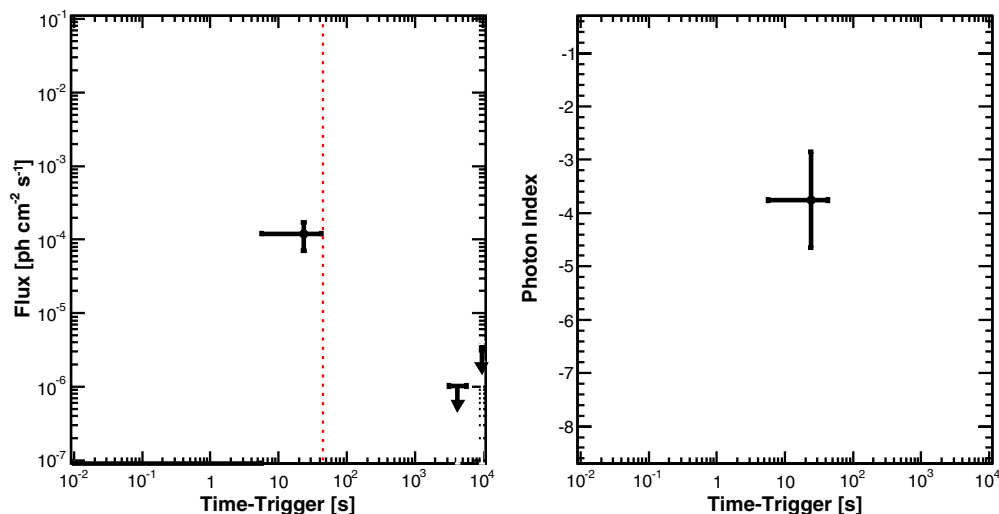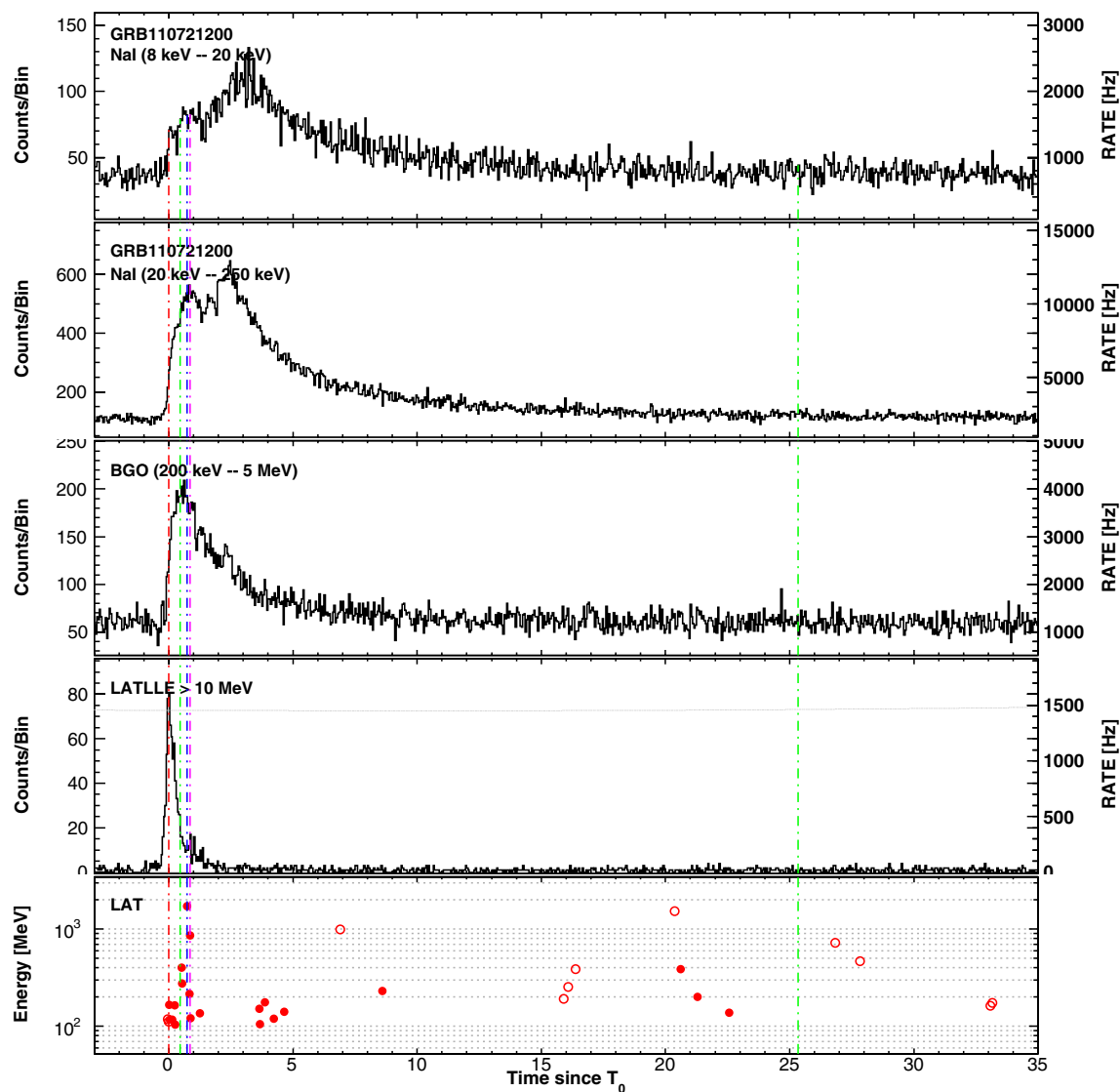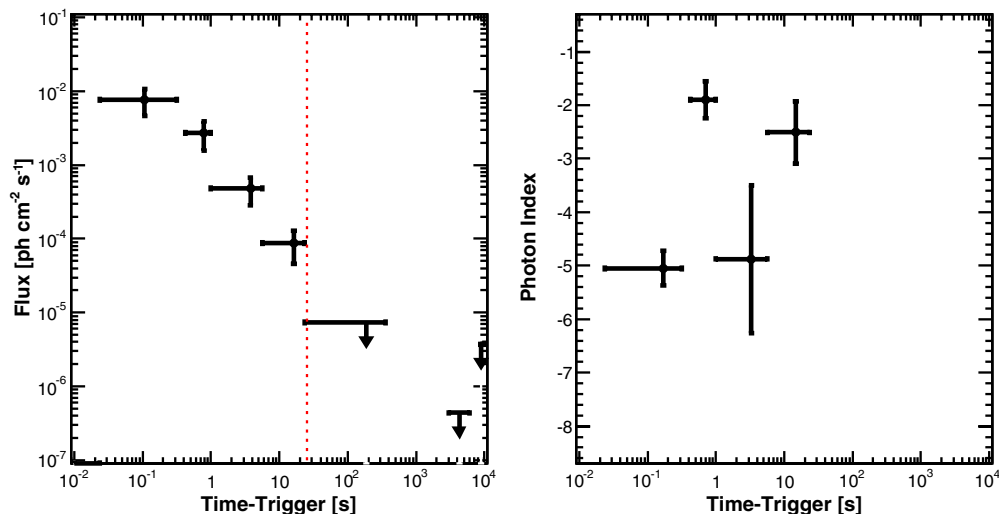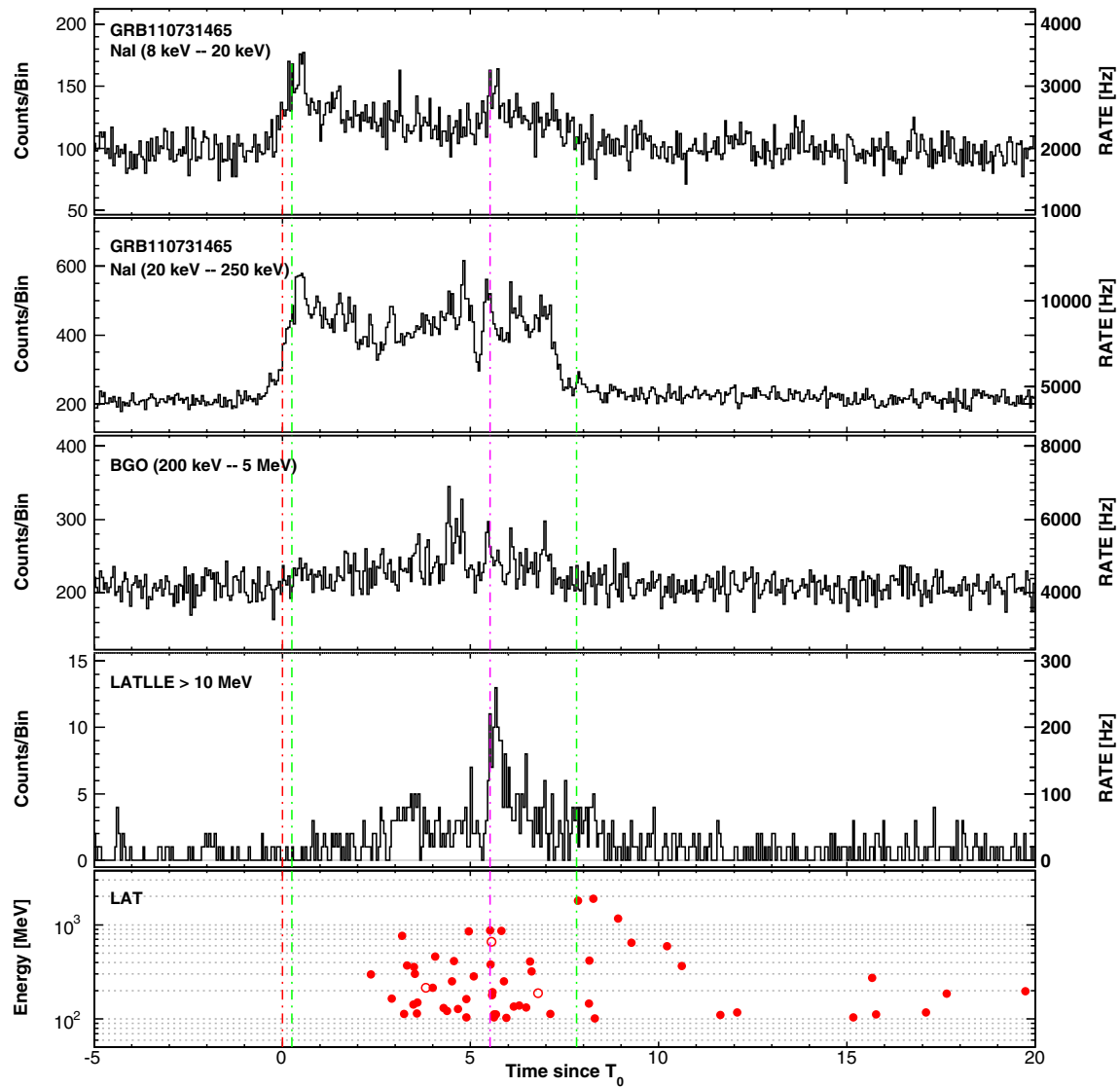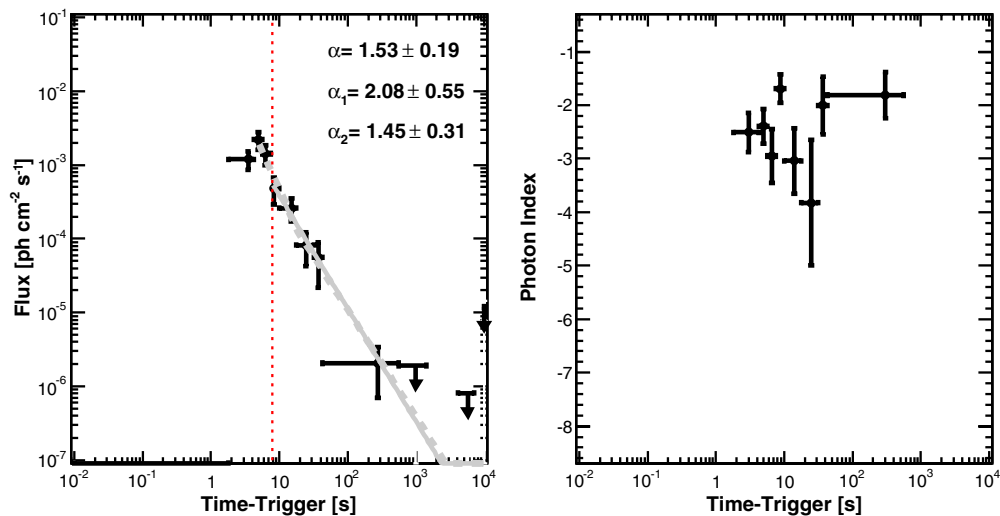(A color version of this figure is available in the online journal.)

Figure 92. Likelihood light curve for GRB 110625A (flux above 100 MeV on the left, photon index on the right). See Appendix B.1 for more information on lines and symbols.

(A color version of this figure is available in the online journal.)

Figure 93. Composite light curve for GRB 110709A: summed GBM/NaI detectors (first two panels), GBM/BGO (third panel), LLE (fourth panel), and LAT Transient-class events above 100 MeV within a 12° ROI (bottom panel). See Appendix B.1 for more information on lines and symbols in the LAT panels.

(A color version of this figure is available in the online journal.)

Figure 94. Likelihood light curve for GRB 110709A (flux above 100 MeV on the left, photon index on the right). See Appendix B.1 for more information on lines and symbols.

(A color version of this figure is available in the online journal.)

Figure 95. Composite light curve for GRB 110721A: summed GBM/NaI detectors (first two panels), GBM/BGO (third panel), LLE (fourth panel), and LAT Transient-class events above 100 MeV within a 12° ROI (bottom panel). See Appendix B.1 for more information on lines and symbols in the LAT panels.

(A color version of this figure is available in the online journal.)

Figure 96. Likelihood light curve for GRB 110721A (flux above 100 MeV on the left, photon index on the right). See Appendix B.1 for more information on lines and symbols.

(A color version of this figure is available in the online journal.)

Figure 97. Composite light curve for GRB 110731A: summed GBM/NaI detectors (first two panels), GBM/BGO (third panel), LLE (fourth panel), and LAT Transient-class events above 100 MeV within a 12° ROI (bottom panel). See Appendix B.1 for more information on lines and symbols in the LAT panels.

(A color version of this figure is available in the online journal.)

Figure 98. Likelihood light curve for GRB 110731A (flux above 100 MeV on the left, photon index on the right). See Appendix B.1 for more information on lines and symbols.

(A color version of this figure is available in the online journal.)

Swift-UVOT detected a bright afterglow candidate consistent with the XRT localization (Oates et al. 2011a). Further analyses refined the position of the burst (Krimm et al. 2011; Beardmore et al. 2011) and further observations confirmed the existence of fading X-ray (Littlejohns et al. 2011) and optical (Oates 2011; Tristram et al. 2011) afterglows. Tanvir et al. (2011) reported a spectroscopic redshift of $z = 2.83$ based on observations of the optical afterglow using GMOS. After a weather-induced delay, GROND detected GRB 110731A at a mean time of 2.74 days after the trigger time. A dedicated analysis of the NIR to GeV observations of GRB 110731A in its prompt and afterglow phases using data from *Fermi*, *Swift*, MOA, and GROND is presented in Ackermann et al. (2013).

The high-energy emission of GRB 110731A lasts much longer than the GBM estimated duration. A 1.90 GeV event is detected at $T_0+8.27$ s, right after the end of the GBM emission (Figure 97). The LAT time-resolved likelihood analysis resulted in a well sampled light curve of the high-energy flux up to ∼562 s (Figure 98). The decay of the flux as a function of time follows a simple PL starting from the GBM T_{95}, with a decay index $\alpha = 1.53 \pm 0.19$, in agreement with the result reported by Ackermann et al. (2013). This relatively steep decay is similar to the first part of the decay observed in GRBs 090510, 090902B, and 090926A (Table 9), for which a significant break was found in the flux light curve. This suggests that GRB 110731A was observed during the transition from the prompt phase to the afterglow phase, as discussed in Section 6.2. Moreover, the time-integrated spectrum of GRB 110731A is best represented by a Band function with an additional PL component. As discussed in Section 4.4.1, the detection of this additional component is marginal in the "GBM" time interval but significant in the other time interval (Tables 11 and 12), in agreement with Ackermann et al. (2013).

REFERENCES

Abdo, A. A., Ackermann, M., Ajello, M., et al. 2009a, ApJL, 706, L138
Abdo, A. A., Ackermann, M., Ajello, M., et al. 2009b, Natur, 462, 331
Abdo, A. A., Ackermann, M., Ajello, M., et al. 2009c, APh, 32, 193
Abdo, A. A., Ackermann, M., Ajello, M., et al. 2010a, ApJ, 723, 1082
Abdo, A. A., Ackermann, M., Ajello, M., et al. 2010b, ApJ, 712, 558
Abdo, A. A., Ackermann, M., Ajello, M., et al. 2011, ApJL, 734, L27
Abdo, A. A., Ackermann, M., Arimoto, M., et al. 2009d, Sci, 323, 1688
Abdo, A. A., Ackermann, M., Asano, K., et al. 2009e, ApJ, 707, 580
Ackermann, M., Ajello, M., Albert, A., et al. 2012a, ApJS, 203, 4
Ackermann, M., Ajello, M., Asano, K., et al. 2011, ApJ, 729, 114
Ackermann, M., Ajello, M., Baldini, L., et al. 2010a, ApJL, 717, L127
Ackermann, M., Ajello, M., Baldini, L., et al. 2012b, ApJ, 754, 121
Ackermann, M., Ajello, M., Baldini, L., et al. 2013, ApJ, 763, 71
Ackermann, M., Asano, K., Atwood, W. B., et al. 2010b, ApJ, 716, 1178
Akerlof, C. W., Zheng, W., Pandey, S. B., & McKay, T. A. 2010, ApJL, 725, L15
Akerlof, C. W., Zheng, W., Pandey, S. B., & McKay, T. A. 2011, ApJ, 726, 22
Allen, B., Yock, P., de Ugarte Postigo, A., et al. 2009, GCN, 9058
Amati, L. 2006, MNRAS, 372, 233
Amati, L., Frontera, F., Tavani, M., et al. 2002, A&A, 390, 81
Andreev, M., Sergeev, A., Parakhin, N., et al. 2009, GCN, 10273
Arnaud, K., Smith, R., & Siemiginowska, A. 2011, Handbook of X-Ray Astronomy (Cambridge: Cambridge Univ. Press)
Asano, K., Inoue, S., & Mészáros, P. 2009, ApJ, 699, 953
Atwood, W. B., Abdo, A. A., Ackermann, M., et al. 2009, ApJ, 697, 1071
Axelsson, M., Baldini, L., Barbiellini, G., et al. 2012, ApJL, 757, L31
Band, D., Matteson, J., Ford, L., et al. 1993, ApJ, 413, 281
Band, D. L., Axelsson, M., Baldini, L., et al. 2009, ApJ, 701, 1673
Baring, M. G., & Harding, A. K. 1997, ApJL, 481, L85
Barniol Duran, R., & Kumar, P. 2011, MNRAS, 417, 1584
Barthelmy, S. D., Barbier, L. M., Cummings, J. R., et al. 2005, SSRv, 120, 143
Beardmore, A. P., Evans, P. A., Goad, M. R., & Osborne, J. P. 2010, GCN, 11005

Beardmore, A. P., Evans, P. A., Goad, M. R., & Osborne, J. P. 2011, GCN, 12219
Berger, E. 2011, GCN, 12193
Bhat, P. N. 2010, GCN, 10977
Bissaldi, E. 2009, GCN, 9933
Bissaldi, E., Briggs, M. S., Piron, F., Takahashi, H., & Uehara, T. 2009, GCN, 9972
Bissaldi, E., & Connaughton, V. 2009, GCN, 9866
Bissaldi, E., von Kienlin, A., Kouveliotou, C., et al. 2011, ApJ, 733, 97
Blandford, R. D., & McKee, C. F. 1976, BAAS, 8, 539
Bošnjak, Ž., Daigne, F., & Dubus, G. 2009, A&A, 498, 677
Bouvier, A., Band, D., Bregeon, J., et al. 2008, GCN, 8183
Bregeon, J., McEnery, J., & Ohno, M. 2011, GCN, 12218
Briggs, M. S., & Connaughton, V. 2010, GCN, 10330
Burgess, J. M., Goldstein, A., & van der Horst, A. J. 2009, GCN, 9698
Burgess, J. M., & Guiriec, S. 2011, GCN, 12047
Burrows, D. N., Hill, J. E., Nousek, J. A., et al. 2005, SSRv, 120, 165
Butler, N. R., Kocevski, D., Bloom, J. S., & Curtis, J. L. 2007, ApJ, 671, 656
Cannizzo, J. K., Baumgartner, W. H., Evans, P. A., et al. 2010a, GCN, 11004
Cannizzo, J. K., Krimm, H. A., Stamatikos, M., Evans, P. A., & Oates, S. R. 2010b, GCNR, 294
Cano, Z., Melandri, A., Mundell, C. G., et al. 2009, GCN, 10262
Cenko, S. B., Bloom, J. S., Morgan, A. N., & Perley, D. A. 2009, GCN, 9053
Cenko, S. B., Frail, D. A., Harrison, F. A., et al. 2011, ApJ, 732, 29
Chandra, P., Cenko, S. B., & Frail, D. A. 2011, GCN, 12245
Chandra, P., & Frail, D. A. 2009, GCN, 9889
Chevalier, R. A., & Li, Z. 2000, ApJ, 536, 195
Chornock, R., Perley, D. A., Cenko, S. B., & Bloom, J. S. 2009, GCN, 9028
Connaughton, V. 2011, GCN, 12133
Connaughton, V., & Briggs, M. 2008, GCN, 8408
Corsi, A., Guetta, D., & Piro, L. 2010, A&A, 524, A92
Cucchiara, A., & Fox, D. B. 2010, GCN, 10606
Cucchiara, A., Fox, D. B., Cenko, S. B., Tanvir, N., & Berger, E. 2009a, GCN, 10031
Cucchiara, A., Fox, D. B., Tanvir, N., & Berger, E. 2009b, GCN, 9873
Cummings, J. R., Barthelmy, S. D., Gehrels, N., et al. 2009, GCN, 9461
Cutini, S., Vasileiou, V., & Chiang, J. 2009, GCN, 9077
de Palma, F., Bissaldi, E., Tajima, H., et al. 2009a, GCN, 9872
de Palma, F., Bregeon, J., & Tajima, H. 2009b, GCN, 9867
de Palma, F., Omodei, N., McEnery, J., & Vasileiou, V. 2009c, GCN, 10163
de Palma, F., Uehara, T., Bregeon, J., et al. 2010, GCN, 10548
de Pasquale, M., & Pagani, C. 2009, GCN, 10267
De Pasquale, M., Schady, P., Kuin, N. P. M., et al. 2010, ApJL, 709, L146
de Ugarte Postigo, A., Castro-Tirado, A. J., Gorosabel, J., et al. 2009, GCN, 10255
Del Monte, E., Barbiellini, G., Donnarumma, I., et al. 2011, A&A, 535, A120
Esposito, J. A., Bertsch, D. L., Chen, A. W., et al. 1999, ApJS, 123, 203
Evans, P. A. 2011, GCN, 12119
Evans, P. A., Osborne, J. P., & Goad, M. R. 2008, GCN, 8203
Fenimore, E. E., Epstein, R. I., & Ho, C. 1993, A&AS, 97, 59
Filgas, R., Kruehler, T., & Greiner, J. 2010, GCN, 10607
Filgas, R., Rossi, A., Kann, A. D., Rau, A., & Greiner, J. 2011, GCN, 12096
Fitzpatrick, G., McBreen, S., Connaughton, V., & Briggs, M. 2012, Proc., SPIE, 8443
Foley, S. 2010, GCN, 10595
Foley, S., & McBreen, S. 2010, GCN, 10449
Frail, D. A., Chandra, P., & Cenko, B. 2009, GCN, 9060
Frail, D. A., Chandra, P., Cenko, S. B., & Harrison, F. 2010, GCN, 10698
Gehrels, N., Chincarini, G., Giommi, P., et al. 2004, ApJ, 611, 1005
Ghirlanda, G., Ghisellini, G., & Nava, L. 2010, A&A, 510, 7
Ghirlanda, G., Ghisellini, G., Salvaterra, R., et al. 2013, MNRAS, 428, 1410
Ghisellini, G., Ghirlanda, G., Nava, L., & Celotti, A. 2010, MNRAS, 403, 926
Giuliani, A., Fuschino, F., Vianello, G., et al. 2010a, ApJL, 708, L84
Giuliani, A., Mereghetti, S., Fornari, F., et al. 2008, A&A, 491, L25
Giuliani, A., Tavani, M., Longo, F., et al. 2010b, GCN, 10996
Godet, O. 2009, GCN, 8907
Goldstein, A., Burgess, J. M., Preece, R. D., et al. 2012, ApJS, 199, 19
Goldstein, A., & van der Horst, A. 2008, GCN, 8245
Golenetskii, S., Aptekar, R., Mazets, E., et al. 2009, GCN, 8925
Golovnya, V. V. 2011, GCN, 12113
González, M. M., Dingus, B. L., Kaneko, Y., et al. 2003, Natur, 424, 749
Gorosabel, J., Terron, V., Ferrero, P., et al. 2011, GCN, 12098
Granot, J., & Sari, R. 2002, ApJ, 568, 820
Greiner, J., Clemens, C., Krühler, T., et al. 2009, A&A, 498, 89
Greiner, J., Updike, A. C., Kruehler, T., & Sudilovsky, V. 2011, GCN, 12192
Gronwall, C., & Starling, R. L. C. 2009, GCN, 9987
Gronwall, C., & Vetere, L. 2009, GCN, 9938

Gruber, D. 2011, GCN, 12221
Gruber, D., Omodei, N., Chaplin, V., et al. 2011, GCN, 12100
Grupe, D., Swenson, C. A., Racusin, J. L., & Wolf, C. 2011, GCN, 12212
Guidorzi, C., Schady, P., Barthelmy, S. D., et al. 2008, GCNR, 178
Guidorzi, C., Tanvir, N. R., Cano, Z., et al. 2009, GCN, 9875
Guiriec, S. 2009a, GCN, 8921
Guiriec, S. 2009b, GCN, 9501
Guiriec, S. 2010, GCN, 11423
Guiriec, S., Briggs, M. S., Connaugthon, V., et al. 2010, ApJ, 725, 225
Guiriec, S., Connaughton, V., & Briggs, M. 2009, GCN, 9336
Guiriec, S., Connaughton, V., Briggs, M. S., et al. 2011, ApJL, 727, L33
Haislip, J., Reichart, D., Ivarsen, K., et al. 2009a, GCN, 9953
Haislip, J., Reichart, D., Ivarsen, K., et al. 2009b, GCN, 9937
Haislip, J., Reichart, D., Ivarsen, K., et al. 2009c, GCN, 9984
Haislip, J., Reichart, D., Ivarsen, K., et al. 2009d, GCN, 10003
Haislip, J., Reichart, D., Ivarsen, K., et al. 2009e, GCN, 9982
Harrison, F., Cenko, B., Frail, D. A., Chandra, P., & Kulkarni, S. 2009, GCN, 9043
He, H.-N., Zhang, B.-B., Wang, X.-Y., Li, Z., & Mészáros, P. 2012, ApJ, 753, 178
Holland, S. T. 2011, GCN, 12148
Holland, S. T., Barthelmy, S. D., Burrows, D. N., et al. 2011a, GCN, 12118
Holland, S. T., Krimm, H. A., Cummings, J. R., & Stratta, G. 2011b, GCNR, 339
Holland, S. T., & Page, K. L. 2011, GCN, 12099
Hoversten, E. A., Barthelmy, S. D., Burrows, D. N., et al. 2009a, GCN, 9331
Hoversten, E. A., Krimm, H. A., Grupe, D., et al. 2009b, GCNR, 218
Hughes, E. B., Hofstadter, R., Rolfe, J., et al. 1980, ITNS, 27, 364
Hurley, K., Dingus, B. L., Mukherjee, R., et al. 1994, Natur, 372, 652
Hurley, K., Goldsten, J., Golenetskii, S., et al. 2011, GCN, 12195
Hurley, K., Mitrofanov, I. G., Golovin, D., et al. 2010, GCN, 11156
Hurley, K., Pal'shin, V. D., Aptekar, R. L., et al. 2013, ApJS, 207, 39
Im, M., Kim, J. H., Kim, D., & Kim, D. 2011, GCN, 12095
Ivanov, K., Poleshchuk, V. A., Yazev, S., et al. 2011, GCN, 12120
Ivarsen, K., Haislip, J., Reichart, D., et al. 2010, GCN, 11008
Kamble, A. P., van der Horst, A. J., Wijers, R. A. M. J., et al. 2010, GCN, 10697
Kanbach, G., Bertsch, D. L., Fichtel, C. E., et al. 1988, SSRv, 49, 69
Kaneko, Y., González, M. M., Preece, R. D., Dingus, B. L., & Briggs, M. S. 2008, ApJ, 677, 1168
Kaneko, Y., Preece, R. D., Briggs, M. S., et al. 2006, ApJS, 166, 298
Katz, J. I., & Piran, T. 1997, ApJ, 490, 772
Kelemen, J. 2011a, GCN, 12094
Kelemen, J. 2011b, GCN, 12146
Kennea, J. 2009, GCN, 9045
Kennea, J., Evans, P., & Goad, M. 2009a, GCN, 9024
Kennea, J., Evans, P., & Goad, M. 2009b, GCN, 9046
Kennea, J., & Stratta, G. 2009, GCN, 9868
Kennea, J. A. 2008, GCN, 8253
Kinugasa, K., Honda, S., Takahashi, H., Taguchi, H., & Hashimoto, O. 2009, GCN, 10275
Kouveliotou, C., Meegan, C. A., Fishman, G. J., et al. 1993, ApJL, 413, L101
Krimm, H. A., Barthelmy, S. D., Baumgartner, W. H., et al. 2011, GCN, 12217
Krolik, J. H., & Pier, E. A. 1991, ApJ, 373, 277
Kumar, P., & Barniol Duran, R. 2009, MNRAS, 400, L75
Kumar, P., & Panaitescu, A. 2000, ApJL, 541, L51
Kuroda, D., Hanayama, H., Miyaji, T., et al. 2011, GCN, 12139
Landsman, W., & Cannizzo, J. 2010, GCN, 10609
Lin, L. 2011, GCN, 11591
Lithwick, Y., & Sari, R. 2001, ApJ, 555, 540
Littlejohns, O. M., Evans, P. A., Beardmore, A. P., & Oates, S. R. 2011, GCN, 12224
Liu, R.-Y., & Wang, X.-Y. 2011, ApJ, 730, 1
Longo, F., Moretti, E., Barbiellini, G., et al. 2009a, GCN, 9343
Longo, F., Moretti, E., Barbiellini, G., et al. 2009b, GCN, 9524
Malesani, D. 2009, GCN, 9340
Malesani, D., Goldoni, P., Fynbo, J. P. U., et al. 2009, GCN, 9942
Mao, J., & Wang, J. 2012, ApJ, 748, 135
Marisaldi, M., Fuschino, F., Labanti, C., et al. 2010, GCN, 10994
Marshall, F. E., & Hoversten, E. A. 2009, GCN, 9332
Marshall, F. E., Oates, S. R., Rowlinson, A., et al. 2009, GCNR, 207
Massaro, F., & Grindlay, J. E. 2011, ApJL, 727, L1
Massaro, F., Grindlay, J. E., & Paggi, A. 2010, ApJL, 714, L299
Mattox, J. R., Bertsch, D. L., Chiang, J., et al. 1996, ApJ, 461, 396
McBreen, S. 2009a, GCN, 9535
McBreen, S. 2009b, GCN, 10266
McBreen, S., & Chaplin, V. 2009, GCN, 10115
McBreen, S., Krühler, T., Rau, A., et al. 2010, A&A, 516, A71

McEnery, J. 2008a, GCN, 8684
McEnery, J. 2008b, GCN, 8726
McEnery, J., Bregeon, J., & Kocevski, D. 2011, GCN, 12044
McEnery, J., Chiang, J., & Hanabata, Y. 2009a, GCN, 9985
McEnery, J., Chiang, J., Omodei, N., & Nakamori, T. 2010, GCN, 10333
McEnery, J., Cutini, S., Ohno, M., Koerding, E., & Connaughton, V. 2009b, GCN, 9044
McEnery, J., & Omodei, N. 2010, GCN, 11155
Meegan, C., Lichti, G., Bhat, P. N., et al. 2009, ApJ, 702, 791
Melandri, A., D'Avanzo, P., Margutti, R., & Sbarufatti, B. 2011a, GCN, 11989
Melandri, A., D'Avanzo, P., Margutti, R., Sbarufatti, B., & Stamatikos, M. 2011b, GCN, 11984
Meszaros, P., & Rees, M. J. 1994, MNRAS, 269, L41
Meszaros, P., & Rees, M. J. 1997, ApJ, 476, 232
Moskvitin, A., Fatkhullin, T., & Sokolov, V. 2010, GCN, 10618
Nakajima, H., Yatsu, Y., Mori, Y. A., et al. 2009, GCN, 10260
Oates, S. R. 2009, GCN, 9048
Oates, S. R. 2011, GCN, 12222
Oates, S. R., Beardmore, A. P., Holland, S. T., et al. 2011a, GCN, 12215
Oates, S. R., Ukwatta, T., Sakamoto, T., et al. 2011b, GCNR, 343
Oates, S. R., & Vetere, L. 2009, GCN, 9948
Ohno, M., Cutini, S., McEnery, J., Chiang, J., & Koerding, E. 2009a, GCN, 9021
Ohno, M., McEnery, J., & Pelassa, V. 2009b, GCN, 8903
Ohno, M., & Pelassa, V. 2009, GCN, 9334
Olivares, E. F., Kruehler, T., Filgas, R., et al. 2010, GCN, 11020
Olivares, F., Afonso, P., Greiner, J., et al. 2009a, GCN, 9874
Olivares, F., Klose, S., Krühler, T., & Greiner, J. 2009b, GCN, 9352
Omodei, N. 2008, GCN, 8407
Omodei, N., Chiang, J., Connaughton, V., & Tanaka, Y. 2011, GCN, 11597
Omodei, N., Granot, J., Meszaros, P., et al. 2009, GCN, 9350
Osborne, J. P., Beardmore, A. P., Evans, P. A., & Goad, M. R. 2009, GCN, 10259
Osborne, J. P., Beardmore, A. P., Evans, P. A., & Goad, M. R. 2011, GCN, 12123
Paciesas, W. S., Meegan, C. A., von Kienlin, A., et al. 2012, ApJS, 199, 18
Pagani, C., Beardmore, A. P., Evans, P. A., et al. 2009, GCN, 10256
Pagani, C., de Pasquale, M., & Baumgartner, W. H. 2010, GCNR, 266
Page, K. L. 2011, GCN, 12092
Page, K. L., Barthelmy, S. D., Beardmore, A. P., et al. 2011a, GCN, 12088
Page, K. L., & Cannizzo, J. K. 2010, GCN, 10632
Page, K. L., Evans, P. A., & Goad, M. R. 2010a, GCN, 10605
Page, K. L., Holland, S. T., Cummings, J. R., et al. 2011b, GCNR, 336
Page, K. L., Racusin, J. L., Kennea, J. A., & Cannizzo, J. K. 2010b, GCN, 10601
Page, K. L., Starling, R. L. C., Evans, P. A., & Beardmore, A. P. 2009, GCN, 9991
Palmer, D. M., Barthelmy, S. D., Baumgartner, W. H., et al. 2011, GCN, 12091
Panaitescu, A., & Kumar, P. 2000, ApJ, 543, 66
Pandey, S. B., Zheng, W., Yuan, F., & Akerlof, C. 2009, GCN, 9878
Pe'er, A., Zhang, B.-B., Ryde, F., et al. 2012, MNRAS, 420, 468
Pelassa, V., & Pesce-Rollins, M. 2010, GCN, 10945
Pelassa, V., Preece, R., Piron, F., et al. 2010, arXiv:1002.2617
Perley, D., Kleiser, I. K. W., & Rex, J. M. 2009a, GCN, 9870
Perley, D. A., Choi, J., Morton, A. J. L., & Ganeshalingam, M. 2009b, GCN, 9997
Perley, D. A., Klein, C. R., Morgan, A. N., & Li, W. 2010, GCN, 11007
Perley, D. A., Prochaska, J. X., Kalas, P., et al. 2009c, GCN, 10272
Perri, M., Preger, B., & Stratta, G. 2008, GCN, 8261
Perri, M., & Stratta, G. 2009, GCN, 9031
Piran, T. 2004, RvMP, 76, 1143
Piron, F., Longo, F., Iafrate, G., et al. 2009, GCN, 9584
Piron, F., Ohno, M., de Palma, F., Moretti, E., & McEnery, J. 2010, GCN, 10450
Preece, R. D., Briggs, M. S., Mallozzi, R. S., et al. 2000, ApJS, 126, 19
Pritchard, T. A., Hoversten, E. A., & Starling, R. L. C. 2009, GCN, 9990
Protassov, R., van Dyk, D. A., Connors, A., Kashyap, V. L., & Siemiginowska, A. 2002, ApJ, 571, 545
Racusin, J. L., Oates, S. R., Schady, P., et al. 2011, ApJ, 738, 138
Rau, A. 2009, GCN, 9983
Rau, A., McBreen, S., & Kruehler, T. 2009, GCN, 9353
Razzaque, S. 2010, ApJL, 724, L109
Razzaque, S., Dermer, C. D., & Finke, J. D. 2010, OAJ, 3, 150
Rees, M. J., & Meszaros, P. 1994, ApJL, 430, L93
Rowlinson, A., & Page, K. 2009, GCN, 9052
Rubtsov, G. I., Pshirkov, M. S., & Tinyakov, P. G. 2012, MNRAS, 421, L14
Ryde, F. 1999, ApL&C, 39, 281
Ryde, F., Axelsson, M., Zhang, B. B., et al. 2010, ApJL, 709, L172
Sari, R. 1997, ApJL, 489, L37

Sari, R., Piran, T., & Narayan, R. 1998, ApJL, 497, L17
Sbarufatti, B., Mangano, V., & Cummings, J. R. 2009, GCN, 9463
Scargle, J. D., Norris, J. P., Jackson, B., & Chiang, J. 2013, ApJ, 764, 167
Schady, P., Baumgartner, W. H., Beardmore, A. P., et al. 2009, GCN, 9512
Sommer, M., Bertsch, D. L., Dingus, B. L., et al. 1994, ApJL, 422, L63
Starling, R. L. C., & Beardmore, A. P. 2009, GCN, 9986
Starling, R. L. C., Page, K. L., Pritchard, T. A., et al. 2009, GCNR, 253
Stratta, G., D'Elia, V., & Perri, M. 2009a, GCN, 9876
Stratta, G., D'Elia, V., Perri, M., et al. 2009b, GCNR, 249
Stratta, G., Perri, M., Preger, B., et al. 2008, GCNR, 166
Swenson, C. A., Maxham, A., Roming, P. W. A., et al. 2010, ApJL, 718, L14
Swenson, C. A., & Siegel, M. H. 2009, GCN, 9869
Swenson, C. A., & Stratta, G. 2009, GCN, 9877
Tajima, H., Bregeon, J., Chiang, J., & Thayer, G. 2008, GCN, 8246
Takahashi, H., Ohno, M., & Omodei, N. 2010, GCN, 10594
Tam, P. H. T., & Kong, A. K. H. 2011, GCN, 12097
Tanaka, Y., Ohno, M., Bregeon, J., et al. 2010a, GCN, 11349
Tanaka, Y., Ohno, M., Takahashi, H., et al. 2010b, GCN, 10978
Tanvir, N. R., Wiersema, K., Levan, A. J., Cenko, S. B., & Geballe, T. 2011, GCN, 12225
Tavani, M., Barbiellini, G., Argan, A., et al. 2008, NIMPA, 588, 52
Tavani, M., Barbiellini, G., Argan, A., et al. 2009, A&A, 502, 995
Tello, J. C., Gorosabel, J., Castro-Tirado, A., Fernandez, M., & Huelamo, N. 2011, GCN, 12134
Thompson, D. J., Bertsch, D. L., Fichtel, C. E., et al. 1993, ApJS, 86, 629
Tierney, D., & Fitzpatrick, G. 2011, GCN, 12012
Tierney, D., & Goldstein, A. 2010, GCN, 11341
Tierney, D., & von Kienlin, A. 2011, GCN, 12187
Toma, K., Wu, X.-F., & Mészáros, P. 2011, MNRAS, 415, 1663
Tristram, P. J., Fukui, A., Ohnishi, K., & Sako, T. 2011, GCN, 12242
Troja, E., Rosswog, S., & Gehrels, N. 2010, ApJ, 723, 1711
Uehara, T., Takahashi, H., & McEnery, J. 2009, GCN, 9934
Updike, A., Klose, S., Clemens, C., & Greiner, J. 2009a, GCN, 9054
Updike, A., Rossi, A., & Greiner, J. 2009b, GCN, 10271
Updike, A. C., Filgas, R., Kruehler, T., Greiner, J., & McBreen, S. 2009c, GCN, 9026
Urata, Y., & Huang, K. Y. 2010, GCN, 10641
van der Horst, A. J. 2008, GCN, 8341
van der Horst, A. J. 2009, GCN, 9047
van der Horst, A. J., & Connaughton, V. 2008, GCN, 8141
van der Horst, A. J., Kamble, A. P., Wijers, R. A. M. J., & Kouveliotou, C. 2009, GCN, 9883
Vasileiou, V. 2013, APh, 48, 61
Vasileiou, V., Omodei, N., Chiang, J., et al. 2011a, GCN, 11835
Vasileiou, V., Omodei, N., Kocevski, D., & Piron, F. 2011b, GCN, 11982
Vasileiou, V., Piron, F., Tierney, D., et al. 2011c, GCN, 12188
Vetere, L. 2009, GCN, 9961
Vetere, L., Evans, P., & Goad, M. 2009a, GCN, 9936
Vetere, L., Oates, S., Barthelmy, S. D., et al. 2009b, GCNR, 254
von Kienlin, A. 2009a, GCN, 8902
von Kienlin, A. 2009b, GCN, 9579
von Kienlin, A. 2010a, GCN, 10546
von Kienlin, A. 2010b, GCN, 11006
von Kienlin, A. 2011, GCN, 11831
Wang, X.-Y., Li, Z., & Mészáros, P. 2006, ApJL, 641, L89
Wiersema, K., Tanvir, N., Levan, A., & Benn, C. 2009a, GCN, 9995
Wiersema, K., Tanvir, N. R., Cucchiara, A., Levan, A. J., & Fox, D. 2009b, GCN, 10263
Wilks, S. S. 1938, Ann. Math. Stat., 9, 60
Wilson-Hodge, C., Connaughton, V., Longo, F., & Omodei, N. 2008, GCN, 8723
Xin, L. P., Qian, S. B., Qiu, Y. L., et al. 2009, GCN, 10279
Xin, L. P., Qiu, Y. L., Wei, J. Y., et al. 2011, GCN, 12125
Xu, D., Leloudas, G., Malesani, D., et al. 2009, GCN, 10269
Yoshida, M., Kuroda, D., Yanagisawa, K., et al. 2009, GCN, 10258
Zhang, B.-B., Zhang, B., Liang, E.-W., et al. 2011, ApJ, 730, 141
Zheng, W., Akerlof, C. W., Pandey, S. B., et al. 2012a, ApJ, 745, 72
Zheng, W., Akerlof, C. W., Pandey, S. B., et al. 2012b, ApJ, 756, 64